



Engineering new urea-based supramolecular polymers for the characterization of weak interactions in solution : the supramolecular balance

Virgile Ayzac

► To cite this version:

Virgile Ayzac. Engineering new urea-based supramolecular polymers for the characterization of weak interactions in solution : the supramolecular balance. Polymers. Université Pierre et Marie Curie - Paris VI, 2016. English. NNT : 2016PA066748 . tel-02999301

HAL Id: tel-02999301

<https://theses.hal.science/tel-02999301>

Submitted on 10 Nov 2020

HAL is a multi-disciplinary open access archive for the deposit and dissemination of scientific research documents, whether they are published or not. The documents may come from teaching and research institutions in France or abroad, or from public or private research centers.

L'archive ouverte pluridisciplinaire **HAL**, est destinée au dépôt et à la diffusion de documents scientifiques de niveau recherche, publiés ou non, émanant des établissements d'enseignement et de recherche français ou étrangers, des laboratoires publics ou privés.

Université Pierre et Marie Curie

Ecole doctorale 397

Institut Parisien de Chimie Moléculaire / Laboratoire de Chimie des Polymères

Engineering new urea-based supramolecular polymers for the characterization of weak interactions in solution : the supramolecular balance

Par Virgile Ayzac

Thèse de doctorat de Chimie

Dirigée par Laurent Bouteiller

Présentée et soutenue publiquement le 13 décembre 2016

Devant un jury composé de :

M. Gilles Guichard	Directeur de recherche	Université de Bordeaux	Rapporteur
M. Franck Meyer	Professeur	Université de Bruxelles	Rapporteur
Mme. Valérie Marvaud	Directeur de recherche	Université Pierre et Marie Curie	Examinateur
M. Scott Cockroft	Professeur	University of Edinburgh	Examinateur
M. Laurent Bouteiller	Directeur de recherche	Université Pierre et Marie Curie	Directeur de thèse



Except where otherwise noted, this work is licensed under
<http://creativecommons.org/licenses/by-nc-nd/3.0/>

“My dear colleague, abandon the idea of giant molecules, organic molecules with a molecular weight of more than 5,000 do not exist. Purify your products, like rubber, and then they will crystallise and prove to be low-molecular substances.”

Heinrich Wieland to Hermann Staudinger (end of the 1920s)

Remerciements

Je souhaiterais avant tout remercier Laurent. Merci de m'avoir fait confiance et de m'avoir donné les conditions idéales pour effectuer mes recherches. En effet, tu as toujours été disponible, patient, prêt à discuter et à te casser la tête pour comprendre mes résultats. Tu as toujours été réceptif à mes idées et m'a laissé suffisamment de liberté pour que je puisse m'épanouir.

Je tiens à remercier les membres du jury pour avoir accepté de prendre de leur temps pour évaluer mes travaux. Je remercie le Dr. Gilles Guichard et le Pr Franck Meyer d'avoir accepté d'être mes rapporteurs et leur souhaite bon courage pour la lecture de ce manuscrit. Merci à Valérie Marvaud pour avoir accepté de présider ce jury.

I would like to thank Pr. Scott Cockroft for his participation to this jury as I could not imagine someone with a better background to judge the main topic of this thesis.

Je souhaite également remercier Matthieu Raynal pour avoir toujours été présent, disponible et fortement impliqué dans mes différents projets. Merci pour avoir commencé la thématique des bis-urées ester, pour les corrections qui t'ont sûrement fait perdre quelques cheveux et pour tes conseils sur la propreté du labo. Je remercie également Benjamin Isare pour avoir participé à mes différents projets, pour ses corrections et pour son enthousiasme politique.

Merci à Patrick Brocorens, Julien Idé et Roberto Lazzaroni de l'université de Mons pour la modélisation des structures de mes bis-urée. Merci à Xavier Assfeld et Antonio Monari de l'université de Nancy pour leur modélisation de la liaison X...X et pour leurs conseils sur le modèle que nous avons développé pour la balance.

Merci à l'ANR pour avoir financé ma thèse.

Merci à Xavier pour m'avoir supporté aussi bien au labo qu'au bureau sachant que je ne suis pas forcément la personne la plus facile à vivre. Merci pour toutes ces discussions, parfois enflammées, sur la chimie comme sur tout autre sujet. Merci pour tes idées, pour ton calme, pour tes crédits à taux whisky, pour m'avoir donné le goût du vélo dans la jungle parisienne et pour avoir fait de notre petit cocon un endroit idéal pour faire notre recherche.

Merci à Morgan pour m'avoir tenu tête et pour tout ce temps privilégié passé à assouvir notre addiction commune. Merci pour toutes ces discussions, souvent enflammées, sur la chimie, le cinéma et sur tout autre sujet. Merci pour avoir été aussi mauvais que moi à l'héritage du risque.

Merci à Alaric pour avoir partagé son savoir et ses anecdotes avec nous durant ses deux ans de post-doc. Merci pour nous avoir initié à l'héritage du risque et merci pour ces quelques coups de marteau.

Merci à Thomas pour son calme. Merci à Léodagand pour sa bonne humeur.

Merci à Gaëlle, Claire, Romain et Ludovic qui font tourner le labo en assurant que toutes les machines soient au meilleur de leur forme et que nous ayons toujours à disposition le matériel nécessaire à notre recherche.

Merci à mes stagiaires Pierre Jaquemot, Fabien Ouvré et Cédric Barcha. Merci plus particulièrement à Cedric pour avoir su se dépasser.

Merci à la Cédric Przybylski pour les analyses HRMS de mes produits.

Merci à Nicolas Vanthyune pour les analyses en HPLC chirale de certains de mes produits.

Merci à tous les autres permanents, post-doctorants et doctorants du laboratoire de chimie des polymères pour m'avoir permis de réaliser mes travaux dans un cadre agréable.

Merci à mes parents pour toujours avoir été là pour moi et pour m'avoir soutenu et encouragé pendant ces trois ans. Merci à ma sœur et à son mari pour m'avoir montré qu'il est plus facile d'écrire une thèse que d'élever deux garçons. Merci à mon frère et à sa femme pour m'avoir montré que l'on peut toujours se réinventer et que le principal reste que notre travail soit notre passion.

Merci à Gwenn pour tous ces moments de joie et de partage. Merci à Adrien pour nos passions partagées. Merci à Vincent, Quentin et Audrey pour avoir gardé une partie de mon âme à Strasbourg. Merci à Clément, Lucas et Alex pour tous ces moments passés ensemble durant ces trois années parisiennes.

En espérant que la lecture de ce manuscrit vous intéressera tout en restant digeste.

Contents

Remerciements	5
Contents	7
Nomenclature.....	11
Abbreviations	12
General introduction	13
Chapter 1: Measuring supramolecular interactions and bis-ureas	17
A. Systems for the measurement of small energy interactions	18
1. Bimolecular systems.....	18
2. Monomolecular system: the molecular torsion balance	25
B. The supramolecular balance concept and bis-ureas.....	40
1. Bis-ureas, an ideal scaffold for the supramolecular balance	40
2. Early results	41
3. Influence of the bis-urea structure on the self-assembly	42
Chapter 2 : Structural study of ester bis-urea assemblies	45
A. Racemic ester bis-ureas.....	46
1. Morphology of the assemblies	47
2. Local structure.....	49
3. Structural transition	52
4. Conclusion	56
B. Enantiopure ester bis-ureas	56
1. Comparison with racemic ester bis-ureas	57
2. Structural determination using CD.....	61
3. Molecular modeling	63
4. Conclusion	69
C. Appendix.....	70
1. SANS analyses.....	70
2. nDSC analyses.....	71
3. FTIR analyses	73
4. Circular Dichroism analyses.....	75
Chapter 3: Majority rules effect in ester bis-ureas	79
A. Majority rules in supramolecular polymers	80
1. A simple system exhibiting the majority rules effect: BTAs	80

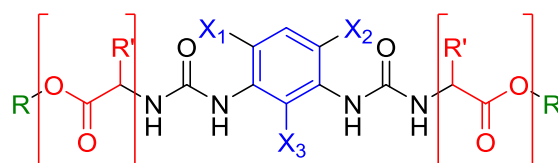
2. Majority rules in alkyl bis-ureas	87
B. Majority rules in ester bis-ureas.....	89
1. Results	90
2. Designing a new model	92
3. Fitting the data	93
Chapter 4 : Using the supramolecular balance to measure halogen···halogen interactions.....	97
A. The halogen···halogen interaction	98
1. Halogen bond history	98
2. Halogen bond definition.....	99
3. Halogen bond properties.....	99
4. Nature of the halogen bond	101
5. Solvent effect.....	101
6. Applications.....	101
7. The particular case of halogen-halogen interactions.....	104
B. Application of the supramolecular balance	106
1. The choice of the molecule	106
2. Detailed study of Br3C11Xyl in aromatic solvents	111
3. Detailed study of Br3C11Xyl in halogenated alkanes.....	114
4. Solvation versus interaction	115
5. Analysis of the data in halogenated alkanes	118
C. Appendix.....	125
1. FTIR analyses	125
2. nDSC analyses.....	127
Chapter 5: Characterization and rheological properties of a new type of assembly.....	133
A. Characterization of the new assembly	134
B. Influence of the chemical structure of the ester bis-ureas	139
1. The spacer	139
2. The aminoacid	141
3. The side chain.....	146
C. Influence of chirality.....	148
D. Influence of the solvent.....	149
E. Influence of the concentration.....	150
F. Towards a thermothickening additive.....	151
G. Appendix: molecular modeling	155

General conclusion	159
Chapter 6 : Synthesis and characterization techniques	161
A. Characterization techniques.....	162
1. SANS	162
2. FTIR.....	163
3. CD	163
4. Rheology.....	163
5. ITC.....	163
6. nDSC	163
7. Molecular modeling	163
B. Synthesis.....	164
1. Common synthetic methods	164
2. Precursors.....	168
3. Ester ammonium tosylate salts	174
4. Ramified ester bis-ureas.....	185
5. Non-ramified ester bis-ureas.....	188
6. Functionalized ester bis-ureas.....	199

Nomenclature

The nomenclature used for bis-ureas in this thesis is general to all chapters but a few differences are present in some chapters in order to highlight the nature of the bis-urea or to shorten its name.

The general structure and nomenclature is described in Figure 1.



alkyl bis-ureas : side chain spacer (e.g. EtHexTol)

ester bis-ureas : side chain amino-acid spacer (e.g. EtHexAlaTol)

Figure 1 : Structure and nomenclature of alkyl and ester bis-ureas

In **Chapter 2**, as we compare alkyl and ester bisureas, the amino-acid is in italics in order to highlight the bis-urea nature. Moreover, as the tolyl spacer is the only one used in this chapter, it does not appear in the nomenclature in order to shorten it. (e.g. EtHex and EtHexAla)

In **Chapter 3**, as the tolyl spacer is the only one used in this chapter, it does not appear in the nomenclature in order to shorten it. (e.g. EtHexAla)

In **Chapter 4**, as the phenylalanine amino-acid is the only one used in this chapter, it does not appear in the nomenclature in order to shorten it. (e.g. H3C11Xyl)

In **Chapter 5**, as the phenylalanine amino-acid is the most used in those chapters, it is not specified in the nomenclature. (e.g. H3C11Xyl)

Abbreviations

AcOEt	ethyl acetate
CD	Circular Dichroism spectroscopy
CSD	Cambridge Structural Database
DCM	dichloromethane
DFT	Density Functional Theory
DIEA	diisopropylethylamine
DIPA	diisopropylamine
DMSO	Dimethylsulfoxide
DSC	Differential Scanning Calorimetry
ESI	Electro-Spray Ionisation
FTIR	Fourier Transform Infra Red spectroscopy
HB or H-bond(ing)	Hydrogen bond(ing)
HMPA	hexamethylphosphoramide
HRMS	High-Resolution Mass Spectrometer
HRP	Helix Reversal Penalty
ITC	Isothermal Titration Calorimetry
IUPAC	International Union of Pure and Applied Chemistry
LCST	Low Critical Solution Temperature
LDA	lithium diisopropylamide
MMP	MisMatch Penalty
nDSC	High Sensitivity Differential Scanning Calorimetry (nano-DSC)
NMR	Nuclear Magnetic Resonance spectroscopy
NOESY	Nuclear Overhauser Effect Spectroscopy
PE	petroleum ether
PEPO	polyethylene-polypropylene oxide
PNIPAM	poly(N-isopropylacrylamide)
PTSA	paratoluenesulfonic acid
SANS	Small Angle Neutron Scattering
THF	tetrahydrofuran
THP	tetrahydropyran
UV	Ultra Violet spectroscopy
XB or X-bond(ing)	Halogen bond(ing)
ee	enantiomeric excess
BTA	benzene-1,3,5-tricarboxamide
EHUT	ethylhexylureido-2,4-toluene
TDI	toluene-2,4-diisocyanate

General introduction

The properties of the materials that form the world we live in are directly related to their structure. The structure of matter from the simple splash of water to more complex systems such as wood can have many levels of complexity but any molecular material is maintained by two types of interactions: covalent interactions which form molecules and non-covalent supramolecular interactions which dictate the way molecules behave with each others in order to form macroscopic structures.

The 20th century has seen the birth of great discoveries concerning covalent chemistry whether organic or inorganic but it has also seen the birth and the beginning of the rationalization of non-covalent chemistry^[1,2]. Nowadays, the control of supramolecular interactions is of outmost importance as it has consequences in numerous scientific fields such as crystal engineering^[3], catalysis^[4], rational drug discovery^[5], protein folding prediction^[6] or nanomechanical devices design^[7]. In order to control these interactions, it is essential to characterize and to measure them. Strong supramolecular interactions such as hydrogen-bonding are now well understood and easily quantifiable but weaker interactions such as π -interactions or σ -hole interactions are less known, particularly in solution. Many molecular or bimolecular systems have been designed to measure such interactions and the initial purpose of this work was to use supramolecular polymers in this context. Indeed, the cooperativity associated with the growth of some supramolecular polymers is expected to hugely increase the sensitivity of the measurement.

Supramolecular polymers are chains of low molar mass molecules (monomers) that self-assemble into linear chains via highly directional non-covalent interactions such as hydrogen bonds, metal-ligand complexation, π - π interactions or host-guest interactions. A structural analogy with polymers can be drawn as supramolecular polymers with long enough chains display similar rheological or mechanical properties. Unlike polymers and their covalent structures, supramolecular polymers have a dynamic structure, meaning the formed chains can break and form again at room temperature allowing properties such as self-healing^[8], stimuli responsiveness^[9] or improved processing^[10].

Plenty of examples of synthetic supramolecular polymers were reported over the last two decades bearing various structures and properties^[11–13]. A few examples of natural supramolecular polymers such as microtubules and actin filaments were reported as well^[14]. Almost all of the synthetic supramolecular polymers that are known self-assemble into a unique and fixed structure through isodesmic, cooperative, or anticooperative mechanisms^[12] (Figure 2).

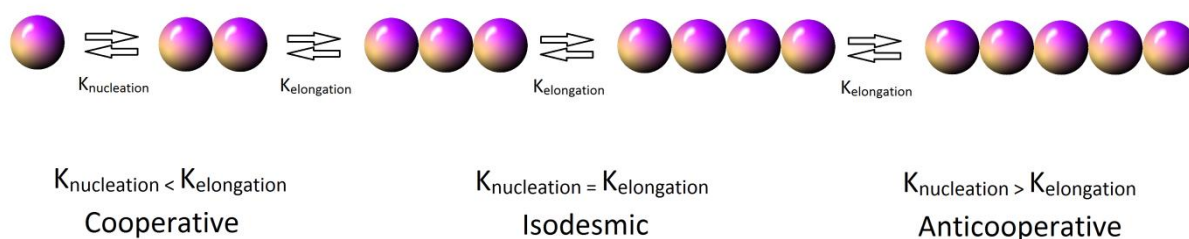


Figure 2 : Supramolecular polymerisation mechanisms

Our lab has been working with bis-ureas as supramolecular polymers since 2000^[15] and has shown in 2005 that a certain bis-urea based supramolecular polymer (EHUT) had the ability to form two different self-assembled structures^[16] (Figure 3) in low-polarity solvents.

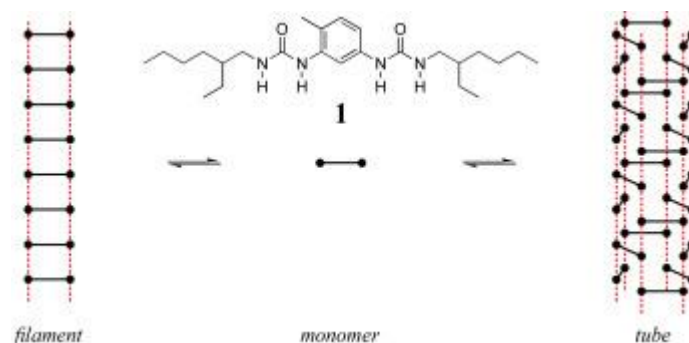


Figure 3 : Schematic structures of the different assemblies in equilibrium^[16]

There is a cooperative transition between those two structures, identified as a tube and a filament^[17], at a temperature T^{**} . The cooperativity of this transition was used as a balance to measure interactions between allyl groups^[18]. Unfortunately, this system presented limits in functionalization, solubility and chirality control, thus leading towards a new design of the bis-urea.

Therefore, my Ph.D. project was the development of a new family of bis-ureas as a versatile platform to quantify weak supramolecular interactions in solution. In principle, this supramolecular balance approach should allow the measurement of weak supramolecular interaction energies with a higher precision than what was previously done with other approaches.

This work involved collaborations with the Lazzaroni group in Mons and the Assfeld group in Nancy for their knowledge in molecular modeling.

The first chapter of this thesis will present the different molecular systems used for the quantification of supramolecular interactions, the concept of the supramolecular balance and what is known about these bis-ureas. Then, in a second chapter, the structural study of a new family of bis-ureas will be presented. The third chapter will show and reason how these molecules can be used to amplify chirality at the supramolecular level, which is of potential interest in the context of catalysis. The results we obtained within the context of the supramolecular balance using these new compounds will be described in the fourth chapter. In the final chapter we will show that this new family of bis-urea can form a third type of assembly with unexpected rheological properties.

- [1] C. Fouquey, J. M. Lehn, A. M. Levelut, *Adv. Mater.* **1990**, *2*, 254–257.
- [2] R. P. Sijbesma, F. H. Beijer, L. Brunsveld, B. J. B. Folmer, Hirschberg, J. H. K. K., R. F. M. Lange, J. K. L. Lowe, E. W. Meijer, *Science* **1997**, *278*, 1601–1604.
- [3] G. Desiraju, T. Steiner, *The Weak Hydrogen Bond*, Oxford University Press, **2001**.
- [4] T. Ikariya, A. J. Blacker, *Acc. Chem. Res.* **2007**, *40*, 1300–1308.
- [5] J. Michel, *Phys. Chem. Chem. Phys.* **2014**, *16*, 4465–4477.
- [6] E. Shakhnovich, *Chem. Rev.* **2006**, *106*, 1559–1588.
- [7] J. N. Munday, F. Capasso, V. A. Parsegian, *Nature* **2009**, *457*, 170–173.
- [8] P. Cordier, F. Tournilhac, C. Soulié-Ziakovic, L. Leibler, *Nature* **2008**, *451*, 977–980.
- [9] M. Burnworth, L. Tang, J. R. Kumpfer, A. J. Duncan, F. L. Beyer, G. L. Fiore, S. J. Rowan, C. Weder, *Nature* **2011**, *472*, 334–337.
- [10] B. J. B. Folmer, R. P. Sijbesma, R. M. Versteegen, J. A. J. Van Der Rijt, E. W. Meijer, *Adv. Mater.* **2000**, *12*, 874–878.
- [11] A. Ciferri, *Macromol. Rapid Commun.* **2002**, *23*, 511–529.
- [12] T. F. A. De Greef, M. M. J. Smulders, M. Wolffs, A. P. H. J. Schenning, R. P. Sijbesma, E. W. Meijer, *Chem. Rev.* **2009**, *109*, 5687–5754.
- [13] E. Elacqua, N. ten Brummelhuis, M. Weck, in *Handbook Metathesis*, Wiley-VCH Verlag GmbH & Co. KGaA, **2015**, pp. 71–92.
- [14] M. F. Carlier, S. Wiesner, C. Le Clainche, D. Pantaloni, *C. R. Biologie* **2003**, *326*, 161–170.
- [15] S. Boileau, L. Bouteiller, F. Lauprêtre, F. Lortie, *New J. Chem.* **2000**, *24*, 845–848.
- [16] L. Bouteiller, O. Colombani, F. Lortie, P. Terech, *J. Am. Chem. Soc.* **2005**, *127*, 8893–8898.
- [17] T. Pinault, B. Isare, L. Bouteiller, *ChemPhysChem* **2006**, *7*, 816–819.
- [18] M. Roman, C. Cannizzo, T. Pinault, B. Isare, B. Andrioletti, P. van der Schoot, L. Bouteiller, *J. Am. Chem. Soc.* **2010**, *132*, 16818–16824.

Chapter 1: Measuring supramolecular interactions and bis-ureas

Abstract: In this chapter, we present the literature. In a first part, we describe different supramolecular systems and methodologies used to measure the strength of supramolecular interactions. In a second part, we describe the structure to property relationship in bis-ureas synthesized in the Bouteiller group and the supramolecular balance principle.

Supramolecular interactions govern the morphology of any existing molecular system. They are responsible via intramolecular interactions for the conformation of single molecules but also via intermolecular interactions for the effect of the solvent on a system (e.g. the solubility of a compound), the structure of polymolecular assemblies in solution or in the bulk and for the crystal packing in the solid-state. With a great knowledge of those interactions (nature, directionality and energy), it would be possible to predict the morphology of any given system. For example, it would be possible to predict the interaction between a drug and the active site of a protein thus facilitating screening or to design more intelligent materials.

Supramolecular interactions can be studied in all three states of matter. In the gas-state, it is usually studied via spectroscopy (FTIR, Raman, ...) at low pressure and temperature. In the solid-state it is usually studied using X-ray diffraction. However, from now on, we will only focus on studies in solution.

Many systems were designed over the years to measure supramolecular interactions in solution relying on multiple techniques such as spectroscopy (UV, FTIR, CD, Raman, NMR, ...), calorimetry (DSC, ITC) and neutron scattering (SANS).

When strong enough, many interactions can be studied via direct titration of the complex of two molecules formed via the studied interaction but here we focus on the study of small energy interactions that are too weak to be measured directly. Different approaches were designed for that goal: some rely on bimolecular systems and the others on monomolecular systems.

A. Systems for the measurement of small energy interactions

1. Bimolecular systems

a. The double mutant cycle

During his work on the assessment of cooperative interactions on the substrate binding properties of an enzyme, Fersht proposed, in 1984, a general thermodynamic cycle^[1] he later called the “double-mutant cycle”^[2] (Figure 4). This system can be applied to synthetic chemical systems for the quantification of non-covalent interactions. It is based on the measurement of the complexation constant between two complementary molecules interacting via multiple interactions (complex A), one of them being the studied interaction ($x \cdots y$). This constant gives the free energy of interaction of the sum of all interactions. To extract the studied interaction energy, a first “mutation” is applied on one of the molecule to suppress one of the interacting moiety (x) of the studied interaction and the complexation constant of B is measured but it now depends on the interaction between the remaining y moiety and the rest of the complex B. The complexation constant of the mutant without the y moiety (complex C) is measured as well. To inhibit the influence of the remaining moiety, a third mutant bearing neither moiety (complex D) is made and its complexation constant is measured. Thus $\Delta G_{x \cdots y}$ can be calculated from ΔG_A , ΔG_B , ΔG_C and ΔG_D (Figure 4).

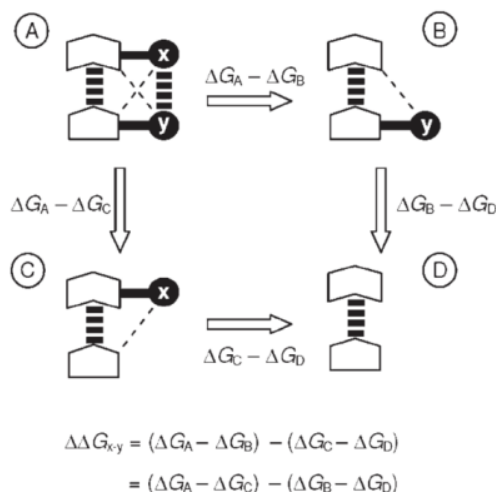


Figure 4 : the double-mutant cycle with supramolecular complexes^[3]

This strategy is reliable within a few constraints. (i) Secondary perturbations must be additive functions of the mutations. (ii) The mutant substitutions should be non-interacting since the double mutant is the reference state. (iii) There should be no difference of conformation within the cycle.

A main advantage of this strategy is that both attractive and repulsive interactions with small energies can be measured ($\sim 1 \text{ kJ.mol}^{-1}$). Moreover, the measurement of the free energies of complexation is easily accessible via ^1H NMR titrations.

i. Early results

Aoyama used bifunctional metalloporphyrins that bind amino-acids and amino-esters to measure H-bonding in chloroform between an aromatic alcohol and an acid/ester (Figure 5).^[4]

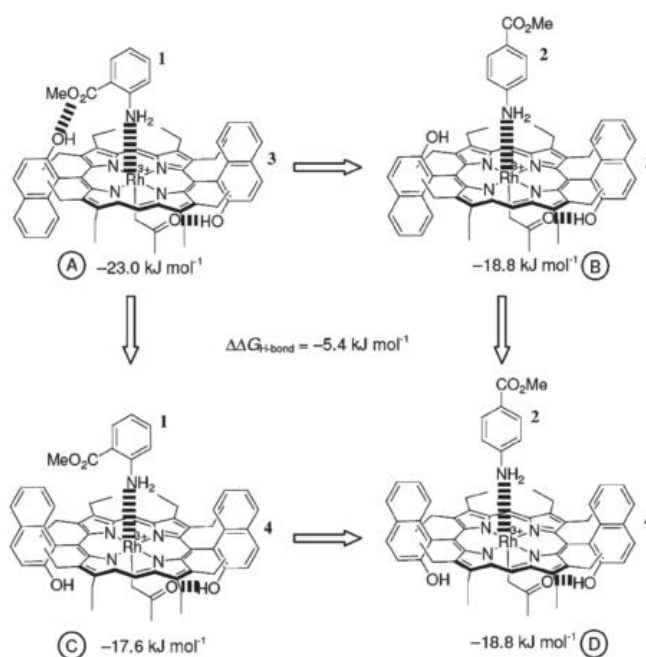


Figure 5 : Aoyama's complexes structures and double-mutant cycle^[4]

The mutations needed for the double mutant strategy are in this case isomerisations: the use of the *para*-isomer of the amino-acid/ester and/or the *cis*-isomer (constrained rotamer) of the porphyrin prevents the formation of the interaction. Those interactions display a free energy of -11.3 kJ/mol for the naphthol/acid and -5.4 kJ/mol for the naphthol/ester. Those values fit with what was measured before in direct complexation. It demonstrates the viability of this approach.

Rebek and coworkers designed a system to measure phosphate-guanidinium interactions in water (Figure 6).^[5]

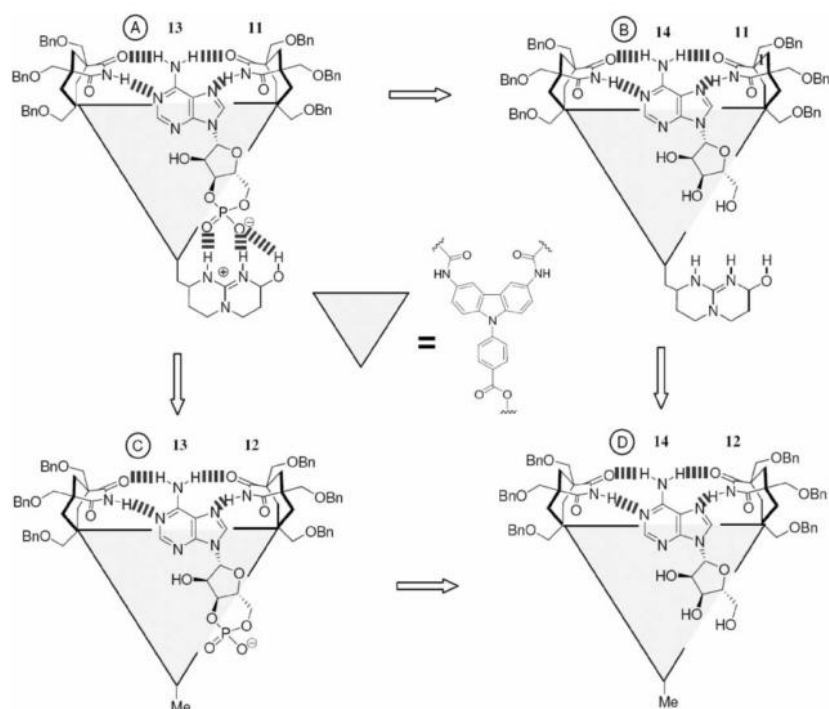
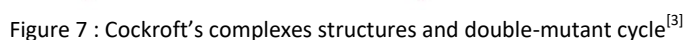


Figure 6 : Rebek's complexes structures and double-mutant cycle^[5]

The complex between the cyclic adenosine monophosphates and their receptors in water is a combination of hydrophobic, H-bonding and electrostatic interactions. The double mutant strategy was applied with the phosphate and the guanidinium as mutating groups. The interaction was shown to be dependent of the ionic strength of the solution with -2.5 kJ/mol at 51 mM and -1.2 kJ/mol at 501 mM. More importantly, it was noted that contrary to complex **B**, **C** and **D**, complex **A** exhibits two constrained rotors thus the measured values represent the lower limits of the interaction free energies.

ii. Aromatic edge-to-face interactions

Cockroft and Hunter developed this strategy as well for the measurement of edge to face aromatic interactions. For this purpose, they developed so-called "zipper" complexes that consist of one bisaniline derivative and one isophthaloyl derivative that form 1:1 complexes in CDCl₃ solutions.



Interaction	X	Y-Substituent		
		NMe ₂	H	NO ₂
	NMe ₂	-0.9	-1.1	-1.4
	H	-1.8	-1.4	-0.2
	NO ₂	-4.6	-3.4	+1.2
	NMe ₂	-1.6 ^a	-2.0 ^a	-2.4 ^a
	H	-1.8	-1.4	-0.2
	NO ₂	-4.3	-3.1	-0.5
	NMe ₂	-1.6 ^a		
	H	+0.9		
	NO ₂	+2.2 ^a		

Figure 8 : edge-to-face interaction energies (kJ/mol) in CDCl_3 at 296K^[3]

The magnitudes of the edge to face interactions were found to correlate with Hammett substituent constants and electrostatic surface potentials demonstrating electrostatics are the main component of the interaction energy.

iii. Aromatic face-to-face interactions

Cockroft and coworkers used the same design to measure the influence of the substituents on the aromatic stacking interactions.^[6] This system forces both aromatic groups in a face-to-face conformation via the introduction of methyl groups in the *ortho*-position of one of the interacting phenyl group (Figure 9).

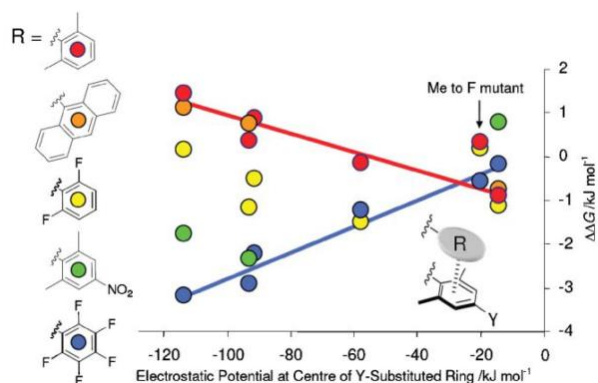


Figure 9 : Plot of experimental aromatic stacking interaction energies measured in zipper complexes (y-axis) against the B3LYP/6-31G* calculated electrostatic surface potential at the ring centre of substituted isophthaloyl derivatives (x-axis from left to right, Y = NMe₂, H, OMe, Cl, H (with both methyl groups mutated to fluorine) and NO₂. Errors are around 1 kJ/mol.^[6]

They varied the substituents in the Y position (NMe₂, H, Cl and H with F in *ortho* instead of the methyl groups) and studied the interaction with five aromatic groups (*ortho*-dimethylphenyl, anthracyl, *ortho*-difluorophenyl, *para*-nitro-*ortho*-dimethylphenyl and pentafluorophenyl). They calculated the electrostatic potential at the center of the Y-substituted ring and plotted it versus the interaction energy.

The interaction is repulsive with electron-rich aromatics and slightly attractive with electron-poor aromatics. A pentafluorophenyl group inverted the substituent induced trend compared to phenyl or anthracene groups. Stacking interaction energies trends can thus be explained by pure electrostatics.

iv. Aromatic-halogen interactions

Cockroft and coworkers also investigated the interaction between a halogen and an aromatic ring.^[7]

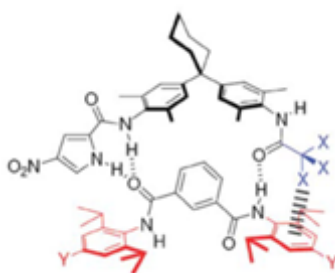


Figure 10 : Cockroft's complex structure^[7]

In this case, the conformational control was improved as a pyrole group was used to lock the conformation on one side of the complex. They found out that the interaction was always repulsive but this design is not ideal as the geometric constraint is really important and thus the measured interactions are highly dependent on steric effects. Moreover, the poor solubility of the bisaniline derivatives in CDCl₃ lowered the accuracy of the association constants measurement.

v. The triple mutant cycle strategy

One of the limitations of the double mutant cycle strategy is cooperativity between interactions when the interaction energies are no longer additive. It is possible to assess the effect of cooperativity between two intermolecular interactions with a combination of two double mutant cycles measuring the same interaction. It is known as a triple mutant cycle (Figure 11).^[2]

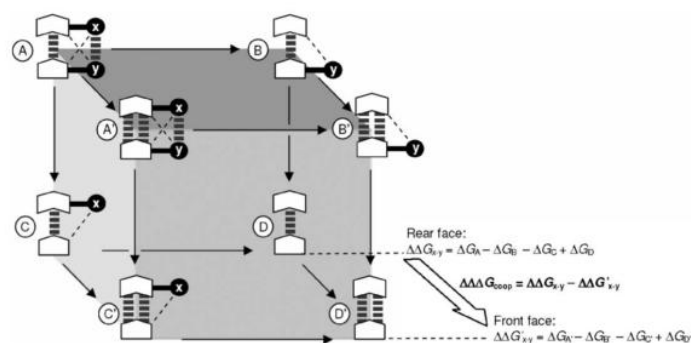


Figure 11 : The triple mutant thermodynamic cycle^[3]

The rear face is a typical double mutant cycle containing a single anchoring interaction and the front face is the same double mutant cycle with an additional anchoring interaction. Thus, the free energy difference between the front and rear faces is a measure of the cooperativity between the additional anchoring interaction and the $x \cdots y$ interaction.

The double-mutant cycle is a robust thermodynamic tool able to extract weak non-covalent interaction energies from the noisy background of multiple secondary interactions. This approach has been widely used in proteins and synthetic chemical systems. Interactions were measured down to -0.4 kJ/mol with errors lower than 1 kJ/mol (as low as 0.9 kJ/mol).^[6] However, this approach is less and less used as the mutations vary the steric constraints affecting the measured interaction.

b. The supramolecular balance for transition metal complexes

A different approach was used by Gschwind and coworkers as they used Pd complexes and ligand exchange equilibrium.^[8]

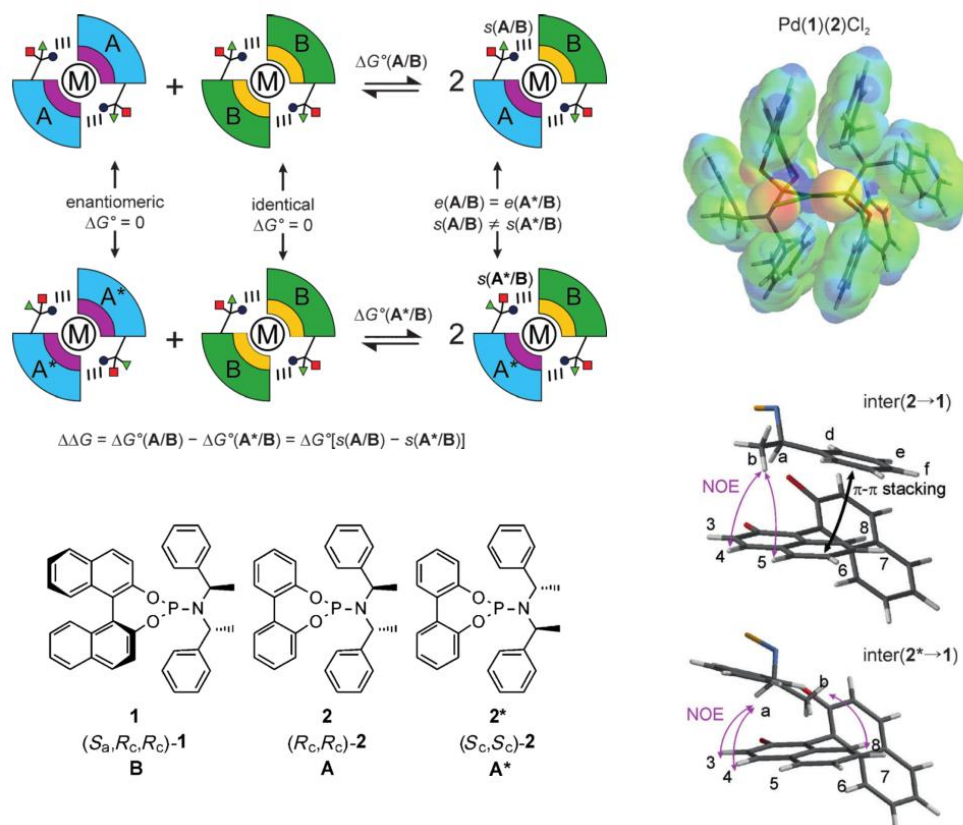


Figure 12 : Structures and equilibrium on which the supramolecular balance for transition metal complexes resides^[8]

This system is based on a palladium complex bearing two chlorine ligands and two phosphoramidite ligands. There are three different possible ligands: **B** bearing a binaphthyl moiety, **A** bearing a biphenyl moiety and **A*** its enantiomer (Figure 12). The structures were determined via X-ray and it was shown that two phosphoramidite ligands on the same palladium atom could interact with one another via $\pi \cdots \pi$ stacking or via a $CH \cdots \pi$ interaction. Homo-complexes of **A** and **B** (and **A*** and **B**) were mixed and hetero-complexes (**MABCl₂** and **MA*BCl₂**) were formed. The equilibrium constants between homo- and hetero-complexes were determined via $^1H^1H$ NOESY experiments. **A** and **A*** being enantiomers, **MA₂Cl₂** and **MA*₂Cl₂** bear the same interactions and only hetero-complexes present different interactions. Using enantiomers also allows both hetero-complexes to present identical stereo electronic and electrostatic effects and to differ only in supramolecular interactions. Thus the difference in equilibrium constants between **A** and **A*** upon the formation of the corresponding hetero-complexes is affected by the $\pi \cdots \pi$ stacking in the **AB** hetero-complex and the $CH \cdots \pi$ interaction in the **A*B** hetero-complex. Thus, the $\Delta\Delta G$ obtained from the measured equilibrium constants reflects the difference in energy between those two interactions. This approach is possible due to retention of the general complex structure in all cases and to the fact that chiral centers are present in the apolar part of the ligand. This method is quite insensitive to solvation effects as the exchange occurs between highly similar ligands but the solvent dielectric constant can still affect the absolute strength of the interactions.

The major issue of bimolecular systems is their time-consuming aspect as in any case they rely on the measurement of a complexation constant. Using a different approach, many monomolecular systems were used for the measurement of non-covalent interaction energies.

2. Monomolecular system: the molecular torsion balance

A molecular torsion balance is a molecule designed to have two restricted conformational states and where there is a particular non-covalent interaction in one of those states. The two conformational states are generally separated by the rotation of a single covalent bond.

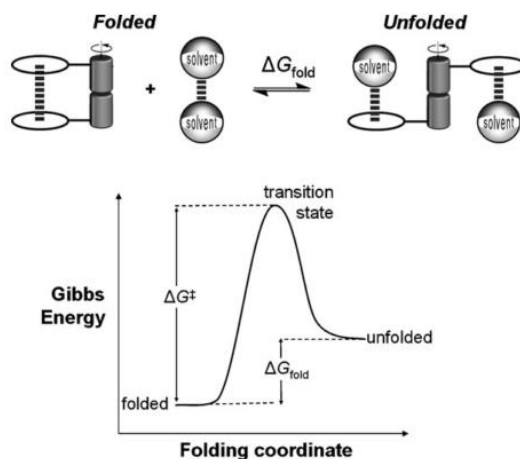


Figure 13 : the torsion balance equilibrium^[9]

Two thermodynamics parameters can be extracted from this equilibrium (Figure 13): the rotational barrier energy (ΔG^\ddagger) measurable via temperature dependant NMR and the difference in free energy of the ground states (ΔG_{fold}) measurable via a single NMR spectrum.

ΔG^\ddagger describes the free energy difference between the folded ground state and the transition state and can thus give indications on the strength of the interaction. It is usually not straightforward as the nature of the transition state can be hard to define.^[9]

Cozzi, Siegel and co-workers used this approach to study the influence of geometry and substituents on aromatic stacking (Figure 14).^[10,11]

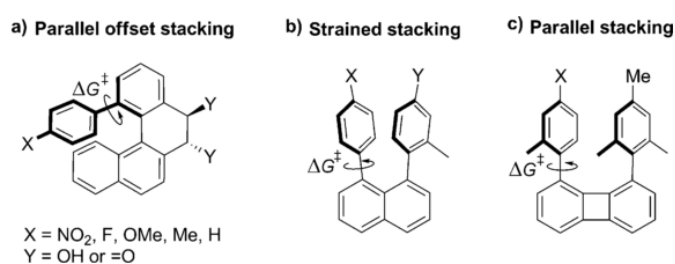


Figure 14 : different geometries of aromatic stacking^[9]

No energy values could be extracted from those systems but all three exhibited linear relationships between ΔG^\ddagger and the Hammett substituent constants indicating a dominance of electrostatics on the system. It was also shown that the more strained the system was, the higher ΔG^\ddagger increased upon addition of an electron-withdrawing group, highlighting the influence of steric effects in these systems.

ΔG_{fold} offers an easier interpretation as both ground-state structures are usually well-determined via X-ray diffraction or NMR. Experimentally a single NMR spectrum is enough to determine K_{fold} (and

thus ΔG_{fold}) by measuring the relative population of both ground-states. However, the influence of the solvent is of particular importance as the solvation of the molecule is different in both ground-states.

Not all folding molecules are suited for the quantitative study of non-covalent interactions. The measurement of this equilibrium is based on NMR measurements and thus the equilibrium need to be slow enough on the NMR time-scale otherwise only conformationally averaged signal would be measured ($\Delta G^\ddagger > 65 \text{ kJ/mol}$) and it needs to be fast enough for equilibrium to be reached on a reasonable timescale.

An advantage of this approach is that NMR titrations or variable temperature experiments are not needed, a single NMR spectrum is enough to have access to K_{fold} .

This approach allows both attractive and repulsive interactions to be measured with a high degree of accuracy (*ca.* 0.5 kJ/mol) only limited by the accuracy of NMR (*ca.* 5%). Due to the range of NMR, ΔG_{fold} can be accurately measured only between -7.3 kJ/mol and +7.3 kJ/mol.

The pioneer of this method is Ōki who back in the 70s worked with triptycene derivatives.^[12] He and his colleagues realized that the rotational barrier of the C-C bond in Figure 15 was strongly influenced by interactions between the 1-(*peri*) and 9-(*bridge-head*) positions.

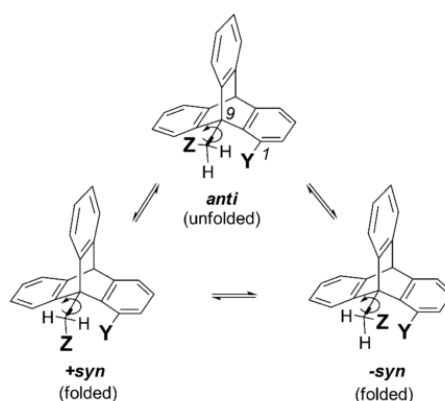


Figure 15 : triptycene derivatives equilibrium^[12]

Based on this equilibrium, the interaction energy between the 1- and 9- substituent can be measured from the deviation to the statically expected 2:1 *syn/anti* ratio.^[12]

a. CH \cdots O interactions

Ōki started with the interaction of a methoxy group with a range of functional group in CDCl_3 (Figure 16 left).

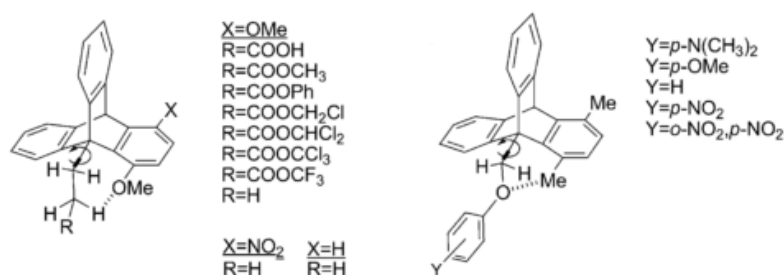


Figure 16 : Ōki's molecular balances structures^[9]

The results were consistent with an interaction between the electronic rich oxygen and the CH_2 group adjacent to the carbonyl group driven by electrostatics. A few exceptions were attributed to differences in conformation and steric hindrance.^[13–16]

The population of the folded conformer is favored with an electron-withdrawing R group, which is consistent with a favorable $\text{CH}\cdots\text{O}$ interaction. Another series of molecular balances was synthesized (Figure 16 right) to investigate those interactions and was compared to the first series with R a hydrogen atom. Thus, both series are just an inversion of the functional group. In both series the major conformer was always the unfolded one which was explained by the dominance of van der Waals repulsion over the electrostatic $\text{CH}\cdots\text{O}$ interactions. In the second series, the folding ratio increased as the oxygen became more electron rich with a more electron-donating Y substituent. However, in the first series with R a hydrogen atom, the folding ratio decreases with a more electron donating X-substituent.^[16] This strange result was explained by the difference of polarity between benzyl CH and ethyl CH but modern days electrostatic surface potential calculations showed that there is only a small difference in polarity. In fact, this strange behavior can be explained with the examination of molecular models showing that the phenolic oxygen is still accessible to the solvent in the folded conformation contrary to the ethylic oxygen. Since chloroform is a better H-bond donor than an alkyl group, solvation overcomes the $\text{CH}\cdots\text{O}$ interaction and thus prevent the ethyl compound to fold.^[17] This first series of experiment shows the subtle effects of geometry and solvation on the molecular balance.

b. $\text{X}\cdots\pi$ interactions

Following this study, Ōki and later Gung, synthesized a series of tryptipene derivatives for investigating arene \cdots functional groups interactions.

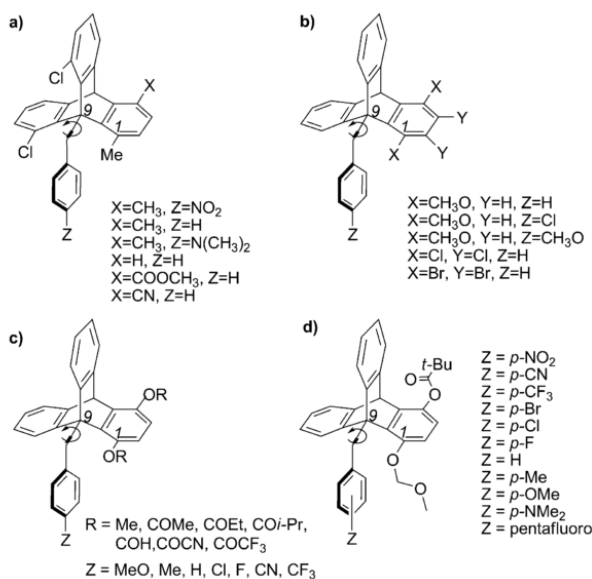


Figure 17 : Gung's molecular balances structures^[18]

In the first series (Figure 17a) chlorine atoms were used in the *peri*-positions to balance the influence of steric hindrance (Cl is isosteric to Me) on the *syn/anti* conformer ratio.^[18] Thus the folding equilibrium is determined by the relative energies of the Cl/CH₃...arene interaction and desolvation effects. Higher *syn/anti* ratios were obtained for the compounds with the most electron-rich aromatic rings and the most positively polarized CH₃ groups which is consistent with a dominant CH...arene interaction.

In the second series (Figure 17b), interactions between oxygen/halogen and arene were studied.^[18] Electron-donating Z-substituent decreased the *syn/anti* ratio due to an electrostatic repulsion between the oxygen atom and the face of the aromatic ring. The *syn/anti* ratio diminished as well when introducing Cl or Br atoms probably because of their larger size.

In the two last series (Figure 17c and d), Gung and co-workers investigated interactions between an aromatic ring and a series of esters and methoxymethyl ether groups.^[19] The folded conformation is preferred in all cases and the greatest ratios are observed in the methoxymethyl ether series particularly with electron-withdrawing Z-substituents. The conformational freedom displayed in those examples and the role of the solvent blur the interpretation but the authors suggest that the folded state preference points towards the importance of van der Waals dispersion forces, with the position of the equilibrium being modulated by electrostatic interactions.

Motherwell and coworkers designed a series of dibenzo-bicyclo[3,2,2]-nonane derivatives to study interactions between functional groups and aromatic rings (Figure 18).^[20,21]

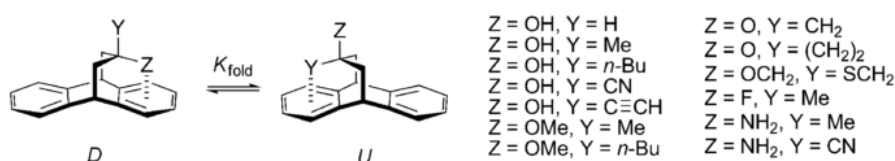


Figure 18 : Motherwell's molecular balances structures^[9]

Contrary to most of the other folding molecules used as a molecular balance, the rotational barrier is low in energy and thus interconversion equilibrium is fast on the NMR scale. Nevertheless, accurate population ratios were obtained via the NMR J-couplings of the conformers.

When Z=OH and Y=Me, the D conformer dominates in low polarity solvents as the hydroxyl group interacts with the aromatic ring. In more polar solvents acting as H-bond acceptors, the U conformer tends to dominate because of the competition with the solvent. When the hydroxyl group is replaced by an amino group, the population of the D conformer decreases, indicating that the OH...arene interaction is stronger than the NH₂...arene interaction in those compounds.^[21] Unfortunately, this system only offers comparisons between interactions.

They later complicated their strategy by adding the triple mutant principle (Figure 19).^[22]

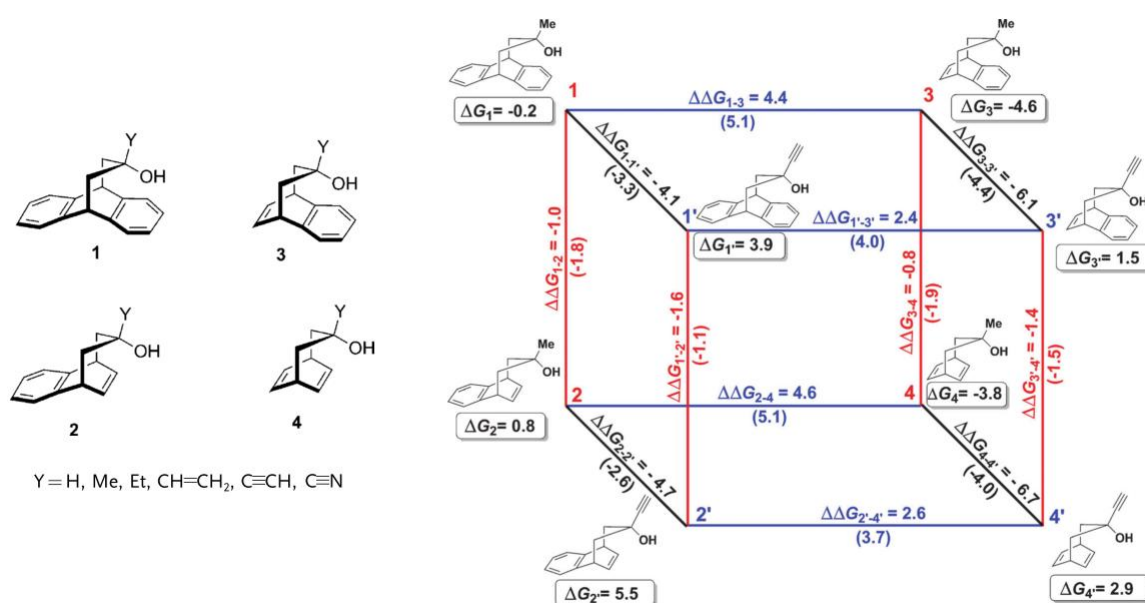


Figure 19 : Motherwell's molecular balances structures and triple-mutant cycle^[22]

A thorough analysis of the data brought interesting information: (i) a OH...arene interaction is stronger than an OH...alkene interaction, (ii) a Y...arene interaction is stronger than an Y...alkene interaction, (iii) the Y-π interactions increased in the following order: CH₂-CH₃ < CH=CH₂ < C≡CH < C≡N and (iv) a C≡N...π interaction is stronger than a OH...π interaction. In the case of the hydroxy, the interaction is obviously between the electron poor hydrogen and the π system but in the case of the Y substituent, the nature of the interaction is more subtle. DFT experiments were carried out and the previous results can be explained either by an interaction between an hydrogen on the α-carbon and the π system in the case of CH₂-CH₃ and CH=CH₂ and by a π...π interaction in the case of C≡CH and C≡N or by an interaction between the α-carbon and the π system (similar to a cation...π interaction). Fitting the natural charge of the α-carbon calculated in DFT and ΔG⁰ value obtained in CDCl₃ yielded a r² > 0.9 which is in agreement with the known linear dependence of the energy of electrostatic interactions on a charge.

Wilcox and co-workers designed molecular torsion balances as well for the measurement of alkyl...arene interactions (Figure 20).^[23,24]

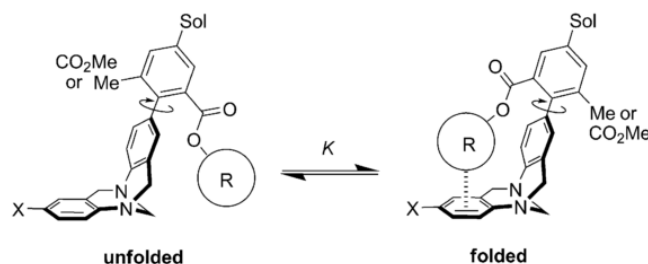


Figure 20 : Wilcox's molecular balance structure (Sol=solubilizing group)^[9]

When R=Me there is no preference for either conformation as the methyl is too far from the aromatic ring to interact. When R is replaced with a larger alkyl, the equilibrium is tipped towards the folded conformer in D₂O and CDCl₃. The most folded case is with R=*i*-Pr in D₂O highlighting the importance of the hydrophobic effect and the shape complementarity in non-covalent interactions.

Shimizu and coworkers introduced a new design and measured CH \cdots π interactions (Figure 21).^[25]

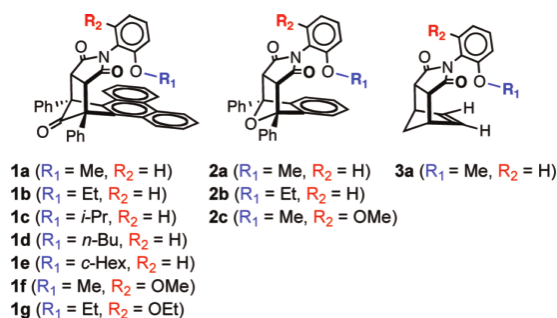


Figure 21 : Shimizu's molecular balance structures^[25]

Using van't Hoff plots, they were able to extract the enthalpic and entropic contributions. By comparing with carefully designed control balances, they were able to isolate the CH \cdots π interaction from the folding constant.

They also took a look at the cooperativity of CH \cdots π interactions (Figure 22).^[26]

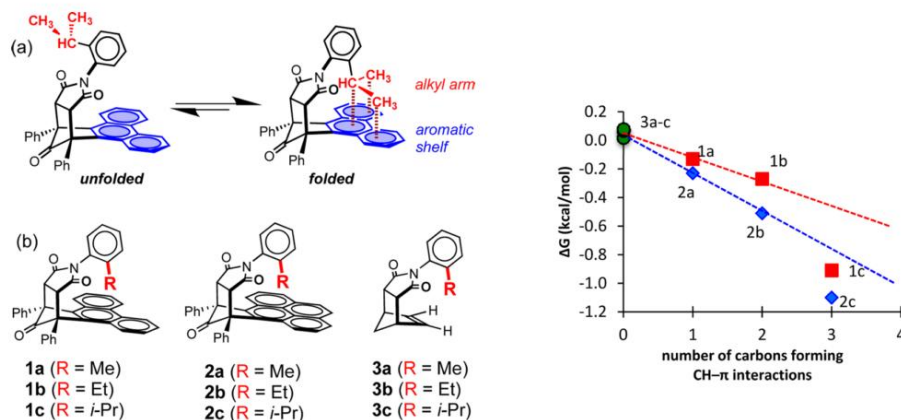


Figure 22 : Shimizu's molecular balance structures for CH \cdots π interactions additivity measurement^[27]

The results showed a strong correlation between interaction energies and the number of participating alkyl carbons. The system displayed additivity for methyl and ethyl groups and positive cooperativity for the isopropyl group for both pyrenes and phenanthrene series. Compounds with the larger pyrene group showed stronger CH $\cdots\pi$ interactions than with phenanthrene groups even though they may not form additional CH $\cdots\pi$ interactions.

They also investigated the position dependency (meta or para) on interactions between bulky alkyl groups and arenes (Figure 23).^[28]

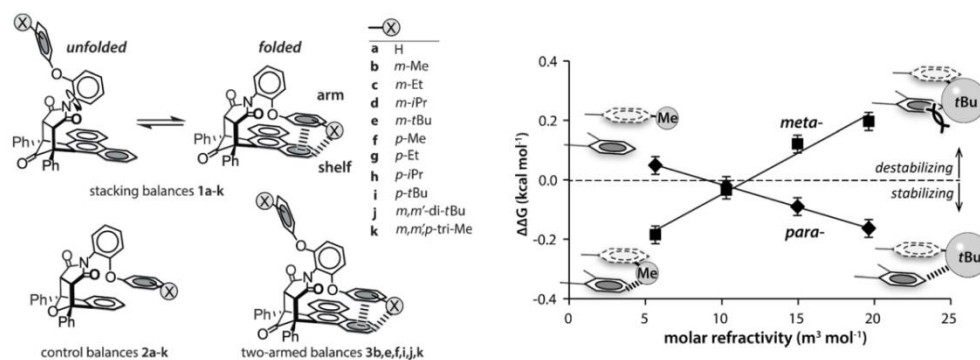


Figure 23 : Shimizu's molecular balance structures for alkyl-arene interactions^[28]

It was found that adding bulky alkyl groups as substituent of the phenyl arm could either stabilize or destabilize the interaction between the two aromatic moieties depending on its position (*meta* or *para*). Upon calculations and X-ray diffraction analysis, it was shown that both trends could be explained with stabilizing (or destabilizing) H \cdots H contacts between the alkyl in *para* (or *meta*) of the upper aromatic ring and the edge of the lower aromatic. In the case of stabilizing contacts, $\Delta\Delta G$ was found to correlate with the van der Waals surface contact area calculated using the X-ray structures. This correlation is also observed when multiple bulky groups are present on the phenyl arm.

They used a similar framework to probe the hydrogen isotopic influence on CH $\cdots\pi$ interactions (Figure 24).^[29]

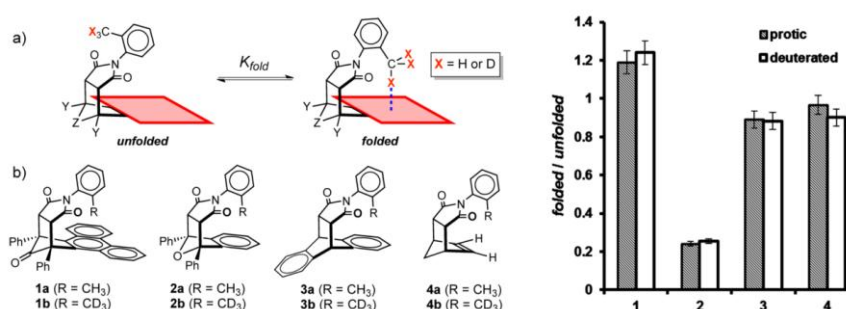


Figure 24 : Shimizu's molecular balance structures for H/D $\cdots\pi$ interactions^[29]

No isotope effect between H and D were observed leading to conclude that in previous studies^[30,31] reporting one, the difference in energy came from a steric effect due to the larger size of CD₃ and a more confined environment.

c. Aromatic edge-to-face interactions

Special attention was brought by Wilcox and co-workers to studying aromatic edge-to-face interactions for their importance in stabilizing the structure of protein and peptides.^[32] They chose different phenyl rings with various substituents as the R group and varied the X group as well (Figure 20). They were able to study the influence of the substitution on the interaction in a systematic manner. With R an aromatic featuring electron withdrawing groups such as CN, CF₃ and NO₂ the equilibrium is shifted towards the folded conformation. It can be explained by an increase in the electrostatic interaction between the partial positive charge of the edge of the aromatic ring and the electron density of the aromatic face.

A more surprising result is the fact that the equilibrium seems to be insensitive to the variation of the X-substituent in CDCl₃ with R an unsubstituted phenyl ring.^[33] The authors concluded that dispersion forces, and not electrostatic forces, dominate aromatic edge-to-face interactions in this system.

The work published by Ren and coworkers in 1997 and Diederich and coworkers in 2004 and 2008 showed that the solvent has a significant influence on the folding behavior of these molecules.^[34–36] It is worthy to note that with R= *p*-trifluoromethyl phenyl, folding energies correlate linearly with Hamett substituent constants in both C₆D₆ and CDCl₃ implying an important role of electrostatic effects in edge-to-face interactions and contradicting Wilcox earlier conclusions.

This discrepancy was explained by Cockroft and Hunter using a simple solvation model (Figure 13).^[37] There is actually a competition between the solvation of the face ring and the edge-to-face aromatic interaction displayed in the folded conformation. If R is an aromatic ring substituted with an electron-withdrawing group, the edge-to-face interaction overcomes the solvation and the influence of the X-substituents on the interaction can be measured. In the case of R being an unsubstituted phenyl ring, there is a competition between the desired interaction and the solvation, both being of similar energies, explaining why there is no influence of the X-substituents on the folding equilibrium. This was confirmed experimentally by Diederich and coworkers as benzene solvation competes equally when R=Ph.^[36]

Diederich and coworkers also used a combination of the Wilcox torsion balance and the double-mutant cycle strategy to measure C-F...carbonyl and carbonyl...carbonyl interactions between orthogonally oriented aromatic substituents (Figure 25).^[36,38]

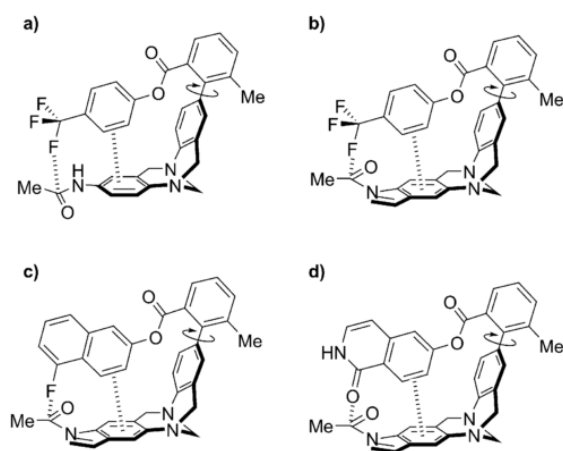


Figure 25 : Diederich's molecular balance structures^[9]

Cozzi and coworkers used another design to measure interactions between a phenyl ring and the edge of another phenyl ring and the nitrogen of a pyridine (Figure 26).^[39] The rotation barriers were increased upon fluorination of the phenyl ring.

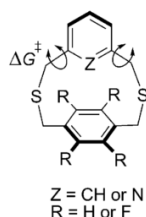


Figure 26 : Cozzi's molecular balance structure^[9]

The interpretation of the data is quite tough with this design as multiple and complex transition states exist.

d. Aromatic stacking interactions

Gellmann and coworkers developed a series of folding molecules to study aromatic interactions (Figure 27).^[40–42]

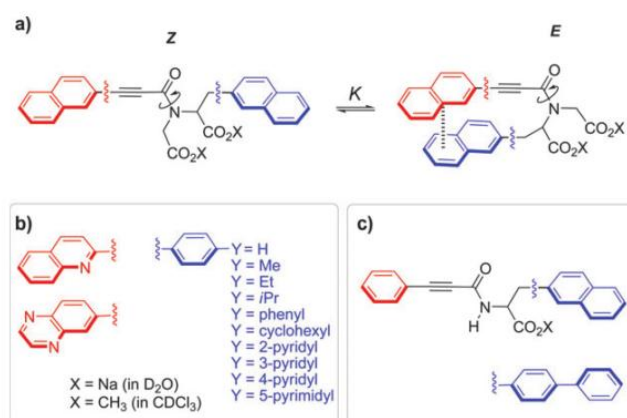


Figure 27 : Gellmann's molecular balance structures^[9]

The Y-substituent did not have much effect on the folding equilibrium in CDCl₃ but it did in D₂O due to the hydrophobic stabilization of the E-conformer. If one of the naphthyl groups is replaced by a phenyl, the folding ratios are similar in CDCl₃ and D₂O showing the phenyl group is too far from the other naphthyl group for an interaction to occur. It allows the use of this later compound as a reference to quantify the folding free energies of the other compounds. The introduction of nitrogen atoms in the aromatic ring increased the folding ratio due to electrostatically driven edge-to-face aromatic contacts as the hydrophobic effect should be diminished.

Zoltewicz and co-coworkers used Cozzi's strained stacking design to study a wide range of stacking interactions by measuring conformational isomerisation equilibrium (Figure 28).^[43,44]

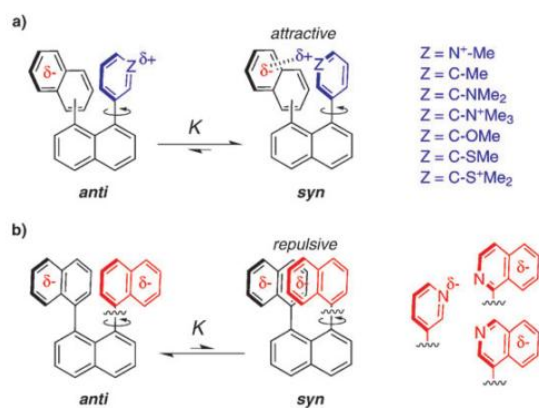


Figure 28 : Zoltewicz's molecular balance structures^[9]

The *syn* conformation is preferred in the case of interactions between an electrophile and an aromatic ring (Figure 28a). Polar solvents were found to stabilize the *anti* conformer probably due to stronger interactions between the solvent and the aromatic ring/electrophile than between the aromatic ring and the electrophile. In the case of interactions between two aromatic rings, when both aromatic rings are electron-poor or electron-rich, the *anti* conformation is preferred due to the domination of electrostatic and steric repulsions (Figure 28b).

Shimizu and coworkers also designed a series of molecular balance to measure aromatic stacking interactions (Figure 29).^[45] The interest of those compounds is the fact that only face-to-face interactions are possible in the folded form as both arenes are too close from each other to allow an edge-to-face interaction.

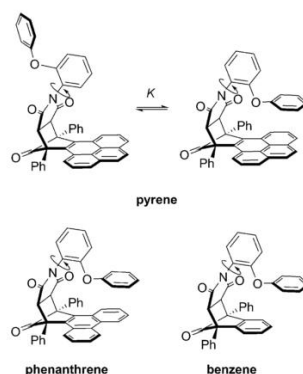


Figure 29 : Shimizu's molecular balance structures for aromatic stacking interactions^[9]

The compounds bearing the pyrene and phenanthrene groups have a higher folding ratio than the benzene one as the benzene is too small to facilitate an aromatic stacking with the phenyl ether arms. This compound was thus used as a control compound to measure secondary interactions.

They used the same design to study the additivity of substituent effects on aromatic stacking interactions (Figure 30).^[27]

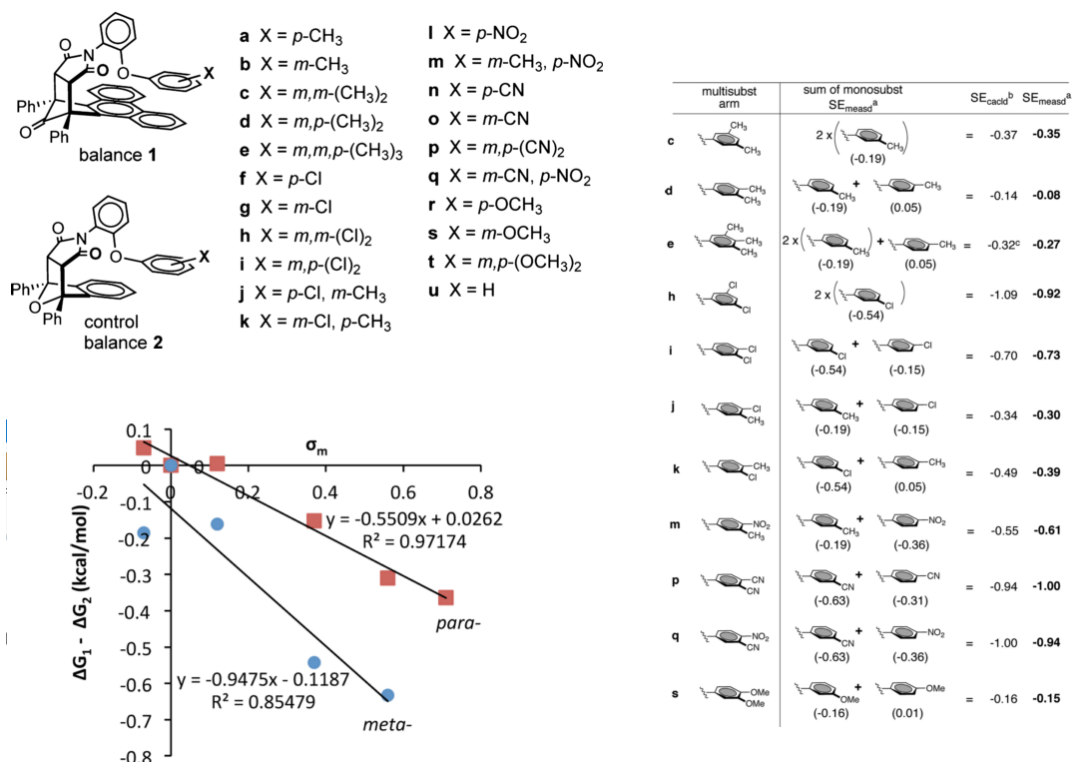


Figure 30 : Structures, Hammett σ_m plot of $\Delta G_1 - \Delta G_2$ for the monosubstituted balances with substituents in the meta (blue) or para position (red) (the substituents from left to right CH₃, H, OCH₃, Cl, CN, NO₂) and comparison of the calculated (SE_{calcd}) and measured (SE_{measd}) multisubstituent effects. SE_{calcd} were calculated from the sum of the SE_{measd} for the constituent mono-SE^[27]

They showed that the data evolved linearly with the Hammett constant and more importantly they showed the additivity of substituent effects to be true, simplifying greatly future modeling of $\pi \cdots \pi$ stacking interactions.

They also designed a torsion balance for measuring aromatic face-to-face contacts that has the particularity to have a very high rotational barrier, allowing them to isolate and crystallize the *anti* atropomer^[46] (Figure 31).

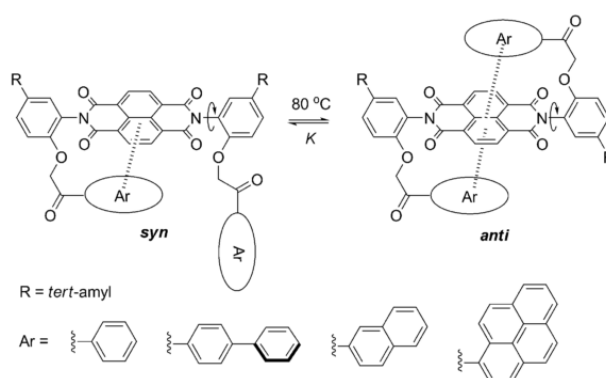


Figure 31 : Structures and equilibrium of Shimizu's molecular balance^[9]

The X-ray crystal structures showed the aromatic groups were stacked on both faces. The folding energies increased in an upwardly curving trend as the area of contact between the interacting aromatic groups increased. It could be explained by either an increase in dispersion interactions as the aromatic increases in size or an entropic cooperative effect (due to the highly parallel nature of

the stacking of large aromatics). The folding energies are not greatly impacted by the solvent as there is no change between tetrachloroethane and DMSO.

Gung and co-workers used Ōki's design to study aromatic interactions in off-stacked geometries (Figure 32).^[47–49]

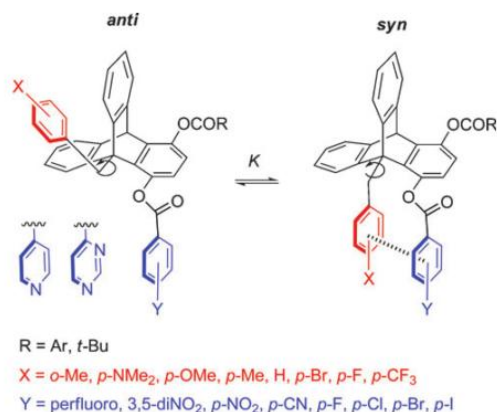


Figure 32 : Gung's molecular balance structures^[9]

These different studies showed that the $\pi\cdots\pi$ stacking interaction is an electrostatic interaction as in most case, the energies measured correlate with the Hammett constants or at least with the electron density of the aromatics. However, when the difference in electron density between both aromatics gets too high, the correlation does not hold anymore. The authors attributed it to charge-transfer between both aromatics.^[47] Their explanation of the fact that other studies involving similar interactions did not find evidence of charge-transfer interactions is the higher degree of freedom of their system, which allows an optimized conformation.

They also designed a compound with a “near perfect” face-to-face interaction (Figure 33).^[50]

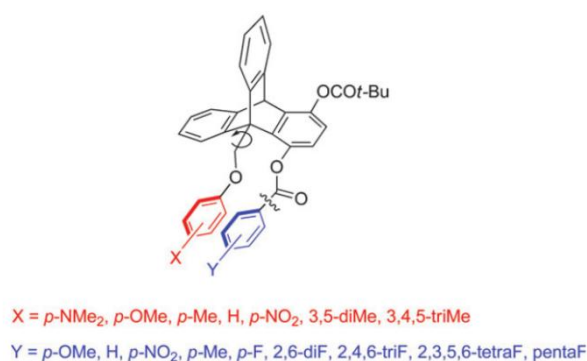


Figure 33 : Gung's “near perfect” molecular balance structure for face-to-face interactions measurement^[9]

Once again adding to one of the arene an electron-withdrawing substituent increased repulsion and adding an electron-withdrawing group increased the interaction strength. It is important to note that as this system has an additional oxygen compared to the previous one (Figure 32), it exhibits more flexibility and can thus present CH $\cdots\pi$ interactions as well.

Shimizu and coworkers had a look on the role of dispersion interactions in aromatic stacking interaction in solution (Figure 34).^[51]

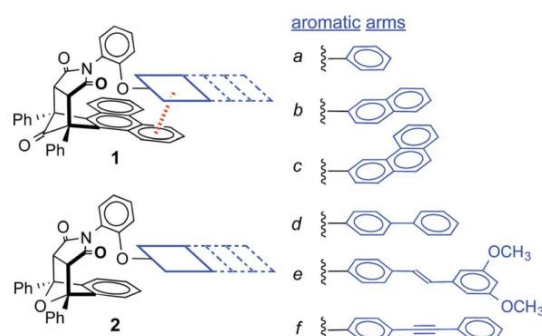


Figure 34 : Shimizu's molecular balance structures for dispersion interactions measurement^[51]

Their strategy was to vary the size and polarizability of the interacting aromatic group. By using control systems **2** (Figure 18) and multiple solvents, they were able to separate the interaction energies from solvophobic, dipole, linker and steric effects. They observed small variance of the interaction energies with the size and conjugation length of aromatic surfaces. It suggests, contrarily to what was found in computational and gas-phases studies^[52], that the dispersion contribution in aromatic stacking is very small. It is not due to the absence of a dispersion contribution but to the dispersion interactions with the solvent that diminishes the overall dispersion term.

e. $\text{Ag}^{\text{I}} \cdots \pi$ interactions

Shimizu and coworkers used their design to measure a more original interaction: the $\text{Ag}^{\text{I}} \cdots \pi$ interaction (Figure 35).^[53]

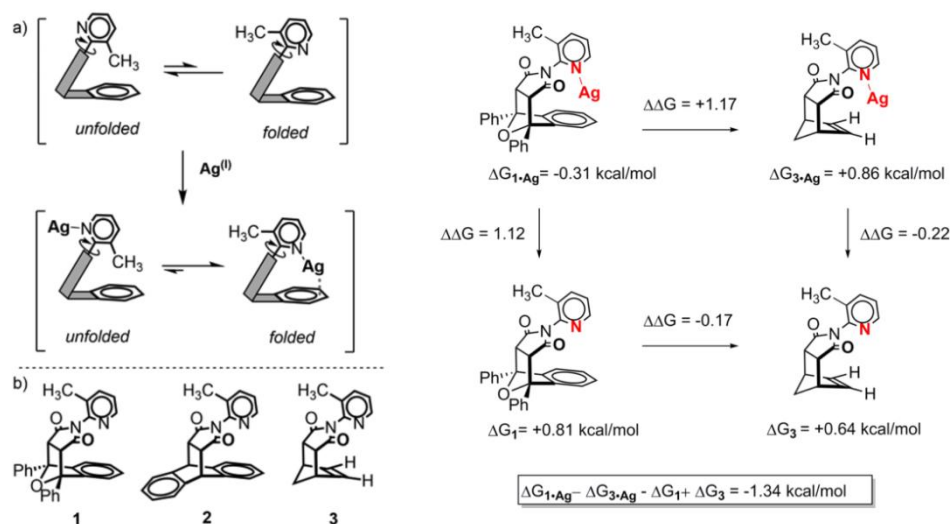


Figure 35 : Shimizu's molecular balance structures for $\text{Ag}^{\text{I}} \cdots \pi$ interactions measurement and double-mutant cycle^[53]

This study showed very weak interactions (-1.34 to -2.63 kcal/mol) which is consistent with the difficulty to make complexes with a single $\text{Ag}^{\text{I}} \cdots \pi$ interaction. The interaction also shows a great dependence on small geometry changes and solvation. The limitation of this system is the coordination of the silver atom to the pyridine as it diminishes the strength of the interaction.

f. Interaction with the solvent

Cockroft and coworkers designed a new balance to have a look at solvent effects (Figure 36).^[54]

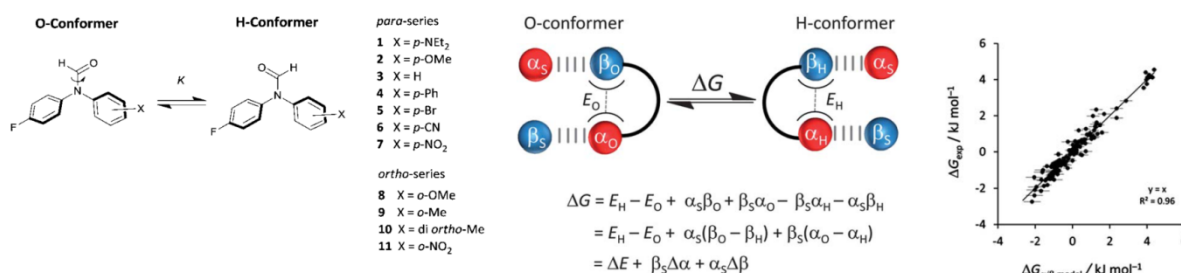


Figure 36 : Cockroft's molecular balance structures for solvent effect measurement, Cockroft's solvation model and correlation between experimentally determined conformational free energies (ΔG_{exp}) and corresponding values predicted from the solvation model^[54]

This system was designed to study the influence of solvent on hydrogen bonding. The oxygen acts as hydrogen bond acceptor and the hydrogen in *ortho* position of the closest ring acts as a hydrogen bond donor. They used a simple but efficient model designed previously to quantify solvation differences induced by the change of conformation of the system.^[37] They proposed that each molecule (solvent or balance) could be characterized by two parameters α and β describing respectively the hydrogen-bond donor and acceptor strength. Thus, by using a simple equation using those parameters (Figure 36) they could dissociate the influence of the solvent from the interaction energy. The ΔG calculated with this model fits with the measured ΔG for 11 molecular balances in 13 different solvents.

They also quantified the solvophobic effects in aromatic edge-to-face, aliphatic and fluororous interactions (Figure 37).^[55]

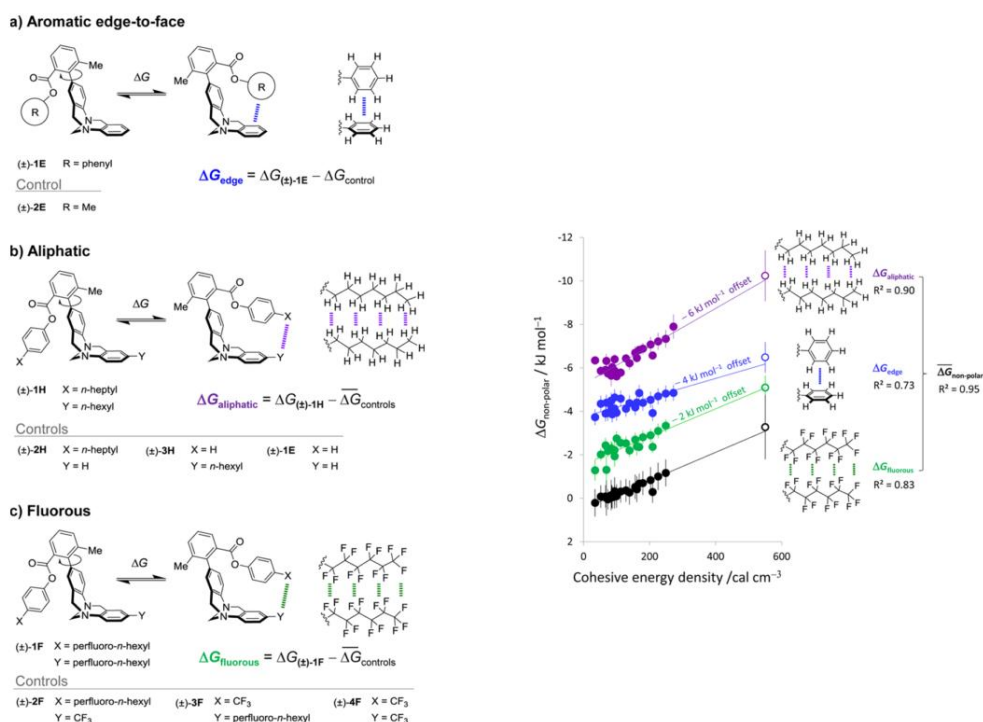


Figure 37 : Cockroft's molecular balance structures for solvophobic effect and correlations of $\Delta G_{\text{aliphatic}}$, ΔG_{edge} , and $\Delta G_{\text{fluorous}}$ (colored circles) and their average (black circles) versus the cohesive energy density of the solvent. For clarity, the plots of $\Delta G_{\text{fluorous}}$, ΔG_{edge} , and $\Delta G_{\text{aliphatic}}$ are offset by -2 , -4 , and -6 kJ mol^{-1} , respectively.^[55]

Three series of balance were designed to measure solvophobic interaction energies for aromatic edge-to-face, aliphatic and fluorous interactions. Previous studies proposed various parameters to describe cohesive solvent interactions: surface tension (γ), internal pressure (P_i), enthalpy of vaporization (ΔH_{vap}), cohesive energy density (ced), Hildebrand solubility parameter (δ_H) and Abraham's solvophobicity parameter (S_p). By screening 23 solvents, they found out the solvent cohesive energy density provided the best correlation with the solvophobic interaction energies measured. They extended their study to previous results on the collapse of single polystyrene molecules^[56] and supramolecular aromatic stacking^[57] and yielded better correlation than with the parameters previously used. Abraham's solvophobicity parameter yielded in all cases almost as good correlations which is not surprising as it is known to correlate with cohesive energy densities.^[58] It is important to note that the ced is directly correlated to the enthalpy of vaporization ($\delta_H^2 = \text{ced} = (\Delta H_{\text{vap}} - RT)/V_m$) whereas the phase transfer energy (from which S_p is calculated) is often dominated by entropy.^[59] This points out the existence of an enthalpy-entropy compensation and that both have an influence on the hydrophobic effect.

They concluded that solvent cohesive energy densities provide the most useful quantitative signature for characterizing solvophobic effects as Gibbs energy of phase transfer (from which S_p values are derived) are far less sourced than enthalpies of vaporization.

In conclusion, molecular balances have many advantages, as they usually are simple model compounds with easily synthetically available derivative compounds allowing systematic variations of interacting groups and geometries. They also easily provide structural data via X-ray diffraction allowing a good knowledge of the interactions geometries. Unfortunately, the reported sensitivity of these systems are usually around 0.5 kJ/mol (as low as 0.12 kJ/mol ^[38]). Many interactions were

studied that way, particularly aromatic interactions, and many other interactions and effects (electronic, steric, geometry, solvent ...) can be studied that way in the future.

The intrinsic limitation of all these existing strategies is the limited sensitivity of NMR. To overcome this limitation, Bouteiller and co-workers developed a concept called the supramolecular balance.^[60]

B. The supramolecular balance concept and bis-ureas

In biochemistry, interactions between DNA bases are commonly quantified by the measurement of the melting temperature of suitable DNA duplexes.^[61,62] Measuring this transition is possible because of its cooperative nature. The concept of the supramolecular balance is to apply this concept on synthetic supramolecular polymers to probe interactions. Indeed, the idea is to use a cooperatively self-associating system and to probe the variation of transition temperature upon modification of the substituents.

1. Bis-ureas, an ideal scaffold for the supramolecular balance

Bis-ureas developed in Bouteiller group are known to self assemble in solution into supramolecular polymers of two different structures depending on the temperature, concentration and solvent.^[63] At low temperature, they self-assemble into tubes with three molecules per section (Figure 38). Upon heating, they reassemble into filaments with one molecule per section via a cooperative transition at a temperature T^{**} . Upon additional heating the filaments are dissociated into monomers in a broad and non-cooperative transition. The equilibrium between the tube and the filament thus fits the requirements for its use in a supramolecular balance.

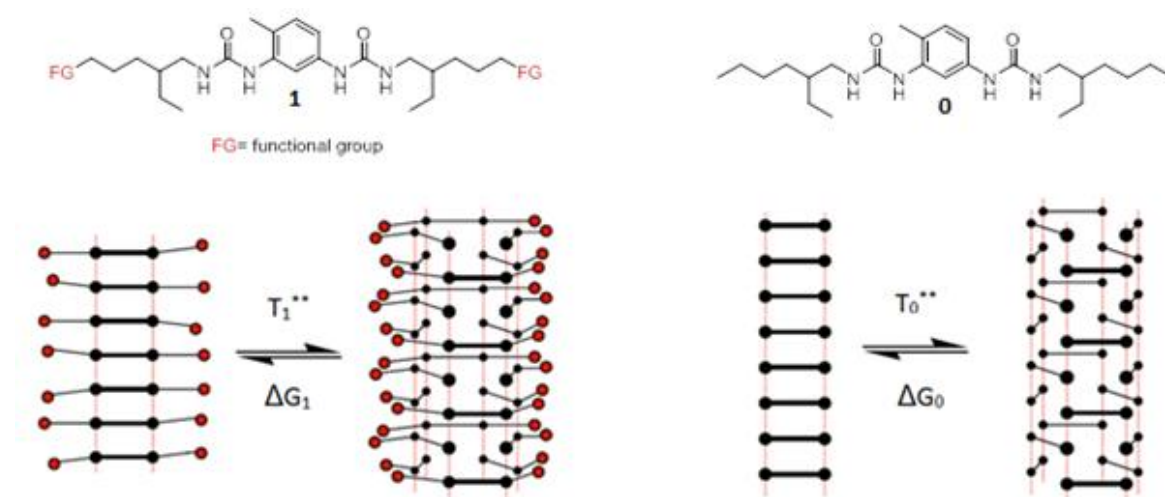


Figure 38 : Structures of the bis-urea monomers and their assemblies

Upon addition of a substituent on the monomer **0**, a new monomer **1** is obtained. **1** should assemble in the same way as the reference bis-urea **0** but with an additional interaction between the added interacting groups (FG in Figure 38) inside the assemblies. As the tube is more compact than the filament, those interactions have more probability to occur in the tube form.

The transition temperature T^{**} and the enthalpy variation ΔH can be measured using nDSC. A thermodynamic study by Paul van der Schoot showed that for a long enough assembly and if the transition enthalpy variation is not impacted by the addition of the interacting group (*i.e.* $\Delta H_1 = \Delta H_0$), the transition temperatures can be directly correlated to the free energy change brought by those new interactions using the following equation.

$$\Delta\Delta G = \Delta G_1(T_0^{**}) - \Delta G_0(T_0^{**}) = \Delta H_1 \left(\frac{T_1^{**} - T_0^{**}}{T_0^{**}} \right)^{[60]}$$

The main advantage of this strategy is its precision. Indeed, the use of calorimetry should allow a sensitivity down to 3 J/mol which is two orders of magnitude lower than with NMR.

2. Early results

This concept was used to probe the interactions between alkyl chains and showed additive energy contributions for alkyl chains up to fourteen carbons long followed by a decrease probably due to steric hindrance for longer chains (Figure 39 up). This concept was also used with vinyl moieties as interacting groups (Figure 39 down) and a $\Delta\Delta G$ of 110 J/mol was found for the bis-urea bearing two vinyl moieties and half that value for the bis-urea bearing a single vinyl moiety.

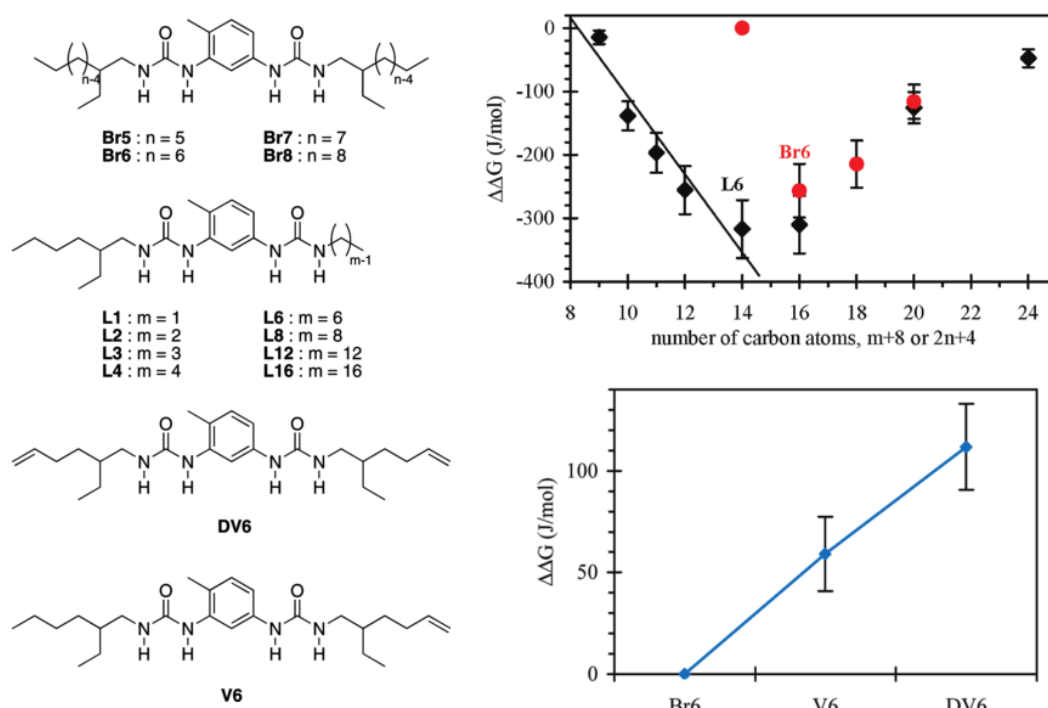


Figure 39 : Structures of the bis-ureas used for the supramolecular balance and the $\Delta\Delta G$ measured

The major issues of this study were a poor knowledge of the participation of the solvent in the interactions and the relative position of the interacting groups.^[60] The other issue regarding the bis-urea scaffold is that for those compounds to be soluble in low-polar solvents, the alkyl side chains need to be branched thus complicating the synthesis of functionalized bis-ureas.

An attempt to use an ether linkage to introduce branched ether-alkyl side chains showed low yields during the Williamson reaction orienting us towards a new design.^[64]

3. Influence of the bis-urea structure on the self-assembly

In order to design a bis-urea that would fill the specifications of the supramolecular balance, the tube to filament transition needs to occur in a measurable temperature range.

Fortunately, during the last decade, Bouteiller and his team studied the self-assembling properties of bis-ureas and tuned their structure to obtain applications in various domains.^[65–72] These compounds can be tuned in two ways: changing the internal spacer or changing the external chains (Figure 40).

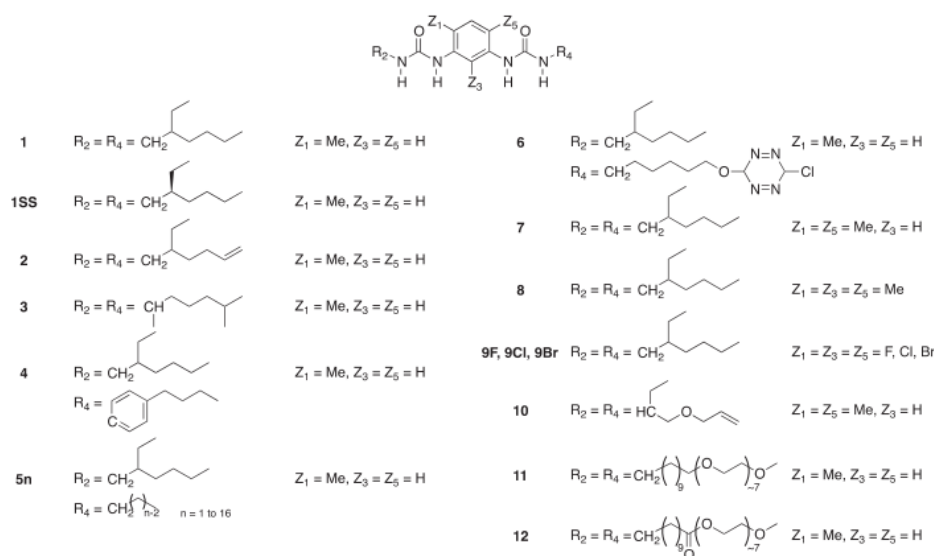


Figure 40 : the different structures of bis-ureas explored^[73]

It is possible to sensitively tune the stability of the assemblies by changing the substituents on the aromatic spacer (Z_1 - Z_5). The study of bis-ureas with different spacers including one or more methyl or ethyl substituents at different positions revealed two main effects^[74,75]: (i) alkyl groups in *ortho* positions to the urea moieties strongly enhance hydrogen bonding by forcing a non-planar conformation between the spacer and the urea moieties. This effect is seen for both the filament and the tube structure. (ii) Adding a substituent in the *ortho* position of both urea moieties (Z_3) destabilizes the tube structure as it is pointing towards the inside of the tube causing some steric congestion. The preorganization effect observed with substituents in *ortho* positions can be enhanced with halogen atoms because of their electronegativity allowing repulsion with the urea oxygen atom.^[76]

Tuning the external chains made obvious the necessity of branched chains to obtain solubility in low polarity solvents as the urea group is a very polar moiety.^[63]

In order to obtain solubility in low polarity solvents and easily synthetically accessible functionalized bis-ureas, a new family of bis-ureas was designed: “ester bis-ureas”. Those bis-ureas contain an additional ester linkage introduced via the use of amino-acids. The ramification of the amino-acid should bring solubility in low-polarity solvents and esterification of the aminoacid with a linear alcohol dramatically simplifies the synthesis of functionalized bis-ureas.

- [1] P. J. Carter, G. Winter, A. J. Wilkinson, A. R. Fersht, *Cell* **1984**, *38*, 835–840.
- [2] A. Horovitz, A. R. Fersht, *J. Mol. Biol.* **1990**, *214*, 613–617.
- [3] S. L. Cockroft, C. A. Hunter, *Chem. Soc. Rev.* **2007**, *36*, 172–188.
- [4] Y. Aoyama, M. Asakawa, A. Yamagishi, H. Toi, H. Ogoshi, *J. Am. Chem. Soc.* **1990**, *112*, 3145–3151.
- [5] Y. Kato, M. M. Conn, J. J. Rebek, *J. Am. Chem. Soc.* **1994**, *116*, 3279–3284.
- [6] H. Adams, C. A. Hunter, K. R. Lawson, J. Perkins, S. E. Spey, C. J. Urch, J. M. Sanderson, *Chem. Eur. J.* **2001**, *7*, 4863–4877.
- [7] H. Adams, S. L. Cockroft, C. Guardigli, C. A. Hunter, K. R. Lawson, J. Perkins, S. E. Spey, C. J. Urch, R. Ford, *ChemBioChem* **2004**, *5*, 657–665.
- [8] E. Hartmann, R. M. Gschwind, *Angew. Chem. Int. Ed.* **2013**, *52*, 2350–2354.
- [9] I. K. Mati, S. L. Cockroft, *Chem. Soc. Rev.* **2010**, *39*, 4195–4205.
- [10] F. Cozzi, R. Annunziata, M. Benaglia, M. Cinquini, L. Raimondi, K. K. Baldridge, J. S. Siegel, *Org. Biomol. Chem.* **2003**, *1*, 157–162.
- [11] F. Cozzi, R. Annunziata, M. Benaglia, K. K. Baldridge, G. Aguirre, J. Estrada, Y. Sritana-Anant, J. S. Siegel, *Phys. Chem. Chem. Phys.* **2008**, *10*, 2686–2694.
- [12] M. Nakamura, M. Oki, H. Nakanishi, O. Yamamoto, *Bull. Chem. Soc. Jpn.* **1974**, *47*, 2415–2419.
- [13] G. Izumi, G. Yamamoto, M. Oki, *Chem. Lett.* **1980**, *9*, 969–972.
- [14] M. Oki, G. Izumi, G. Yamamoto, N. Nakamura, *Bull. Chem. Soc. Jpn.* **1982**, *55*, 159–166.
- [15] Y. Tamura, G. Yamamoto, M. Oki, *Chem. Lett.* **1986**, 1619–1622.
- [16] Y. Tamura, G. Yamamoto, M. Oki, *Bull. Chem. Soc. Jpn.* **1987**, *60*, 1781–1788.
- [17] C. A. Hunter, *Angew. Chem. Int. Ed.* **2004**, *43*, 5310–5324.
- [18] B. Gung, X. Xue, *J. Org. Chem.* **2005**, *70*, 7232–7237.
- [19] B. W. Gung, Y. Zou, Z. Xu, J. C. Amicangelo, D. G. Irwin, S. Ma, H. C. Zhou, *J. Org. Chem.* **2008**, *73*, 689–693.
- [20] W. B. Motherwell, J. Moïse, A. E. Aliev, M. Nič, S. J. Coles, P. N. Horton, M. B. Hursthouse, G. Chessari, C. A. Hunter, J. G. Vinter, *Angew. Chem. Int. Ed.* **2007**, *46*, 7823–7826.
- [21] A. E. Aliev, J. Moïse, W. B. Motherwell, M. Nic, D. Courtier-Murias, D. A. Tocher, *Phys. Chem. Chem. Phys.* **2009**, *11*, 97–100.
- [22] A. E. Aliev, J. R. T. Arendorf, I. Pavlakos, R. B. Moreno, M. J. Porter, H. S. Rzepa, W. B. Motherwell, *Angew. Chem. Int. Ed.* **2015**, *54*, 551–5.
- [23] S. Paliwal, S. Geib, C. S. Wilcox, *J. Am. Chem. Soc.* **1994**, *116*, 4497–4498.
- [24] B. Bhayana, C. S. Wilcox, *Angew. Chem. Int. Ed.* **2007**, *46*, 6833–6836.
- [25] W. R. Carroll, C. Zhao, M. D. Smith, P. J. Pellechia, K. D. Shimizu, *Org. Lett.* **2011**, *13*, 4320–4323.
- [26] C. Zhao, P. Li, M. D. Smith, P. J. Pellechia, K. D. Shimizu, *Org. Lett.* **2014**, *16*, 3520–3523.
- [27] J. Hwang, P. Li, W. R. Carroll, M. D. Smith, P. J. Pellechia, K. D. Shimizu, *J. Am. Chem. Soc.* **2014**, *136*, 14060–14067.
- [28] J. Hwang, P. Li, M. D. Smith, K. D. Shimizu, *Angew. Chem. Int. Ed.* **2016**, 1–5.
- [29] C. Zhao, R. M. Parrish, M. D. Smith, P. J. Pellechia, C. D. Sherrill, K. D. Shimizu, *J. Am. Chem. Soc.* **2012**, *134*, 14306–14309.
- [30] M. Turowski, N. Yamakawa, J. Meller, K. Kimata, T. Ikegami, K. Hosoya, N. Tanaka, E. R. Thornton, *J. Am. Chem. Soc.* **2003**, *125*, 13836–13849.
- [31] S. S. Iyer, Z.-P. Zhang, G. E. Kellogg, H. T. Karnes, *J. Chromatogr. Sci.* **2004**, *42*, 383–387.
- [32] C. D. Tatko, M. L. Waters, *J. Am. Chem. Soc.* **2002**, *124*, 9372–9373.
- [33] E. Kim, S. Paliwal, C. S. Wilcox, *J. Am. Chem. Soc.* **1998**, *120*, 11192–11193.
- [34] T. Ren, Y. Jin, K. S. Kim, D. H. Kim, *J. Biomol. Struct. Dyn.* **1997**, *15*, 401–405.
- [35] F. Hof, D. M. Scofield, W. B. Schweizer, F. Diederich, *Angew. Chem. Int. Ed.* **2004**, *43*, 5056–5059.
- [36] F. R. Fischer, W. B. Schweizer, F. Diederich, *Chem. Comm.* **2008**, 4031–4033.
- [37] S. L. Cockroft, C. A. Hunter, *Chem. Comm.* **2009**, 3961–3963.
- [38] F. R. Fischer, W. B. Schweizer, F. Diederich, *Angew. Chem. Int. Ed.* **2007**, *46*, 8270–8273.
- [39] R. Annunziata, M. Benaglia, F. Cozzi, A. Mazzanti, *Chem. Eur. J.* **2009**, *15*, 4373–4381.
- [40] R. R. Gardner, S. L. McKay, S. H. Gellman, *Org. Lett.* **2000**, *2*, 2335–2338.
- [41] R. R. Gardner, L. A. Christianson, S. H. Gellman, *J. Am. Chem. Soc.* **1997**, *119*, 5041–5042.
- [42] S. L. McKay, B. Haptonstall, S. H. Gellman, *J. Am. Chem. Soc.* **2001**, *123*, 1244–1245.
- [43] S. Lavieri, J. A. Zoltewicz, *J. Org. Chem.* **2001**, *66*, 7227–7230.
- [44] J. A. Zoltewicz, N. M. Maier, S. Lavieri, I. Ghiviriga, K. A. Abboud, W. M. F. Fabian, *Tetrahedron* **1997**, *53*, 5379–5388.
- [45] W. R. Carroll, P. Pellechia, K. D. Shimizu, *Org. Lett.* **2008**, *10*, 3547–3550.

- [46] Y. S. Chong, W. R. Carroll, W. G. Burns, M. D. Smith, K. D. Shimizu, *Chem. Eur. J.* **2009**, *15*, 9117–9126.
- [47] B. W. Gung, M. Patel, X. Xue, *J. Org. Chem.* **2005**, *70*, 10532–10537.
- [48] B. W. Gung, X. Xue, H. J. Reich, *J. Org. Chem.* **2005**, *70*, 3641–3644.
- [49] B. W. Gung, B. U. Emenike, C. N. Alvarez, J. Rakovan, K. Kirschbaum, N. Jain, *Tet. Lett.* **2010**, *51*, 1648–1650.
- [50] B. W. Gung, X. Xue, Y. Zou, *J. Org. Chem.* **2007**, *72*, 2469–2475.
- [51] J. Hwang, B. E. Dial, P. Li, M. E. Kozik, M. D. Smith, K. D. Shimizu, *Chem. Sci.* **2015**, *6*, 4358–4364.
- [52] C. F. R. A. C. Lima, M. A. A. Rocha, L. R. Gomes, J. N. Low, A. M. S. Silva, L. M. N. B. F. Santos, *Chem. Eur. J.* **2012**, *18*, 8934–8943.
- [53] J. M. Maier, P. Li, J. Hwang, M. D. Smith, K. D. Shimizu, *J. Am. Chem. Soc.* **2015**, *137*, 8014–8017.
- [54] I. K. Mati, C. Adam, S. L. Cockcroft, *Chem. Sci.* **2013**, *4*, 3965–3972.
- [55] L. Yang, C. Adam, S. L. Cockcroft, *J. Am. Chem. Soc.* **2015**, *137*, 10084–10087.
- [56] I. T. S. Li, G. C. Walker, *J. Am. Chem. Soc.* **2010**, *132*, 6530–6540.
- [57] M. S. Cubberley, B. L. Iverson, *J. Am. Chem. Soc.* **2001**, *123*, 7560–7563.
- [58] M. H. Abraham, P. L. Grellier, R. A. McGill, *J. Chem. Soc. Perkin Trans. 2* **1988**, 339–345.
- [59] H. S. Frank, M. W. Evans, *J. Chem. Phys.* **1945**, *13*, 507.
- [60] M. Roman, C. Cannizzo, T. Pinault, B. Isare, B. Andrioletti, P. van der Schoot, L. Bouteiller, *J. Am. Chem. Soc.* **2010**, *132*, 16818–16824.
- [61] M. Petersheim, D. H. Turner, *Biochemistry* **1983**, *22*, 256–263.
- [62] K. M. Guckian, B. A. Schweitzer, R. X. F. Ren, C. J. Sheils, P. L. Paris, D. C. Tahmassebi, E. T. Kool, *J. Am. Chem. Soc.* **1996**, *118*, 8182–8183.
- [63] V. Simic, L. Bouteiller, M. Jalabert, *J. Am. Chem. Soc.* **2003**, *125*, 13148–13154.
- [64] F. Ouhib, M. Raynal, B. Jouvet, B. Isare, L. Bouteiller, *Chem. Comm.* **2011**, *47*, 10683–10685.
- [65] G. G. K.S. Chodorowski, N. Baghdadli, R.M. Arnaud, L. Bouteiller, *Cosmetic Composition Textured by a Specific Symmetric Bis-Urea Derivative FR 2894476 A1 20070615*, **2007**.
- [66] K. S. Chodorowski, *Bisurea Type Compound, Composition Comprising Its Use, and Cosmetic Treatment Process for Hair and Skin, FR 2900819 A1 20071116*, **2007**.
- [67] I. R. K.S. Chodorowski, A. Livoreil, N. Baghdadli, *Cosmetic Bisurea, Compositions with a Liquid Fatty Phase Textured by a Compound, FR 2892303 A1 20070427*, **2007**.
- [68] C. Feltin, *Cosmetic Composition Containing a Bis-Urea Derivative, EP 1938788 A1 20080702*, **2008**.
- [69] L. B. J. Prevost, G. Papin, *Preparation of a Gelled Hydrocarbon-Based Fuel Composition, WO 2014096323 A1 20140626*, **2014**.
- [70] B. Poulet, *Petrol Fuel Composition, and Method for the Preparation of and Use of Such a Composition, WO2014096310 A1 20140626*, **2014**.
- [71] B. Poulet, *Use of a Viscosifying Compound for Improving the Storage Stability of a Liquid Hydrocarbon Fuel, WO 2014096326 A1 20140626*, **2014**.
- [72] J. B. F. Foti, A. Arnaud, L. Bouteiller, *Manufacture of Glass Windows Having Polyurethane-based Hydrophilic Coatings with High Scratch Resistance*, **2015**.
- [73] B. Isare, S. Pensec, M. Raynal, L. Bouteiller, *C. R. Chimie* **2016**, *19*, 148–156.
- [74] B. Isare, M. Linares, R. Lazzaroni, L. Bouteiller, *J. Phys. Chem. B* **2009**, *113*, 3360–3364.
- [75] B. Isare, G. Pembouong, F. Boué, L. Bouteiller, *Langmuir* **2012**, *28*, 7535–7541.
- [76] I. Giannicchi, B. Jouvet, B. Isare, M. Linares, A. Dalla Cort, L. Bouteiller, *Chem. Commun.* **2014**, *50*, 611–613.

Chapter 2 : Structural study of ester bis-urea assemblies

Abstract: In this chapter, we present the structural study of ester-bis-ureas. In a first part, racemic ester bis-ureas were synthesized and their self-assembling structures in toluene were studied. Those were then compared to previously synthesized alkyl bis-ureas and shown to differentiate in structure. In a second part, enantiopure ester bis-ureas were synthesized and their self-assembling structures proved to be identical to those of the racemic ones. The enantiopure ester bis-ureas were studied by CD and the experimental data was compared to simulated CD spectra from molecular dynamics.

The part A of this chapter has been published in *Langmuir* (Dirany, M.; Ayzac, V.; Isare, B.; Raynal, M.; Bouteiller, L. *Langmuir* **2015**, *31*, 11443). My contribution was the acquisition of the variable-temperature FTIR spectra.

Alkyl bis-ureas have been largely investigated by our team for almost two decades now and it was shown that it is possible to change the relative thermodynamic stability of the tube and filament structures by tuning the monomer structure (aromatic spacer or alkyl side-chains). In contrast, the morphology (tube or filament) of the assemblies is not affected by these modifications in the chemical structure of the bisurea monomers.

The main issues in the diversification of the chemical structures of alkyl bis-ureas are: i) only bis-ureas with branched alkyl groups are soluble in apolar solvents and ii) a limited number of branched amines are commercially available. Moreover, the functionalization of those amines can be complicated from a synthetic point of view and the supramolecular balance project was in need of such functionalization.

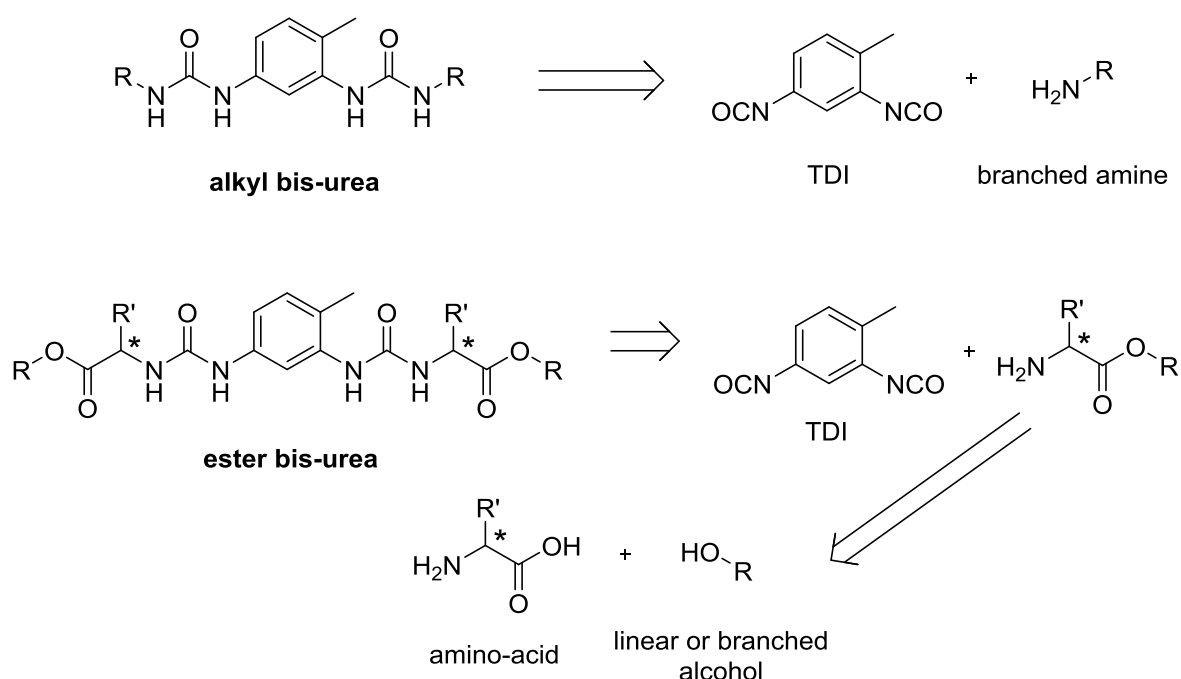


Figure 41 : retrosynthetic scheme of alkyl and ester bis-ureas

The initial idea was to add an aminoacid in the side chain to get a ramification to improve solubility, to incorporate a stereogenic center (substituent attached to the α -carbon) and to be able to easily functionalize the rest of the side chain as it is now derived from a simple linear or branched alcohol (Figure 41). A precise representation of the morphology and molecular arrangement of the monomers within the ester bis-urea assemblies are crucial for the use of such scaffolds in the supramolecular balance project. We present below our combined experimental and computational study aimed at determining the structure of the assemblies formed by ester bis-ureas.

A. Racemic ester bis-ureas

In a first step, racemic monomers of ester bis-ureas were studied. Synthesis and characterization of the molecules are presented in chapter 6.

1. Morphology of the assemblies

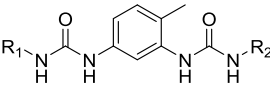
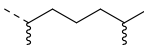
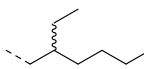
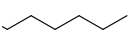
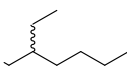
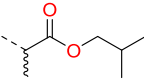
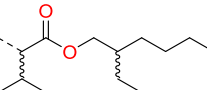
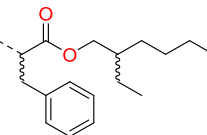
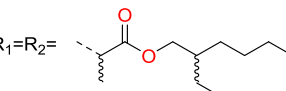
	diMeHex	$R_1=R_2=$ 
	EtHex	$R_1=R_2=$ 
	HexEtHex	$R_1=$  $R_2=$ 
	i-BuAla	$R_1=R_2=$ 
	EtHexVal	$R_1=R_2=$ 
	EtHexPhe	$R_1=R_2=$ 
	EtHexAla	$R_1=R_2=$ 

Figure 42 : Structures of the alkyl and ester bis-ureas present in this study

The alkyl bis-ureas used as references in this study were already investigated.^[1–11] Interestingly, the only difference in the chemical structures of **diMeHex** and **i-BuAla** is the presence of the ester moiety in β -position of the urea groups in the former case. It will allow a direct probing of the influence of the ester function on the morphology of the assemblies.

All the ester bis-ureas formed gels when dissolved in toluene (10 mM), indicating the formation of long assemblies (Figure 43).

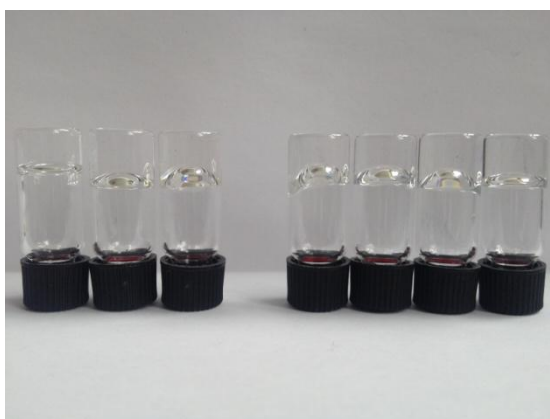


Figure 43 : Gels formed by alkyl and ester bis-urea assemblies in toluene (10mM). From the left to the right: **diMeHex**, **EtHex**, **HexEtHex**, **i-BuAla**, **EtHexVal**, **EtHexPhe** and **EtHexAla**

All bis-ureas were analyzed by SANS (Figure 44 and Figure 65 in appendix) in toluene- d_8 at *ca.* 0.6 wt% (*ca.* 3 mM). They all showed similar scattering profiles showing a q^{-1} dependence typical of rod-like objects, at intermediate q values. At 20°C, the dependence is maintained down to the lowest scattering vector ($q=0.004 \text{ \AA}^{-1}$) indicating that the length of the rods is larger than 250 Å. The SANS

data were fitted according to a model for rigid rods with a circular cross-section and a uniform scattering length density which enabled the determination of the geometrical radius (r) of the rods as well as the linear density (n_L) of the repeating units along the central axis of the rods.

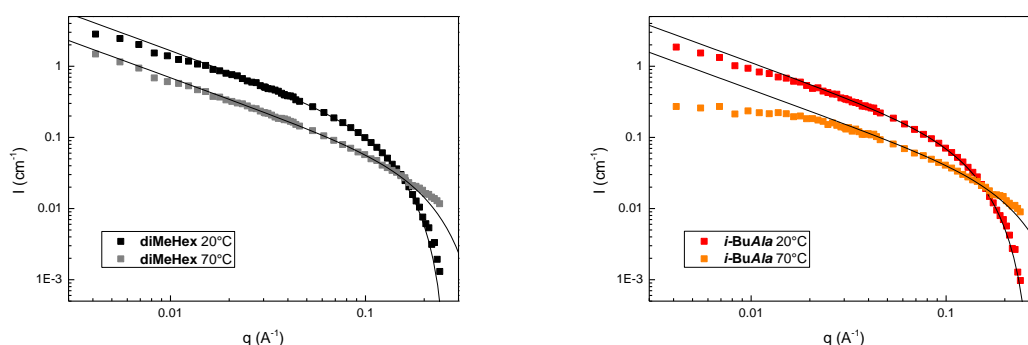


Figure 44 : SANS experiments on **diMeHex** and **i-BuAla** in toluene- d_8 ca. 0.6 wt%.

The number of bis-urea monomers in the cross-section of the rods (n) was determined by assuming a repeat distance between bis-urea monomers within the rods of 4.6 Å (as measured in the X-ray structure of 1,3-dimethylurea, the number of bis-urea monomers in the cross-section of the rods can be determined $n=4.6n_L$). The results of the fits are listed in Table 1.

Table 1 : Geometrical radius (r), linear density (n_L) and number of bis-urea molecules (n) in the cross-section of the cylindrical objects deduced from the fit of the SANS data below and above the transition temperature (T^{**})^{a,b}

bisurea	20°C (< T^{**})			70°C (> T^{**})			T^{**} (°C) ^c
	r (Å)	n_L (Å ⁻¹)	n^d	r (Å)	n_L (Å ⁻¹)	n^d	
diMeHex	14.4	0.56	2.6	9.0	0.23	1.1	61.1
EtHex	14.1	0.55	2.5	8.6	0.22	1.0	43.0
HexEtHex	14.4	0.53	2.4	8.3	0.22	1.0	49.1
i-BuAla	13.9±0.2	0.41±0.02	1.9±0.1	8.1	0.17	0.78	60.3
EtHexVal	16.1±0.1	0.48±0.02	2.2±0.1	9.1	0.18	0.83	35.5
EtHexPhe	16.3±0.1	0.46±0.05	2.1±0.2	9.5	0.17	0.78	34.3
EtHexAla	15.4±0.2	0.45±0.01	2.1±0.01	8.9	0.17	0.78	33.0

^a SANS experiments were performed at ca. 0.6 wt% except for **EtHex** (0.8 wt%). For each ester bis-urea, SANS measurements at 20°C were made on two different samples and the indicated values correspond to an average of the resulting fitted data. ^b For alkyl bis-ureas, $2H > 250$ Å. For ester bis-ureas, $2H > 250$ Å at 20°C and $2H = 160, 120, 120$, and 130 Å at 70°C for **i-BuAla**, **EtHexVal**, **EtHexPhe** and **EtHexAla** respectively. ^c T^{**} = transition temperature between structures as determined by nano-DSC experiments (*vide infra*) performed at 5 mM in toluene. ^d n = the number of bis-urea molecules in the cross-section, assuming a repeat distance of 4.6 Å.

At 20°C, alkyl bis-ureas show a linear density of ca. 0.55 Å⁻¹ corresponding to a number of molecules in the cross-section of ca. 2.5. Ester bis-ureas exhibit a smaller linear density (0.41 to 0.48 Å⁻¹), giving a number of molecules in the cross section between 1.9 and 2.2. The radius of the cylindrical assemblies formed by **diMeHex** and **i-BuAla** are similar (ca. 14 Å) and consistent with the half-length of their extended conformation (ca. 12.9 Å).

At 70°C, for both alkyl and ester bis-ureas, the assemblies rearrange into supramolecular polymers with ca. a single bis-urea molecule in the cross-section, *i.e.*, filaments ($1.0 < n < 1.1$ for alkyl bis-ureas and $0.78 < n < 0.83$ for ester bis-ureas). In the case of ester bis-ureas at 70°C, the leveling of the scattered intensity at low q is a clear indication of the limited size of the filaments. Fitting the SANS data at 70°C for ester bis-ureas with a model for monodisperse filaments provided their average

length (2H, see the caption of Table 1). At this temperature, the average length of the filaments formed by ester bis-ureas is comprised between 120 and 160 Å which corresponds to *ca.* 30 bis-urea units.

SANS experiments clearly indicate a difference in morphology between the assemblies formed by alkyl and ester bis-ureas at low temperature as they do not contain the same number of molecules in the cross-section (*ca.* 2.5 for alkyl bis-ureas and *ca.* 2 for ester bis-ureas). However, no definite structural information could be gained solely from these data. Moreover, the low scattering intensity at high *q* values prevented comparing the data with a more elaborated model such as a core-shell model which would have allowed us to probe the tubular nature of the assemblies. The existence of a cavity inside the tubular assemblies of alkyl bis-ureas was previously proved by various experimental techniques and corroborated by molecular dynamic simulations.^[4,5,10] It was shown that the nanotubes formed by alkyl bis-ureas were destabilized in bulky aromatic solvents since they could hardly fit in the cavity of the tubes. Indeed, the transition temperature (which is related to the stability of the tubular assembly) was found to be strongly affected by the solvent width.^[10]

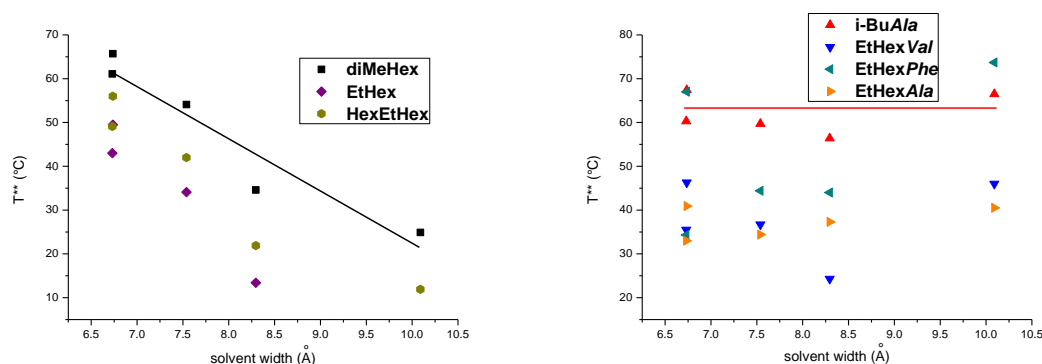


Figure 45 : Transition temperature versus solvent width for alkyl (left) and ester (right) bis-ureas. The transition temperatures measured by nDSC are compiled in Table 4 in appendix.

Therefore, the transition temperature for each alkyl and ester bis-urea was measured by nDSC in toluene, *p*-xylene, 1,2,4-trimethylbenzene, 1,3,5-trimethylbenzene and 1,3,5-triethylbenzene *i.e.* five solvents of varying bulkiness (Figure 45).

Unlike alkyl bis-ureas, the transition temperature of ester bis-ureas is little affected by the solvent width. This result proves that ester bis-ureas assemble into a rod-like structure which is not tubular in aromatic solvents.

2. Local structure

SANS and nDSC analyses performed in various aromatic solvents yielded information on the morphology of the assemblies. The local structure of the assemblies and the exact nature of the non-covalent interactions involved in the assembly process were probed by variable-temperature FTIR analyses. These analyses were performed in toluene below and just above the transition temperature of each bis-urea monomer (Figure 46). For both the rod-like and filament ester bis-urea assemblies, FTIR analyses exhibit two stretching frequencies with maxima at $\nu=3334\pm10\text{ cm}^{-1}$ and $\nu=3275\pm10\text{ cm}^{-1}$, corresponding to urea-bonded aliphatic and aromatic N-H, respectively.^[2] The absence of a peak corresponding to free N-H bonds (at *ca.* 3410 cm^{-1}) confirms the presence of long assemblies. Therefore, similarly to alkyl bis-ureas, the structural transition of ester bisureas occurs between two long urea-bonded assemblies.

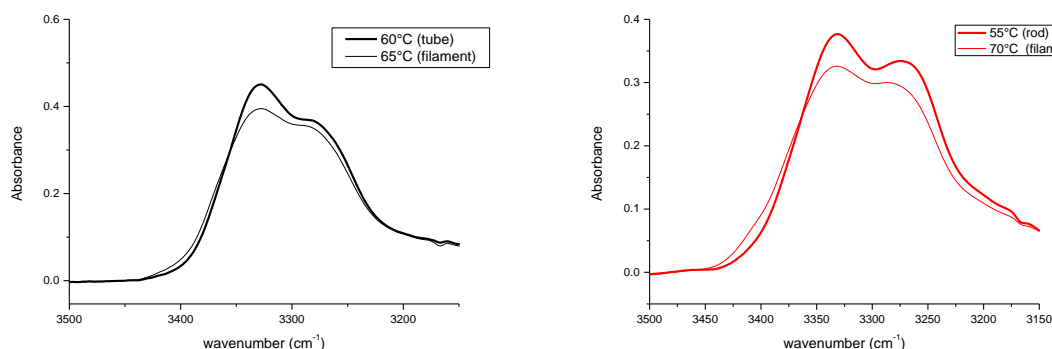


Figure 46 : FTIR spectra in toluene of **diMeHex** at 12.5 mM (left) and **i-BuAla** at 10 mM (right) below and above their T^{**}. Zoom on the N-H region.

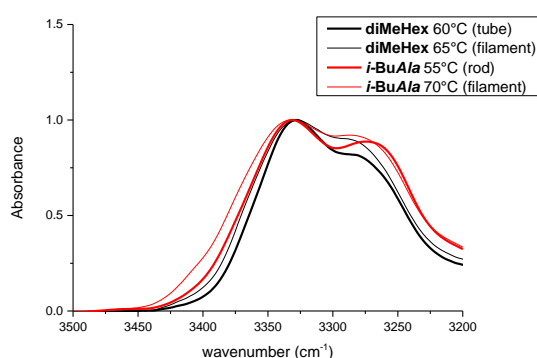


Figure 47: Normalized FTIR spectra in toluene of **diMeHex** at 12.5 mM and **i-BuAla** at 10 mM below and above their T^{**}. Zoom on the N-H region.

Moreover, the shape of the N-H stretching bands is related to the conformation and environment of the urea functions within the H-bond network. For alkyl bis-ureas, the aliphatic N-H band decreases in intensity and becomes wider above the transition due to a different pattern of the N-H bonds in the tube and filament H-bond networks. Based on this observation, it was postulated that the filament is a less regular structure than the tubular structure.^[3] In the case of ester bis-ureas, a similar decrease and broadening is observed for the aliphatic N-H band, but the aromatic N-H band also undergoes a significant decrease in intensity. Therefore, the difference in the shape of the N-H bands between the rod-like and filament structures is less obvious for the ester bisureas than it is for alkyl bisureas between the tube and filament structures (see normalized FTIR spectra, Figure 47). It is not possible at that time to obtain a more precise description of the arrangement of the ester bis-urea monomers in the rod-like and filament structures but the different temperature evolution of the FTIR spectra points out a different reorganization of ester bis-urea monomers during the structural transition compared to alkyl bis-ureas.

A closer look at the carbonyl region of the FTIR spectra of **EtHexVal** in toluene and cyclohexane reveals that the urea carbonyls are involved in hydrogen bonding, but not the ester carbonyls (Figure 48). Indeed, for **EtHexVal**, the stretching frequency associated with the ester carbonyl is the same in THF (in which **EtHexVal** is under the monomeric form) and in toluene and cyclohexane (in which **EtHexVal** is fully associated). A significant red-shift of the ester carbonyl frequency was expected if engaged in a hydrogen bond interaction.^[12] Consequently, one can deduce that in toluene and

cyclohexane, the ester moieties of ester bis-ureas in Figure 42 are not involved in the hydrogen bond network of their rod-like assemblies.

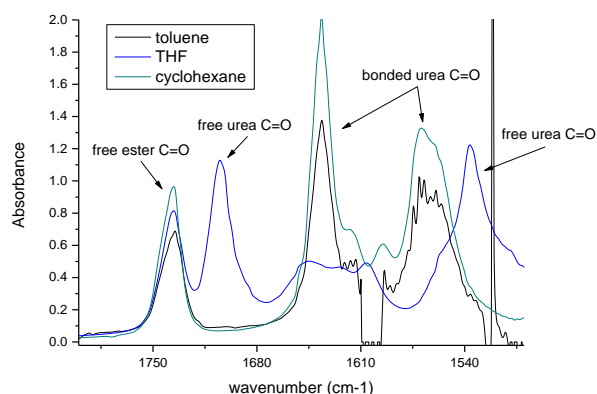


Figure 48 : FTIR spectra of **EtHexVal** at 10 mM in various solvents. Zoom on the CO region.

According to the above-mentioned analyses, two tentative structures for the rod-like assemblies formed by ester bis-ureas are represented schematically in Figure 49. The hydrogen bonds are formed along the rod axis and there are two bis-urea molecules in the cross-section. In the “alternate structure”, two bis-ureas at stage i are orthogonal to two bis-ureas at the stage $i+1$ and thus the relative position of the bis-urea molecules in the structure is alternated. In contrast, the “double filament structure” is generated by the lateral packing of two filaments resulting in two intertwined single filaments. In both cases, the close-packing of the bis-urea molecules would prevent the encapsulation of solvent molecules, corroborating the fact that the stability of these structures is not significantly affected by the size of the solvent.

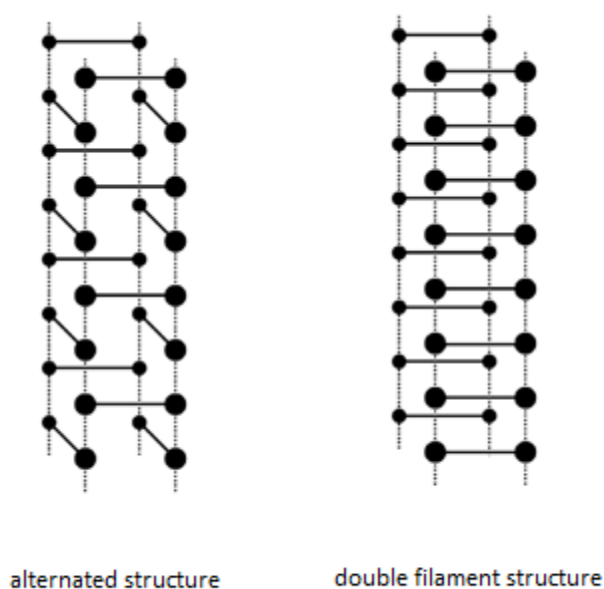


Figure 49 : Tentative molecular arrangements of the ester bis-urea molecules within their rod-like structure. Hydrogen bonds are symbolized by dotted lines connecting the urea functions

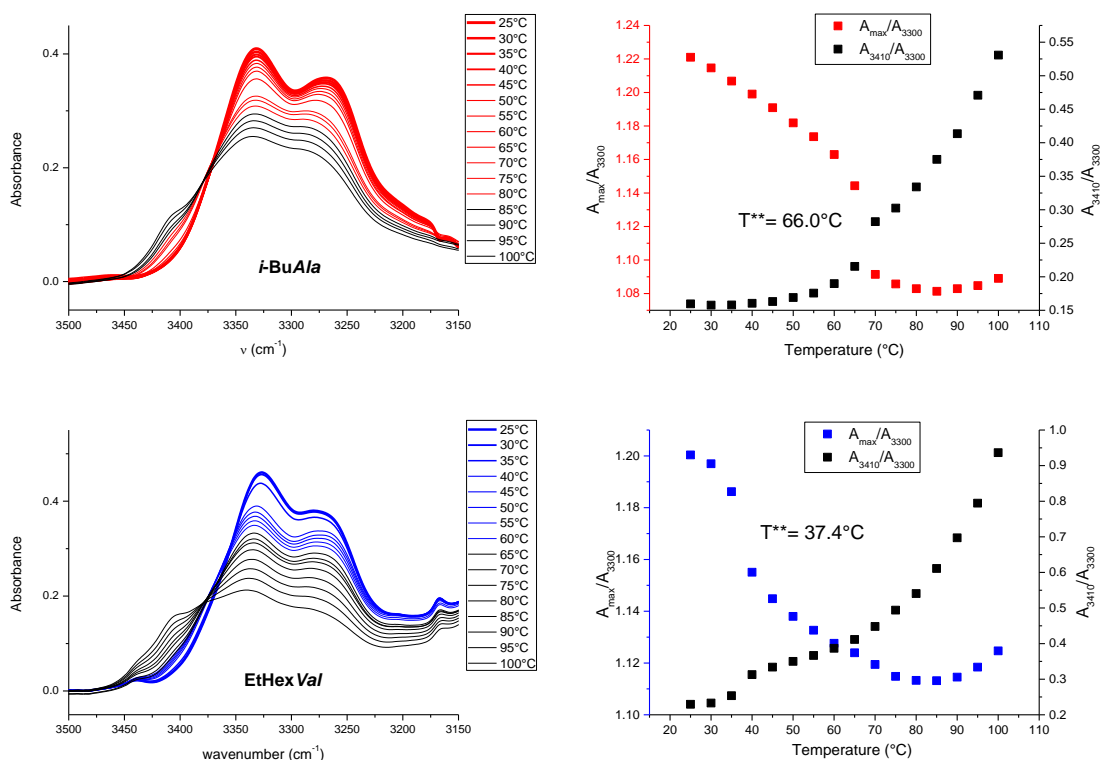
3. Structural transition

The structural transition between the rod-like and filament structures of ester bis-ureas was determined precisely using nDSC, variable-temperature FTIR and ITC analyses.

The nDSC traces showed a wider transition (*ca.* 15°C) compared to alkyl bis-ureas (*ca.* 5°C) thus the transition is only moderately cooperative (Figure 67 in appendix). Despite this difference, the transition temperatures and enthalpies of **diMeHex** and ***i*-BuAla** were found to be quite similar in toluene ($T^{**} = 61.1$ and 60.3°C , respectively, and $\Delta H^{**} \approx 1.0$ kcal/mol).

As expected, the relative stability of the structures formed by ester bis-ureas was tuned by changing the nature of the alkyl group of the ester function (isobutyrate or 2-ethylhexanoate) and the nature of the substituent in the α -position of the urea functions (*i*-Pr, Me or Bn). Even though ***i*-BuAla** and **EtHexAla** share a similar structure in solution (see SANS and FTIR analyses), **EtHexAla** exhibited significantly lower transition temperatures in all the aromatic solvents studied ($32.6 < T^{**} < 40.6^{\circ}\text{C}$ for **EtHexAla** vs $56.4 < T^{**} < 67.4^{\circ}\text{C}$ for ***i*-BuAla**). It demonstrates that the 2-ethylhexyl side chain strongly destabilizes the rod-like structure. This can be explained by repulsive interactions between alkyl chains or by solvation effects.^[11]

The structural transition of ester bis-ureas was also followed by recording FTIR spectra every 5°C between 25 and 100°C in toluene (10 mM). The maximum of the aliphatic N-H band absorbance was normalized by the absorbance at 3300 cm^{-1} and plotted versus the temperature (Figure 50).



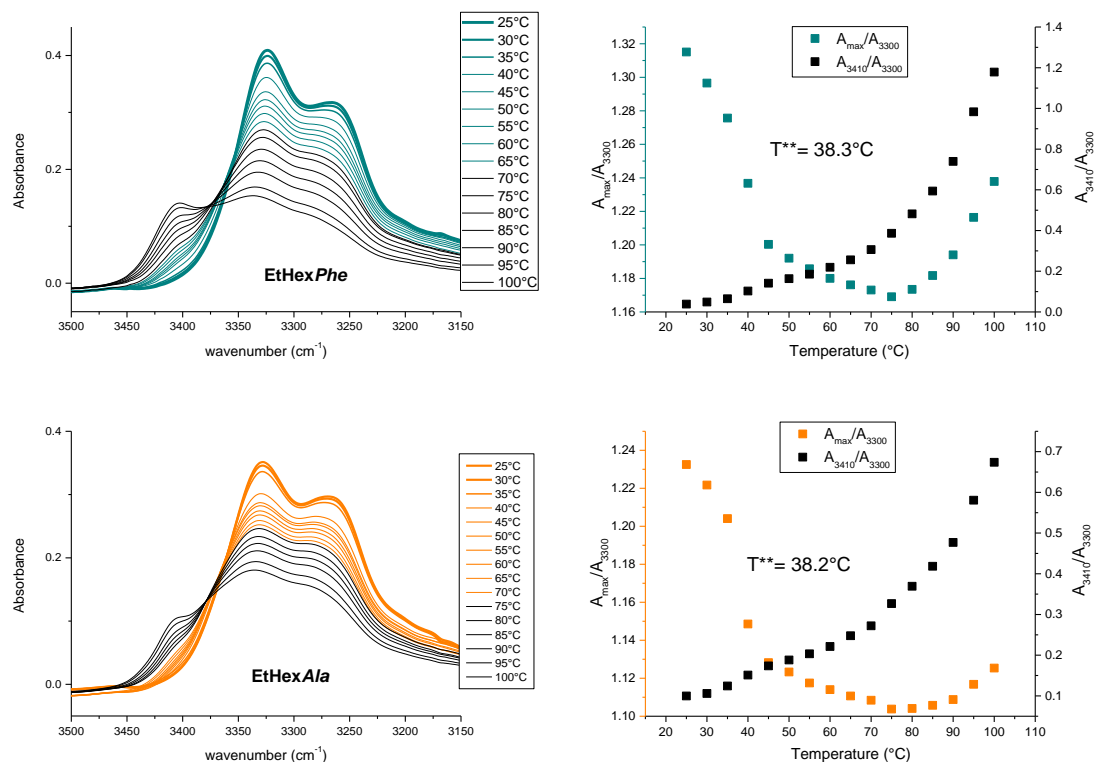


Figure 50 : Left: FTIR spectra vs temperature for ester bis-ureas (toluene, 10mM). Right: plots of A_{max}/A_{3300} and A_{3410}/A_{3300} against temperature. A_{max}/A_{3300} corresponds to the normalized intensity of the aromatic NH band and its plot against T° reflects the structural transition. T^* corresponds to the mid-point temperature. The T^* values determined by FTIR are in accordance with those measured by nDSC. A_{3410}/A_{3300} reflects the amount of free NH which sharply increases above the structural transition.

For all ester bis-ureas, a steep decrease of the absorbance ratio was observed at a temperature close to the transition temperature determined by nDSC. The decrease happened on a wide temperature range, confirming the moderate cooperativity of the transition. The intensity of the shoulder at *ca.* 3410 cm^{-1} which corresponds to free N-H, sharply increased above the transition. This free N-H corresponds to extremities of the filament and/or to free monomers. This corroborates the SANS experiments and confirms that filaments formed by ester bis-ureas at high temperature are short. The structural transition of ester bis-urea assemblies was also investigated by ITC by injecting a 1 mM solution in toluene into a calorimetric cell containing pure toluene at 20°C. At this concentration, all ester bis-ureas are assembled under the rod-like structure. For all bis-ureas, similar heat flow curves were obtained and were composed of endothermic peaks of decreasing intensity upon addition of the bis-urea solution. Those peaks are related to the disruption of the hydrogen bond network upon dilution. No more dissociation was observed above a certain critical concentration corresponding to stable self-assemblies. Enthalpograms of ester bis-ureas (Figure 51) were derived from the integration of the heat flow peaks.

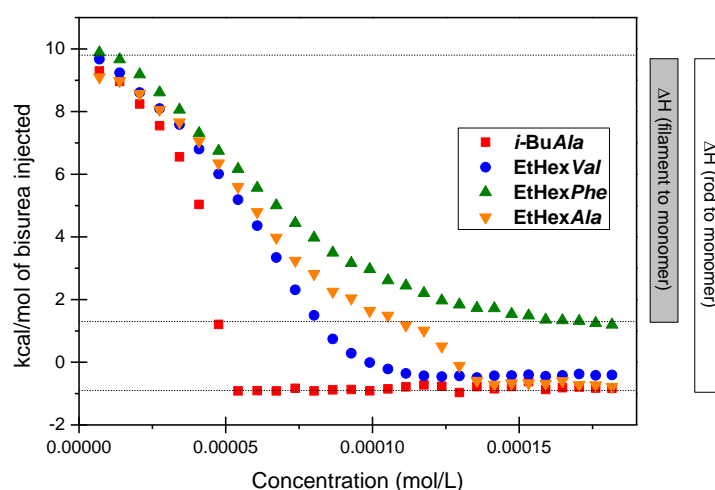


Figure 51 : ITC enthalpograms of 1 mM ester bis-urea solutions in toluene injected into pure toluene versus total bis-urea ester concentration in the cell ($T = 20^{\circ}\text{C}$). For *i-BuAla* and *EtHexVal*: transition from monomers to the rod-like structure ($c^* = 8.4 \times 10^{-5}$ M and 1.3×10^{-4} M respectively). For *EtHexPhe*: transition from monomers to filament structure ($c^* = 1.3 \times 10^{-4}$ M). For *EtHexAla*: transitions from monomers to filament structure ($c^* = 1.2 \times 10^{-4}$ M), and then from filament to rod-like structure ($c^{**} = 2.8 \times 10^{-4}$ M). Critical concentrations (c^{**} and c^*) were approximated by taking twice the mid-point concentration.^[1]

i-BuAla presented a similar enthalpogram to *diMeHex*^[9] with a sharp decrease of the heat of dissociation. It was shown that the transition observed for *diMeHex* was the dissociation of the tubular assemblies into monomers. Given that the transition enthalpy of *diMeHex* and *i-BuAla* are similar and that no dissociation is observed after the transition, we can assume that the transition observed in ITC for *i-BuAla* is also a rod to monomer transition. The critical concentration c^* , which corresponds to the concentration for which the rod-like structure is predominant over the monomers, can be extracted from the ITC data (2.6×10^{-5} M and 1.5×10^{-4} M for *diMeHex* and *i-BuAla* respectively). The c^* is higher for *i-BuAla* than for *diMeHex*, suggesting that the ester moiety decreases the capacity of the bis-urea monomers to self-assemble. However, the ester moiety does not prevent the association of ester bis-ureas into long supramolecular polymers.

EtHexVal also shows the direct dissociation of rods into monomers as its transition enthalpy was found to be similar (Figure 51). However, its c^* is higher (1.3×10^{-4} M) than for *i-BuAla* which is consistent with the lower stability of its rod-like structure observed by nDSC. For *EtHexPhe*, the first injections correspond to the dissociation of rods into monomer as well but the significant heat effects that remain ($\Delta H = 1.8$ kcal/mol) indicate that the monomers rearrange into filaments, because of the sufficiently high concentration in the cell. Thus, the transition observed ($c^* = 1.3 \times 10^{-4}$ M) is the transition from the monomers to the filaments. For *EtHexAla*, both transitions were clearly visible. After a first regime in which rods were dissociated into monomers upon dilution ($\Delta H^* = 9.0$ kcal/mol), a second regime occurred in which the rods dissociate into filaments ($\Delta H^{**} = 1.8$ kcal/mol). The enthalpy value of the rod-like to filament transition is in agreement with the value obtained in nDSC. Since the two transitions are well distinguished, two critical concentrations are measured (1.2×10^{-4} M for the monomer to filament transition and 2.8×10^{-4} M for the filament to rod transition). Interestingly, even though ethylhexyl functionalized ester bis-ureas exhibit similar T^{**} at mM concentrations, they show different critical concentrations at 20°C .

Using the transition temperatures determined by ITC, nDSC and variable-temperature FTIR analyses, it is possible to construct a pseudo-phase diagram highlighting the stability of hydrogen-bonded polymers in toluene relatively to their monomers (Figure 52 and Figure 53).

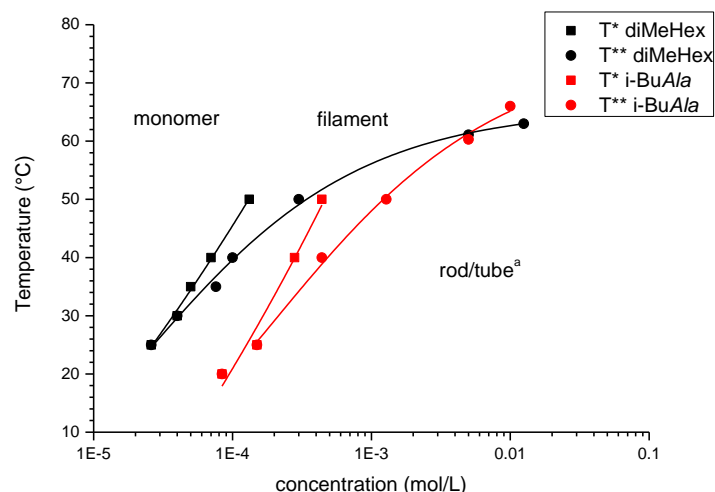


Figure 52 : Comparison of the pseudophase diagrams of **diMeHex** and **i-BuAla** in toluene. ^a The low temperature structures displayed by **diMeHex** and **i-BuAla** have different morphologies (*vide supra*). The lines are drawn to guide the eye.

Comparing **diMeHex** and **i-BuAla** pseudo-phase diagrams (Figure 52) provides information on the impact of the ester moiety on the self-assembly properties of the bis-urea monomer. At low concentration, the tubular structure formed by **diMeHex** is more stable than the rod-like structure of **i-BuAla** as they show a difference of *ca.* 20°C between their transition temperatures. At higher concentration, **diMeHex** and **i-BuAla** assemblies show similar stabilities even though they have different morphologies.

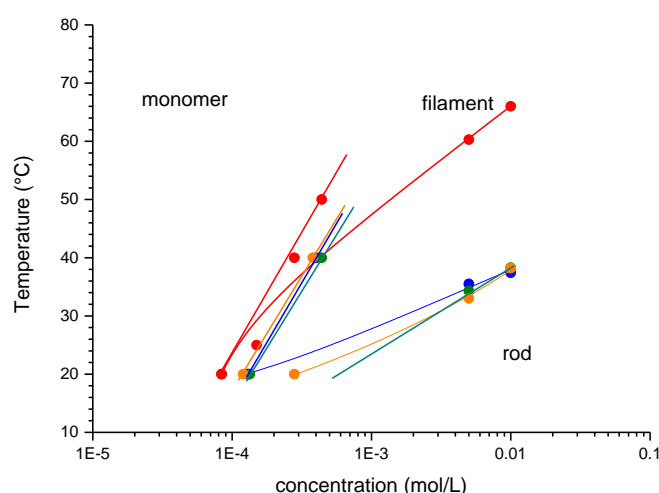


Figure 53 : Pseudo-phase diagrams of the ester bis-ureas in toluene as determined by ITC, DSC and variable-temperature FTIR analyses. Red: **i-BuAla**, blue: **EtHexVal**, green: **EtHexPhe**, orange: **EtHexAla**.

When comparing the pseudo-phase diagrams of *i*-BuAla and EtHexAla (Figure 53), it clearly appears that the nature of the alkyl chain has a strong influence on the stability of the rod-like structure. Also, the predominance domain of the rod-like structure decreases in the order *i*-BuAla >> EtHexVal > EtHexAla > EtHexPhe which roughly follows the bulkiness of the group attached to the α -carbon. In contrast, no influence is seen on the filament to monomer transition, probably due to a less densely packed structure. The nature of the ester moiety and the alkyl chain can thus be used to tune the stability of the rod-like structure.

4. Conclusion

Alkyl and ester bis-ureas have similar association properties as they form long and rigid assemblies at mM concentrations in toluene and form gels. They share a filament structure with one molecule of bis-urea in the cross-section above the transition but they differ in the morphology of the assemblies (tubular vs rod-like) formed below the transition. The rod-like structure formed by ester bis-urea assemblies does not present any cavity and has only two molecules per section. A more precise determination of the molecular arrangement of the ester bis-urea molecules in this rod-like structure is not possible at that time.

It was shown that the ester moiety does not participate in the hydrogen bond network but it does impact: i) the morphology of the polymer structure formed, ii) the cooperativity of the transition between the assemblies and iii) the relative stability of the assemblies. The nature of the substituent attached to the α -carbon and the nature of the alkyl chain can be used to tune the relative stability of both assemblies.

B. Enantiopure ester bis-ureas

One of the important advantages in the design of bis-ureas derived from α -amino esters is the easier access to enantiopure monomers. There are several examples of enantio-enriched alkyl bis-urea monomers derived from chiral amines such as methylbenzylamine, methylheptylamine or 2-ethylhexylamine but (*S,S*)-EHUT and (*R,R*)-EHUT were the only ones to be soluble in low polarity solvents. Moreover, the synthesis of the enantio-enriched 2-ethylhexylamine used for the preparation of EHUT is tedious.^[13] By using amino-acids as a chiral pool, we have access to highly enantiopure and cheap compounds. Enantiopure EHUT monomers form chiral tubular assemblies as the result of the transfer of chirality from the stereogenic centres to the whole supramolecular assembly.^[13] The goal is first to obtain such an effect with ester bis-urea assemblies *i.e.* to demonstrate that the assemblies formed by ester bisureas are chiral at the supramolecular level. Then, the experimental CD signature obtained for the assemblies of ester bisureas will be compared with simulated CD signatures for a set of modeled supramolecular structures. The aim is to discriminate between the two possible structures proposed in Figure 49 and to tentatively propose a molecular arrangement of the ester bis-urea molecules in their rod-like structure.

1. Comparison with racemic ester bis-ureas

The racemic ester bis-urea monomers studied in part A were composed of the enantiopure monomers (25% each) and the heterochiral monomers (50%), not counting for the chirality of the lateral alkyl chain. The enantiopure ester bis-urea monomers selected in this part bear the same 2-ethylhexyl side-chain and only differ in the nature of the substituent attached to the α -carbon. Compared to part A, we chose to replace **EtHexPhe** by **EtHexLeu** for two reasons: i) **S-EtHexPhe** exhibits a significantly higher transition temperature than the other enantiopure ester bis-urea monomers in alkanes which suggests a different association behavior for this monomer and ii) **EtHexPhe** bears an additional chromophore which was anticipated to complicate the comparison of the CD data.

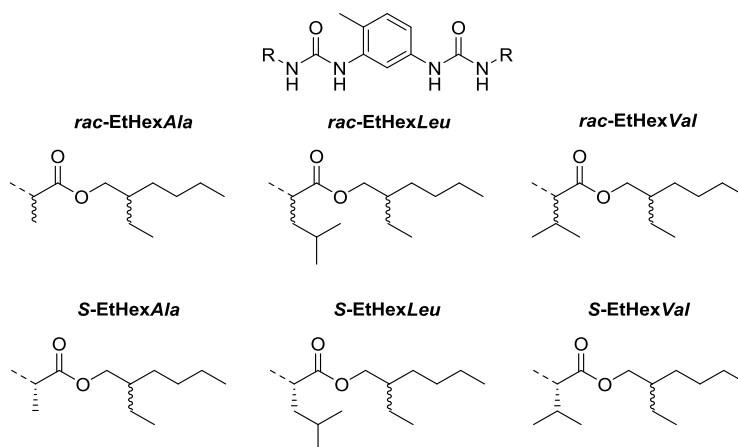


Figure 54 : chemical structures of the bis-urea monomers studied in this part

The first interesting observation is that *rac*-EtHexAla and *rac*-EtHexVal bis-ureas form gels at 10 mM in toluene whereas *rac*-EtHexLeu and all three enantiopure bis-ureas only form viscous solutions. It implies that *rac*-EtHexAla and *rac*-EtHexVal form longer or less flexible assemblies than *S*-EtHexAla and *S*-EtHexVal in toluene at the same concentration. The higher gelation ability of a racemic compound compared to its enantiomer is not unusual but remains rare compared to the opposite situation in which the enantiopure molecules form stronger gels than their racemic analogues.^[14]

SANS experiments were performed on all compounds in toluene- d_8 at *ca.* 0.6 wt% (*ca.* 3 mM) (Figure 66 in appendix) and the data were fitted with a model for long cylindrical objects. The results are summed up in Table 2.

Table 2 : Geometrical Radius (r), linear Density (n_L) and number of bis-urea molecules (n) in the cross-section of the cylindrical objects deduced from the fit of the SANS data below and above the transition temperature (T^{**})^a

bisurea	20°C			70°C			T^{**} (°C) ^b
	r (Å)	n_L (Å ⁻¹)	n^c	r (Å)	n_L (Å ⁻¹)	n^c	
<i>rac</i>-EtHexAla	15.4	0.45	2.1	8.9	0.16	0.74	33.0
<i>rac</i>-EtHexLeu	14.0	0.24	1.1	<i>n.d.</i>	<i>n.d.</i>	<i>n.d.</i>	<i>n.d.</i>
<i>rac</i>-EtHexVal	16.1	0.50	2.3	9.1	0.17	0.77	35.5
<i>S</i>-EtHexAla	11.4	0.24	1.1	<i>n.d.</i>	<i>n.d.</i>	<i>n.d.</i>	<i>n.d.</i>
<i>S</i>-EtHexLeu	12.0	0.26	1.2	<i>n.d.</i>	<i>n.d.</i>	<i>n.d.</i>	<i>n.d.</i>
<i>S</i>-EtHexVal	15.7	0.24	1.1	<i>n.d.</i>	<i>n.d.</i>	<i>n.d.</i>	<i>n.d.</i>

^a SANS experiments were performed at *ca.* 0.6 wt% in toluene- d_8 . ^b T^{**} = transition temperature between structures as determined by nDSC experiments (*vide infra*) performed at 5 mM in toluene. ^c n = the number of bis-urea molecules in the cross-section, assuming a repeat distance of 4.6 Å.

As mentioned in part A, ***rac*-EtHexAla** and ***rac*-EtHexVal** form a rod-like structure with two molecules per section. In contrast, ***rac*-EtHexLeu** and the enantiopure bis-ureas are assembled under the form of a filament (one molecule per section). This implies that 20°C is above the transition temperature (if it exists) of ***rac*-EtHexLeu** and of the enantiopure bis-ureas. Indeed, variable-temperature FTIR analyses of ***rac*-EtHexLeu** did not show any evidence of a transition (Figure 69 in appendix). ***rac*-EtHexAla** and ***rac*-EtHexVal** have a higher transition temperature than their respective enantiopure which is in agreement with their better gelation ability. It can be explained: i) by a different structure or molecular arrangement for the enantiopure vs racemic assemblies, or ii) by the presence of defects in the racemic assemblies. Concerning the last point, if the energetic cost of the defects is more important in the filament than in the rod-like structure (see chapter 3), then the transition temperature is higher for the racemic than for the enantiopure ester bis-urea assemblies.

As the purpose here is to use circular dichroism to compare experimental and simulated CD spectra, the study cannot be pursued in toluene because of its too strong UV-absorbance. Me-cyclohexane was chosen instead given its low melting point and high boiling point. Moreover, the transition temperatures of the assemblies formed by the enantiopure bis-ureas are higher in this solvent as determined by means of nDSC analyses (T^{**} = 14.9°C for ***S*-EtHexAla** and T^{**} = 6.7°C for ***S*-EtHexLeu** at 10 mM) or variable-temperature CD measurements (T^{**} = -3°C for ***S*-EtHexVal** at 1 mM). SANS and FTIR experiments were performed in Me-cyclohexane and the results were used to compare the nature of the assemblies formed by the enantiopure bis-ureas in this solvent with those formed by racemic bis-ureas in toluene.

SANS experiments were performed for the three enantiopure ester bis-ureas in Me-cyclohexane- d_{14} at *ca.* 0.6 wt% and the results were fitted with a model for long cylindrical objects (Figure 66 in appendix). The results are displayed in Table 3.

Table 3 : Geometrical radius (r), linear density (n_L) and number of bis-urea molecules (n) in the cross-section of the cylindrical objects deduced from the fit of the SANS data below and above the transition temperature (T^{**})^a

bisurea	20°C			66°C			T^{**} (°C)
	r (Å)	n_L (Å ⁻¹)	n^d	r (Å)	n_L (Å ⁻¹)	n^d	
S-EtHexAla	14,6 ^b	0,58 ^b	2,6 ^b	15.0	0,46	2.1	14.9 ^c
S-EtHexLeu	12.5	0.24	1.1	13.6	0.22	1.0	6.7 ^c
S-EtHexVal	12.9	0.24	1.1	13.4	0.22	1.0	-3.0 ^e

^a SANS experiments were performed at *ca.* 0.6 wt% in Me-cyclohexane-d₁₄. ^b measured at 10°C. ^c T^{**} = transition temperature between structures as determined by nano-DSC experiments (*vide infra*) performed at 10 mM in Me-cyclohexane. ^d n = the number of bis-urea molecules in the cross-section, assuming a repeat distance of 4.6 Å. ^e T^{**} = transition temperature between structures as determined by CD experiments (*vide infra*) performed at 1 mM in Me-cyclohexane.

Unfortunately, the SANS instrument did not allow us to perform analyses below 10°C i.e. below the transition temperature of **S-EtHexLeu** and **S-EtHexVal**. **S-EtHexAla** forms, as expected, a rod-like structure with two or three molecules in the cross-section ($n = 2.6$) at 10°C but oddly the rod-like structure does not rearrange into filaments above the transition (see Figure 66 in appendix). This result is not in agreement with the nDSC, FTIR and CD analyses (*vide infra*) and likely comes from a confusion in the preparation of the sample. A new measurement will be made to ascertain the result of the SANS analyses for **S-EtHexAla**. For **S-EtHexLeu** and **S-EtHexVal** the SANS data confirm the presence of a filament structure at 20°C ($n = 1.1$ for both bis-ureas) which remains stable up to 66°C (Figure 66 in Appendix). An interesting fact is that contrary to what was observed in toluene for racemic bis-ureas at 70°C, the enantiopure bis-ureas still form long assemblies at 66°C (Figure 55). It points out an important effect of the solvent on the size of the assemblies.

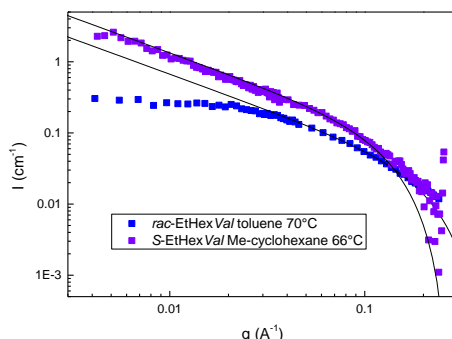


Figure 55 : SANS analyses of **S-EtHexVal** in Me-cyclohexane-d₁₄ and **rac-EtHexVal** in toluene-d₈ (*ca.* 0.6 wt%).

Variable-temperature FTIR analyses were performed in order to get the FTIR signature of the assemblies formed by these enantiopure bis-ureas below and above the transition in methyl-cyclohexane (Figure 56). Spectra were recorded each 5°C between 0 and 105°C (Figure 70 in Appendix). For **S-EtHexAla** and **S-EtHexLeu**, these FTIR analyses revealed a transition between two long polymer structures with $T^{**} \approx 15^\circ\text{C}$ and $T^{**} \approx 5^\circ\text{C}$. These transition temperatures are in agreement with those measured by nDSC ($T^{**} = 14.9^\circ\text{C}$ and $T^{**} = 6.7^\circ\text{C}$ respectively, Figure 68 in appendix). Combined with SANS analyses, these results clearly show that the transition observed by FTIR and nDSC analyses for **S-EtHexAla** and **S-EtHexLeu** is the transition between the rod-like and the filament structure. In contrast, for **S-EtHexVal**, no transition was observed by FTIR and nDSC analyses which indicated that the transition is below 0°C. Interestingly, the trend in the stability of the rod-like structures is not the same for racemic and enantiopure bis-ureas. For racemic bis-ureas in toluene

T** increases in the order **EtHexLeu**<<**EtHexAla**<**EtHexVal** whilst for enantiopure bis-ureas in Me-cyclohexane T** increases in the order **EtHexVal**<**EtHexLeu**<**EtHexAla**. For enantiopure bis-ureas, the stability of the rod-like structure seems to be related with the bulkiness of the substituent attached to the α -carbon. Several hypotheses can be made to explain the different trend observed between this small series of racemic and enantiopure ester bis-urea monomers: i) a conformational effect induced by the solvent and ii) energetic differences in the defects within the assemblies formed by the racemic ester bis-ureas; *e.g.* filaments of **rac-EtHexVal** are more destabilized relatively to their rod-like structure than filaments of **rac-EtHexAla** leading to a more stable rod-like structure for **rac-EtHexVal** (see chapter 3).

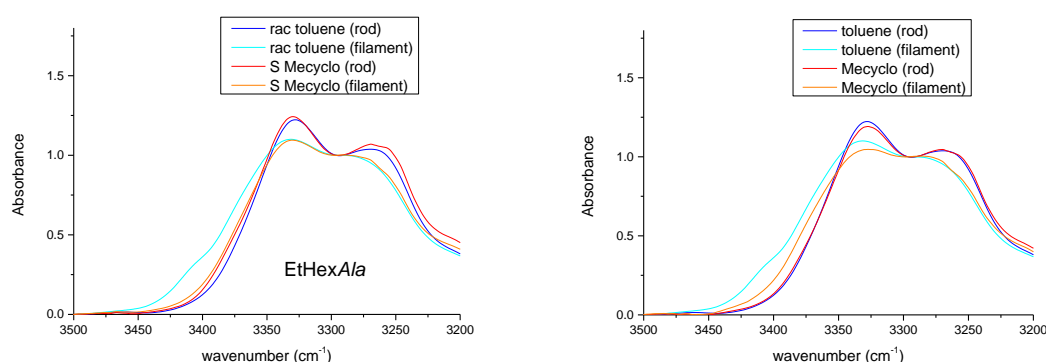


Figure 56 : Comparison of FTIR spectra of **S-EtHexAla** (Me-cyclohexane) and **rac-EtHexAla** (toluene) (left) and **S-EtHexAla** in toluene and Me-cyclohexane (right) 10°C below (rod) and above (filament) the transition temperature at 10 mM. Zoom on the NH region.

Our aim was to compare the FTIR signature of the rod-like assemblies formed by racemic ester bis-ureas in toluene (since these assemblies have been characterized in part A) and those formed by enantiopure ester bis-ureas in Me-cyclohexane (characterized above). Unfortunately, the FTIR signature of the rod-like assemblies formed by **rac-EtHexLeu** in toluene and by **S-EtHexVal** in Me-cyclohexane cannot be established since their transitions occur at too low temperatures. Therefore, we limited our comparison to **S-EtHexAla**. Clearly, the rod-like assemblies of **rac-EtHexAla** (in toluene) and **S-EtHexAla** (in Me-cyclohexane) display the same FTIR signature (Figure 56). Together with the SANS data and the in-depth structural analysis of the assemblies formed by **rac-EtHexAla** in the first part of this chapter, we can assume that the **S-EtHexAla** forms the same non-tubular rod-like assembly than **rac-EtHexAla** with two molecules in the cross section. The filament structures have also similar FTIR signature at the exception of the presence of a free N-H band for **rac-EtHexAla** due to weaker hydrogen bonding in toluene than in Me-cyclohexane as exhibited by the FTIR spectra of **S-EtHexAla** in both solvents (Figure 56). It presumes that the filament assemblies also possess a similar morphology.

Finally, the rod-like assemblies formed by **S-EtHexAla**, **S-EtHexLeu** and **S-EtHexVal** display virtually identical CD signature in Me-cyclohexane (*vide infra*) corroborating the fact that these three enantiopure bis-ureas assemble under the same rod-like structure.

2. Structural determination using CD

The assemblies formed by the enantiopure bis-ureas were studied by circular dichroism spectroscopy as circular dichroism spectra can be simulated from a modeled structure.

To avoid saturation of the absorbance, CD measurements were made at 1 mM in Me-cyclohexane.

A variable-temperature CD analysis of **S-EtHexLeu** at 1mM in Me-cyclohexane performed in a closed 1 mm quartz cell between -10 and 105 °C by recording spectra each 5°C (heating rate= 1°C/min) (Figure 57) exhibited the existence of two CD signatures stable in large temperature ranges which may correspond to the rod-like and filament structures.

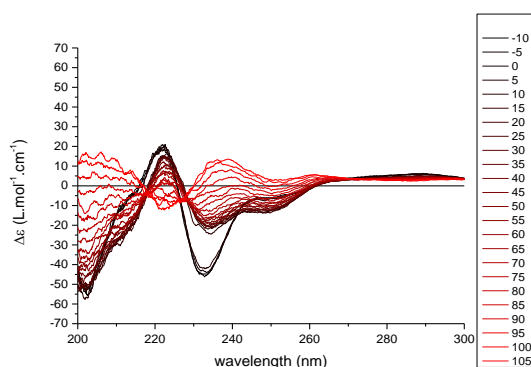


Figure 57 : variable-temperature CD analyses of **S-EtHexLeu** at 1mM in Me-cyclohexane between -10 and 105°C (heating rate= 1°C/min)

For the three enantiopure bis-ureas, the molar ellipticity at 233 nm was measured between -10 and 130°C (every 0.1°C). According to the result of the plot of the molar CD value as a function of the temperature, three full spectra were also recorded 15 degrees below the transition, 15 degrees above the transition and at 130°C (Figure 58). The objective was to get a CD signature for each assembly.

The plot of the molar CD value as a function of the temperature clearly revealed a first transition between two CD active supramolecular assemblies (Figure 58). This transition occurs at 11.3 °C, 8.0°C and -3.0°C for **S-EtHexAla**, **S-EtHexLeu** and **S-EtHexVal** respectively, and these transition temperatures are in accordance with those determined by nDSC and FTIR analyses (*vide supra*). This transition can also be followed by UV analyses by plotting the value of the absorbance at 249 nm as a function of the temperature (Figure 71-34 in appendix).

After this first transition, the molar CD value remains stable during *ca.* 50°C and then gradually decreases, showing another less cooperative transition between the strongly CD active filament assemblies and a species showing only a residual CD signal. This second transition likely corresponds to the filament to monomer transition or to the dissociation of the long filaments into small assemblies.

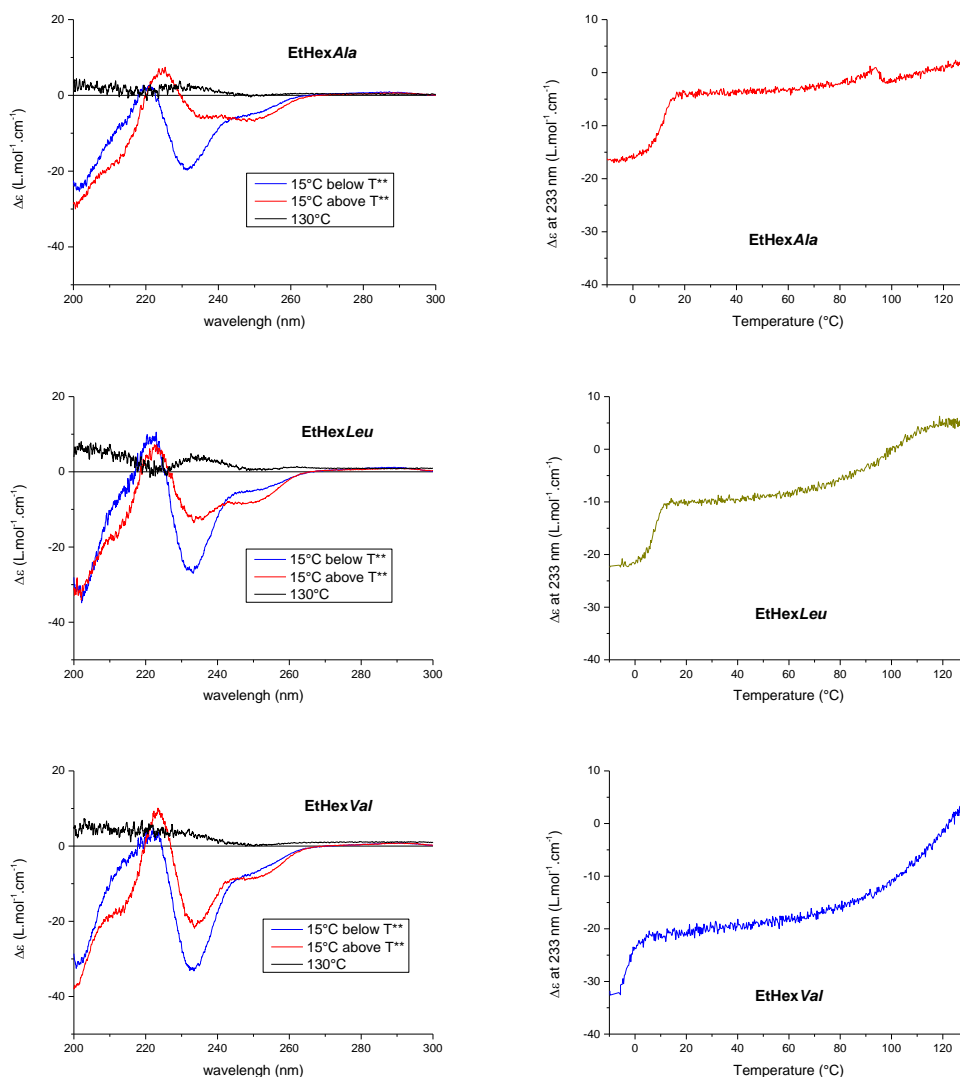


Figure 58 : CD analyses of **S-EtHexAla**, **S-EtHexLeu** and **S-EtHexVal** in Me-cyclohexane (1 mM). Left: Circular Dichroism spectra recorded 15 degrees below the transition, 15 degrees above the transition and at 130°C. Right: plot of the molar CD value at 233 nm as a function of the temperature.

We observed significant differences in the shape and intensity of the CD spectra recorded below and above the structural transition. Firstly, it is important to note that both the rod-like and filament structures formed by enantiopure ester bis-urea monomers are chiral at the supramolecular level. This is in striking contrast with the assemblies formed by an enantiopure alkyl bis-urea (**R,R-EHUT**) for which only the tubular form adopted a chiral configuration in solution.^[15] The differences between the CD signature of the rod-like and filament structures are: (i) the presence of a band around 215 nm for the filament form, (ii) the decrease of the band around 235 nm upon going from the rod-like to filament structure and (iii) the increase of the band around 250 nm for the filament form. It is worth to note that these differences are very small which seem to indicate that the bis-urea ester unit adopts a similar chiral conformation in both the rod-like and filament structures. Also, the CD and UV signal exhibited by the rod-like and filament structures of the three ester bis-ureas are quite similar which indicates that these three ester bis-ureas form similar chiral supramolecular assemblies in solution (Figure 59).

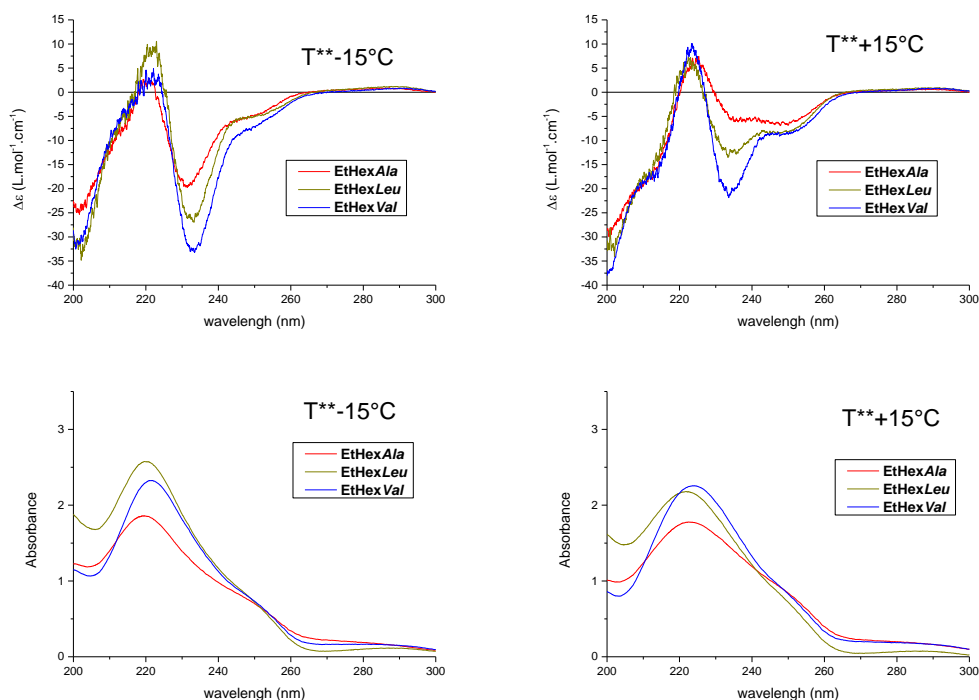


Figure 59 : Comparison of the CD and UV signature of the rod-like and filament structures of **S-EtHexAla**, **S-EtHexLeu** and **S-EtHexVal** at 1 mM in Me-cyclohexane 15 degrees below the transition for the rod-like structure and 15 degrees above the transition for the filament structure.

3. Molecular modeling

Lazzaroni and coworkers (Mons University, Belgium) constructed the single and double filament structures of **S-EtHexAla**, using a random distribution of *S* and *R* ethylhexyl side chains, and analyzed their morphology and stability from the equilibrated trajectory obtained from a 20 ns molecular dynamics (MD). Despite several attempts, no stable construction of the “alternated structure” proposed in Figure 49 was obtained.

a. Analysis of the morphology of the filament and double filament structures formed by S-EtHexAla

Figure 60 shows the representative structures of the single (left) and double (right) filaments of **S-EtHexAla**. The single filament has a repetitive motif of *ca.* 9 units, a pitch of *ca.* 34.5 Å, and a linear density of *ca.* 0.26 Å⁻¹. The double filament has a repetitive motif of *ca.* 30 units (15 units/filament), a pitch of *ca.* 53.5 Å, and a linear density of *ca.* 0.56 Å⁻¹. Using a repeat distance of 4.6 Å between the monomers, *i.e.* the same value used for interpreting the SANS measurements, the number of molecules in the cross section, *n*, is of *ca.* 1.2 and 2.6, for the single and double filaments, respectively. SANS experiments in Me-cyclohexane at 10°C provided a *n* value of 2.6, thus in good correspondence with the double filament simulated by MD at room temperature (300K). The values of the linear density and the number of the molecules in the cross-section for the filament structure also fit with the experimental data (Table 3).

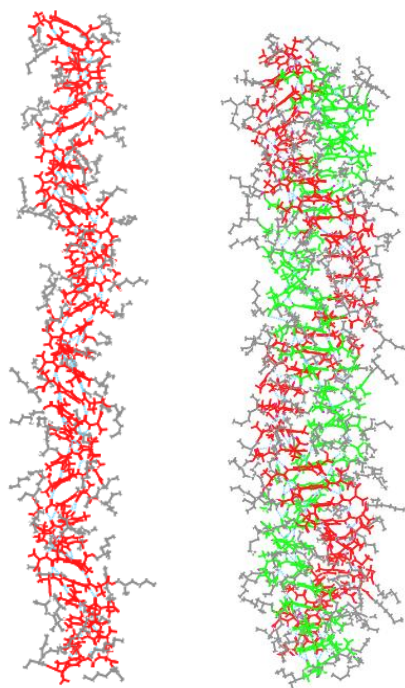


Figure 60: Representative structure of a single (left) and double (right) filament of **EtHexAla** generated during MD. The tolyl bis-urea fragment is displayed in red (filament structure) and in red and green (double filament structure) whilst the 2-ethylhexyl side chains are in grey.

To characterize the structure, a potential energy map, function of specific dihedral angles, has been created for an isolated **S-EtHexAla** molecule (see Figure 61 and Figure 62). The values of the dihedral angles adopted by the conformations generated during the MD in the single filament and double filament structure, are then visualized on the map as dots; the density of these dots is scaled from white (low density) to black (high density).

The dihedral angles ϕ_1 and ϕ_2 define the orientation of the urea moieties with respect to the core. In the single filament, ϕ_1 and ϕ_2 are located in a well-defined area at about 137° and 146° , respectively, characteristic of a M-helix (ϕ_1 and ϕ_2 would have a negative sign in a P-helix). As reported for other bis-urea systems, these values do not correspond to their preferential orientation in isolated molecules, but correspond to an orientation of the urea moieties that allows the formation of the hydrogen bond network.^[6] These values change only slightly in the double filament, with ϕ_1 and ϕ_2 at about 134° and 135° , respectively, thus showing the conservation of the helicity and of the strong hydrogen bond network of the parent single filaments.

The other dihedral angles are related to the orientation of the rest of the side chains with respect to the urea moieties. In the single filament, ϕ_3 and ϕ_4 , the angle nearest to the urea moiety, show a preferential orientation at -74° . In the double filament, this orientation decreases in intensity and another maximum appears at -119° , attributed to the inter-filament interactions. The other dihedral angles show a larger variability, which is representative of the disorder allowed farther from the core and its hydrogen bond constraints.

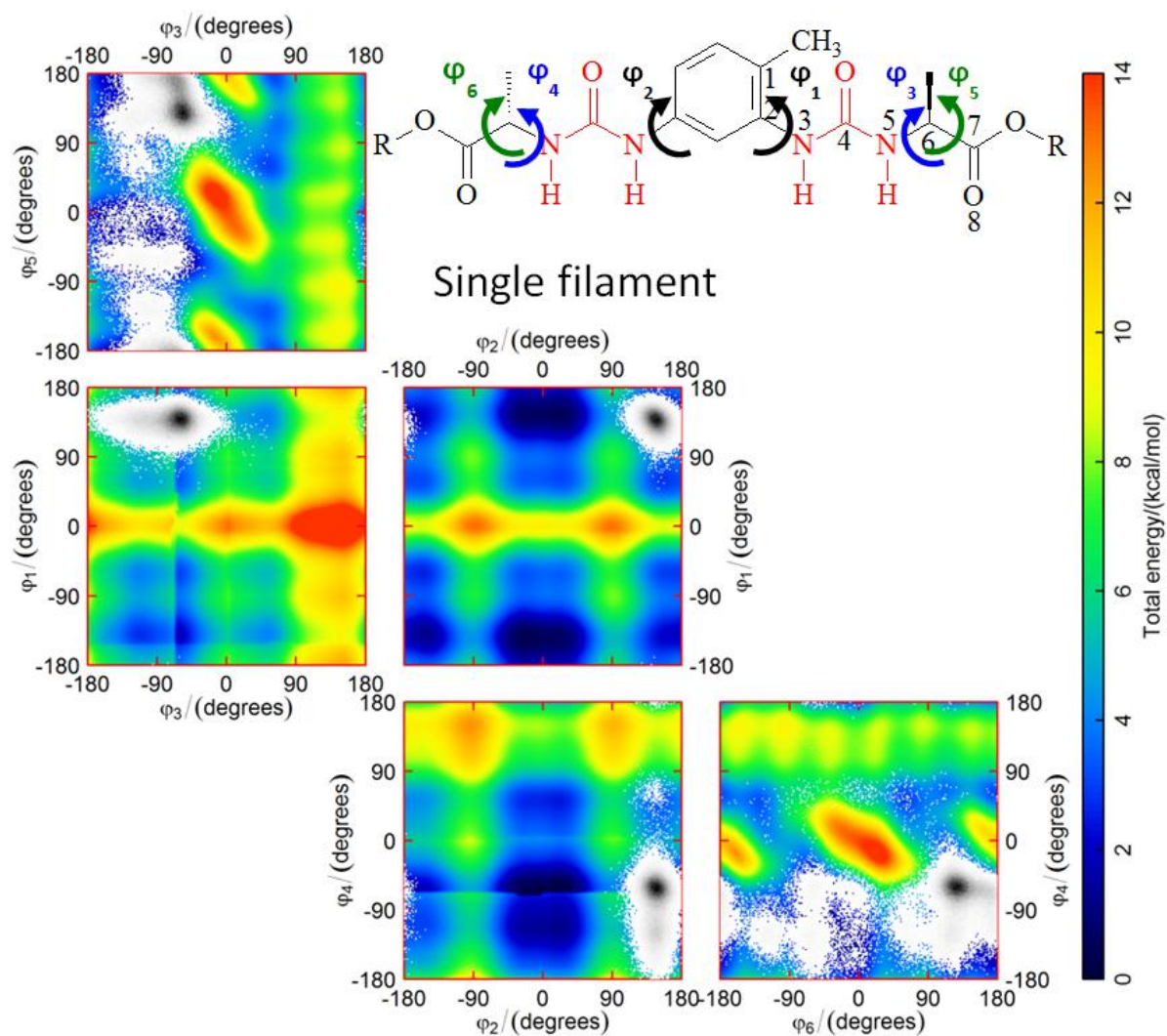


Figure 61: Map of relative potential energy of an isolated *S*-EtHexAla molecule in function of the value of characteristic dihedral angles; on this map, the population distribution of the dihedral angles spanned during MD is plotted for the single filament of *S*-EtHexAla, as a white to black scale. To avoid an incorrect attribution of atoms for the torsion angles, numbers were added to the molecular scheme. The atoms 1-4 correspond to ϕ_1 , 4-7 to ϕ_3 and 5-8 to ϕ_5 .

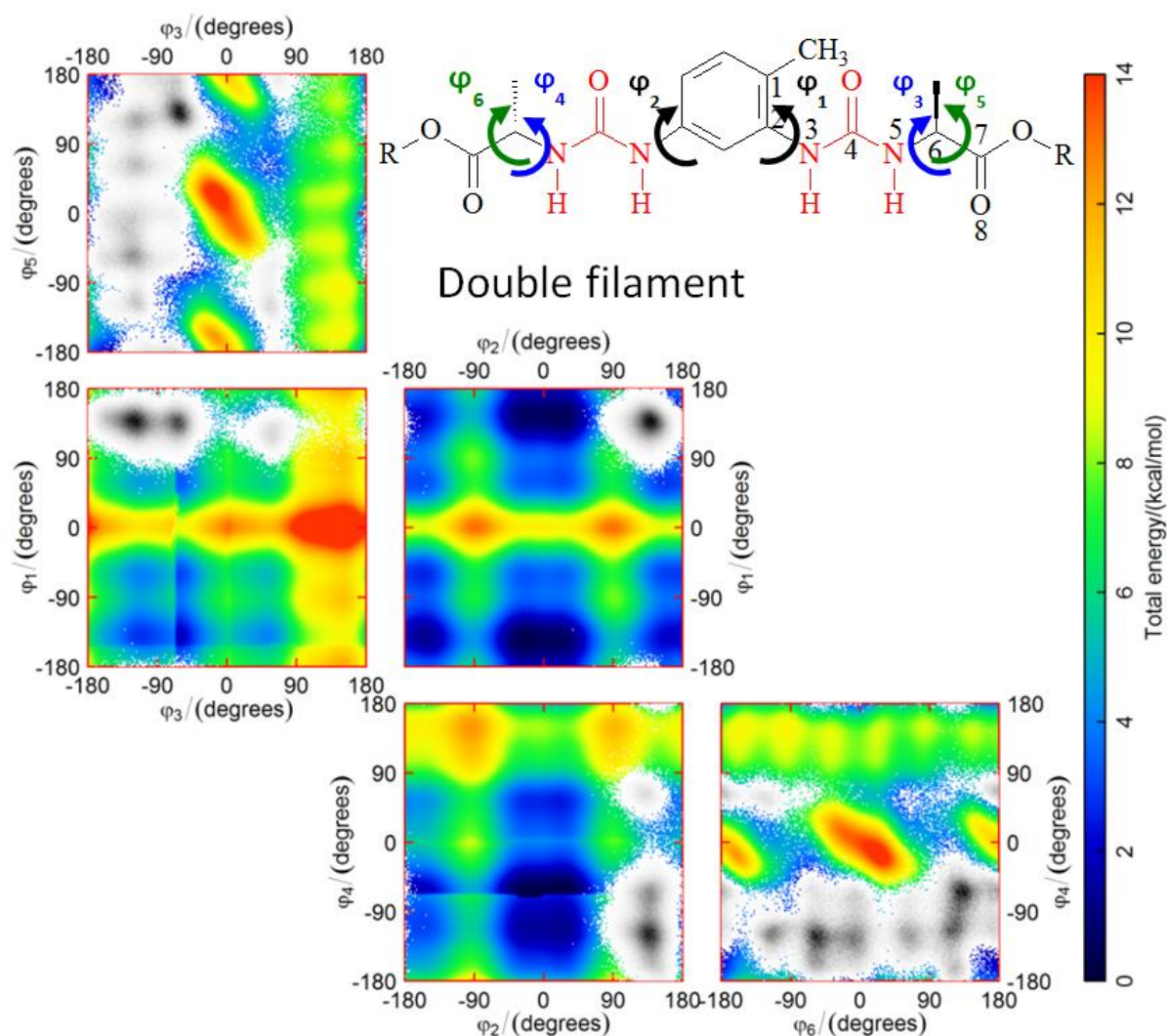


Figure 62: Map of relative potential energy of an isolated **S-EtHexAla** molecule in function of the value of characteristic dihedral angles; on this map, the population distribution of the dihedral angles spanned during MD is plotted for the double filament of **S-EtHexAla**, as a white to black scale. To avoid an incorrect attribution of atoms for the torsion angles, numbers were added to the molecular scheme. The atoms 1-4 correspond to ϕ_1 , 4-7 to ϕ_3 and 5-8 to ϕ_5 .

To characterize the hydrogen bond network, we calculated the radial distribution function between the hydrogen atoms of the urea moieties and the oxygen atoms of either the urea, either the ester moieties. The presence of hydrogen bonds is seen by a peak at the typical hydrogen bond distance of 2 Å. Such a peak is clearly visible with the oxygen atoms of urea, and absent with the oxygen atoms of ester, both in the single and double filaments (Figure 63). This result indicates that hydrogen bonds occur only with urea, in agreement with experiments in Me-cyclohexane and toluene for **S-EtHexAla** and the other bis-ureas studied in this chapter.

From the radial distribution function, we also calculated the cumulative number of oxygen atoms, n_o , found in function of the distance from the hydrogen atoms of the urea moieties. This calculation allows determining the proportion of hydrogens involved in hydrogen bonds. At 2 Å, $n_{o \text{ urea}}$ jumps from 0 to *ca.* 1, *i.e.* each hydrogen atom of urea is involved in hydrogen bonds with urea; there is no free hydrogen (with the exception of the hydrogen atoms belonging to the monomer(s) located at one extremity of the helix). These results are found for both the single and double filaments, showing the persistence and completeness of the hydrogen bond network.

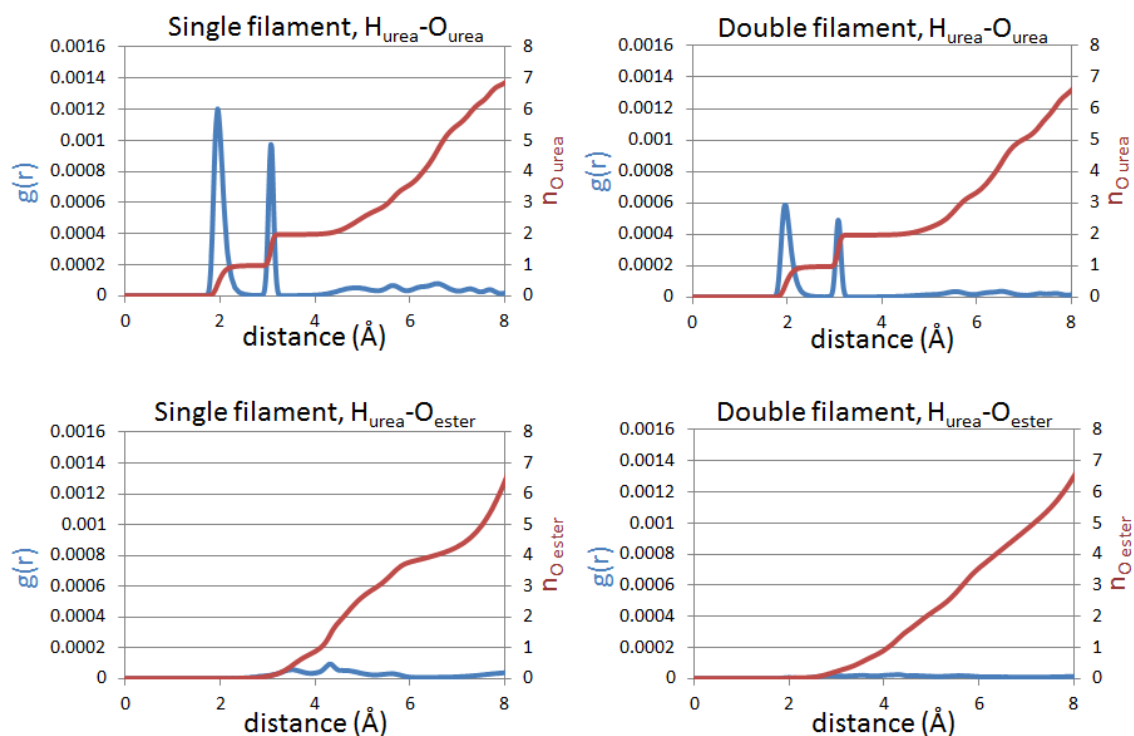


Figure 63 : Radial distribution function, $g(r)$, between H_{urea} and O, and cumulative number of O around H_{urea} in function of the H_{urea} -O distance, for the single (left) and double (right) filaments of **S-EtHexAla**. The oxygen atoms are either O_{urea} (top) or O_{ester} (bottom)

b. Analysis of the optical properties of S-EtHexAla

Having demonstrated the stability of the constructed single filament and double filament structures of **S-EtHexAla**, we next simulated their respective UV and CD spectra. The simulated UV spectrum of the single filament shows two peaks at *ca.* 240 and 215 nm, which in the CD spectrum corresponds to the zero crossings of two successive bisignated signals (Figure 64). A -/+/-/+ pattern is thus obtained, with these signals partly overlapping at 230 nm, where they are of opposite signs. Experimentally, a similar evolution is observed, though with a different intensity attributed to the sensitivity of the CD spectra: a negative band appears with a minimum at 250 nm. Then, a plateau composed of a small increase followed by a small decline appears, which we attribute to the mutual partial cancellation of the positive band of the first bisignated signal and of the negative band of the second bisignated signal. Then the positive band of the second bisignated signal appears with a maximum at 225 nm.

For the double filament, the UV spectrum is similar to the one of the single filament, though less resolved, and with a decrease of the relative intensity of the low-energy peak with respect to the high energy one. The CD spectrum is also roughly similar to the one of the single filament, though with a lower amplitude of the first bisignated signal, which corresponds to what is observed experimentally.

The similarity of the experimental CD spectra of the single and double filament structures indicates that their organization is likely similar, and all the information obtained from the simulations (CD, structural characterization) support this interpretation, as a double filament appears as two intertwined single filaments with relatively minor organizational changes.

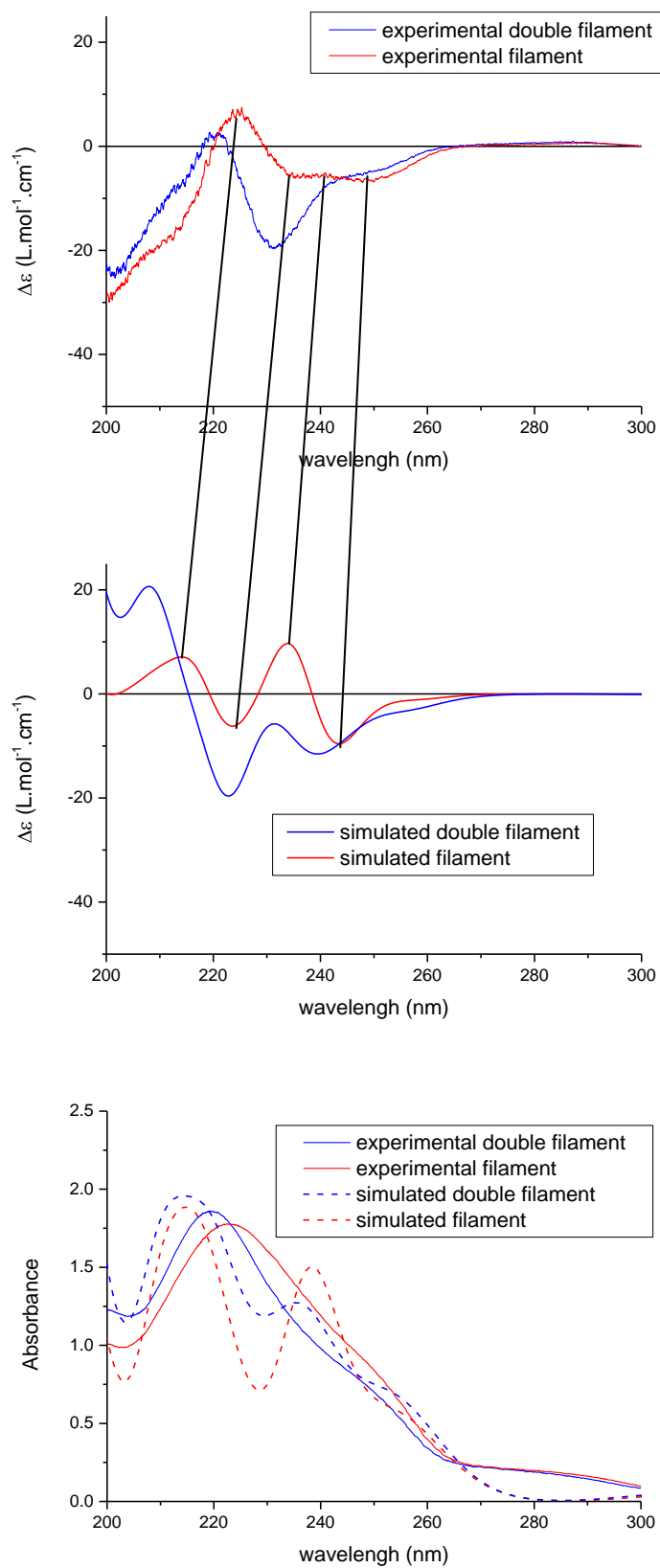


Figure 64 : UV and CD spectra of the single and double filaments of **S-EtHexAla**, as obtained from experiment and from simulation. The match between the experimental and simulated CD bands is represented by lines.

4. Conclusion

We first compared the structure of the self-assemblies formed by ester bis-ureas with those formed by alkyl bis-ureas. Both racemic ester bis-ureas and alkyl bis-ureas were found to assemble into very long 1D assemblies in toluene. SANS analyses revealed a strong difference between the “thick structures” of both type of bis-ureas: ester bis-ureas formed cylindrical objects with two molecules in the cross-section compared to three for alkyl bis-ureas. nDSC analyses performed in various aromatic solvents confirmed the non-tubular nature of the ester bis-urea assemblies. The difference in the nature of the assemblies between the two bis-urea families was quite surprising considering that the ester function was not involved in the hydrogen bond network.

A combined experimental/computational study was then performed in order to gain more information on the molecular arrangement adopted by the ester bis-urea monomers within the assemblies. FTIR and SANS analyses showed enantiopure ester bis-ureas form similar structures in Me-cyclohexane than racemic ester bis-ureas in toluene. CD analyses in Me-cyclohexane indicated that both the rod-like and filament structures are chiral at a supramolecular level. Single filament and double filament structures of the ester bis-urea derived from *S*-Alanine were constructed and their UV and CD spectra were simulated. The modeled double filament structure gave a CD signal which is similar to the one obtained experimentally. The modeled double filament and single filament structures are thus probable structures for the assemblies formed by ester bis-ureas.

The determination of these structures is of dramatic importance in the understanding of the interactions taking place on the side chains in the context of the supramolecular balance.

As the enantiopure ester bis-urea assemblies exhibit chirality at the supramolecular level, their properties of amplification of chirality were studied in the following chapter.

C. Appendix

1. SANS analyses

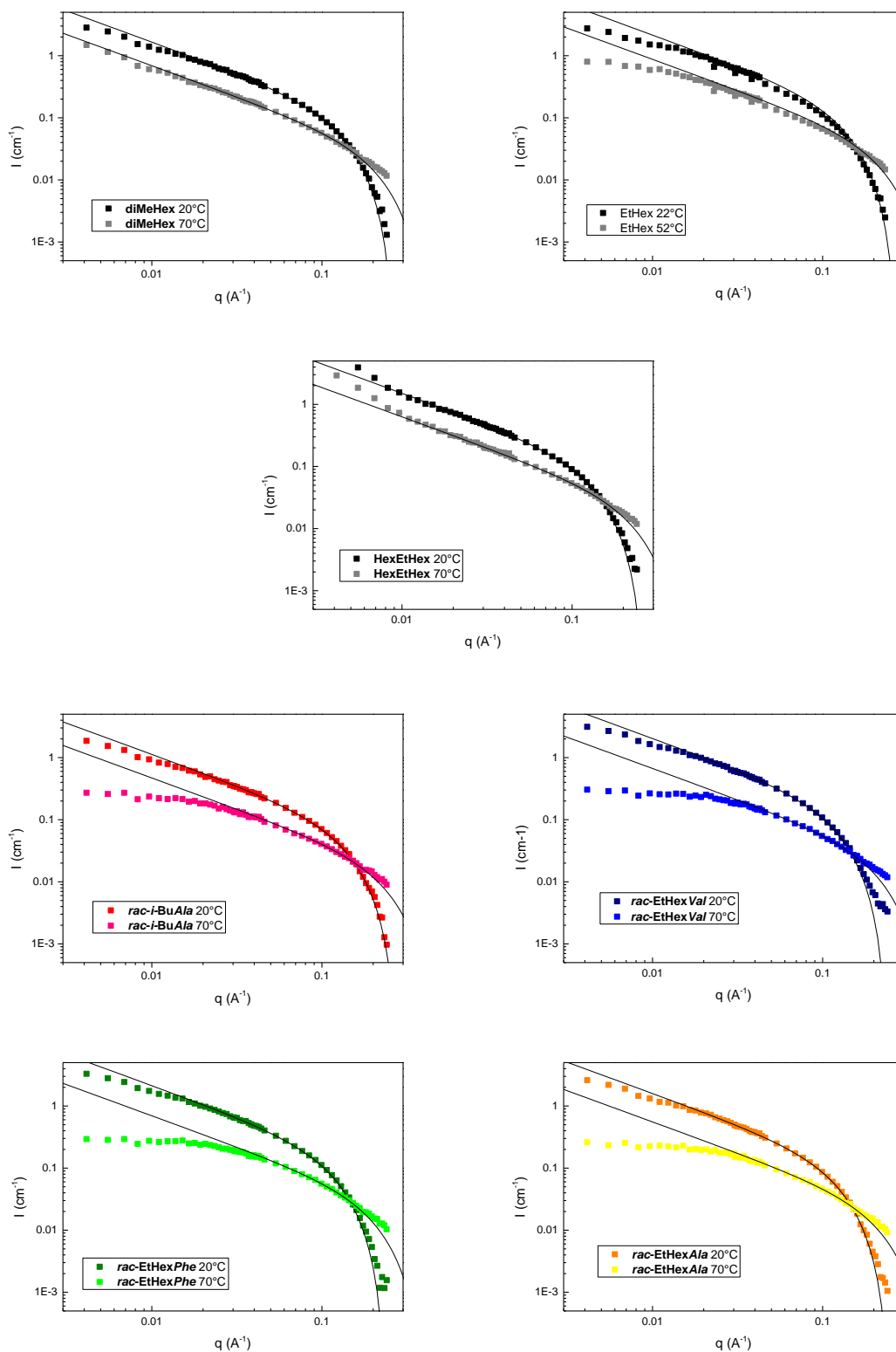


Figure 65 : SANS analyses of alkyl and racemic ester bis-ureas performed at 20 and 70°C and at a concentration of *ca.* 0.6 wt% except for **EtHex** (at 22 and 52°C and at 0.8 wt%) in toluene- d_8 . The curves are fitted according to the form factor for rigid rods with a circular cross section and a uniform scattering length density

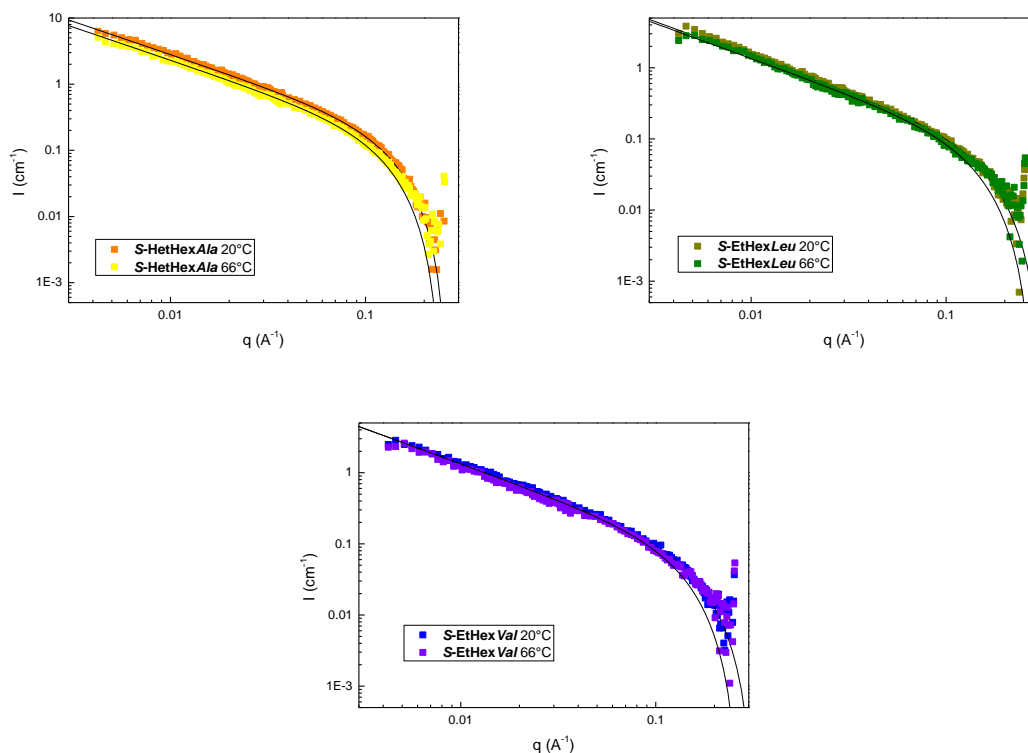
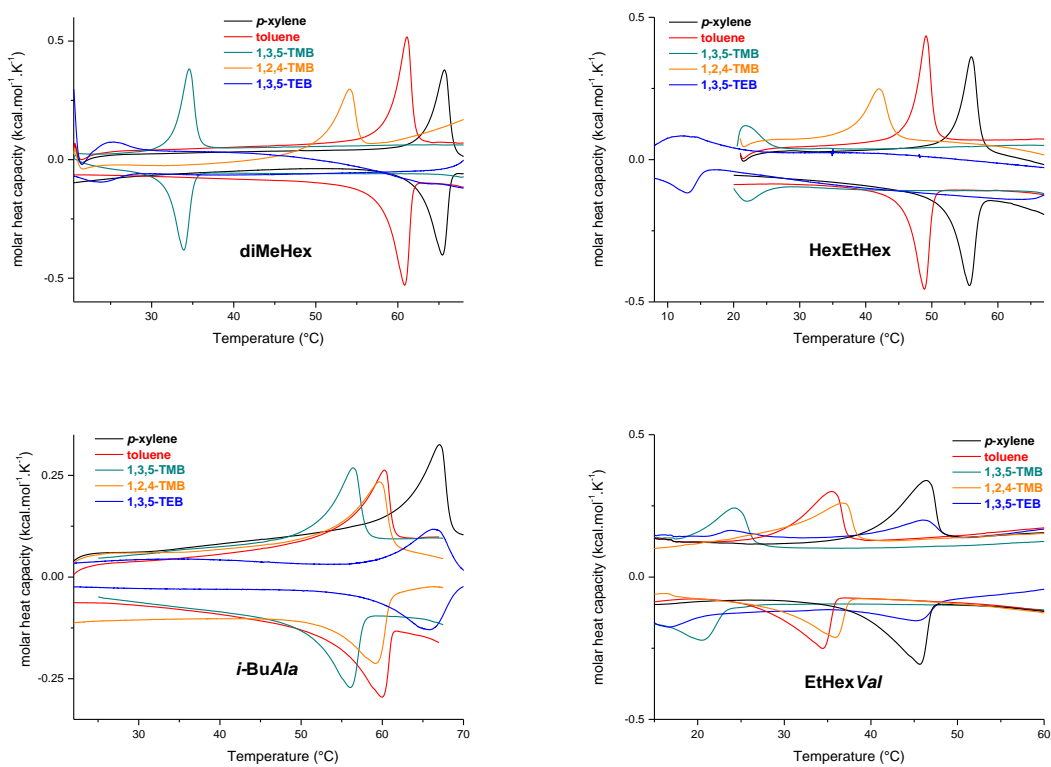


Figure 66: SANS analyses of enantiopure ester bis-ureas performed at 10 or 20°C and 70°C and at a concentration of *ca.* 0.6 wt% in Me-cyclohexane- d_{14} . The curves are fitted according to the form factor for rigid rods with a circular cross section and a uniform scattering length density.

2. nDSC analyses



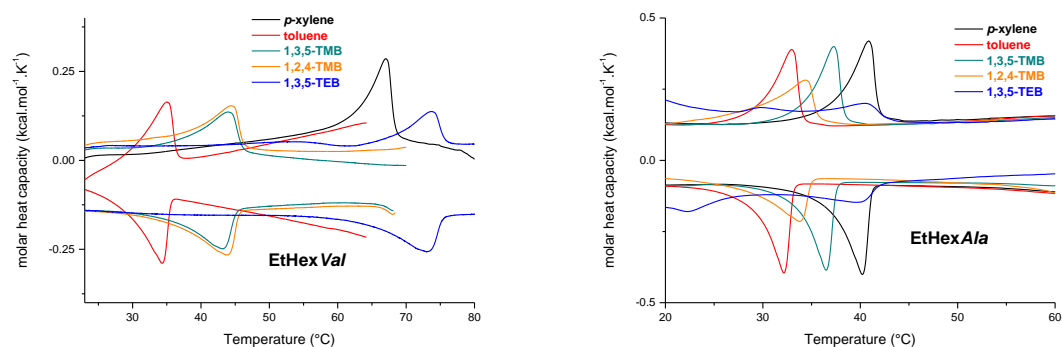


Figure 67 : DSC traces (heating and cooling run) for 5 mM solutions of alkyl and ester bis-ureas in *p*-xylene, toluene, 1,3,5-TMB, 1,2,4-TMB and 1,3,5-TEB. T^{**} corresponds to the temperature at the maximum of the endothermal peak. $\Delta H^{**} \approx 1 \text{ kcal.mol}^{-1}$ (tube to filament or rod-like structure to filament transition)

Table 4 : Transition temperature (T^{**} , °C) between assemblies as determined by nano-DSC (5mM) in aromatic solvents of various widths.^a

solvent	W (Å) ^c	diMeHex	diMeHex	HexEtHex	<i>i</i> -BuAla	EtHexVal	EtHexPhe	EtHexAla
toluene	6.7	61.1	43.0d	49.1	60.3	35.5	34.3	33.0
<i>p</i> -xylene	6.7	65.7	49.5d	56.0	67.4	46.3	67.0	40.9
1,2,4-TMB ^b	7.5	54.1	34.1d	42.0	59.7	36.7	44.4	34.4
1,3,5-TMB ^b	8.3	34.6	13.4d	21.9	56.4	24.3	44.0	37.3
1,3,5-TEB ^b	10.1	24.9	<10 ^e	11.9	66.5	46.0	73.7	40.5

^a For DSC traces see Figure S3. Indicated T^{**} values taken as the maximum of the endothermal peak of the heating runs. ^b 1,2,4-TMB = 1,2,4-trimethylbenzene, 1,3,5-TMB = 1,3,5-trimethylbenzene, 1,3,5-TEB = 1,3,5-triethylbenzene. ^c Herein the width corresponds to the diameter of the cylinder having minimum diameter in which the solvent molecule inscribes (Winmostar® software). Geometry optimization was performed through molecular mechanic method (MM3) using the software Scigress (Fujitsu®). ^d T^{**} determined by FTIR. ^e No transition detected by nano-DSC ($T^{**} < 10^\circ\text{C}$).

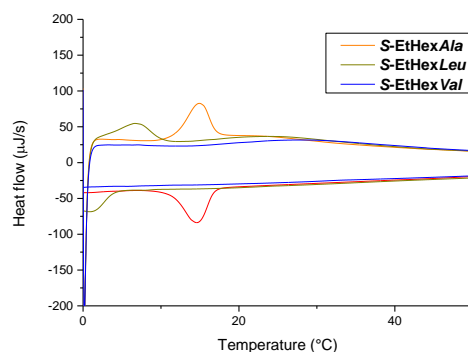


Figure 68 : DSC traces (heating and cooling rate) of *S*-EtHexAla ($T^{**}=14.9^\circ\text{C}$), *S*-EtHexLeu ($T^{**}=6.7^\circ\text{C}$) and *S*-EtHexVal ($T^{**}<0^\circ\text{C}$) at 10 mM in Me-cyclohexane (1°C/min).

3. FTIR analyses

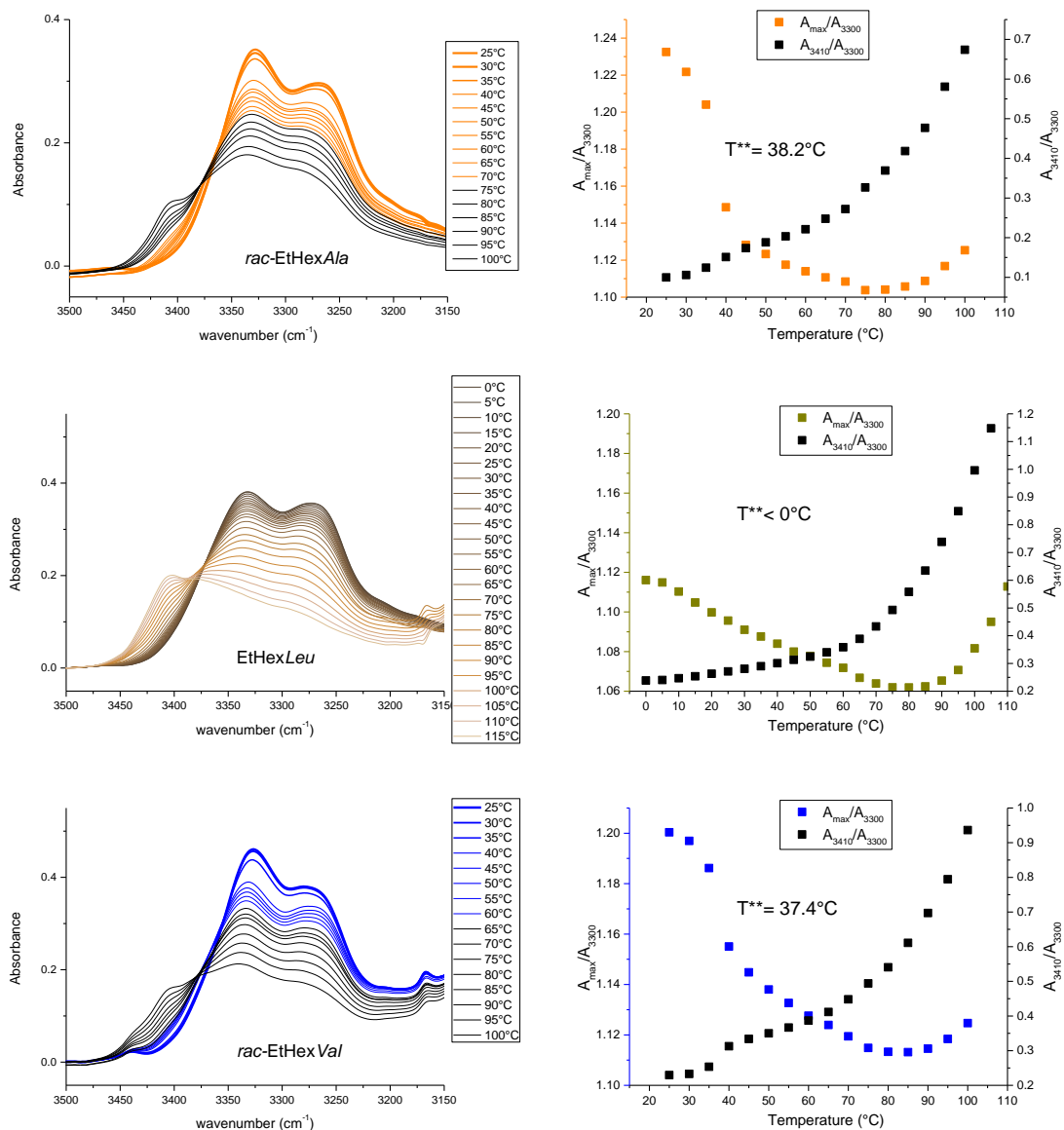


Figure 69 : Left: IR spectra vs temperature for ester bis-ureas (toluene, 10mM). Right: plots of A_{max}/A_{3300} and A_{3410}/A_{3300} against temperature. A_{max}/A_{3300} corresponds to the normalized intensity of the aromatic NH band and its plot against T° reflects the structural transition. T^{**} corresponds to the mid-point temperature. The T^{**} values determined by FT-IR are in accordance with those measured by nDSC. A_{3410}/A_{3300} reflects the amount of free NH which sharply increases above the structural transition.

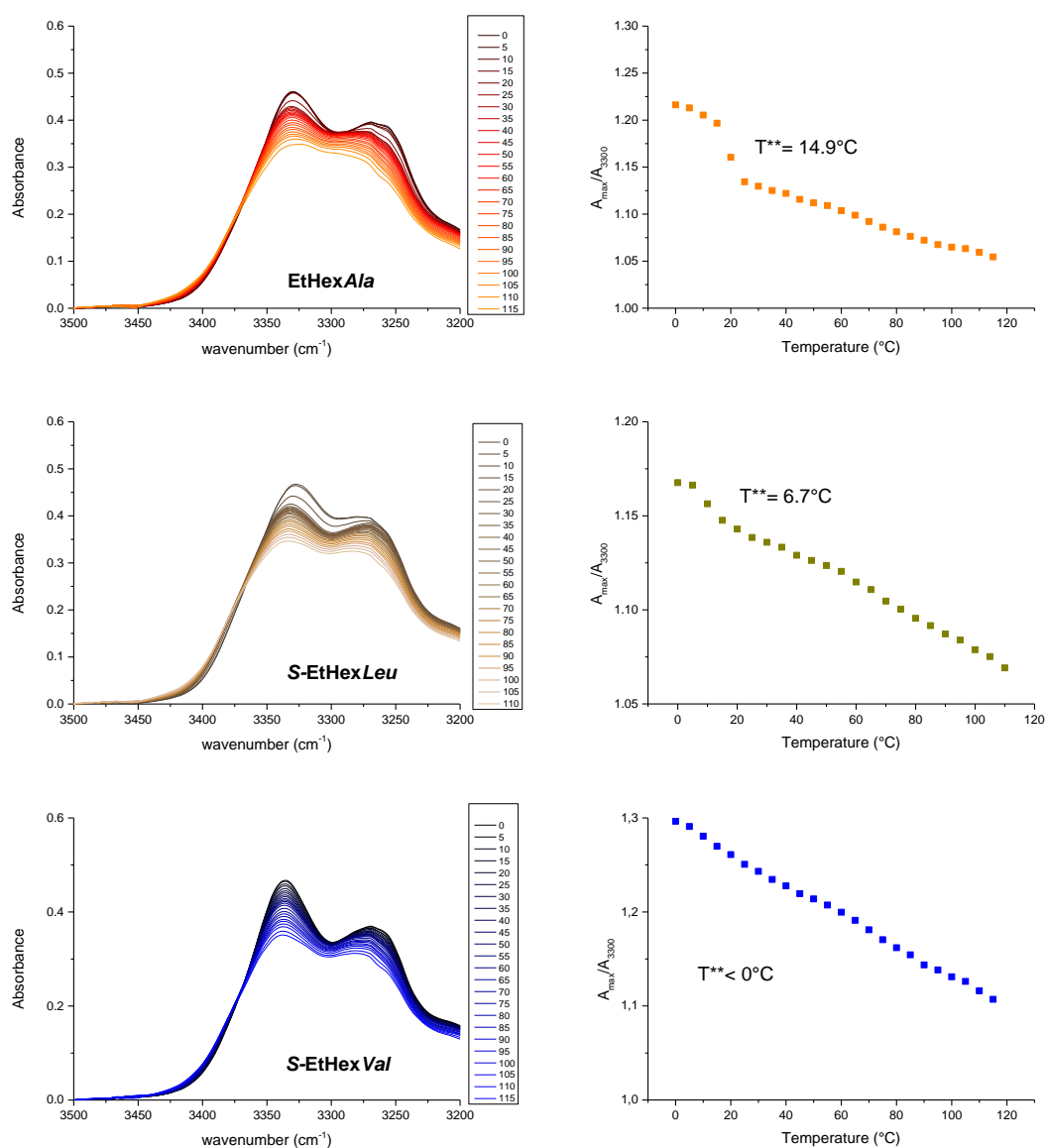


Figure 70 : Left: IR spectra vs temperature for ester bis-ureas (Me-cyclohexane, 10mM). Right: plots of A_{max}/A_{3300} against temperature. A_{max}/A_{3300} corresponds to the normalized intensity of the aromatic NH band and its plot against T° reflects the structural transition. T^{**} corresponds to the mid-point temperature. The T^{**} values determined by FT-IR are in accordance with those measured by nDSC.

4. Circular Dichroism analyses

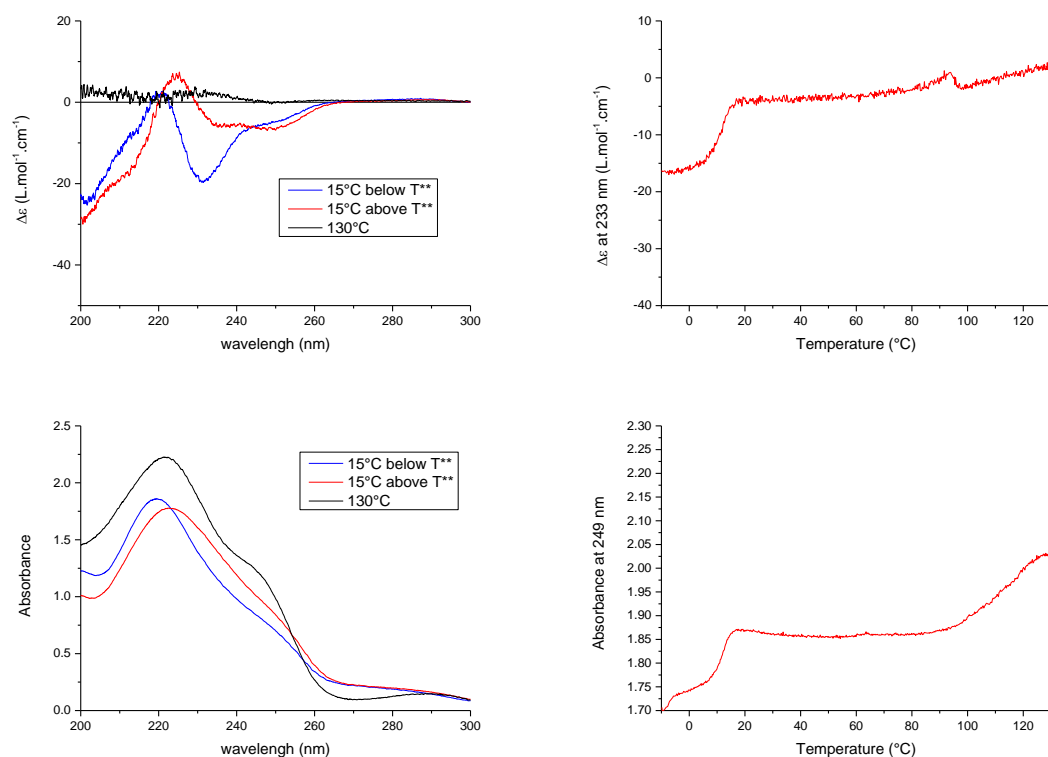


Figure 71 : Left: Circular Dichroism spectra (up) and UV spectra (down) of *S*-EtHexAla at 1mM in Me-cyclohexane at three temperatures. Right: evolution of the CD signal at 223 nm (up) and UV absorbance at 249 nm (down) with temperature.

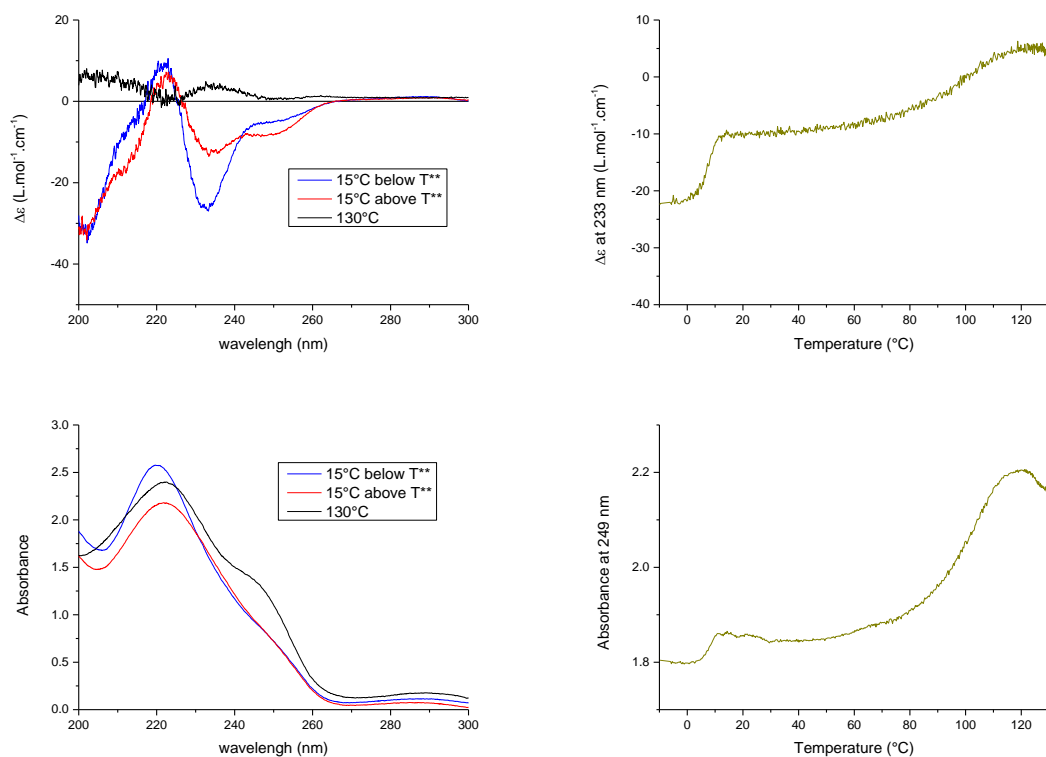


Figure 72 : Left: Circular Dichroism spectra (up) and UV spectra (down) of **S-EtHexLeu** at 1mM in Me-cyclohexane at three temperatures. Right: evolution of the CD signal at 223 nm (up) and UV absorbance at 249 nm (down) with temperature.

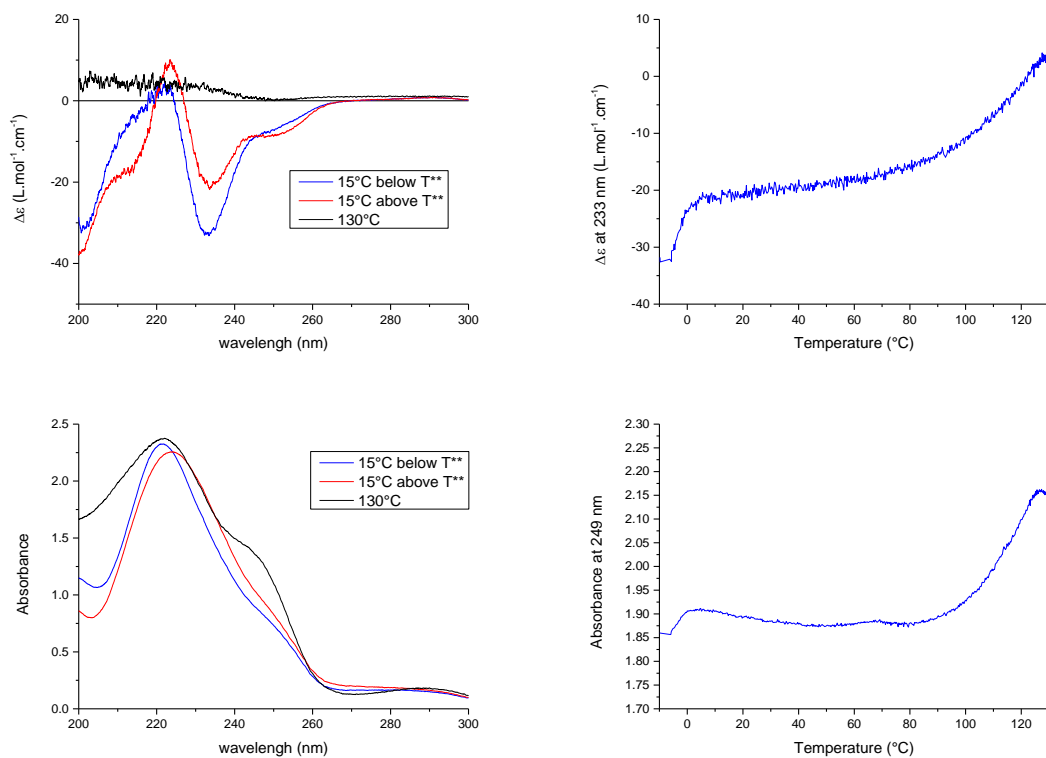


Figure 73 : Left: Circular Dichroism spectra (up) and UV spectra (down) of **S-EtHexVal** at 1mM in Me-cyclohexane at three temperatures. Right: evolution of the CD signal at 223 nm (up) and UV absorbance at 249 nm (down) with temperature.

- [1] M. Bellot, L. Bouteiller, *Langmuir* **2008**, *24*, 14176–14182.
- [2] V. Simic, L. Bouteiller, M. Jalabert, *J. Am. Chem. Soc.* **2003**, *125*, 13148–13154.
- [3] L. Bouteiller, O. Colombani, F. Lortie, P. Terech, *J. Am. Chem. Soc.* **2005**, *127*, 8893–8898.
- [4] T. Shikata, T. Nishida, B. Isare, M. Linares, R. Lazzaroni, L. Bouteiller, *J. Phys. Chem. B* **2008**, *112*, 8459–8465.
- [5] B. Isare, M. Linares, R. Lazzaroni, L. Bouteiller, *J. Phys. Chem. B* **2009**, *113*, 3360–3364.
- [6] P. Brocorens, M. Linares, C. Guyard-Duhayon, R. Guillot, B. Andrioletti, D. Suhr, B. Isare, R. Lazzaroni, L. Bouteiller, *J. Phys. Chem. B* **2013**, *117*, 5379–5386.
- [7] F. Lortie, S. Boileau, L. Bouteiller, C. Chassenieux, B. Demé, G. Ducouret, M. Jalabert, F. Lauprêtre, P. Terech, *Langmuir* **2002**, *18*, 7218–7222.
- [8] B. Isare, L. Bouteiller, G. Ducouret, F. Lequeux, *Supramol. Chem.* **2009**, *21*, 416–421.
- [9] A. Arnaud, L. Bouteiller, *Langmuir* **2004**, *20*, 6858–6863.
- [10] T. Pinault, B. Isare, L. Bouteiller, *ChemPhysChem* **2006**, *7*, 816–819.
- [11] M. Roman, C. Cannizzo, T. Pinault, B. Isare, B. Andrioletti, P. van der Schoot, L. Bouteiller, *J. Am. Chem. Soc.* **2010**, *132*, 16818–16824.
- [12] M. T. Scerba, A. F. DeBlase, S. Bloom, T. Dudding, M. a Johnson, T. Lectka, *J. Phys. Chem. A* **2012**, *116*, 3556–60.
- [13] B. Jouvelet, B. Isare, L. Bouteiller, P. Van Der Schoot, *Langmuir* **2014**, *30*, 4570–4575.
- [14] X. Luo, C. Li, Y. Liang, *Chem. Comm.* **2000**, *5*, 2091–2092.
- [15] B. Isare, M. Linares, L. Zargarian, S. Femandjian, M. Miura, S. Motohashi, N. Vanthuyne, R. Lazzaroni, L. Bouteiller, *Chem. Eur. J.* **2010**, *16*, 173–7.

Chapter 3: Majority rules effect in ester bis-ureas

Abstract: In this chapter, we present in a first part the literature dealing with the majority rules effect in supramolecular polymers. In a second part, we studied the influence of the aminoacid used to synthesize ester bis-ureas on the majority rules effect exhibited by their assemblies. CD experiments were performed on both the double filament and filament and energetic penalty values were extracted using the supramolecular balance adaptated with the van Gestel model for the majority rules effect.

The strong difference in stability of enantiopure versus racemic bis-urea assemblies noticed in the previous chapter can potentially be explained by the presence of packing defects in the assemblies. This in turn is related to the phenomenon of chirality amplification, i.e. the ability of an enantiomer to impose its supramolecular chirality to the other enantiomer.

The amplification of chirality has been highly studied in many different systems as it could be part of the answer to the origin of homochirality in biological systems.^[1] There is an important distinction between the amplification of chirality observed in molecular systems, which corresponds to an increase of the enantiopurity of a compound usually via the use of a chiral catalytic system, and the amplification of chirality in macromolecular systems. Here, we will only discuss the amplification of chirality in the macromolecular sense and more precisely in helical macromolecular systems.

Polymers that present a helical conformation are characterized by both an enantiomeric excess corresponding to their molecular structure and a perceived chirality, called helicity, which corresponds to the chirality of the formed helix. In the 90's, Green and coworkers studied the relation between the enantiomeric excess of the polymer and its perceived chirality. They used polyisocyanate, which is known to have an helical conformation, to discover that only small amounts of chiral monomers were enough to produce a homochiral polymer.^[2,3]

This concept was later called the "sergeant and soldiers" principle since a single chiral unit can command the chiral conformation of multiple achiral units.^[4,5] While studying this effect, they also tried to mix enantiomeric monomers in different proportions and observed a non-linear relationship as well. This effect was called the "majority rules" principle.^[6]

Both effects are exhibited as well in supramolecular polymers but for now on, we will focus on the majority rules effect.

A. Majority rules in supramolecular polymers

Fenniri and coworkers reported the first example of a majority rules effect in a supramolecular system with their helical rosette nanotubes but many different designs were used over the years.^[7]

1. A simple system exhibiting the majority rules effect: BTAs

One of the best systems to understand what is the "majority rules effect" are BTAs (benzene-1,3,5-tricarboxamides). The first conformational study of a BTA assembly came from the a X-ray crystal structure obtained by Lightfoot and coworkers in 1999 (Figure 74).^[8] It showed a triple helical network of hydrogen bonds. IR spectroscopy in both solid and solution states showed a typical NH stretch of an intermolecularly hydrogen-bonded amide group at 3223 cm^{-1} which was retained in alkane solution up to high dilutions (10^{-5} M in cyclohexane).^[9,10]

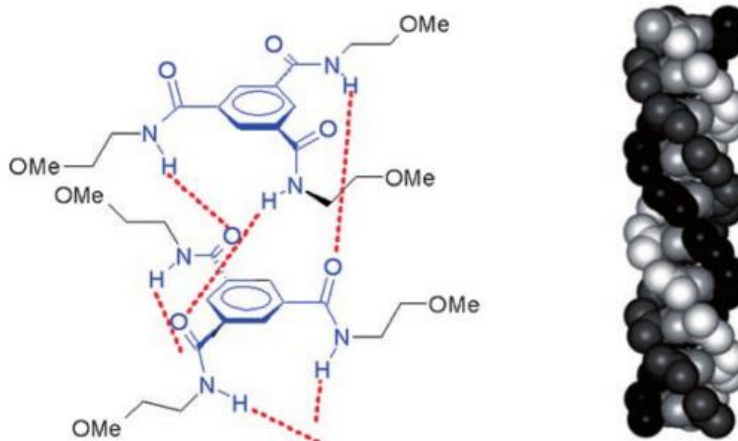


Figure 74 : Structure of Lightfoot's BTA assembly^[8]

This helical structure is due to the presence of two types of interactions: π -stacking and HB which exhibit different lengths (3.5 and 4.6 Å respectively) thus forcing a slight rotation between monomers within the assembly. In the case of achiral monomers the same quantity of left and right-handed helices is formed. Upon introduction of chirality in the side chains Meijer and coworkers observed that only one of the helices formed (Figure 75).^[11]

These compounds showed high cooperativity in the assembly process. This degree of cooperativity seems to be more pronounced where chiral molecules are employed.^[11]



Figure 75 : Meijer's chiral BTA design^[12]

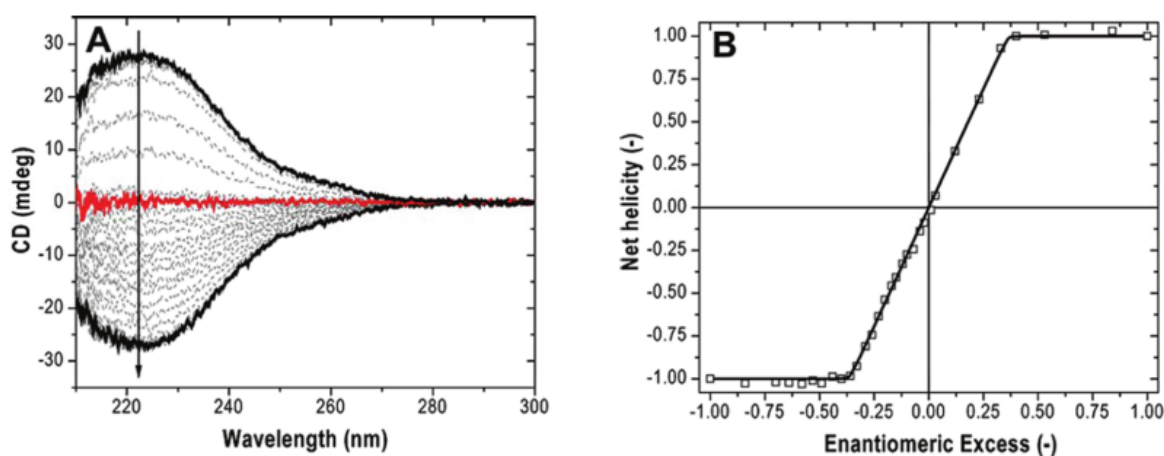


Figure 76 : CD spectra (left) and net helicity vs enantiomeric excess (right) of mixtures of **(S)-1** and **(R)-1** (20°C, 2.0×10^{-5} M in Me-cyclohexane)

Upon mixing the two enantiomers, Meijer's compound exhibited a majority rules effect as the maximum helicity is obtained with as low as 30%ee (Figure 76).^[12]

In order to understand the origin of this majority rules effect, different models based on what had been previously done on covalent polymers were designed.

a. Majority rules models

Many models were designed over the years to take into account this effect. The first one was the Ising model which was used for polymeric systems by Green and coworkers.^[2] The adaptation of this model for supramolecular polymers is the van Gestel model and was developed for both the sergeant and soldiers^[13] and the majority rules effect^[14].

Van Gestel explained the majority rules effect by using two energetic penalties he called the helix reversal penalty (HRP) and the mismatch penalty (MMP). The HRP is the energy needed to have a change in the sense of the screw within an assembly and MMP is the energy needed to incorporate a molecule in a stack of its non-preferred screw sense (Figure 77).

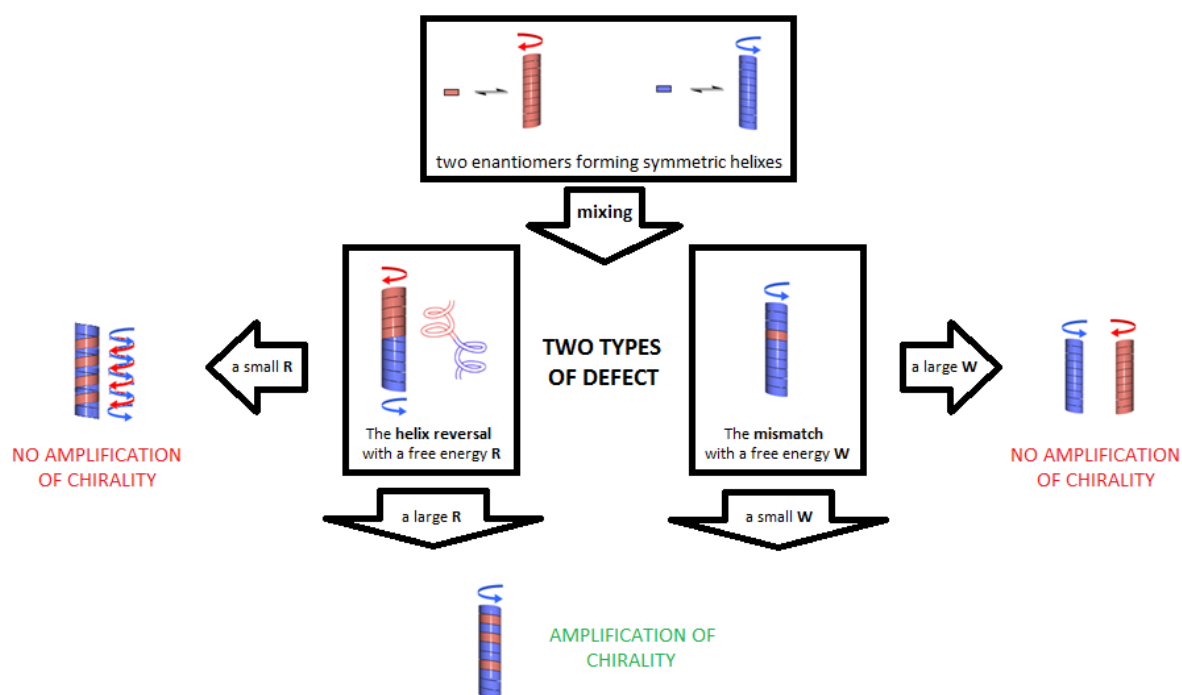


Figure 77: Schematic representation of the helix reversal and mismatch defects

If the HRP is too low, helix reversals are highly present and there is no amplification of chirality. When the MMP is too high, mismatches cannot happen then there is a self sorting of both assemblies and thus no chiral amplification. To obtain chiral amplification both a high HRP and a low MMP values are required.

Meijer's BTA's could be fitted with van Gestel's model and an HRP of 17 kJ/mol and a MMP of 1.8 kJ/mol were obtained thus explaining the majority rules effect obtained.^[12] The mean correlation length between sites of helix reversal was estimated to be 225 monomer units.^[9,10]

b. Structural influence

Meijer and coworkers studied the influence of the position and number of the chiral centers on the BTAs majority rules effect.^[12]

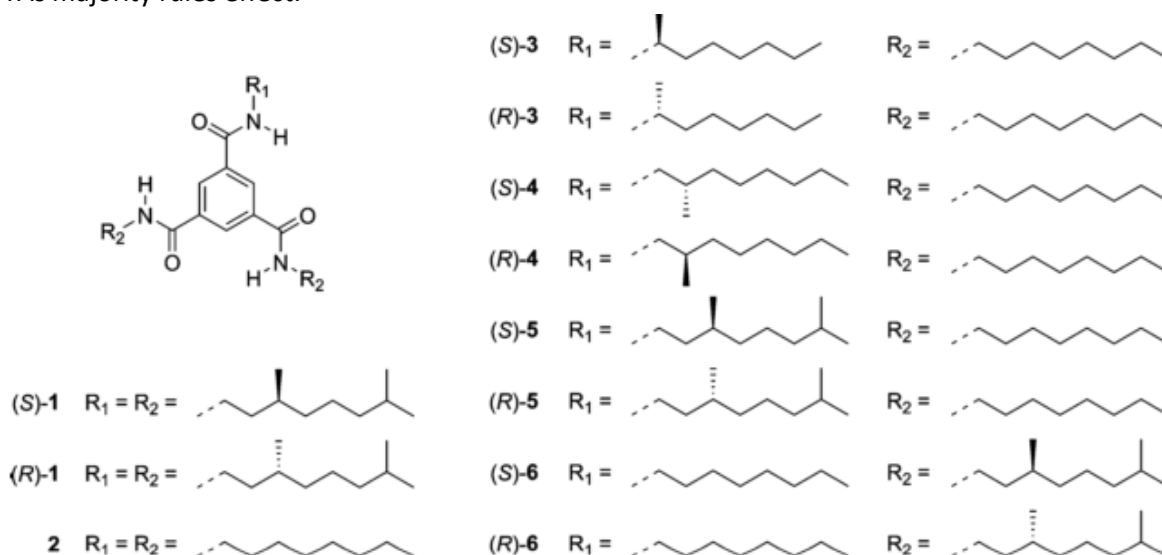


Figure 78 : Structure of various BTAs^[12]

All BTAs of Figure 78 presented a large and similar helix reversal penalty thus related to the intermolecular hydrogen bonds present in all derivatives. Upon variation of the position of the stereogenic center (BTAs **1** and **3-5**), an odd-even effect in the sense of the helix was observed in CD. All four compounds yielded similar HRP's but various MMP's. **4** yielded the smallest MMP with 0.5 kJ/mol and thus the strongest majority rules effect (Table 5: energetic penalties in kJ/mol at 20°C determined from fitting with the van Gestel model^[12]

). **1** yielded the largest MMP with 1.9 kJ/mol. **3** and **5** shared an intermediate value of 1.0 kJ/mol.

disc	majority-rules	
	HRP	MMP
1	15 ± 4	1.9 ± 0.2
3	15 ± 4	1.0 ± 0.2
4	16 ± 4	0.5 ± 0.2
5	15 ± 4	1.0 ± 0.2

Table 5: energetic penalties in kJ/mol at 20°C determined from fitting with the van Gestel model^[12]

It was also found that the mismatch penalty is directly related to the number of stereocenters present in the molecules as increasing this number from one to three (BTAs **5** and **1**) resulted in an increase of the MMP while the HRP was unaffected. Multiple majority rules and mixed majority rules experiments on those BTAs showed further evidence that MMP is directly related to the number of stereocenters.

They used this example to investigate the limits of chiral amplification and showed that given a certain HRP, there is actually an optimum where MMP can be reduced in order to enhance the degree of chiral amplification.^[12] It shows the relevance of both energies in enhancing chiral amplification for the majority rules principle.

c. Temperature influence

Early results on the study of bypyridine BTAs (see part d) majority rules effect at 20 and 50°C in octane showed a weaker effect at 50°C which was attributed to the partial disassembly of the supramolecular polymer at higher temperature.

In light of those results, Meijer and coworkers systematically investigated the effect of temperature in the majority rules effect.^[15]

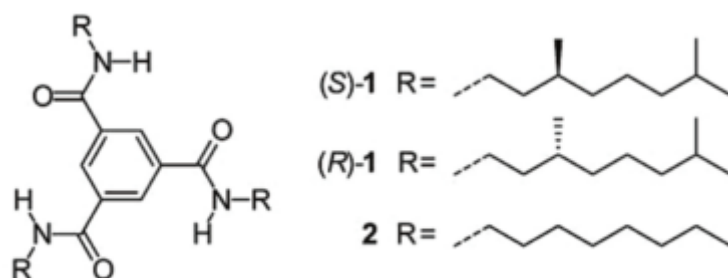


Figure 79 : BTA structures^[12]

They used previous compounds that were thoroughly studied (Figure 79).^[12] To study the influence of temperature on cooperatively self-assembled supramolecular polymers, they used the van Gestel model and extracted both HRP and MMP energies at different temperatures.

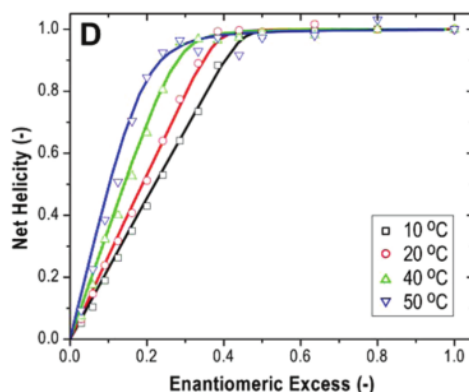


Figure 80 : Majority rules effect of BTA 1 at 2.10^{-5} M in methylcyclohexane^[15]

It is surprising to notice that the majority rules effect (Figure 80) increases with temperature (whereas the sergeant and soldiers effect decreases). The authors explained the former observations using a steric approach: when increasing the temperature, the molecules are getting slightly apart, reducing unfavorable steric interactions in the side-chains, thus lowering the MMP (Table 6). At the same time, the H-bond network remains intact and thus the HRP remains more or less the same.

temp (°C)	majority-rules	
	HRP	MMP
10	13 ± 3	2.2 ± 0.3
20	15 ± 4	1.9 ± 0.2
40	16 ± 4	1.5 ± 0.2
50	16 ± 3	1.1 ± 0.2

Table 6: energetic penalties in kJ/mol determined from fitting with the van Gestel model^[15]

When measuring the CD intensity at 233 nm versus the temperature for different ee values of BTA **1**, different observations were made (Figure 81). For the four lowest ee values, an initial increase of the CD values is observed, followed by a decrease leading to a value of zero around 60°C where only monomers are left. The increase in CD intensity observed is due to the reduction in MMP allowing a larger fraction of the minor enantiomer to be incorporated in the stacks of the major enantiomer. The decrease subsequently observed is due to the shortening of the stacks with temperature. At some point, every heating curve follow the pure enantiomer curve, indicating a homochiral system can be obtained for every ee by increasing the temperature.

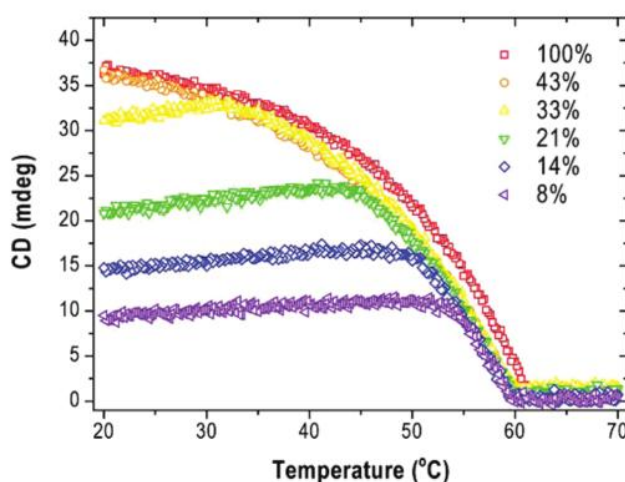


Figure 81 : Temperature-dependent CD intensity at 233 nm for different ee of **1** at $2.5 \cdot 10^{-5}$ M in methylcyclohexane^[15]

They also studied the influence of concentration on these systems and found that the temperature difference between the temperature at which homochirality is obtained and the elongation temperature is independent from the concentration.

This study showed how the majority rules effect is highly dependent of temperature and explained the use of the van Gestel model.

d. Other designs exhibiting the majority rules effect

Meijer and coworkers also worked on more complex bipyridine BTA derivatives in the 90s as liquid crystals.^[16] They mixed chiral **1a** and achiral **1b** in hexane and performed CD experiments (Figure 82).

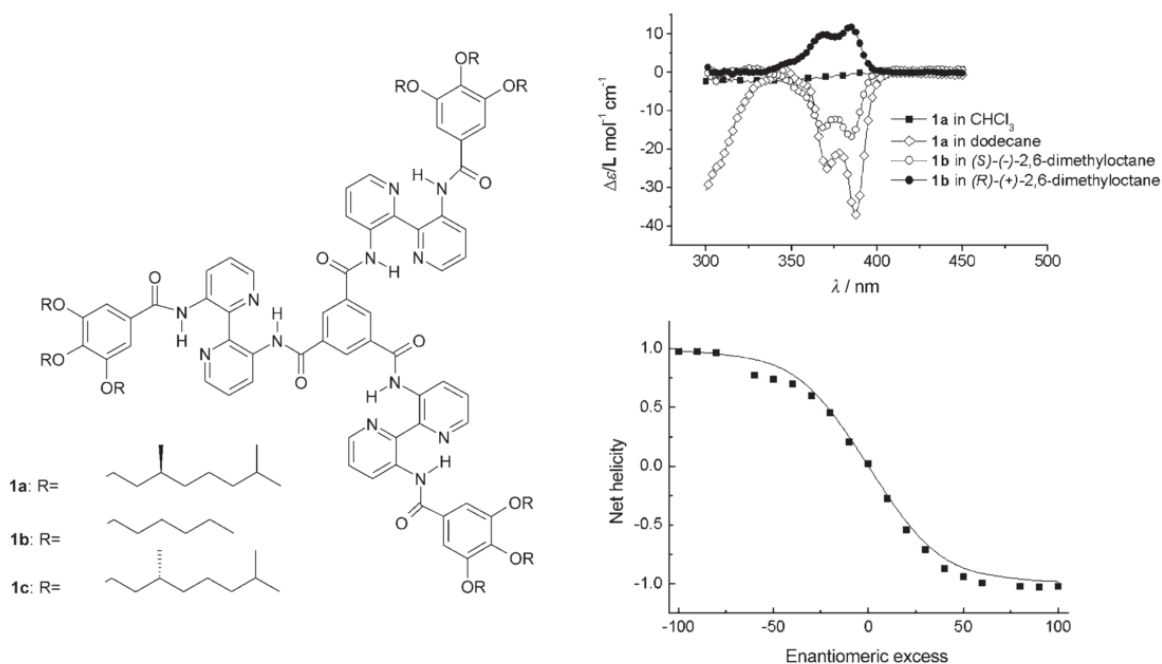


Figure 82 : Meijer's bipyrindine BTAs structures, CD experiments and net helicity as a function of ee measured by CD on mixture of **1a** and **1c** in n-octane at 20°C^[17]

A strong amplification of chirality was observed and a series of bipyrindine BTA derivatives were synthesized to study the origin of the amplification of chirality observed and the energies involved in the assembly process. No assemblies of **1a** were observed in chloroform but the assembly in dodecane could be fitted with Havinga's model and an association constant K_{ass} of $5.10^8 \text{ L.mol}^{-1}$ was calculated.^[18] One molecule of **1a** was showed to dictate the helical sense of 80 molecules of achiral **1b**.^[18]

It was also shown that a chiral solvent is capable of dictating the sense of helicity of achiral **1a** assemblies (Figure 82).

An intrinsic conformational chirality of the assembly is needed to obtain amplification of chirality. **1** was designed to be planar due intramolecular hydrogen bonds but the above results could only be explained by a non planar conformation were the bipyrindine moieties are tilted with respect to the benzene core. This assembly resembles a propeller due to an optimized stacking (Figure 83). Equal amounts of P (right screw) and M (left screw) helixes are present within the stack of achiral **1b**. This assembly is highly dynamic as the addition of small amounts of **1a** into **1b** instantly results in a CD effect suggesting a fast exchange between stacks.^[19]

Majority rules experiments were performed as well by mixing **1a** and **1c** and chiral amplification was observed.^[17] This was fitted with the van Gestel model and an MMP of 0.94 kJ.mol^{-1} was obtained which is eight times lower than the HRP measured (7.8 kJ.mol^{-1})^[14]

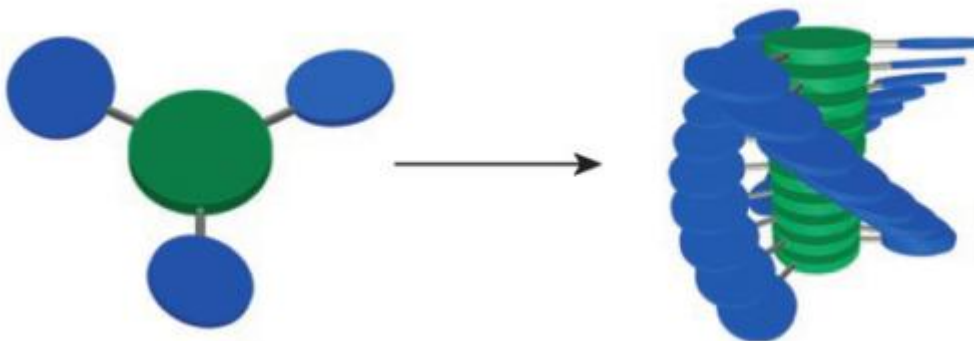


Figure 83 : Schematic structure of bipyridine BTA 1 assembly^[19]

The bis-ureas developed by Bouteiller and co-workers are also good candidates as the assemblies they form present a possible chiral structure and show a highly cooperative transition.

2. Majority rules in alkyl bis-ureas

To study the amplification of chirality and particularly the majority rules effect a chiral version of Bouteiller's blockbuster **EHUT** was synthesized (both SS and RR enantiomers).^[20,21]

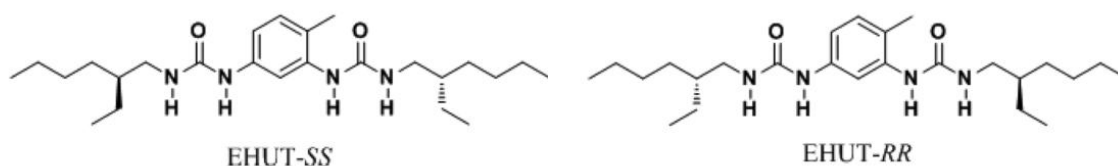


Figure 84 : chiral EHUT enantiomers structure^[21]

EHUT is known to self-assemble in low polar solvents into nanotubes at low temperature and into filaments at higher temperature. There is a cooperative transition between those two assemblies at a measurable temperature T^{**} (measured using nDSC). The nanotubes exhibit a signal in CD spectroscopy whereas the filaments are CD-silent indicating the absence of chirality transfer to the assembly.

Chiral **EHUT** nanotubes showed a strong majority rules effect (Figure 85) as only ca. 10% ee was necessary to obtain full helicity.

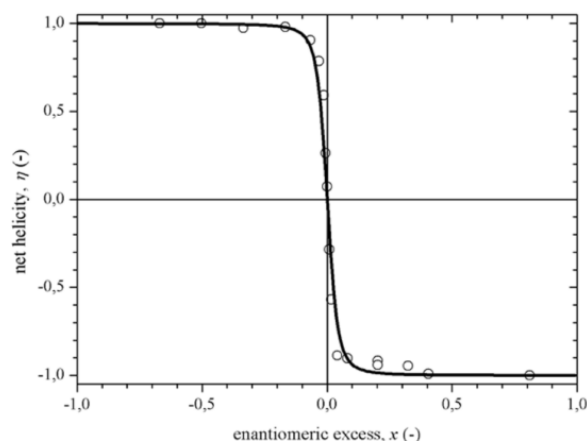


Figure 85 : Net helicity versus ee of EHUT in cyclohexane at 1 mM.^[21] The line represents a fit with the van Gestel model for HRP = 19.5 kJ/mol and MMP = 0.05 kJ/mol.

They have chosen to fit their data with the van Gestel model and showed that in many situations more than one pair of values can produce a good fit for a given set of data as the net helicity is not a sensitive function of the HRP. They have introduced the use of calorimetry experiments in order to obtain the energetic penalties (MMP and HRP) from the transition temperature using the supramolecular balance principle.^[22] Indeed, the transition temperature T^{**} depends on the relative stability of the nanotubes and filament structures. If one assumes that no defects due to chirality are present in the filament structure (since it is CD silent), then T^{**} is a direct measure of the amount of defects in the nanotube structure and of its energetic penalties (HRP and MMP).

Therefore, a simultaneous fit of both the helicity (measured by CD, Figure 85) and T^{**} (measured by nDSC, Figure 86) versus the enantiomeric excess yielded an HRP of 19.5 kJ/mol and an MMP of 0.05 kJ/mol.

This refined analysis allows a better thermodynamic description of the chiral amplification in bis-urea nanotubes such as the calculation of the amounts of defects in the assembly (Figure 86).

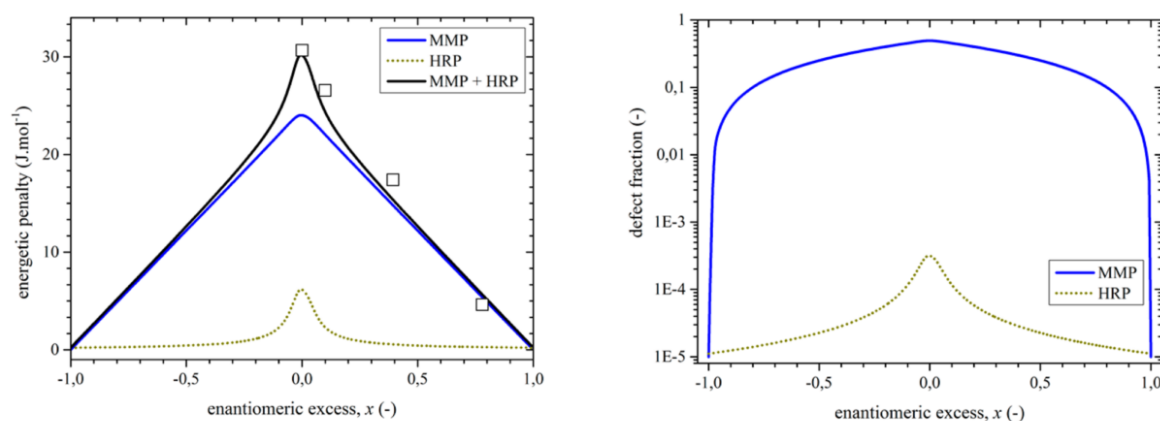


Figure 86 : Left: energetic penalties of EHUT versus ee. The points are derived from the measurement of the transition temperature (T^{**}). The black line is a fit of the data (HRP = 19.5 kJ/mol and MMP = 0.05 kJ/mol). The overall energetic penalty is decomposed into the contributions from helix reversal (blue line) and mismatch (dotted line) defects. Right: defect fraction (*i.e.* defect concentration normalized by EHUT concentration) deduced from the model.^[21]

For example, in the racemic mixture, 49% of the monomers are mismatched which is responsible for most of the energetic costs due to the defects. The lower but non-negligible fraction of helix reversals ($3.3 \cdot 10^{-4}$) corresponds to 1 helix reversal every 3000 units, which means several reversals

per nanotube. The size of the assemblies in cyclohexane could not be measured due to the insufficient sensitivity of ITC, but in toluene, the degree of polymerization is 7400 (at 1mM and 20°C). The degree of polymerization is expected to be much larger in cyclohexane than in toluene as the former is less polar than toluene and T^{**} is higher in cyclohexane (51 vs 43°C).

This study showed how the van Gestel model can be extended to more complex systems and how calorimetry data can now be used in this model.

B. Majority rules in ester bis-ureas

Ester bis-ureas allowed the use of amino-acids as building blocks, which are known for their vast chiral pool, and showed to be an alternative to alkyl bis-ureas in the study of the majority rules effect. Three amino-acids were chosen for this study: Ala, Leu and Val as they were studied in the previous chapter. The chosen alkyl chain is racemic 2-ethylhexyl as before.

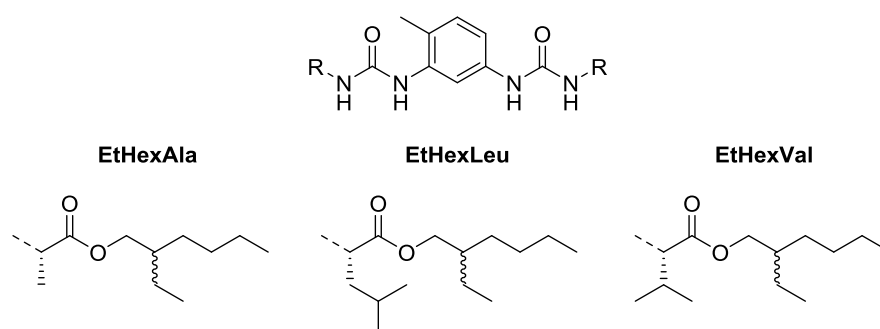


Figure 87 : Structure of the studied bis-ureas

All these compounds were studied with CD spectroscopy and nDSC at different ee in methylcyclohexane at 1mM.

1. Results

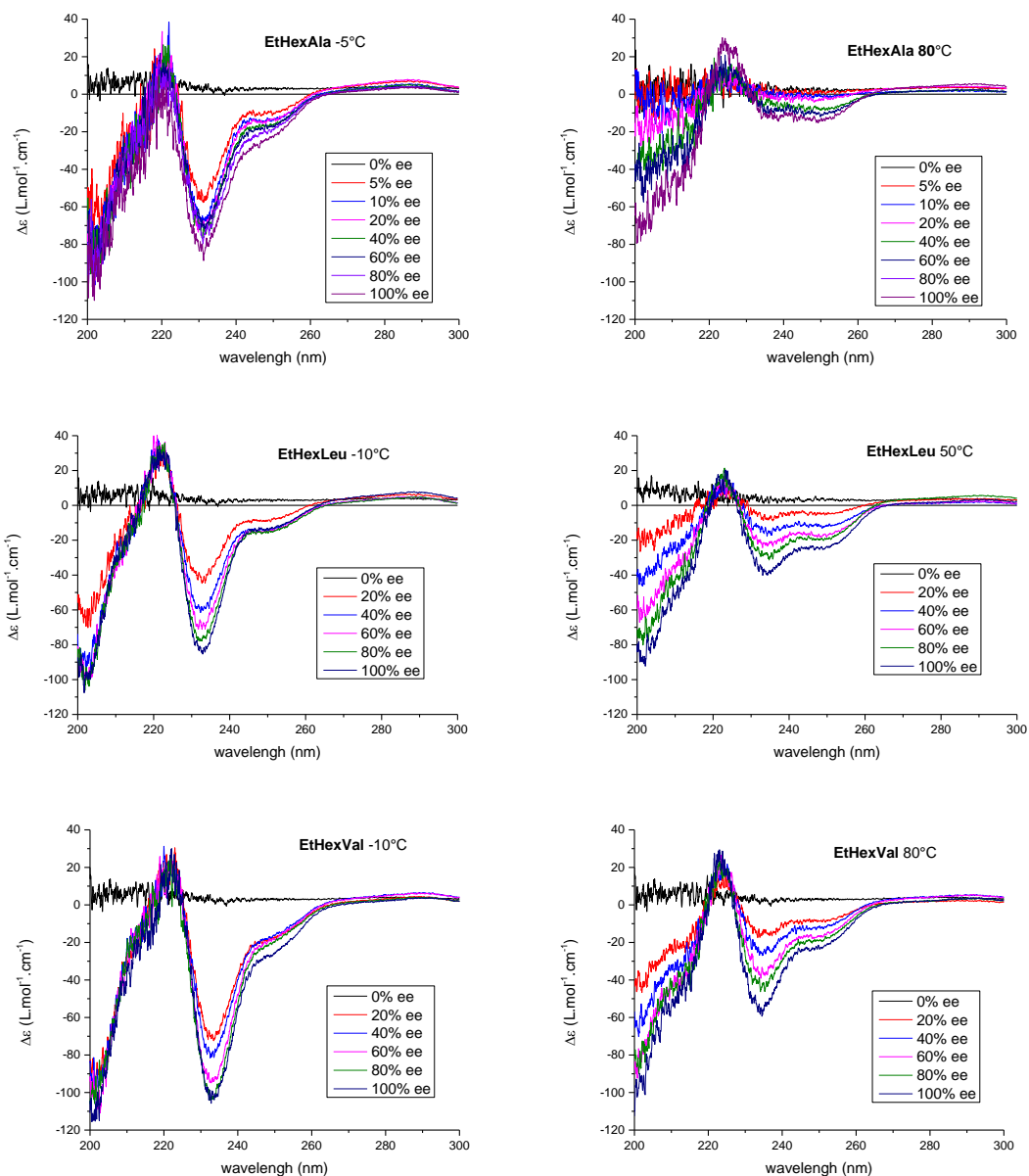


Figure 88 : CD spectra at 1 mM in methylcyclohexane below and above T** for **EtHexAla** at -5 (up left) and 80°C (up right), **EtHexLeu** at -10 (middle left) and 50°C (middle right) and **EtHexVal** at -10 (down left) and 80°C (down right)

The CD spectra of all three bis-ureas present two peaks at 233 and 255nm (Figure 88). We have chosen to measure the CD at 233 nm as it presents the highest intensity.

As it was shown for BTAs by Meijer and coworkers, the temperature can have a great influence on the CD signal.^[15] We thus measured the evolution of the CD signal at 233 nm with temperature for all three bis-ureas at different ee (Figure 89).

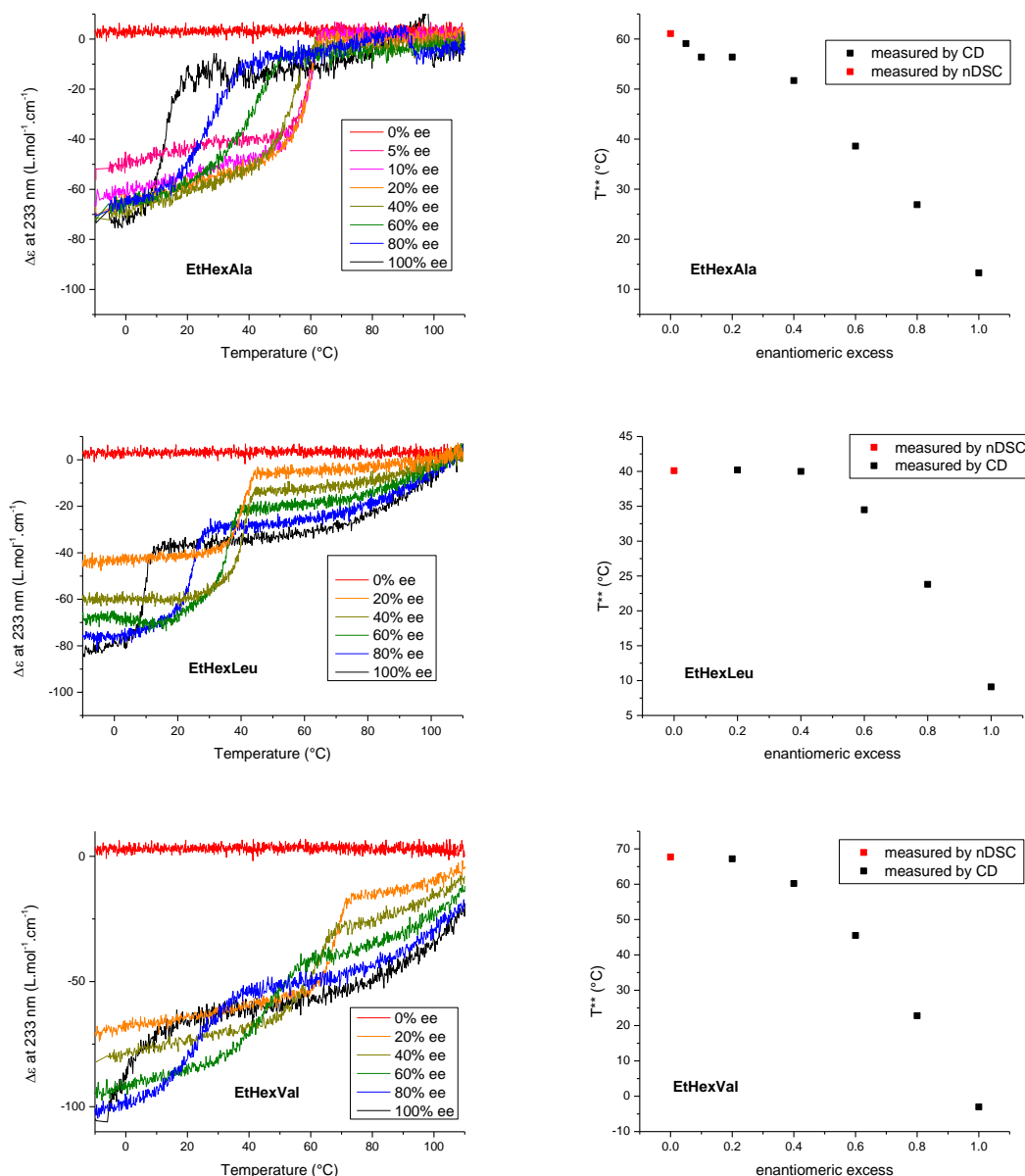


Figure 89 : CD signal at 233 nm vs temperature for different ee and T^{**} versus ee. **EtHexAla**, **EtHexLeu** and **EtHexVal** at 1 mM in methylcyclohexane

The first observation to be made (as showed in chapter 2) is that the transition between double filaments and filaments is highly visible in CD and thus T^{**} can easily be extracted as the midpoint of the CD intensity jump (Figure 89). T^{**} at 0%ee was measured by nDSC. In each case the transition temperature of the enantiopure bis-urea is more than 30 $^{\circ}\text{C}$ lower than for the racemic bi-urea. This indicates that a lower ee stabilizes the double filament compared to the filament. The other observation is that outside the transition, the CD signal is either stable or decreasing in absolute value. The increase of the CD signal with temperature observed for BTA is not present here, indicating a lower influence of the temperature on the majority rules effect. The observed decrease of the signal is probably due to the shortening of the assemblies. In one case the filament to monomer transition is observable at higher temperature (**EtHexLeu**) but the ee does not seem to have much impact on this transition.

With such a complex system, the use of a model is necessary to extract the HRP and MMP energies of both the double filament and the filament. For that reason, we modified the van Gestel model to use it in the case of two competing chiral assemblies.

2. Designing a new model

To apply the van Gestel model to this system, we have measured three parameters at different enantiomeric excesses: the net helicity of the double filament, the net helicity of the filament and the transition temperature. The net helicity is a measure of the difference between the relative number of right- and left-handed helical bonds and can be obtained by dividing the CD signal by its value at 100% ee.^[21] The helicity is correlated to the values of HRP and MMP using the Ising model.^[14] The Ising model can be applied to both the double filament and the single filament but in order to determine the exact values of HRP^{df} , MMP^{df} (double filament), HRP^f and MMP^f (filament) relationship is needed between all four parameters.

In both the double filament and the filament, no defects are expected to be present in the enantiopure assembly. Therefore, we take the enantiopure systems as reference and define for a mixture of enantiomers:

$$\Delta G_{defect}^f(ee) = \Delta G_{helix\ reversal}^f(ee) + \Delta G_{mismatch}^f(ee) = h^f(ee).HRP^f + m^f(ee).MMP^f$$

and

$$\Delta G_{defect}^{df}(ee) = \Delta G_{helix\ reversal}^{df}(ee) + \Delta G_{mismatch}^{df}(ee) = h^{df}(ee).HRP^{df} + m^{df}(ee).MMP^{df}$$

As the overall energetic penalties of the defects present in a scalemic mixture of monomers assembled into filaments or double filaments, respectively. $h^f(ee)$ represents the fraction of helix reversals present in a filament and HRP^f is the helix reversal penalty for the filament. The other parameters are defined analogously. According to the van Gestel theory, the fraction of helix reversals (h) and mismatches (m) are in fact unambiguously fixed by the values of HRP and MMP. The equations are not recalled here but can be found in the original publication.

The relative stability of the filament and double filament structures are measured by:

$$\Delta\Delta G_{defect}(ee) = \Delta G_{defect}^{df}(ee) - \Delta G_{defect}^f(ee)$$

Using the supramolecular balance principle we can relate $\Delta G_{defect}(ee)$ to the transition temperature:

$$\Delta\Delta G_{defect}(ee) = \Delta H \frac{T_{scalemic\ assembly}^{**} - T_{enantiopure\ assembly}^{**}}{T_{enantiopure\ assembly}^{**}}$$

Therefore the measure of the transition temperature gives an additional relationship between the four energetic penalties. Finally, fitting the transition temperature data together with the net helicity data should yield the values of HRP^{df} , MMP^{df} , HRP^f and MMP^f .

3. Fitting the data

The CD and nDSC data were fitted with the previously extended van Gestel model. Transition temperatures at 0%ee and transition enthalpies were extracted from nDSC data at 1mM (Figure 90).

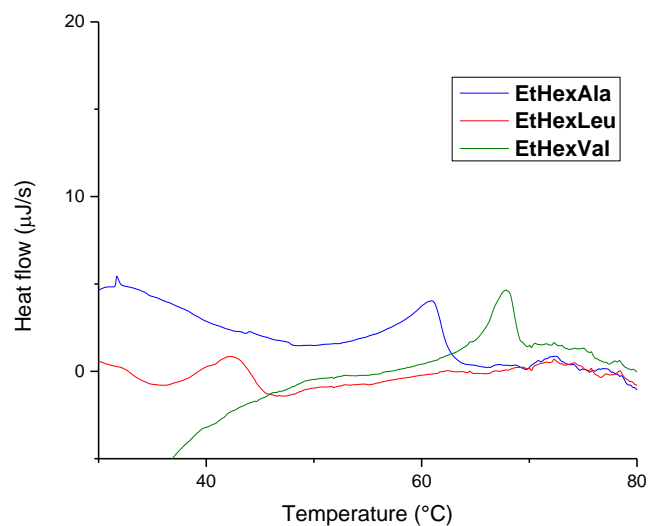


Figure 90 : nDSC of **EtHexAla**, **EtHexLeu** and **EtHexVal** at 0%ee at 1mM in Mécyclohexane (1°C/min)

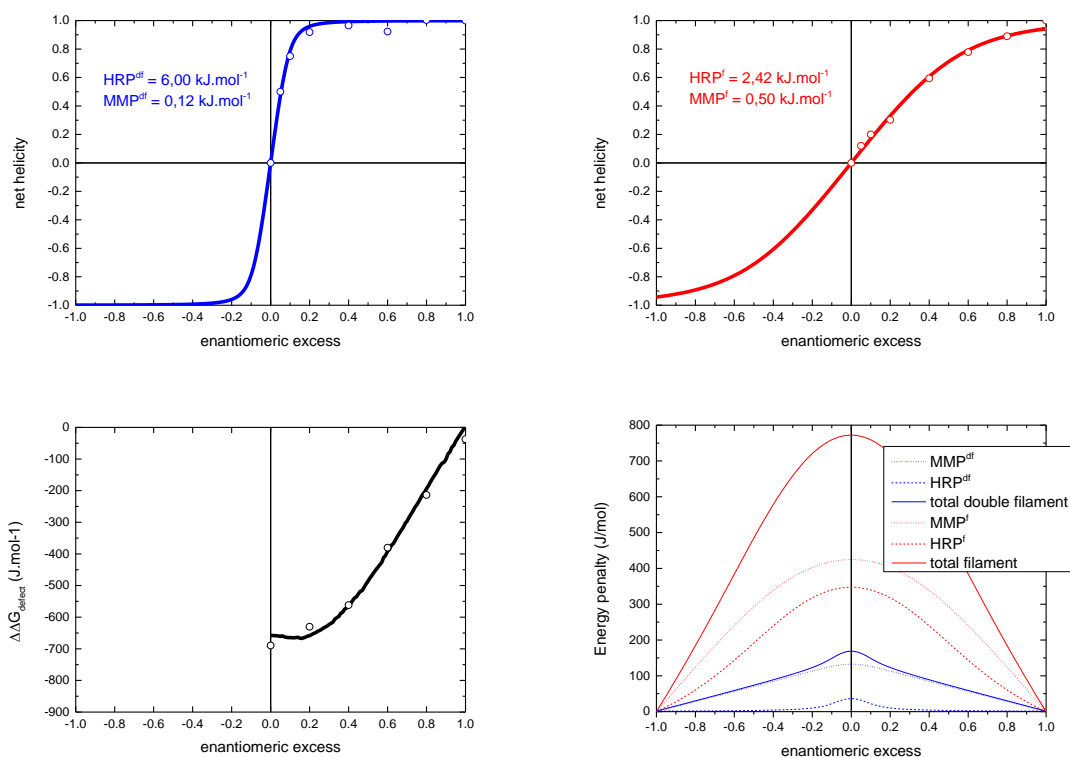


Figure 91 : Majority rules experiments on **EtHexAla** fitted with the extended van Gestel model (helicity vs ee of the double filament in blue at -5°C and of the filament in red at 80°C and the difference in energetic penalty due to defects (E) vs ee)

Figure 91 shows the data and the fits for **EtHexAla**. A first glimpse shows a good majority rules effect in the double filament form and a small one in the filament form. Concerning the filament, the HRP was divided by two and MMP multiplied by four compared to the double filament.

Taking into account the structures of both the filament and double filament, the increase in MMP can possibly be explained by a conformational effect. Indeed, according to the simulations shown in chapter 2 (Figure 60) the helical pitch of the double filament is larger than for the filament. In other words, the double filament is less twisted than the filament as expected because the close packing of two helices is only possible if the helices are partially unwound^[23]. It seems logical that the mismatched packing of the wrong enantiomer is less costly in the less twisted double filament than in the filament.

As for the HRP it can be explained by the size of the section as a helix reversal is less costly when there are fewer molecules per section.

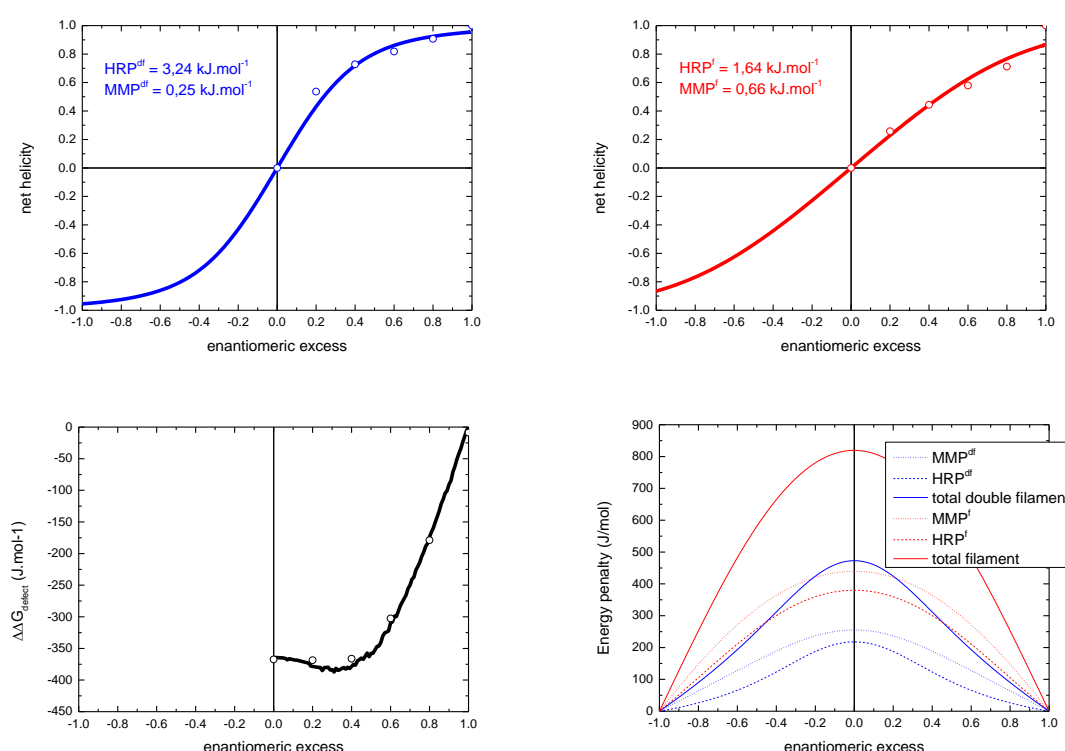


Figure 92 : Majority rules experiments on **EtHexLeu** fitted with the extended van Gestel model (helicity vs ee of the double filament in blue at -10°C and of the filament in red at 50°C and defect energy vs ee)

Figure 92 and Figure 93 show the results of the same experiments on **EtHexLeu** and **EtHexVal**.

Qualitatively the comments made in the case of **EtHexAla** can still be made: the HRP is larger and the MMP is smaller in the double filament compared to the filament.

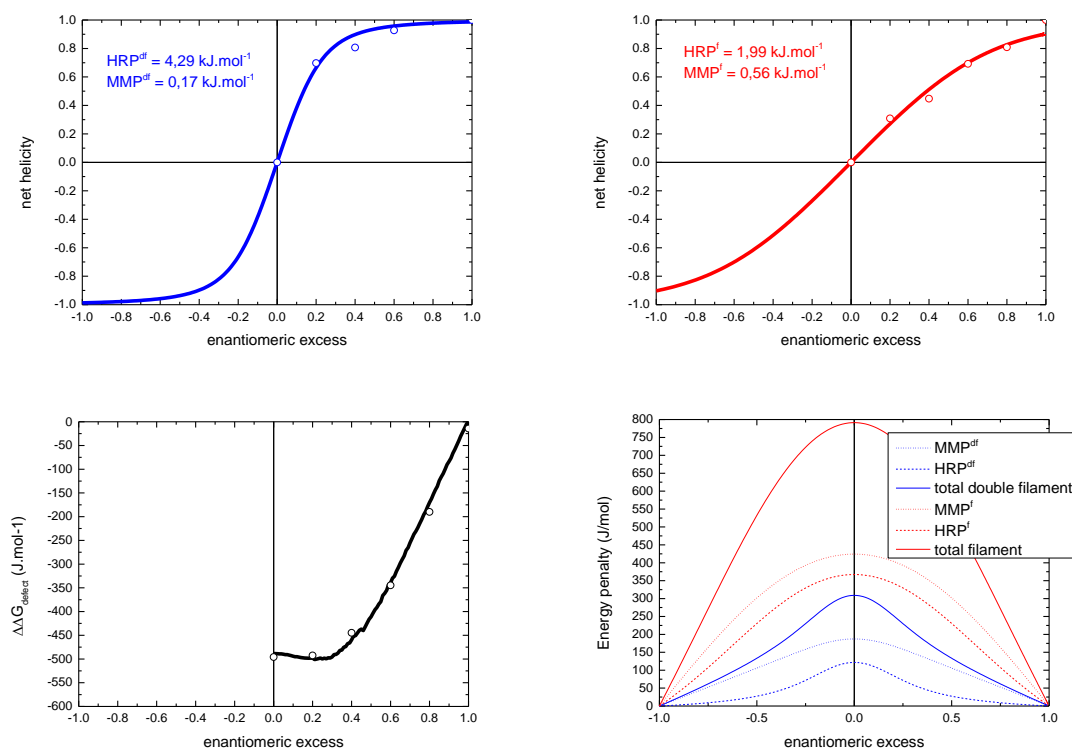


Figure 93 : Majority rules experiments on **EtHexVal** fitted with the extended van Gestel model (helicity vs ee of the double filament in blue at -10°C and of the filament in red at 80°C and defect energy vs ee)

Table 7 summarizes the values of HRP and MMP obtained for the three systems.

	double filament		filament	
aminoacid	HRP ^{df} (kJ/mol)	MMP ^{df} (kJ/mol)	HRP ^f (kJ/mol)	MMP ^f (kJ/mol)
Ala	6.00	0.12	2.42	0.50
Leu	4.29	0.17	1.99	0.56
Val	3.24	0.25	1.64	0.66

Table 7 : HRP and MMP values in the different assemblies

Upon comparison between all the results, we observe in both structures an increase of the MMP and a decrease of HRP with the size of the side chain of the aminoacid. The effect on the MMP is probably due to the increase of the steric hindrance within the assembly. The effect on the HRP is more complicated to interpret without modeling. However, it is interesting to note that we obtain values of HRP *ca.* twice higher in the double filament assembly compared to the filament, which could indicate a direct influence of the number of hydrogen bonds (and molecular contacts) involved in the helix reversal. Moreover, in the case of the EHUT tube structure that contains three molecules in the cross-section, the HRP was shown to be even larger (19.5 kJ/mol).

We can conclude that the more impacting factor of the majority rules effect in bis-ureas is the number of molecules present per section of the assembly as a greater number of molecules lowers the MMP by increasing the pitch of the helix and increases the HRP by increasing the size of the section and thus its rigidity. We have also shown a strong influence of the amino-acid alkyl side chain

due to steric hindrance in the double filament allowing us to conclude that Ala is the best amino acid to obtain an amplification of chirality. It would be interesting to have a look on the influence of the terminal alkyl side chains (branching and size) and of the spacer.

We have shown that the enantiopure versions of these bis-ureas are adequate for the supramolecular balance as they fulfill all the requirements. This design will be used in the next chapter to measure halogen-halogen interactions in solution.

- [1] W. A. Bonner, *Orig. Life Evol. Biosph.* **1991**, *21*, 59–111.
- [2] M. M. Green, J. Park, T. Sato, A. Teramoto, S. Lifson, R. L. B. Selinger, J. V Selinger, *Angew. Chem. Int. Ed.* **1999**, *38*, 3138–3154.
- [3] M. M. Green, S. K. Jha, *Chirality* **1997**, *9*, 424–427.
- [4] M. M. Green, M. P. Reidy, R. D. Johnson, G. Darling, D. J. O’Leary, G. Willson, *J. Am. Chem. Soc.* **1989**, *111*, 6452–6454.
- [5] H. Gu, Y. Nakamura, T. Sato, A. Teramoto, M. M. Green, S. K. Jha, C. Andreola, M. P. Reidy, *Macromolecules* **1998**, *31*, 6362–6368.
- [6] M. M. Green, B. A. Garetz, B. Munoz, H. Chang, S. Hoke, R. G. Cooks, *J. Am. Chem. Soc.* **1995**, *117*, 4181–4182.
- [7] H. Fenniri, B.-L. Deng, A. E. Ribbe, *J. Am. Chem. Soc.* **2002**, *124*, 11064–11072.
- [8] M. P. Lightfoot, F. S. Mair, R. G. Pritchard, J. E. Warren, *Chem. Comm.* **1999**, 1945–1946.
- [9] A. J. Wilson, J. van Gestel, R. P. Sijbesma, E. W. Meijer, *Chem. Comm.* **2006**, 4404–4406.
- [10] L. Brunsveld, A. P. H. J. Schenning, M. A. C. Broeren, H. M. Janssen, J. A. J. M. Vekemans, E. W. Meijer, *Chem. Lett.* **2000**, *29*, 292–293.
- [11] M. M. J. Smulders, A. P. H. J. Schenning, E. W. Meijer, *J. Am. Chem. Soc.* **2008**, *130*, 606–611.
- [12] M. M. J. Smulders, P. J. M. Stals, T. Mes, T. F. E. Paffen, A. P. H. J. Schenning, A. R. A. Palmans, E. W. Meijer, *J. Am. Chem. Soc.* **2010**, *132*, 620–626.
- [13] J. van Gestel, *J. Phys. Chem. B* **2006**, *110*, 4365–4370.
- [14] J. van Gestel, *Macromolecules* **2004**, *37*, 3894–3898.
- [15] M. M. J. Smulders, I. A. W. Filot, J. M. A. Leenders, P. Van Der Schoot, A. R. A. Palmans, A. P. H. J. Schenning, E. W. Meijer, *J. Am. Chem. Soc.* **2010**, *132*, 611–619.
- [16] A. R. Palmans, J. A. Vekemans, H. Fischer, R. A. Hikmet, E. W. Meijer, *Chem. Eur. J.* **1997**, *3*, 300–307.
- [17] J. van Gestel, A. R. A. Palmans, B. Titulaer, J. A. J. M. Vekemans, E. W. Meijer, *J. Am. Chem. Soc.* **2005**, *127*, 5490–5494.
- [18] A. R. A. Palmans, J. A. J. M. Vekemans, E. E. Havinga, E. W. Meijer, *Angew. Chem. Int. Ed.* **1997**, *36*, 2648–2651.
- [19] A. R. A. Palmans, E. W. Meijer, *Angew. Chem. Int. Ed.* **2007**, *46*, 8948–8968.
- [20] B. Isare, M. Linares, L. Zargarian, S. Fermannjian, M. Miura, S. Motohashi, N. Vanthuyne, R. Lazzaroni, L. Bouteiller, *Chem. Eur. J.* **2010**, *16*, 173–7.
- [21] B. Jouvet, B. Isare, L. Bouteiller, P. Van Der Schoot, *Langmuir* **2014**, *30*, 4570–4575.
- [22] M. Roman, C. Cannizzo, T. Pinault, B. Isare, B. Andrioletti, P. van der Schoot, L. Bouteiller, *J. Am. Chem. Soc.* **2010**, *132*, 16818–16824.
- [23] A. Aggeli, I. A. Nyrkova, M. Bell, R. Harding, L. Carrick, T. C. B. McLeish, A. N. Semenov, N. Boden, *Proc. Natl. Acad. Sci. USA* **2001**, *98*, 11857–11862.

Chapter 4 : Using the supramolecular balance to measure halogen...halogen interactions

Abstract: In this chapter, we describe the use of a bis-urea scaffold to measure halogen...halogen interactions. In a first part, we describe the literature on the halogen bond. In a second part we describe the evolution of the design of the bis ureas used for this purpose and the methodology developed in order to measure such interactions.

A. The halogen...halogen interaction

Halogens present high electronegativities (and even the highest one for F) and are generally considered as nucleophiles. They have thus been recognized as hydrogen bond acceptors for more than 60 years.^[1] Interestingly, the electron density of halogen atoms presents an anisotropic distribution when covalently bonded to another atom as a depletion of electron appears opposite to the bond along with a belt of high electronic density orthogonal to the bond.^[2] This cap of depleted electron density is called a σ -hole and allows the halogen atom to interact with nucleophiles and form the so-called halogen bond. A precise definition of the halogen bond was issued by the IUPAC in 2013^[3] but the halogen bond history actually started 200 years ago.

1. Halogen bond history

The first reported halogen-bonded complex was $I_2 \cdots NH_3$ and was synthesized by Colin in 1814 while he worked in Gay-Lussac's laboratory.^[4] He observed the formation of a metallic-looking liquid when exposing dry iodine to dry gaseous ammonia but the exact structure of this liquid was only established 50 years later by Guthrie who obtained the same compound using iodine and aqueous ammonia and proposed the $I_2 \cdots NH_3$ structure.^[5] Another century and the discovery of charge-transfer interactions by Mulliken^[6] and Hassel^[7] were needed to begin to understand the nature of the interaction involved in such a complex. In 1819, Pelletier and Caventou published the synthesis of strychnine triiodide from strychnine iodide and iodine, revealing the ability of a dihalogen to interact with anions.^[8] Later, in 1883, Rhoussopoulos showed that halocarbons form adducts with Lewis bases just as dihalogens when he synthesized the quinoline/iodoform adduct.^[9] Halogen bonded adducts with bromine and chlorine were synthesized a few years later by Ramsen and Norris who used various amines as nucleophiles.^[10] The first adducts using fluorine appeared only in the 1990s due to the extreme conditions necessary.^[11]

Adducts between bromine or chlorine and benzene were synthesized by Hassel in 1958 and 1959 and exhibited endless chains of alternated benzene and dihalogen.^[12,13] Kochi showed halocarbons can form adducts with π -donating species as well.^[14]

Bent was the first to discuss, based on crystal structures, the geometric features of the interaction present in those adducts in a review from 1968.^[15] Those results were confirmed 20 years later via a statistical analysis of Cambridge Structural Database (CSD) structures by Parthasarathy and Desiraju.^[16] Around the same time, Dumas, Gomel and Guerin studied interactions involving haloorganics in solution and showed interaction features similar to those in the crystal phase.^[17] Legon and coworkers systematically studied a variety of halogen-bonded adducts in the gas phase using microwave spectroscopy and obtained similar features thus concluding lattice and solvent effects have minor influence on halogen bonding.^[11]

The first step in understanding the nature of the halogen bond came from computational studies of the electron density distribution of a halogen atom forming a covalent bond by Politzer and Murray in the 1990s and the first observation of the later called σ -hole.^[18] Following this observation, two consecutive reviews by Metrangolo and Resnati showed that the electrophilicity of halogens has an impact in "all the fields where design and manipulation of aggregation processes play a key role"^[19] and the common features of halogen bonded adducts with many types of nucleophile and in all three phases^[20].

A IUPAC project to define the halogen bond was launched in 2009 and led to a precise definition in 2013 as stated below.^[3]

2. Halogen bond definition

The concept of halogen bond began to appear in the middle of the 20th century and the term “halogen bond” first appeared in a 1961 paper by Zingaro and Hedges.^[21] However, the first classification of a wide range of experimental results under the term halogen bond was the 1983 review written by Dumas, Gomel and Guerin.^[17] The term became of common use after a paper by Metrangolo and Resnati describing general principles correlating the structure of donors and acceptors with the strength of the resulting interaction.^[20] At that time, this term was also used to describe interactions where the halogen acts as a nucleophile.^[22]

In 2013, the IUPAC described the halogen bond (XB) as the interaction between the electrophilic region of a halogen covalently bonded to another atom defined as the XB donor and the nucleophilic region of another atom described as the XB acceptor.^[3]

The rationalization of the halogen bond nature allowed the understanding of the interactions between groups XIV-XVI atoms and nucleophiles as they present σ -holes in the extension of single covalent bonds as well.^[23]

3. Halogen bond properties

The halogen bond features two main properties making it highly useful in supramolecular synthesis: it is highly directional and its strength is easily tunable. It bears some resemblance with the hydrogen bond (HB) but some interesting differences as well.

a. Directionality

The XB has been shown, contrary to the HB, to be highly directional.^[24] It is due to the localization of the σ -hole on the elongation of the covalent bond causing a flattening of the halogen bond and thus forcing the interaction to present an angle of around 180° with the covalent bond.^[25] This property has been shown in both experimental^[26] and theoretical^[2] studies. It has also been shown that the strength of the bond affects greatly this property as the shorter the distance, the more directional the interaction is (Figure 94).^[27]

When the XB acceptor is a heteroatom possessing n-pairs, the interaction is along the axis of the donated n-pair. When the acceptor is a non-aromatic π -system, the covalent bond lies around the symmetry center of the π -bonding orbital of the acceptor. With two equivalent conjugated π bonds, the interaction is perpendicular to the plane containing the two π -systems and is localized on one of the π -system with no evidence of tunneling. Aromatic π -systems as acceptors exhibit interactions with the covalent bond of the XB donor almost perpendicular to the aromatic plane and the halogen atom just above the center of the aromatic. When both n-pairs and π -systems are present in the acceptor, n-pairs preferentially interact with the halogen (exception made of furan and thiophene).^[28]

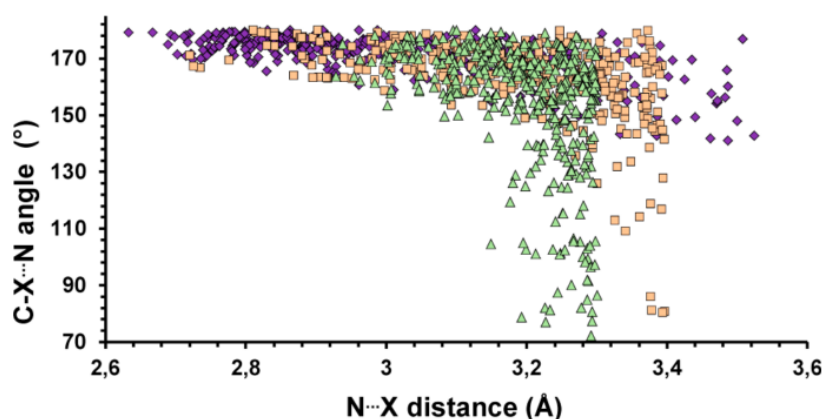


Figure 94 : Scatterplot derived from a CSD search reporting the C–X...N angle (deg) versus the X...N distance (Å) for crystal structures containing X...N contacts.^[28] Color code: blue rhombuses, I...N contacts; pink squares, Br...N contacts; green triangles, Cl...N contacts. Only error-free and nonpolymeric structures containing single-bonded I, Br, or Cl atoms and showing no disorder with $R < 0.05$ are considered.

b. Tunability

The strength of the XB is highly tunable by changing the nature of both the donor and the acceptor. Concerning the donor, simply changing the nature of the halogen atom has a dramatic effect since the size and electron density of the σ -hole is highly dependent on the size and polarizability of the halogen atom (Figure 95).^[25] The strength of the interaction decreases in the order $I > Br > Cl > F$.

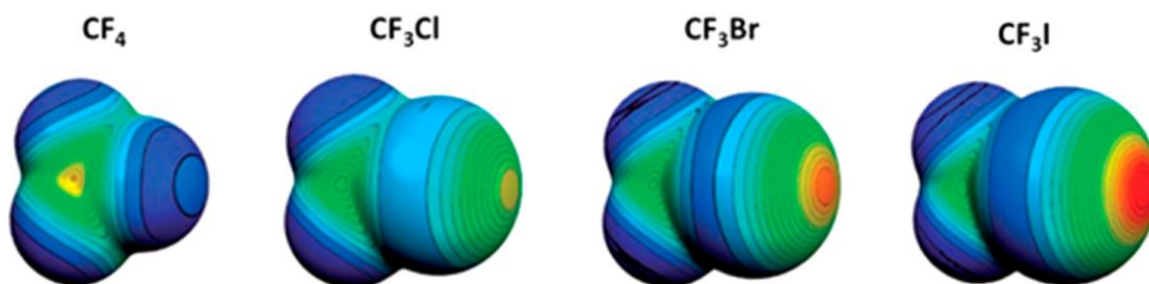


Figure 95 : Molecular electrostatic potential at the isodensity surface with 0.001 au for CF₄, CF₃Cl, CF₃Br, and CF₃I. Color ranges: red, greater than 27 kcal/mol; yellow, between 20 and 14 kcal/mol; green, between 12 and 6 kcal/mol; blue, negative^[25].

Fluorine is the poorest XB donor but a positive σ -hole can be observed when it is bonded to another fluorine atom or when it is linked to other atoms bearing strong electron-withdrawing substituents.^[29,30]

The size of the σ -hole, and thus the strength of the interaction, can also be tuned by modifying the electron-withdrawing character of the moiety covalently linked to the halogen atom. For example, haloarenes are known to be good XB donor. It has also been shown that the more you substitute hydrogens by fluorines on halogenobenzenes, the better the XB donor is.^[31] Similarly haloheteroarenes^[32] and haloperfluoroalkanes^[33] exhibit a high XB donor ability.

Interaction energies from 10 kJ/mol (some N...Cl contacts)^[34] to 150 kJ/mol (I₂...I⁻ adduct)^[35] were measured. The competition between multiple donors/acceptors demonstrates that best donor-best acceptor pairing occurs just as in hydrogen bonded systems.^[36] This property can be used to compare the XB acceptor ability of different sites within a single molecule and to form hierarchical supramolecular complexes.^[37]

c. Differences with the hydrogen bond

As mentioned before, the principal difference between XB and HB is the directionality of the XB but another interesting property is the hydrophobicity of the halogen residue making a typical XB donor site less hydrophilic than a typical HB donor site (e.g. OH or NH) thus allowing the complementarity of both interactions.^[28]

Another difference with HB is the bigger size of the XB donors as the van de Waals radii of halogens are higher than the hydrogen one yielding a higher sensitivity to steric hindrance compared to HB.^[38]

4. Nature of the halogen bond

The nature of the halogen bond is actually an important contemporary debate as anyone who attended the 2nd International Symposium on XB (ISXB2) at Gothenburg in June 2016 could realize.^[28] Even though the σ -hole concept introduced by Politzer^[25] is of common use, some experimental results cannot be explained using only the σ -hole^[39,40]. Computational chemists have proposed electrostatic, charge-transfer, dispersion and polarization interactions to cooperate in XB.

The issue in this situation, as Politzer and Clark pointed out, is that only the total binding energy is measurable experimentally, thus leaving this discussion to computational chemists.^[41] Contrary to the other parts, charge transfer can be estimated experimentally by calculating the laplacian of the charge density from X-ray data.^[42,43] For more details, please consult the review by Metrangolo and coworkers.^[28]

5. Solvent effect

It was shown that this interaction exists in solution as well and that its strength is highly dependent on the nature of the solvent (Table 8).^[44] It was shown that HB donor solvents limit XB in solution, orienting towards HB and that Lewis basic solvents compete with the halogen bond acceptor. In this example, the experimental data fits well with an electrostatic model but also reveals subtle differences.

solvent	K_a^a (M^{-1})	$\log K_a$
cyclohexane	2.8 ± 0.6	0.45
benzene	2.6 ± 0.5	0.41
acetonitrile	1.9 ± 0.4	0.20
dichloromethane	1.8 ± 0.3	0.20
acetone	1.3 ± 0.3	0.11
tetrahydrofuran	1.2 ± 0.2	0.08
dioxane	1.1 ± 0.2	0.04
<i>tert</i> -butyl alcohol	0.7 ± 0.3	-0.15
chloroform	0.6 ± 0.4	-0.2
2-propanol	0.3 ± 0.7	-0.4

Table 8: Association constants for the iodoperfluorooctane-triethylamine complex in various solvents.^[44] ^a Association constant K_a for the $Et_3N-IC_8F_{17}$ halogen bond (298 K) obtained by curve-fitting ^{19}F NMR titration data to a 1:1 binding isotherm

6. Applications

Many applications of this kind of interaction were developed over the years. This list is not exhaustive but is here to show how large the scope of application can be.

a. Crystal engineering

The XB is highly interesting in crystal engineering for its complementarity with HB, allowing the design and synthesis of 2D and 3D systems. Many interpenetrated structures were designed that way as well. A full comprehensive review of those is present in Metrangolo and coworkers review.^[28] This approach has been used to design a variety of functional materials such as opto-electronics material.^[45]

b. Soft materials

The XB has been used by Bruce and coworkers in the design of liquid crystals.^[46] He replaced a covalent bond present in a previous design by a non-covalent XB and showed the complex had liquid crystal properties whereas separately or when the interaction was prevented no liquid crystal property was seen.

Taylor designed two polymers, one bearing XB donors and the other bearing XB acceptor for them to co-assemble (Figure 96).^[47] They observed a variety of structures upon dilution such as spheres or nanotubes.

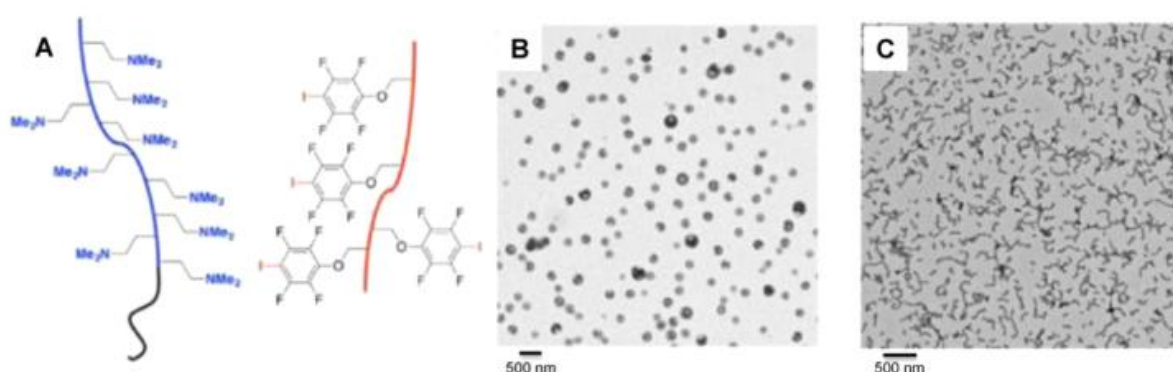


Figure 96 : Cartoon representing complementary halogen-bonded polymers (A) and self-assembly in solution into vesicle (B) and wormlike (C) structures, as observed by TEM micrographs^[47].

Steed and coworkers used the XB interaction between pyridines and diiodotetrafluorobenzene to form 2D supramolecular gels in cooperativity with HB between ureas (Figure 97).^[48]

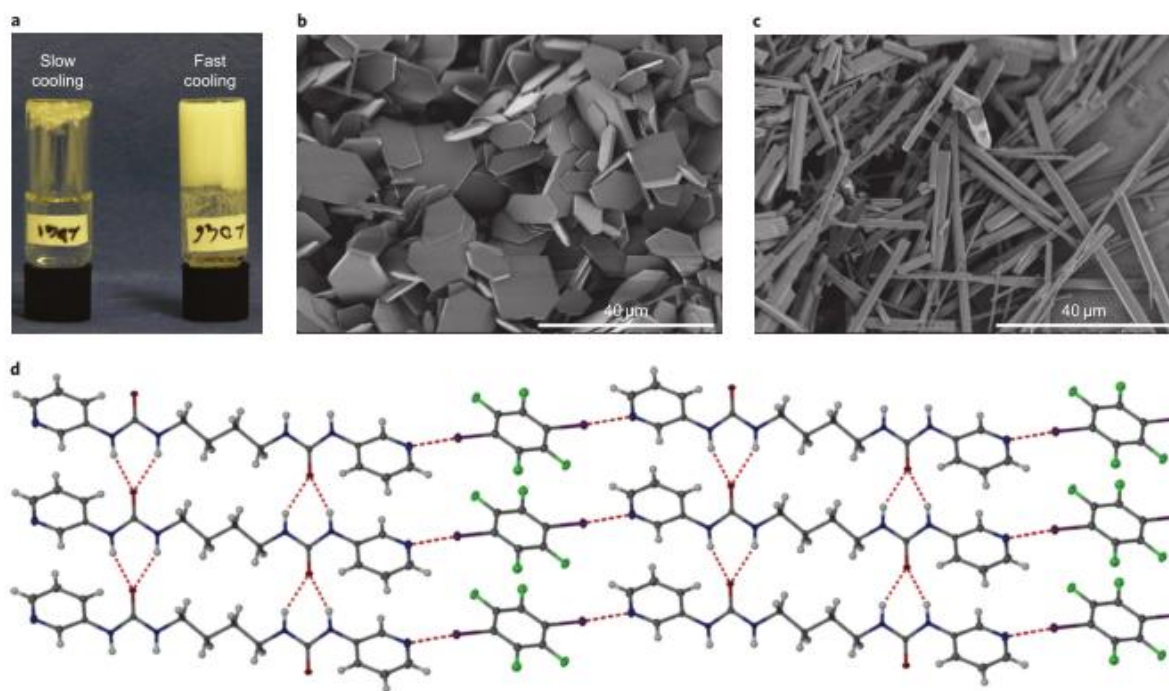


Figure 97 : a, Rapid cooling of an equimolar mixture of bis(pyridyl urea) and diiodotetrafluorobenzene in methanol/water (4:1 vol/vol) results in a robust hydrogel, while slow cooling gives a fibrous crystalline precipitate. b, SEM image of crystalline 1, which has a plate-like morphology. c, SEM image of the system, which has a needle morphology. d, X-ray crystal structure of the system showing the anticipated gel-forming urea-tape interaction and the halogen-bonding crosslinks involving the pyridyl groups. The crystalline materials in b–d were obtained under slow cooling conditions.^[48]

c. Biological systems

Halogens are known to have a dramatic influence on biological systems. Their regular introduction in pharmaceutical compounds is due to their high lipophilicity, allowing the molecule to enter cells in an easier way. However, they seem to have a more complex role in biological systems as they can lead or modify the interaction of a compound with the active site of a protein. One of many example is the structure activity relationship of a class of hepatitis virus C protease inhibitors where the presence of halogen atom dramatically enhances the activity of the inhibitor (Figure 98).^[49]

	X	EC ₅₀ (nM)
	Me	17 ± 8
	F	36 ± 10
	Cl	11 ± 2
	Br	5 ± 2

Figure 98 : EC₅₀ values calculated using a cell-based replicon assay. EC₅₀ refers to the inhibitor concentration required for half-maximal activity in this assay^[49]

d. Catalysis

Many examples of XB driven organic synthesis and organocatalysis exist and a nice review by Huber, who is a leader in this field, was published.^[50] The first example was a templated 2+2 cyclisation in the solid-state by Metrangolo and coworkers (Figure 99).^[51]

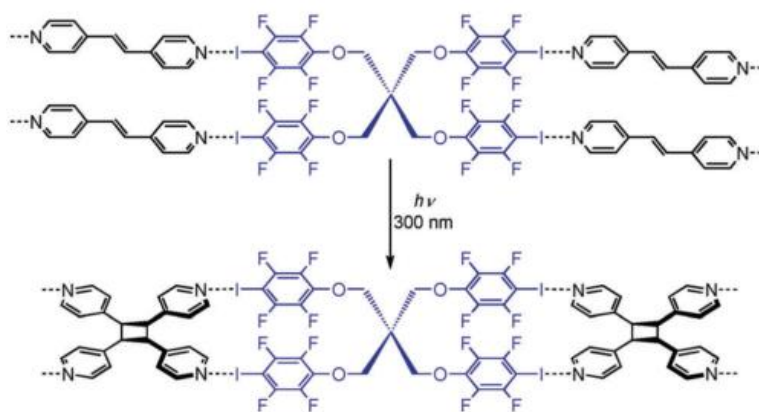


Figure 99 : 2+2 cyclisation scheme^[51]

e. Ion sensors

The XB can also be used in an anion sensor as it can interact with them and sometimes even selectively. To improve selectivity, the usual designs are more or less congested pincers. For example, Taylor and coworkers designed a molecule that complexes very easily with halides but not with tosylates, sulfates or nitrates (Figure 100).^[52]

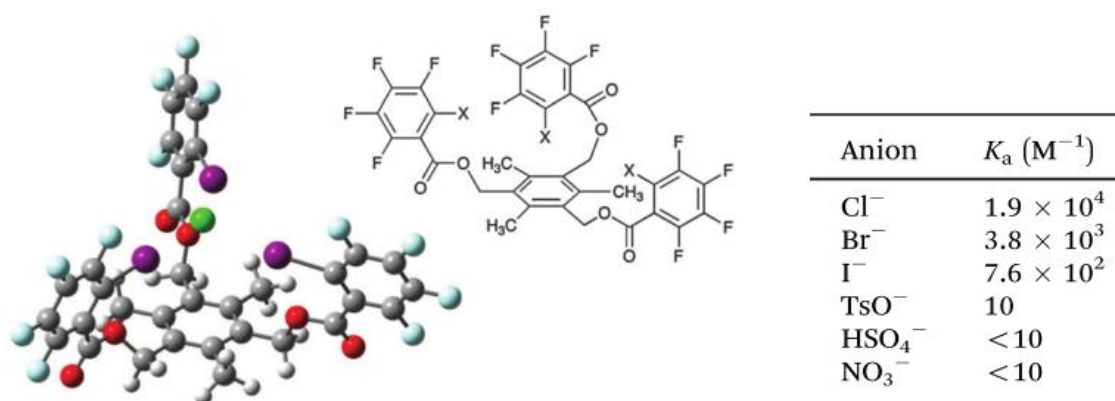


Figure 100 : Structure, X-ray and complexation constant in deuterated acetone of Taylor's sensor ($\text{X}=\text{I}$)^[52]

7. The particular case of halogen-halogen interactions

We will now focus on the weakest type of XB: the case where the XB acceptor is also a halogen. The first example of such an interaction is solid chlorine. Its layered structure was reported in 1952^[53] and its laplacian electronic distribution was determined in 1995^[54]. It shows contacts between the σ -hole of one molecule and the electro-enriched ring of its neighbor in an approximate 90° angle (Figure 101).

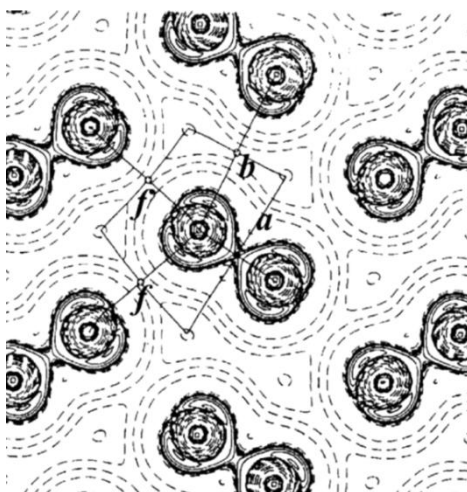


Figure 101 : Laplacian distribution of solide Cl_2 ^[54]

It was noted in 1963 by Sakurai and coworkers that $\text{R-X}\cdots\text{X-R}$ contacts exhibited only two types of geometries^[55] but it was only years later that Desiraju and coworkers classified them^[56] as type I (symmetrical and in line interactions) and type II (asymmetrical and orthogonal) (Figure 102).

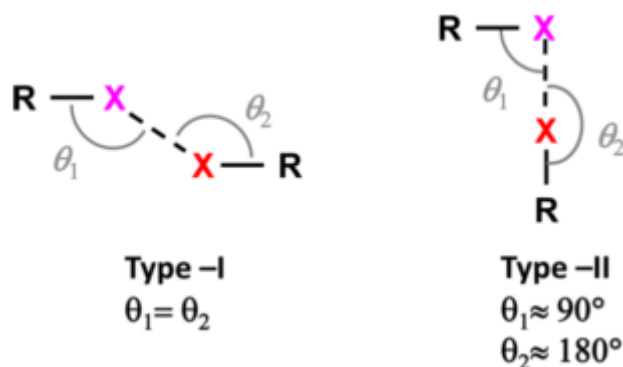


Figure 102 : scheme of the two types of X-X contacts ^[28]

Type I contacts are not true XB according to the IUPAC definition but only arise from close-packing requirements. Type II originates from the interaction between the σ -hole of a halogen and the nucleophilic ring of another halogen. A CSD statistical study by Desiraju and coworkers found that type II contacts were more favored with iodinated derivatives, less in brominated derivatives and the least in chlorinated derivatives.^[57] They also showed that type I interactions were extremely short due to their dispersive nature whereas type II were closer to the van der Waals limit.

Another CSD statistical study by Twamley and coworkers pointed out the effect of hybridization and substituents of the ipso carbon in halogenocarbon species.^[58] They found out the size of the σ -hole tends to increase as the s character of the ipso carbon increases but also that the negative electrostatic potential of the ring tends to decrease, leading to a strength of the interaction in the order $\text{sp}^2 > \text{sp} > \text{sp}^3$. They also observed that attaching electronegative substituents to the ipso carbon strengthen the interaction. Moreover, they designed a model based solely on electrostatics and all their observations agreed with that model, tending to prove that inter-halogen contacts are purely electrostatic in nature. Another interesting observation they made is that in fluorotribromomethane, fluorine prefers to act as a halogen bond acceptor and forms a hetero interaction rather than assisting a homo interaction.

This kind of interaction can be in competition with HB^[59] or π -stacking^[60] and has been shown to be complementary in certain cases. There are multiple examples where both halogen...halogen and halogen...nucleophile interactions coexist^[57] and even with HB sometimes^[61].

This particular kind of XB does have applications as well such as the preparation of highly stereoregular organic polymers in the solid phase.^[62]

Those interactions have been used to obtain self-assemblies on surface with both bromine^[63] and fluorine^[64] derivatives.

Halogen...halogen interactions have been characterized in the gas-phase as well by mixing halogenomethane and halogenotrifluoromethane in liquid krypton and using FTIR and Raman spectroscopy.^[65] They obtained complexation enthalpies of around 7 kJ/mol for all complexes.

To our knowledge, there is no example of halogen...halogen bonding in solution probably due to the high competition with the solvent.

In light of those results we wanted to introduce halogen-halogen interactions inside our assemblies and to use the supramolecular balance principle to measure the energy of those interactions.

B. Application of the supramolecular balance

1. The choice of the molecule

When designing the bis-urea platform to measure halogen...halogen interactions we had to choose a bis-urea that (i) self-assembles in long-enough polymers to be able to use the supramolecular balance principle (see chapter 1), (ii) exhibits a double filament to filament transition temperature in a measurable range and (iii) in which the addition of a halogenated interacting group does not change the self-assembly structure. We also had to choose an interacting group that acts both as a good XB donor and acceptor. To simplify the system we chose a symmetrical interacting group.

a. The 3,5-dibromobenzene moiety

We started with the 3,5-dibromobenzene moiety as it could present both Br...Br and Br... π interactions.^[66] For the design of the bis-urea, we initially chose the tolyl spacer as toluene-2,4-diisocyanate (TDI) is commercially available, phenylalanine (Phe) as the amino-acid as it has been shown to form the most resistant self-assemblies (see chapter 2) and several sizes of bromoalcohols to modulate the solubility (Figure 103).^[67] The synthesis is presented in chapter 6.

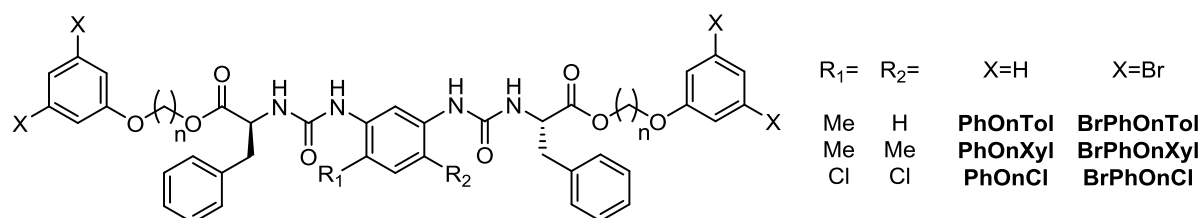


Figure 103 : structures of bis-ureas designed to measure Ph-Br...Br-Ph interactions

nom	cyclohexane	toluene	CHCl ₃	DCM	MeTHF	THF	Et ₂ O	AcOEt	Cl-benzene	Cl-cyclohexane
BrPhO6Tol	I	S(V)	S	S	S	S	I	S	S(V)	S
PhO6Tol	I	S(V)	S	S	S	S	I	S	S(V)	S
BrPhO11Tol	I	S(V)	S	S	S	S	I	S	S(V)	S
PhO11Tol	I	S(V)	S	S	S	S	I	S	S(V)	S
BrPhO6Cl	I	I	I	I	S	S	I	I	S(G)	S(G)
PhO6Cl	I	I	I	I	S	S	I	I	S(G)	S(G)
BrPhO11Cl	I	I	S	I	S	S	I	I	S(G)	S(G)
PhO11Cl	I	I	S	S	S	S	I	I	S(G)	S(G)
BrPhO9Xyl	I	I	S	S	S	S	I	S	S(G)	S(G)
PhO9Xyl	I	I	S	S	S	S	I	S	S(G)	S(G)
BrPhO11Xyl	I	I	S	S	S	S	I	S	S(G)	S(G)
PhO11Xyl	I	I	S	S	S	S	I	S	S(G)	S(G)

Table 9 : solubilities of the compounds at 10 mM in various solvents (I=insoluble, S=soluble, V=viscous, G=gel)

The first issue we encountered was a lack of solubility in cyclohexane (Table 9) thus orienting us to study the assembly in toluene. Even though IR studies showed the bis-ureas with a tolyl spacer were assembled in toluene, we were not able to measure any transition temperature. It could be due to a transition temperature lower than 0°C as we obtained viscous solutions but not gels. We thus decided to change the spacer as previous studies indicated that it had a dramatic impact on the self-assembling properties of bis-ureas: a dichlorophenyl or xylyl spacer is expected to raise the transition temperature.^[68] Bis-ureas with dichlorophenyl and xylyl spacer were synthesized (Figure 103) but unfortunately those were not soluble in non polar solvents such as toluene or cyclohexane (Table 9). We thus extended the solubility tests to halogenated solvents and all compounds proved to be soluble in chlorocyclohexane, chloro-, bromo- and iodobenzene. Moreover, bis-ureas bearing the dichlorophenyl or xylyl spacer formed strong gels in all those solvents at room temperature. A temperature dependent IR study showed that above the transition the filaments are rapidly disassembled in the case of tolyl and dichlorophenyl spacers which is not ideal for our objective because the equations published for the supramolecular balance are only valid if the change of length of the objects can be neglected in the vicinity of the transition temperature (T^{**}). However, the situation seems more favorable with the xylyl spacer (Figure 104).

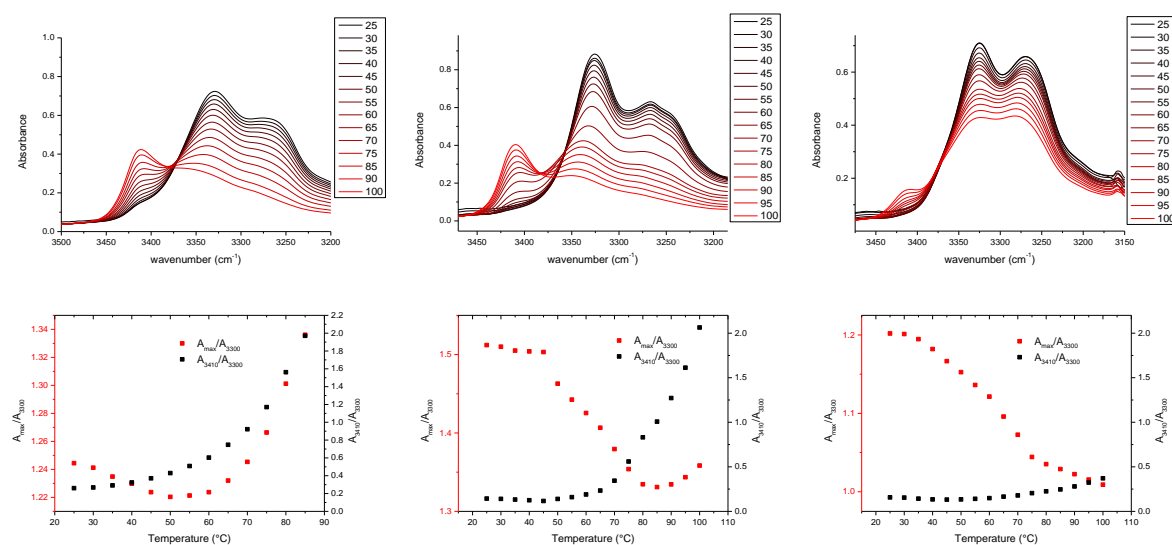


Figure 104 : FTIR spectra in the region of N-H stretching at different temperatures (up) and plots of A_{\max}/A_{3300} and A_{3410}/A_{3300} against temperature of **BrPhO6Tol**, **BrPhO6Cl** and **BrPhO9Xyl** (from left to right) at 10mM in Br-benzene. A_{\max}/A_{3300} corresponds to the normalized intensity of the aromatic NH band and its plot against temperature reflects the structural transition. A_{3410}/A_{3300} reflects the amount of free NH.

Moreover the results obtained in SANS (Figure 105) show that the transitions detected by FTIR are indeed a filament to monomer transition for **BrPhO6Tol**, a double filament to monomer transition for **BrPhO6Cl** and a double filament to short filament transition for **BrPhO6Xyl** (Table 10).

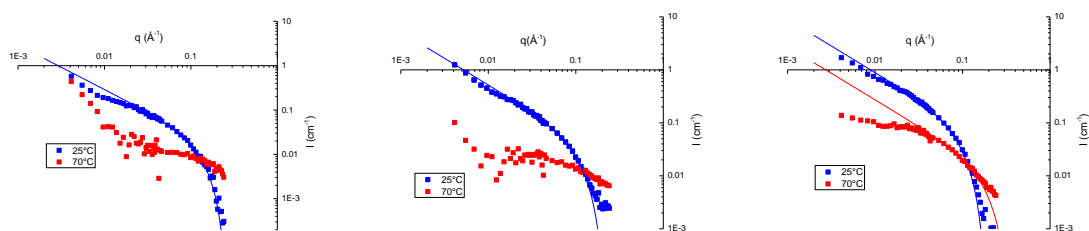


Figure 105 : SANS of **BrPhO6Tol**, **BrPhO6Cl** and **BrPhO9Xyl** (from left to right) at *ca.* 1 wt% in Br-benzene

	25°C			70°C		
	n	r (Å)	structure	n	r (Å)	structure
BrPhO6Tol	0.7	15.0	filament	no fit	no fit	monomer
BrPhO6Cl	1.5	17.6	double f	no fit	no fit	monomer
BrPhO9Xyl	1.6	20.4	double f	0.5	10.8	filament

Table 10 : number of molecule per section (n) and radii (r) of the rod structure deduced by the fit of the SANS data with the form factor for a rigid rod of circular cross-section. Double f = double filament.

Moreover, bis-ureas bearing the dichlorophenyl spacer showed a more cooperative and thus a more precisely measurable transition in X-benzenes (Figure 106).

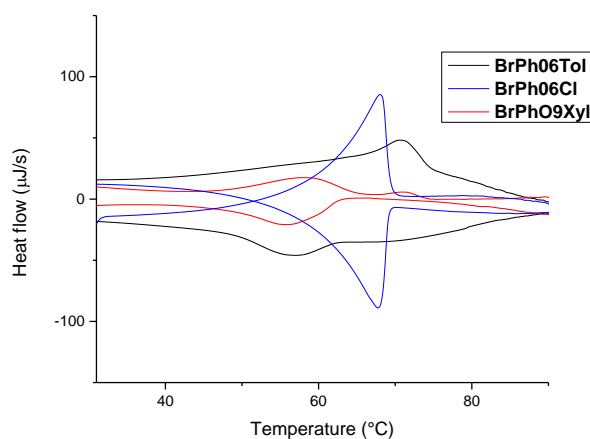


Figure 106 : nDSC thermogram of **BrPhO6Tol**, **BrPhO6Cl** and **BrPhO9Xyl** at 10 mM in Br-benzene (1°C/min)

As the interactions between the dibromobenzene moieties are more likely to occur in the double filament, we can disqualify **BrPhO6Tol** that only forms filaments in the accessible temperature range. **BrPhO9Xyl** exhibits short filaments at 70°C (Figure 105) and a weakly cooperative transition (Figure 106) thus forbidding the use of the supramolecular balance principle. As **BrPhO6Cl** exhibits a double filament to monomer transition, it might be used to probe the change in stability provided by the addition of the bromines of the phenyl moiety, even if the equations presented in chapter 1 would

have to be modified. Therefore, the transition temperature of **BrPhO6Cl/PhO6Cl** and **BrPhO11Cl/PhO11Cl** were measured in X-benzenes for X = I, Br and Cl (Figure 107 and Table 11).

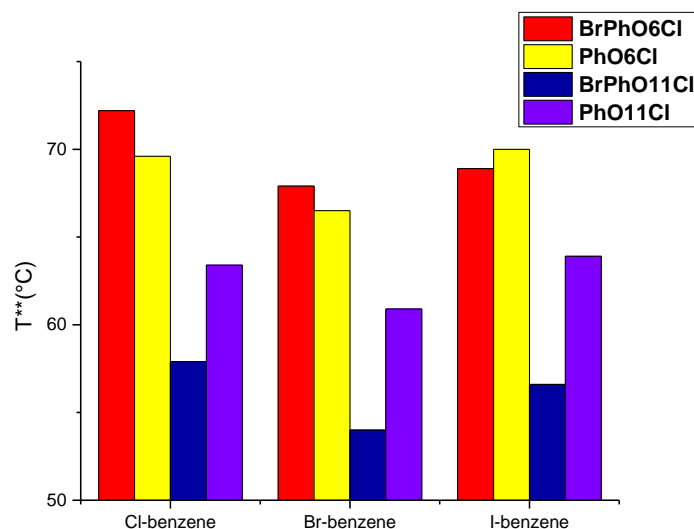


Figure 107 : Transition temperatures of **BrPhOnCl/PhOnCl** in X-benzenes

$\Delta T (T_{Br}-T_H)$	Cl-benzene	Br-benzene	I-benzene
n=6	2.6	1.4	-1.1
n=11	-5.5	-6.9	-7.3

Table 11 : transition temperature of **BrPhOnCl/PhOnCl** in X-benzenes

A first observation to be made is that the longer the alkyl chain, the lower the transition temperature is, which can be used to tune T^{**} . The other interesting thing is that the sign of ΔT is not the same in all cases (thus it cannot simply be explained by a stabilization/destabilization of the assembly upon bromination of the phenyl moiety). Nevertheless, ΔT shows the same trend for both alkyl chain sizes: it decreases when the solvent goes from chlorobenzene to bromobenzene and to iodobenzene. As this transition corresponds to a double filament to monomer transition, this evolution of ΔT can be explained two ways: it can either result from the influence of the solvent on the interactions present within the double filament of the brominated bis-urea (relatively to its reference bis-urea) or it can result from a difference in solvation between the assembly and the monomer or even a mix of both effects. As the observed trend follows the electronegativity of the solvent halogen atom, it is possible that X-bonding to the solvent is present. However, the rationalization of these results is getting tough as many different interactions may occur. In the non-brominated assembly π - π stacking, C-H \cdots π interactions and even maybe C-H \cdots O interactions can be present. In the brominated assembly, π - π stacking, C-Br \cdots Br-C interactions, C-Br \cdots π interactions and even maybe C-Br \cdots O interactions can be present. Moreover, the interaction with the solvent is as much complicated as it can exhibit all those interactions as well.

Because of the difficulties to rationalize the results obtained we chose a simpler system which should be able to form only Br \cdots Br interactions.

b. The CBr₃ moiety

We thus chose the CBr₃ moiety which has been shown to form Br...Br interactions in the crystal phase as Br is a good XB donor reinforced by the presence of the two electronegative Br on the ipso carbon and a correct XB acceptor.^[69] Moreover the CBr₃ symmetry should simplify future interpretations. We synthesized the corresponding bis-ureas with the three different spacers and the same alkyl chain (Figure 108).

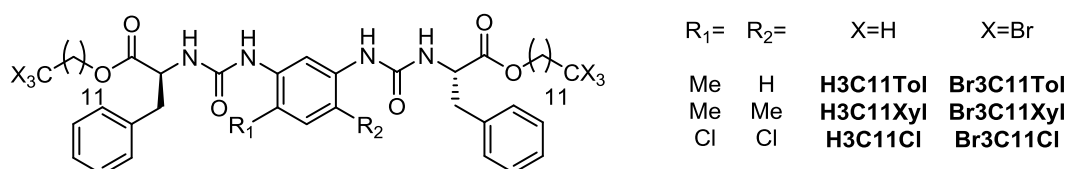


Figure 108 : structures of bis-ureas designed to measure CBr₃...Br₃C interactions

	cyclohexane	toluene	DCM	THF	Et2O	AcOEt	benzene	propylbenzene	Br-hexane	Cl-hexane
Br3C11Tol	I	S(G)	S	S	I	I	I	S(G)	S(G)	S(G)
H3C11Tol	S(G)	S(G)	S	S	I	I	S(G)	S(G)	S(G)	S(G)
Br3C11Cl	I	S(G)	S	S	I	I	I	S(G)	S(G)	S(G)
H3C11Cl	S(G)	S(G)	S	S	I	I	S(G)	S(G)	S(G)	S(G)
Br3C11Xyl	I	S(G)	S	S	I	I	I	S(G)	S(G)	S(G)
H3C11Xyl	S(G)	S(G)	S	S	I	I	S(G)	S(G)	S(G)	S(G)

Table 12: solubilities of the compounds at 10 mM in different solvents (I=insoluble, S=soluble, G=gel)

The CBr₃ moiety showed a poor solubility in cyclohexane but adequate solubility in toluene (Table 12). Bis-ureas based on all three spacers showed cooperative transitions in toluene (Figure 110) but only the ones with the xyllyl spacer remained strongly associated at high temperature (Figure 109).

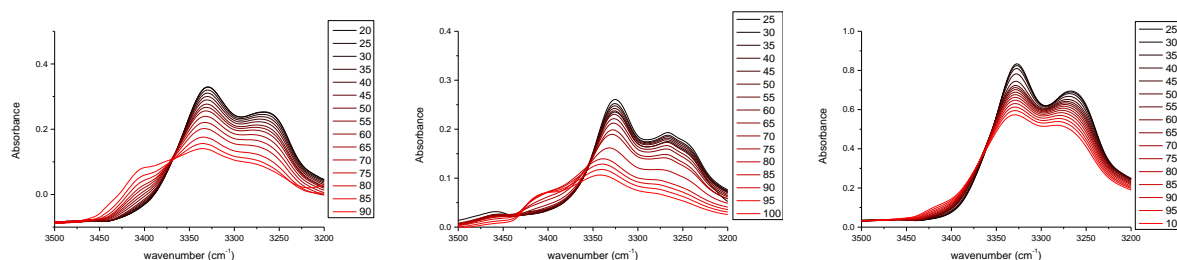


Figure 109: IR of **Br3C11Tol**, **Br3C11Cl**, **Br3C11Xyl** (from left to right) at 10mM in toluene

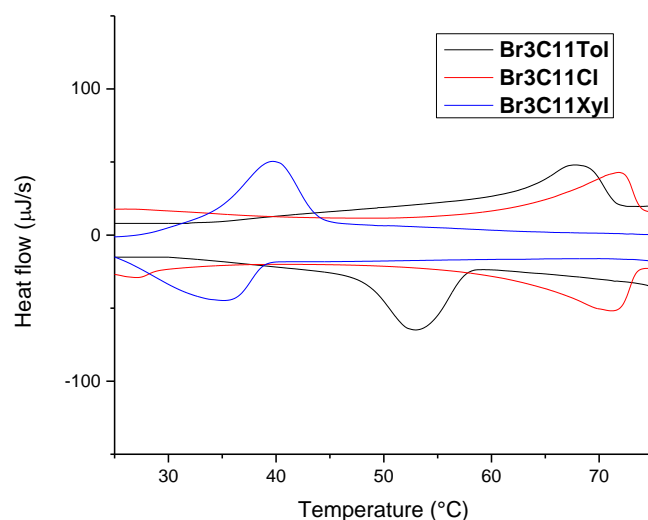


Figure 110 : nDSC thermogram of **Br3C11Tol**, **Br3C11Cl**, **Br3C11Xyl** at 10mM in toluene (1°C/min)

These transitions were confirmed by SANS experiments to occur between short filaments and monomers for **Br3C11Tol**, between filaments and monomers for **Br3C11Cl** and between double filaments and short filaments for **Br3C11Xyl** (Figure 111 and Table 13).

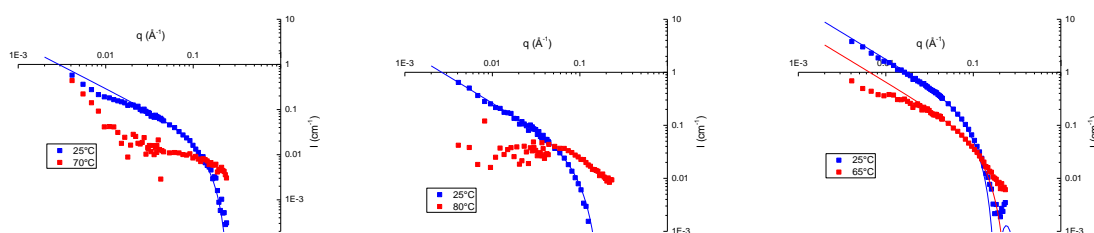


Figure 111 : SANS of **Br3C11Tol**, **Br3C11Cl** and **Br3C11Xyl** (from left to right) at *ca.* 1 wt% in toluene

	25°C			80°C (65°C for Xyl)		
	n	r (Å)	Structure	n	r (Å)	structure
Br3C11Tol	1.0	18.4	filament	no fit	no fit	monomer
Br3C11Cl	0.4	21.5	filament	no fit	no fit	monomer
Br3C11Xyl	2.2	21.1	double f	0.8	15.3	filament

Table 13 : number of molecule per section (n) and radii (r) of the rod structure deduced by the fit of the SANS data with the form factor for a rigid rod of circular cross-section. Double f = double filament.

We thus selected the **Br3C11Xyl** system for in depth analysis

2. Detailed study of **Br3C11Xyl** in aromatic solvents

Br3C11Xyl and **H3C11Xyl** showed highly similar IR spectra both below and above the transition indicating they have the same HB network (Figure 112). They showed similar results as well in SANS

(Figure 113) indicating they form assemblies of the same form and size as fitting those data with long rods gave respectively for **Br3C11Xyl** and **H3C11Xyl** 2.2 and 2.3 molecules per section at 20°C (double filament) and 0.8 and 0.9 at 65°C (filament). Interestingly, they also showed different transition temperatures in nDSC (Figure 114).

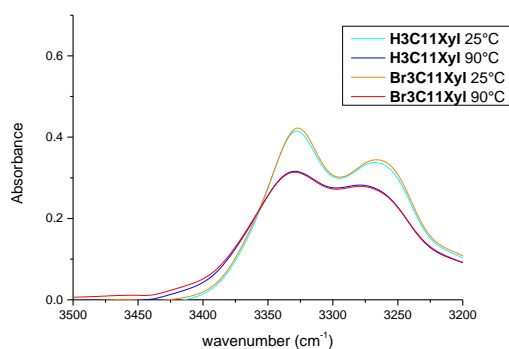


Figure 112 : Infra-red spectra of **Br3C11Xyl** and **H3C11Xyl** below and above the transition at 10 mM in toluene

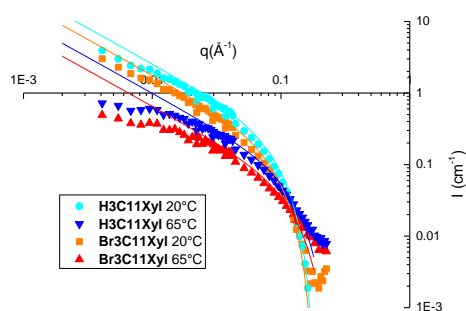


Figure 113 : SANS of **Br3C11Xyl** and **H3C11Xyl** below and above the transition at *ca.* 1 wt% in toluene

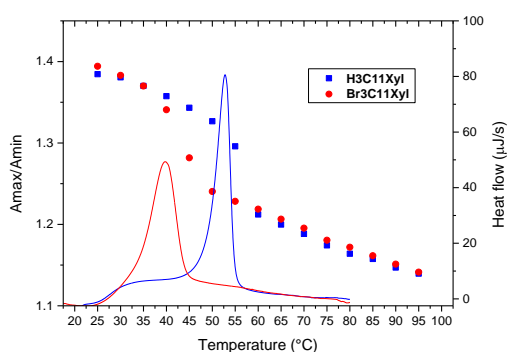


Figure 114 : nDSC (heat flow, heating run, 1°C/min) and FTIR (absorbance ratio $A_{3325\text{cm}^{-1}}/A_{3295\text{cm}^{-1}}$) data for **Br3C11Xyl** and **H3C11Xyl** solutions in toluene (10 mM)

We found out that **Br3C11Xyl** and **H3C11Xyl** are soluble in various alkyl benzene solvents and decided to investigate the influence of the size of the solvent alkyl chain on the transition temperatures (Figure 115).

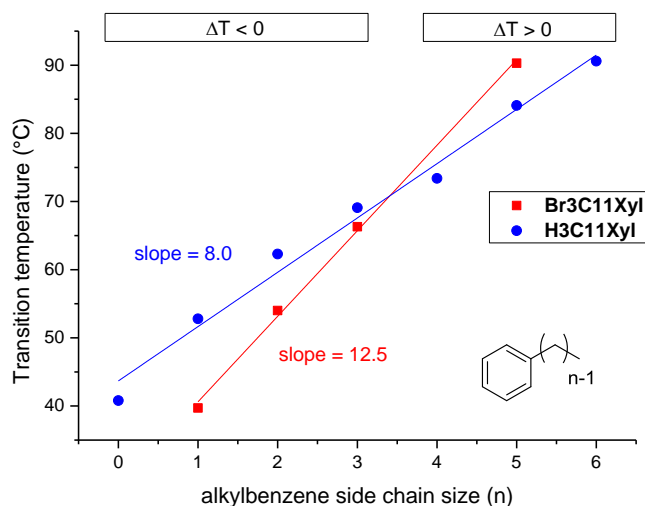


Figure 115 : Transition temperature of **Br3C11Xyl** and **H3C11Xyl** in linear monoalkylbenzene vs the size of the solvent alkyl chain (10 mM measured by nDSC)

The fact that the difference between the transition temperatures of **Br3C11Xyl** and **H3C11Xyl** depends on the solvent is a clear indication that solvation effects are important in this system. More precisely, we can interpret the variation of ΔT by a different difference of solvation between the double filament and filament assemblies for CBr_3 and CH_3 , and the evolution of this difference of solvation with the nature of the solvent. Let us assume that the solvation is more important in the filament assembly as it is less compact than the double filament. Then a negative ΔT ($T^{**}_{\text{CBr}_3} - T^{**}_{\text{CH}_3}$) corresponds to a more stable filament upon bromination and thus a better solvation of the CBr_3 moiety. With the same logic, a positive ΔT corresponds to a better solvation of CH_3 . The data of Figure 115 then means that CBr_3 is better solvated by the aromatic part of the solvent (probably due to $\text{C-Br} \cdots \pi$ interactions) and that CH_3 is better solvated by the aliphatic part of the solvent.

In order to test this analysis, we confronted these results with other bis-ureas with different alkyl chain size and/or bearing a phenyl terminal group (Figure 116).

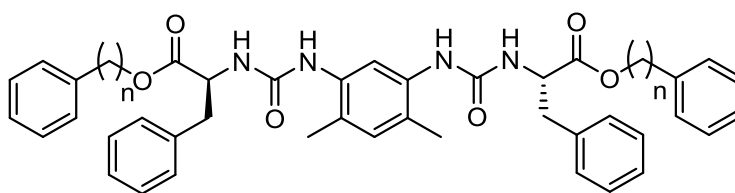


Figure 116 : Structure of **PhnXyl**

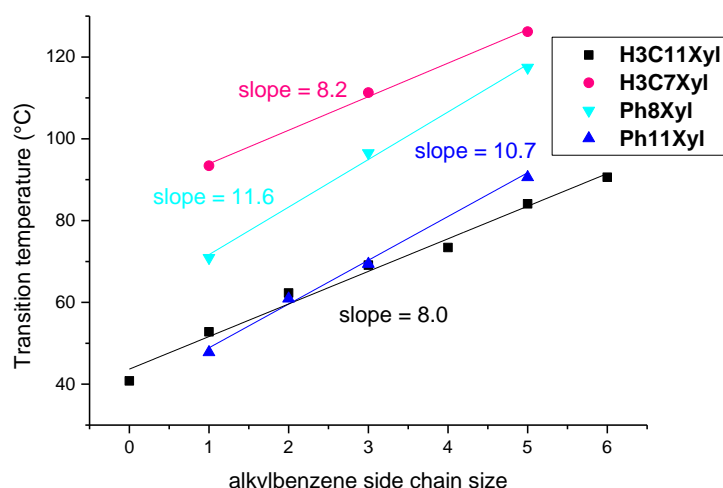


Figure 117 : Transition temperature of some bis-ureas in linear monoalkylbenzene vs the size of the solvent (10 mM measured by nDSC)

The first interesting observation (Figure 117) is that two bis-ureas bearing the same interacting moiety (CH_3 or phenyl) but different alkyl chain sizes exhibit different transition temperatures in a solvent but the similar slopes on the plot versus the size of the alkyl side chain of the solvent. This observation corroborates our previous analysis. Therefore, this system could be interesting to measure solvation energies but the main issue is to be able to extract such an energy because what we measure is actually a difference of solvation. Moreover, this solvation effect does not involve $\text{Br}\cdots\text{Br}$ interactions, which is why we did not continue in this direction.

However, the combination of this observation and the discovery that these compounds are also soluble in halogenoalkanes (see Table 12) lead us to measure the influence of the solvent alkyl chain size of linear 1-halogenoalkanes on the transition temperatures measured. Our thinking was that even if what we measure are solvation energies, those have a great chance to come from $\text{X}\cdots\text{X}$ interactions.

3. Detailed study of Br3C11Xyl in halogenated alkanes

As we did in toluene, the **Br3C11Xyl/H3C11Xyl** system was characterized in Cl-hexane using IR spectroscopy and nDSC (Figure 118 and Figure 119). Circular dichroism (CD) spectroscopy experiments were performed in Cl-decane because it absorbs less in UV than Cl-hexane and should exhibit similar properties (Figure 118). SANS was not performed in Cl-hexane as deuterated Cl-hexane is highly expensive.

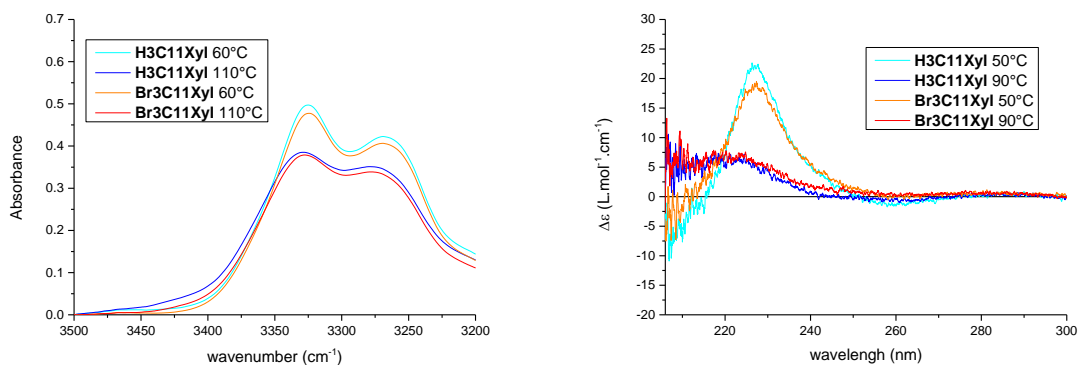


Figure 118 : Infra-red (left) and CD (right) spectra of **Br3C11Xyl** and **H3C11Xyl** below and above the transition (IR at 10 mM in Cl-hexane and CD at 1 mM in Cl-decane)

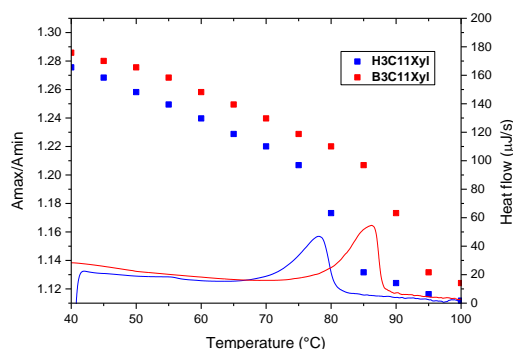


Figure 119 : nDSC thermogram and A_{\max}/A_{\min} ($A_{3325\text{cm}^{-1}}/A_{3295\text{cm}^{-1}}$) measured by FTIR of **Br3C11Xyl** and **H3C11Xyl** at 10 mM in Cl-hexane

Both molecules provide similar results (Figure 118) and as CD spectroscopy is highly sensitive to changes in the assembly, these results show they share highly similar structures both below and above the transition. A difference of around 10°C in the transition temperature is observed between the two compounds (Figure 119). The issue we now have to resolve is the origin of this difference.

4. Solvation versus interaction

Even though we changed the solvent, the same issue remains: how to know where this difference of transition temperature comes from. Is it due to interactions within the assembly, to a difference of solvation between the CBr_3 and CH_3 moieties or a combination of both?

To be able to detect if there are interactions within the assembly or not, we had the idea to mix the brominated and non-brominated ureas in different ratios and to measure the change in transition temperature. We postulated that if this difference of transition temperature was due to solvation we would have a linear evolution of the transition temperature with the composition whereas if there were interactions within the assembly we should observe a deviation from linearity. To confirm our idea and to be able to extract quantitative data, we proposed a simple model.

a. Model

To simplify the notations, we will name D the double filament, S the single filament, **H** the **H3C11Xyl** bis-urea and **B** the **Br3C11Xyl** bis-urea.

With pure **H**, we have an equilibrium $D_H \leftrightarrow 2 S_H$ at the transition temperature T_H .

With pure **B**, we have an equilibrium $D_B \leftrightarrow 2 S_B$ at the transition temperature T_B .

Thus in both cases $\Delta G = 2G(S) - G(D)$

We can postulate that the free energy of the filament and double filament are respectively $G(S) = G_{intra}(S) + G_{solv}(S)$ and $G(D) = 2G_{intra}(S) + G_{inter} + G_{solv}(D)$ with $G_{intra}(S)$ corresponding to interactions within the filament, G_{inter} the interactions between the two filaments in a double filament and G_{solv} the interactions with the solvent.

We assume G_{intra} as identical in both assemblies.

Thus $\Delta G = \Delta G_{solv} - G_{inter}$ with $\Delta G_{solv} = 2G_{solv}(S) - G_{solv}(D)$

If we now mix **H** and **B** molecules with x the proportion of **B** (and thus $1-x$ the proportion of **H**) then the free energy difference between the filament and double filament is:

$$\Delta G(x) = \Delta G_{solv}(x) - G_{inter}(x)$$

Finally, if we take the composition $x=0$ as a reference, we can define:

$$\Delta \Delta G(x) = \Delta \Delta G_{solv}(x) - \Delta G_{inter}(x)$$

with

$$\Delta \Delta G_{solv}(x) = \Delta G_{solv}(x) - \Delta G_{solv}(H)$$

$$\Delta G_{solv}(x) = x\Delta G_{solv}(B) + (1-x)\Delta G_{solv}(H)$$

$$\Delta \Delta G_{solv}(x) = x(\Delta G_{solv}(B) - \Delta G_{solv}(H)) = x\Delta \Delta G_{solv}$$

and

$$\Delta G_{inter}(x) = G_{inter}(x) - G_{inter}(H)$$

$$G_{inter}(x) = x^2 G_{BB} + x(1-x)G_{BH} + (1-x)xG_{BH} + (1-x)^2 G_{HH}$$

$$G_{inter}(H) = G_{HH}$$

$$\Delta G_{inter}(x) = x^2(G_{BB} - 2G_{BH} + G_{HH}) - 2x(G_{HH} - G_{BH})$$

G_{BB} is the free energy of interaction between two CBr_3 groups i.e. a **Br...Br interaction**

G_{BH} is the free energy of interaction between a CH_3 group and a CBr_3 group i.e. an **HB**

G_{HH} is the free energy of interaction between two CH_3 groups i.e. a **London interaction**

Combining these equations yields:

$$\Delta \Delta G(x) = x(\Delta \Delta G_{solv} + 2(G_{HH} - G_{BH})) - x^2(G_{BB} - 2G_{BH} + G_{HH})$$

Usually, London interactions are far weaker than HB and $X \cdots X$ interactions as they do not originate from electrostatics thus we can simplify our equation:

$$\Delta \Delta G(x) \approx x(\Delta \Delta G_{solv} - 2G_{BH}) - x^2(G_{BB} - 2G_{BH})$$

A simple fit of our experimental data would therefore provide us the value of each term (linear and quadratic) but we would still have a system with two equations and three unknown parameters ($\Delta \Delta G_{solv}$, G_{BB} and G_{BH}).

Thus we present two limiting cases, the validity of which will be discussed later when confronted with actual data.

In a case where solvation differences overcome intra-assembly interactions:

$$\Delta\Delta G(\mathbf{x}) \approx \mathbf{x}\Delta\Delta G_{solv}$$

A linear relationship is thus expected.

On the other hand if the intra-assembly interactions dominate the change in solvation then:

$$\Delta\Delta G(\mathbf{x}) \approx -2G_{BH}\mathbf{x} - (G_{BB} - 2G_{BH})\mathbf{x}^2$$

Using the supramolecular balance principle^[70], we can link the variation of the transition temperature (T** noted here T(x)) to the free energy difference.

$$\Delta\Delta G(\mathbf{x}) = \Delta H \frac{T(\mathbf{x}) - T_H}{T_H}$$

Where T_H and ΔH are respectively the temperature and the enthalpy of the transition for the **H** bis-urea. Then:

$$\begin{aligned} T(\mathbf{x}) &= T_H \left(1 + \frac{\Delta\Delta G(\mathbf{x})}{\Delta H}\right) \\ T(\mathbf{x}) &= T_H \left(1 + \frac{\mathbf{x}(\Delta\Delta G_{solv} - 2G_{BH}) - \mathbf{x}^2(G_{BB} - 2G_{BH})}{\Delta H}\right) \end{aligned} \quad (1)$$

In the first limiting case:

$$T(\mathbf{x}) \approx T_H \left(1 + \frac{\mathbf{x}\Delta\Delta G_{solv}}{\Delta H}\right) \quad (2)$$

In the second limiting case:

$$T(\mathbf{x}) \approx T_H \left(1 + \frac{-2G_{BH}\mathbf{x} - (G_{BB} - 2G_{BH})\mathbf{x}^2}{\Delta H}\right) \quad (3)$$

b. The example of toluene

We first confronted our model with the results we obtained in toluene (Figure 120).

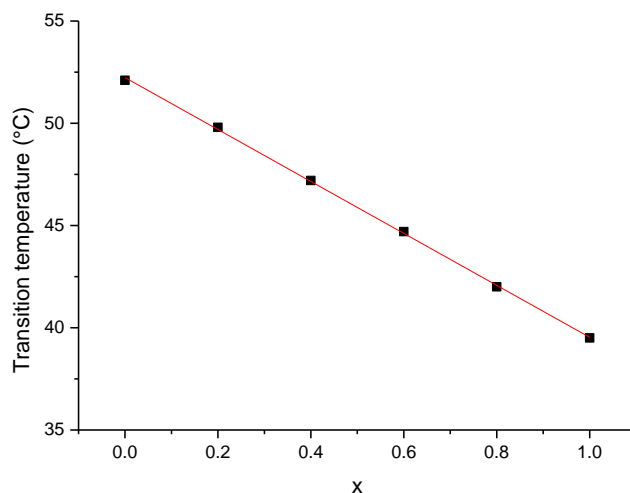


Figure 120 : Evolution of the transition temperature (measured by nDSC) upon mixing **B** (Br3C11Xyl) and **H** (H3C11Xyl) at 10 mM in toluene ($x=0$ is pure **H** and $x=1$ is pure **B**). The full line represents the best fit with equation 2. $\Delta H = 5.66$ kJ/mol was measured by nDSC

We obtained a linear relationship. Mathematically, the linearity of the curve (equation 1) can be explained either by $G_{BB} = 2 G_{BH}$ which would be highly improbable or $G_{BB}, G_{BH} \ll \Delta\Delta G_{solv}$ which is more likely. This situation corresponds to the first limiting case of our model (equation 2) and the fit gave us a $\Delta\Delta G_{solv}$ of -220 J/mol. This value of $\Delta\Delta G_{solv}$ corresponds to a difference of a difference of solvation and is thus difficult to visualize.

$$\Delta\Delta G_{solv} = \Delta G_{solv}(B) - \Delta G_{solv}(H) = (2G_{solv}(S_B) - G_{solv}(D_B)) - (2G_{solv}(S_H) - G_{solv}(D_H))$$

An attempt to understand its signification can be made by assuming, for each molecule, $G_{solv}(S) \approx G_{solv}(D) \approx G_{solv}$, because both objects (single or double filament) have roughly the same interfacial area. Then:

$$\Delta\Delta G_{solv} \approx G_{solv}(B) - G_{solv}(H)$$

The negative value of $\Delta\Delta G_{solv}$ would indicate that **B** is more solvated in toluene than **H** which confirms the results previously obtained in alkylbenzenes (Figure 115).

These results confirmed that toluene is too competitive and thus we performed the same experiments in a less-competing but still solubilizing solvent: chlorohexane.

5. Analysis of the data in halogenated alkanes

To test the consistency of this approach, we also synthesized **Cl3C11Xyl** (**C**) (Figure 121) to measure the interaction energy between two CCl_3 groups and performed the same experiments on **B** and **C**.

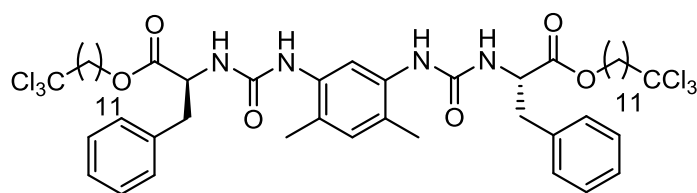


Figure 121 : Structure of **Cl3C11Xyl (C)**

a. The influence of the size of the solvent alkyl chain

As we did before in alkylbenzene, we wanted first to have a look on the influence of the size of the alkyl chain of the solvent and thus measured the transition temperature of **H**, **B** and **C** in different halogenoalkanes.

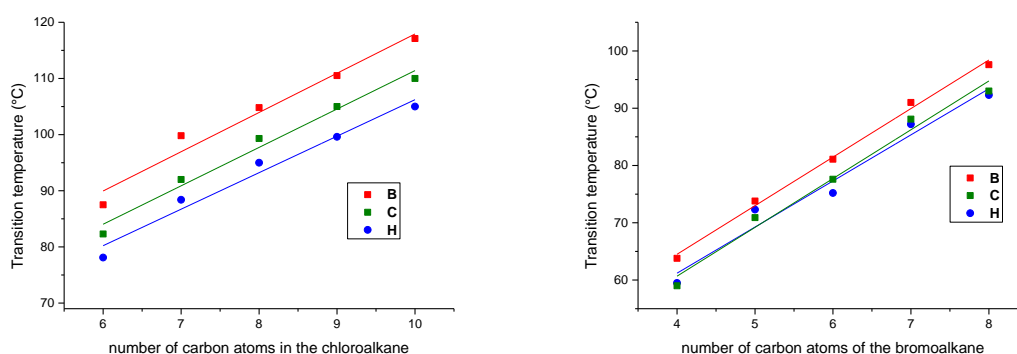


Figure 122 : Evolution of the transition temperature (measured by nDSC) of **B (Br3C11Xyl)**, **C (Cl3C11Xyl)** and **H (H3C11Xyl)** at 10mM in chloroalkanes (left) and bromoalkanes (right) vs the number of carbon atoms of the solvent

In chloroalkanes, we observed a quasi linear evolution of the transition temperature with the size of the alkyl chain and even more interestingly we observed that ΔT is independent of the solvent for both **B** and **C**, thus showing a constant influence of the solvent (Figure 122 left).

In bromoalkanes (Figure 122 right), we observed the same situation except that ΔT is close to zero in the case of **C**. Qualitatively, these results show that CBr_3 groups affect the stability of the assemblies more than CCl_3 , which is in line with an expected stronger $\text{Br}\cdots\text{Br}$ than $\text{Cl}\cdots\text{Cl}$ interaction. Moreover, the effect is less intense in bromoalkanes, which are expected to compete more than chloroalkanes for the formation of halogen bonds.

Interestingly, the transition temperature of **H** has a similar value in bromo and chloroalkanes bearing the same number of carbons (Figure 123). As this temperature is directly correlated to the solvating properties of the solvent, we can assume that bromo and chloroalkanes have a similar polarity and thus have an almost identical influence on the hydrogen bonded network. Therefore, the results show that CH_3 groups are solvated the same way in bromoalkanes and chloroalkanes.

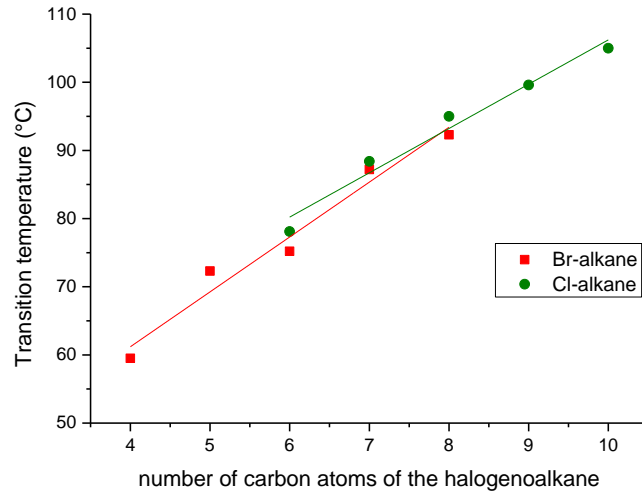


Figure 123 : Evolution of the transition temperature (measured by nDSC) of **H3C11Xyl** at 10mM in halogenoalkanes vs the number of carbon atoms of the solvent

The data of Figure 122 can be further exploited using the model presented above. Indeed, equation 1 reads:

$$T_X(x) = T_H \left(1 + \frac{x(\Delta\Delta G_{solv}(CX_3/CH_3) - 2G_{XH}) - x^2(G_{XX} - 2G_{XH})}{\Delta H} \right)$$

For any mixtures of composition x. Thus, for x=1

$$T_X = T_H \left(1 + \frac{\Delta\Delta G_{solv}(CX_3/CH_3) - G_{XX}}{\Delta H} \right)$$

or

$$G_{XX} - \Delta\Delta G_{solv}\left(\frac{CX_3}{CH_3}\right) = -\Delta H \left(\frac{T_X - T_H}{T_H} \right)$$

which can be written as

$$G_{XX} - \Delta\Delta G_{solv}(CX_3) + \Delta\Delta G_{solv}(CH_3) = -\Delta H \left(\frac{T_X - T_H}{T_H} \right)$$

The term $G_{XX} - \Delta\Delta G_{solv}(CX_3)$ is in fact the free energy of the $X \cdots X$ interaction in the solvent of the experiment, i.e. the free energy of the $X \cdots X$ interaction corrected by the desolvation of the CX_3 groups, that we note $G_{XX}^{solvent}$.

$\Delta\Delta G_{solv}(CH_3)$ is the difference in solvation of the CH_3 group in the double filament and filament structures. It has the same value in chloro and bromoheptane (Figure 123) and it involves only weak interactions between the CH_3 group and the solvent. If we assume that that term is negligible, then:

$$G_{XX}^{solvent} \approx -\Delta H \left(\frac{T_X - T_H}{T_H} \right)$$

Therefore, the data of Figure 122 can be processed to evaluate $G_{XX}^{solvent}$ for both CBr_3 and CCl_3 groups in all the solvents (Figure 124).

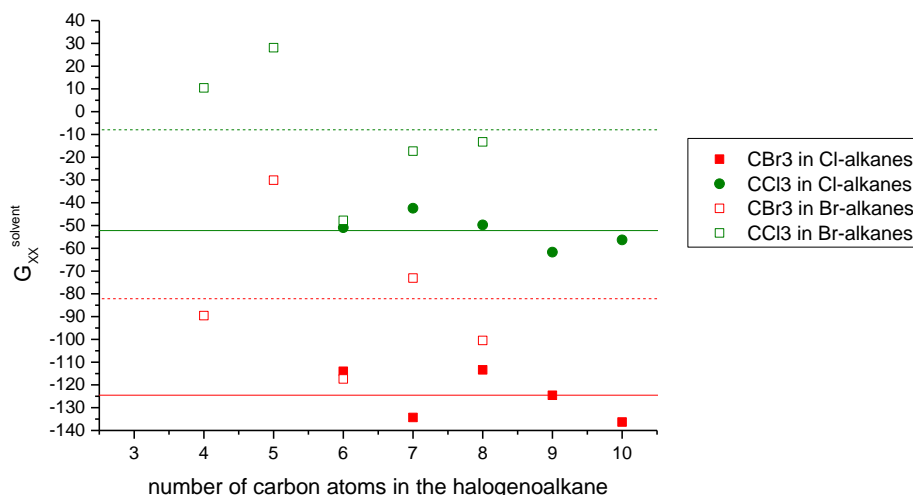


Figure 124 : Evolution of $G_{XX}^{solvent}$ at 10mM in halogenoalkanes vs the number of carbon atoms of the solvent

The values of $G_{XX}^{solvent}$ are approximately constant for each system when the size of the solvent is changed, so that we can take the average value in chloroalkanes and in bromoalkanes. The values are reported in Table 14.

$G_{CBr3-CBr3}^{chloroalkane}$	$G_{CCl3-CCl3}^{chloroalkane}$	$G_{CBr3-CBr3}^{bromoalkane}$	$G_{CCl3-CCl3}^{bromoalkane}$
$-125 \pm 10 \text{ J/mol}$	$-52 \pm 10 \text{ J/mol}$	$-82 \pm 40 \text{ J/mol}$	$-8 \pm 40 \text{ J/mol}$

Table 14: Values of $G_{XX}^{solvent}$ deduced from Figure 124

In order to further test this analysis, we characterized mixtures of bis-ureas.

b. Mixtures of bis-ureas in chlorohexane

We confronted our model with the results we obtained in chlorohexane (Figure 125 and Figure 126). Both mixtures (H/B and H/C) display a non-linear variation of the transition temperature versus the composition. Fitting the data with equation 1 yields values for $\Delta\Delta G_{solv}(\frac{CX_3}{CH_3}) - 2G_{XH}$ and $G_{XX} - 2G_{XH}$. With the same approach as before, these values can be used to get approximate values of $G_{XX}^{solvent}$ and of the free energy of the $X \cdots H$ interaction corrected by the desolvation $G_{XH}^{solvent}$. Indeed:

$$\Delta\Delta G_{solv}\left(\frac{CX_3}{CH_3}\right) - 2G_{XH} \approx -2G_{XH}^{solvent}$$

and

$$G_{XX} - 2G_{XH} \approx G_{XX}^{solvent} - 2G_{XH}^{solvent}$$

(we again neglect the term $\Delta G_{solv}(CH_3)$).

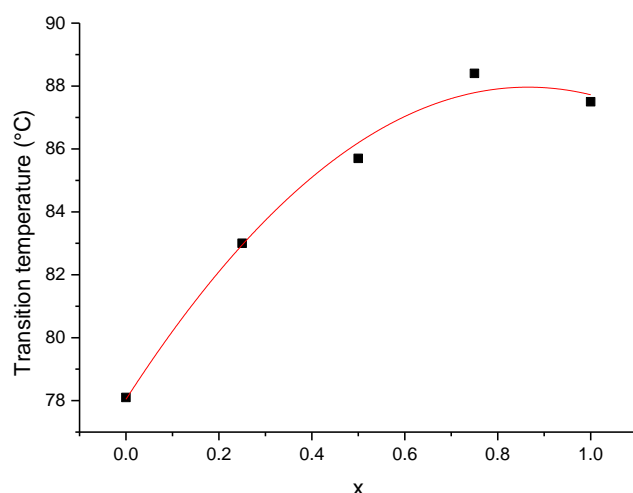


Figure 125 : Evolution of the transition temperature (measured by nDSC) upon mixing **B (Br3C11Xyl)** and **H (H3C11Xyl)** at 10 mM in Cl-hexane ($x=0$ is pure **H** and $x=1$ is pure **B**). The full line represents the best fit with equation 1 yielding $\Delta\Delta G_{\text{solv}} - 2 G_{\text{BH}} = 276 \text{ J/mol}$ and $G_{\text{BB}} - 2 G_{\text{BH}} = 159 \text{ J/mol}$. $\Delta H = 4.26 \text{ kJ/mol}$ was measured by nDSC.

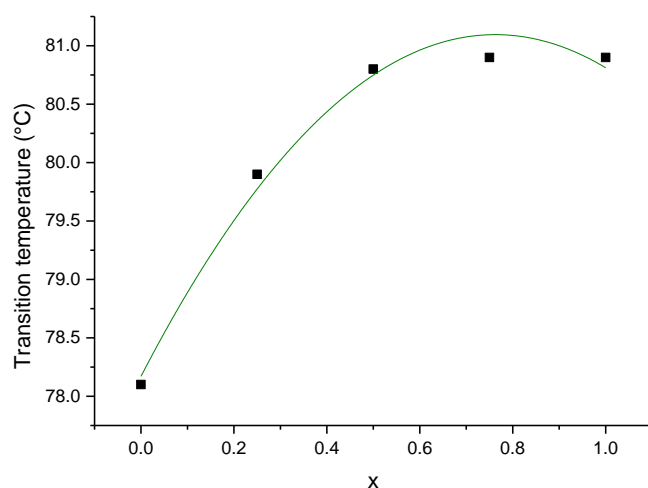


Figure 126 : Evolution of the transition temperature (measured by nDSC) upon mixing **C (CCl311Xyl)** and **H (CH311Xyl)** at 10 mM in Cl-hexane ($x=0$ is pure **H** and $x=1$ is pure **C**). The full line represents the best fit with equation 1 yielding $\Delta\Delta G_{\text{solv}} - 2 G_{\text{CH}} = 96 \text{ J/mol}$ and $G_{\text{CC}} - 2 G_{\text{BC}} = 63 \text{ J/mol}$. $\Delta H = 4.26 \text{ kJ/mol}$ measured by nDSC.

$G_{\text{CBr3-CBr3}}^{\text{chlorohexane}}$	$G_{\text{CCl3-CCl3}}^{\text{chlorohexane}}$	$G_{\text{CBr3-CBr3}}^{\text{bromoheptane}}$
$-117 \pm 8 \text{ J/mol}$	$-33 \pm 5 \text{ J/mol}$	$-58 \pm 3 \text{ J/mol}$
$G_{\text{CBr3-CH3}}^{\text{chlorohexane}}$	$G_{\text{CCl3-CH3}}^{\text{chlorohexane}}$	$G_{\text{CBr3-CH3}}^{\text{bromoheptane}}$
$-138 \pm 12 \text{ J/mol}$	$-48 \pm 6 \text{ J/mol}$	$-29 \pm 3 \text{ J/mol}$

Table 15: Values of $G_{\text{XX}}^{\text{solvent}}$ deduced from Figure 125, 126 and 129

The results are summarized in Table 15. The values obtained for $G_{\text{XX}}^{\text{solvent}}$ through this approach are very similar to the values obtained above by the analysis in a range of similar solvent. This is not completely surprising as the data for $x=1$ in chlorohexane is common to both data sets, but is nevertheless an indication of the coherence of the approaches. Moreover, the analysis of the

mixtures of bis-ureas also yields the values for $G_{XH}^{solvent}$ (Table 15) that prove to be of the same order of magnitude as $G_{XX}^{solvent}$.

As a blank experiment, and to confirm that the non-linearity of the curves in Figure 125 and Figure 126 is directly related to the presence of the CBr_3 and CCl_3 moieties, we mixed two bis-ureas **H3C15Xyl** (**H'**) and **H3C11Xyl** (**H**) (Figure 127) in Cl-hexane to observe the variation of the transition temperature with the composition (Figure 128).

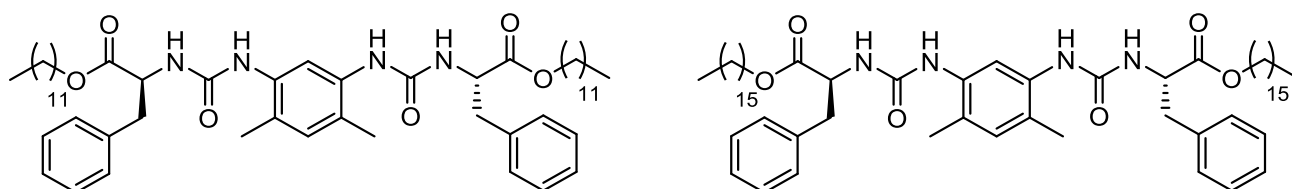


Figure 127 : Structure of **H3C11Xyl** (**H**) and **H3C15Xyl** (**H'**)

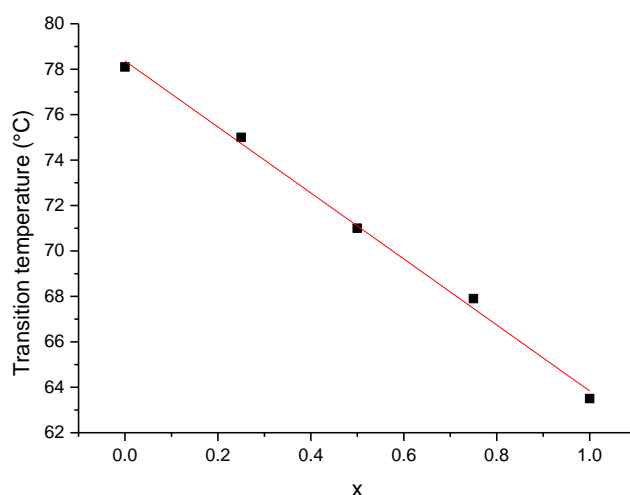


Figure 128 : Evolution of the transition temperature (measured by nDSC) upon mixing **H'** (**H3C15Xyl**) and **H** (**H3C11Xyl**) at 10mM in Cl-hexane ($x=0$ is pure **H** and $x=1$ is pure **H'**). The full line represents the best fit with equation 2. $\Delta H = 4.26$ kJ/mol measured by nDSC.

The linearity of the variation shows that only solvation accounted for this difference of transition temperature thus confirming our previous hypothesis that London interactions are negligible in those systems and that the non-linearity observed in Figure 125 is due to the CBr_3 moiety. The fit yields a $\Delta\Delta G_{\text{solv}}$ of -172 J/mol.

c. Mixtures of bis-ureas in bromoheptane

We also mixed **B** and **H** in different proportions in the more competitive solvent Br-heptane and measured the variation of the transition temperature (Figure 129).

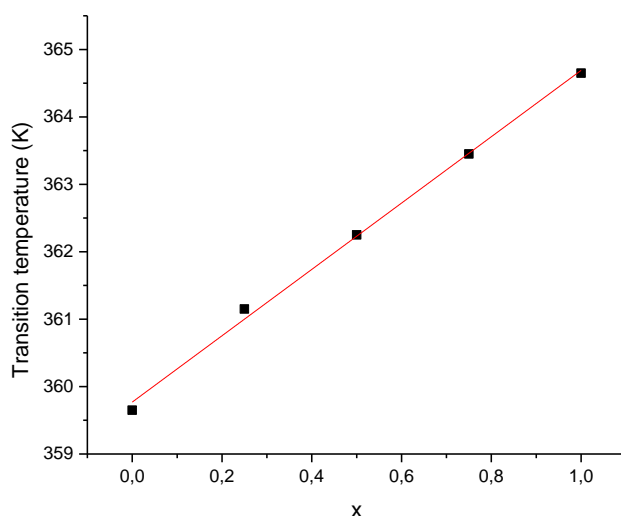


Figure 129 : Evolution of the transition temperature (measured by nDSC) upon mixing **B** (**Br3C11Xyl**) and **H** (**H3C11Xyl**) at 10 mM in Br-heptane ($x=0$ is pure **H** and $x=1$ is pure **B**). The full line represents the best fit with equation 1 yielding $\Delta\Delta G_{\text{solv}} - 2 G_{\text{BH}} = 58 \text{ J/mol}$ and $G_{\text{BB}} - 2 G_{\text{BH}} = 0 \text{ J/mol}$. $\Delta H = 6.93 \text{ kJ/mol}$ measured by nDSC.

In this case, a linear variation is obtained which makes the interpretation ambiguous. The first interpretation would be that solvation effects overcome intra-assembly interactions. However, this interpretation is in disagreement with the fact that parallel lines are obtained for **B** and **H** in bromoalkanes (Figure 122).

Therefore, this leaves us with the second interpretation that $G_{\text{BB}} - 2 G_{\text{BH}} = 0$. The result of the fit with equation 1 is summarized in Table 15.

To conclude, we were able to detect and measure $\text{Br}\cdots\text{Br}$, $\text{Cl}\cdots\text{Cl}$, $\text{Br}\cdots\text{H}$ and $\text{Cl}\cdots\text{H}$ interactions in halogenoalkanes. Of course, our model is far from perfect because:

(i) We are not certain of how the assembly behaves in terms of interactions and of solvation in both the double and single filament. This means that the measured values are lower estimates for these interactions. Indeed, if not all CBr_3 are involved in a $\text{Br}\cdots\text{Br}$ interaction in the double filament, then the measured values are in fact the average between the bonded and free CBr_3 moieties;

(ii) We are not sure that the interactions within a filament are identical in both the double and single filament;

And (iii) our model may be too simplistic as both HB and $\text{X}\cdots\text{X}$ interactions can cooperate within the assembly and have an impact on each other values.

Nevertheless we are confident that the non-linearity of the transition temperature observed upon changing the proportion of **B** in a mix of **H** and **B** is a clear sign of the existence of $\text{X}\cdots\text{X}$ interactions in Cl-hexane and is thus the first observation of $\text{X}\cdots\text{X}$ interactions in solution.

Future modeling experiments will take place in order to investigate the type and geometries of the possible interactions in both the double and single filament to design a better model and to be able to obtain more precise values.

C. Appendix

1. FTIR analyses

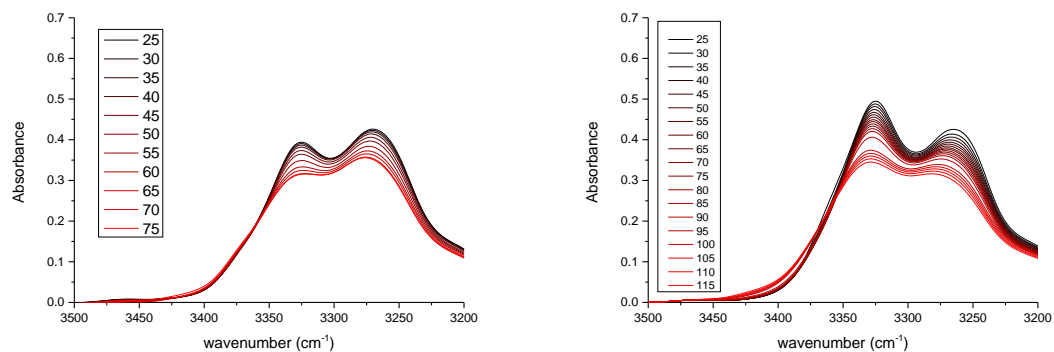


Figure 130 : IR of **H3C11Xyl** at 10mM in toluene and pentylbenzene (from left to right)

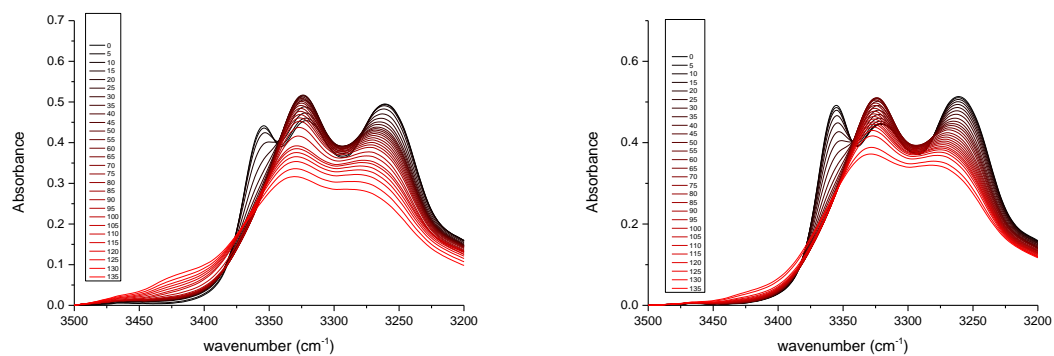


Figure 131 : IR of **H3C11Xyl** at 10mM in chlorohexane and chlorodecane (from left to right)

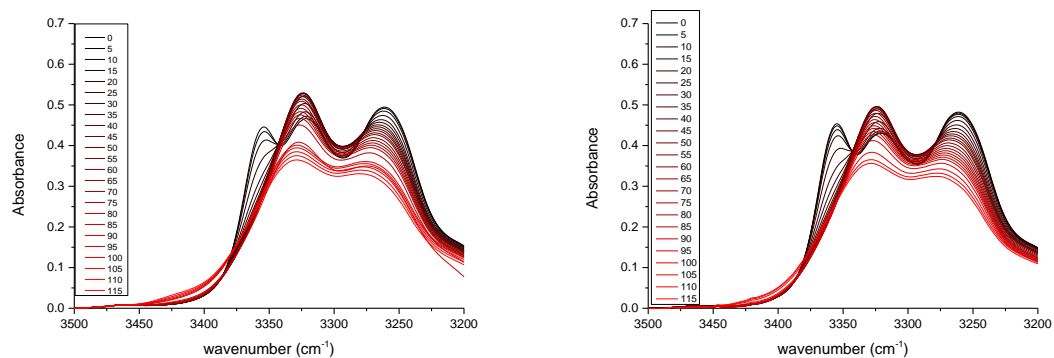


Figure 132 : IR of **H3C11Xyl** at 10mM in bromopentane and bromoheptane (from left to right)

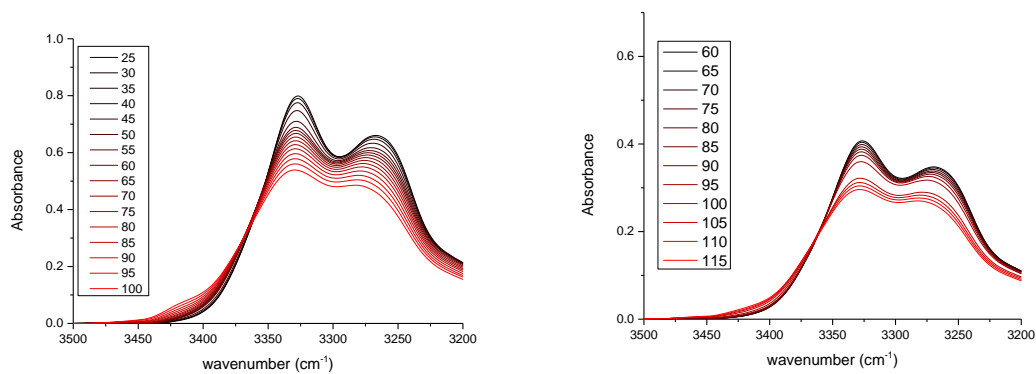


Figure 133 : IR of **Br3C11Xyl** at 10mM in toluene and pentylbenzene (from left to right)

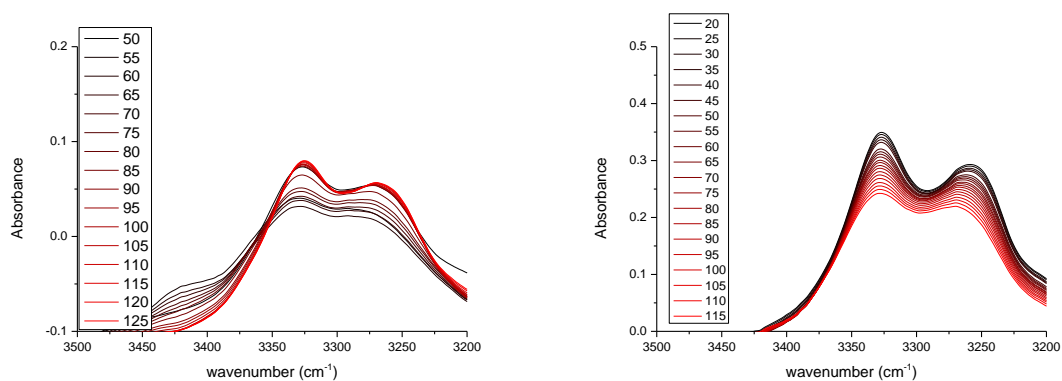


Figure 134 : IR of **Br3C11Xyl** at 10mM in chlorohexane and chlorodecane (from left to right)

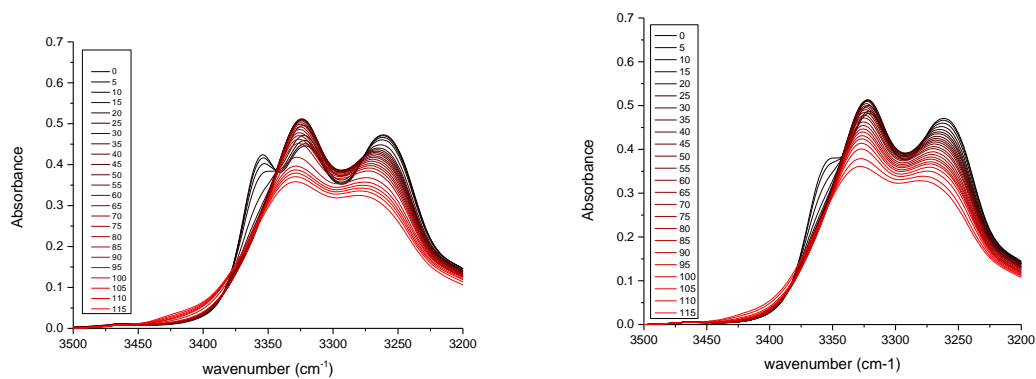


Figure 135 : IR of **Br3C11Xyl** at 10mM in bromopentane and bromoheptane (from left to right)

2. nDSC analyses

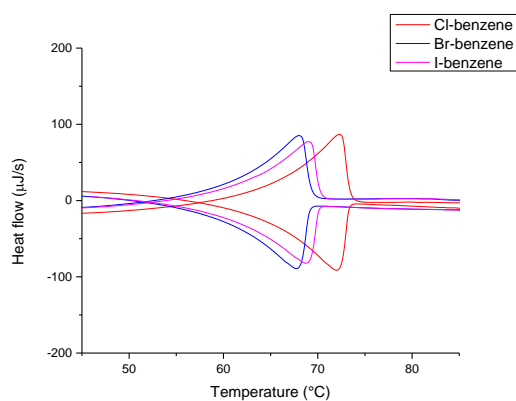


Figure 136 : nDSC traces of **BrPh6Cl** at 10 mM in X-benzene

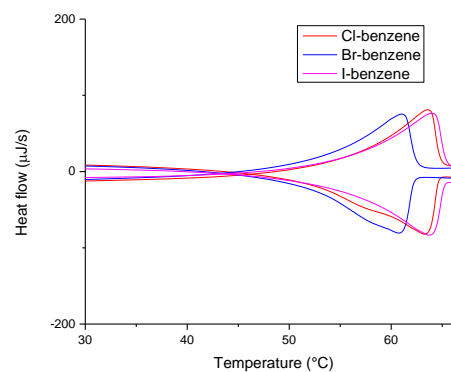


Figure 139: nDSC traces of **Ph11Cl** at 10 mM in X-benzene

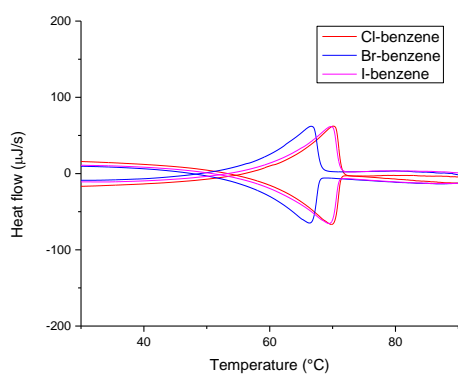


Figure 137: nDSC traces of **Ph6Cl** at 10 mM in X-benzene

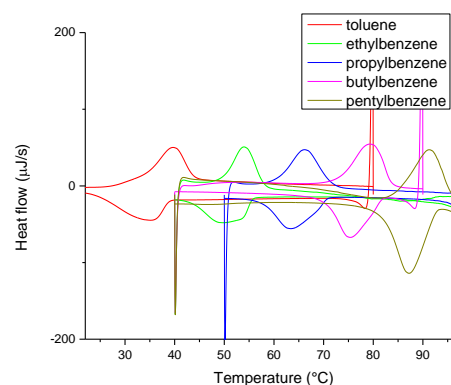


Figure 140: nDSC traces of **Br3C11Xyl** at 10 mM in alkylbenzene

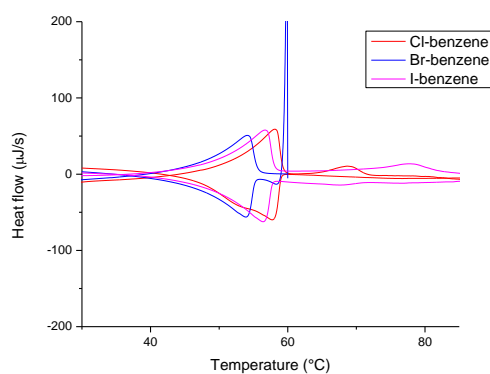


Figure 138: nDSC traces of **BrPh11Cl** at 10 mM in X-benzene

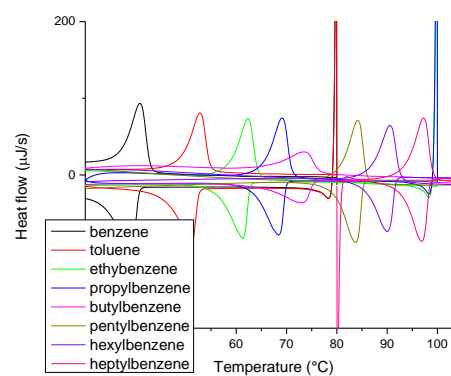


Figure 141: nDSC traces of **H3C11Xyl** at 10 mM in alkylbenzene

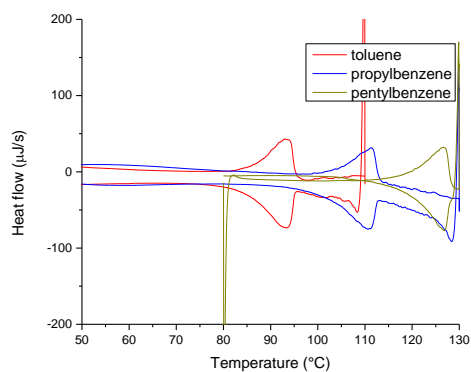


Figure 142: nDSC traces of **H3C7Xyl** at 10 mM in alkylbenzene

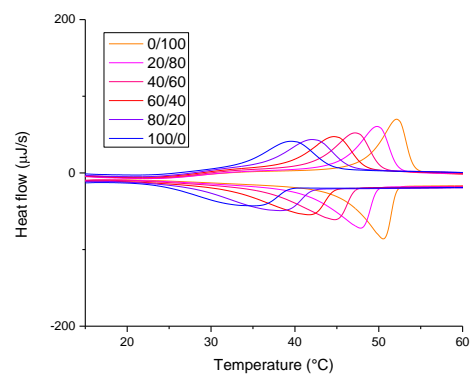


Figure 145: nDSC traces of mixes of **Br3C11Xyl/H3C11Xyl** at 10 mM in toluene

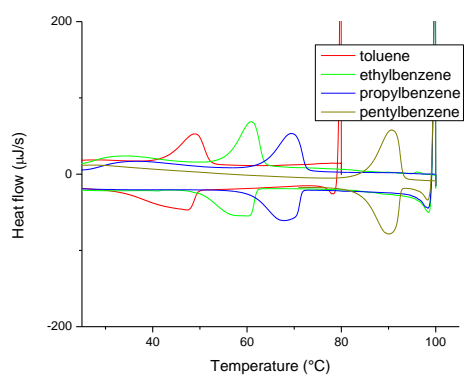


Figure 143: nDSC traces of **Ph11Xyl** at 10 mM in alkylbenzene

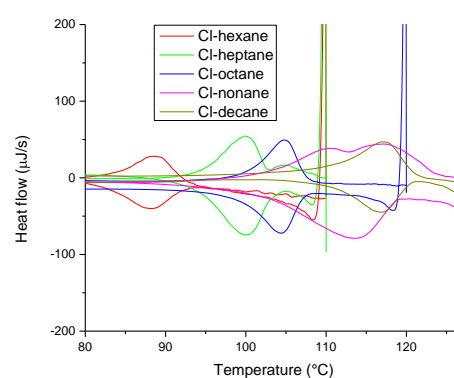


Figure 146 : nDSC traces of **Br3C11Xyl** at 10 mM in Cl-alkanes

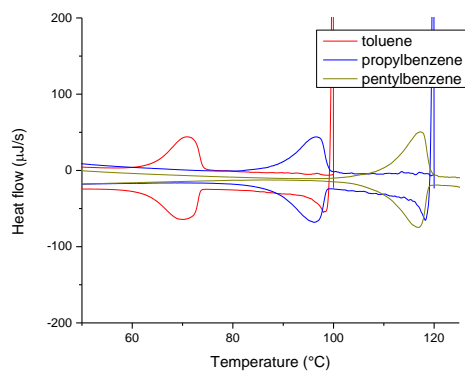


Figure 144: nDSC traces of **Ph8Xyl** at 10 mM in alkylbenzene

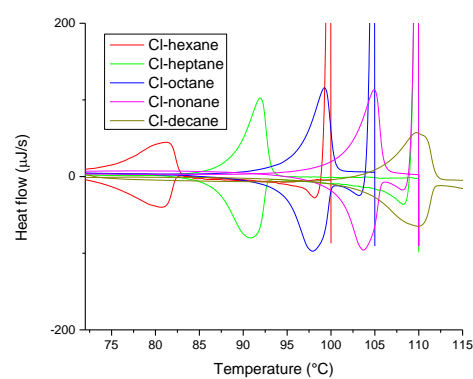


Figure 147 : nDSC traces of **Cl3C11Xyl** at 10 mM in Cl-alkanes

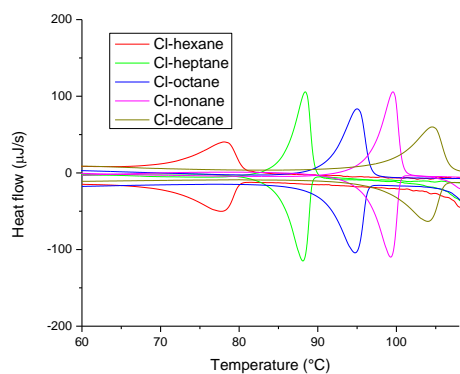


Figure 148 : nDSC traces of **H3C11Xyl** at 10 mM in Cl-alkanes

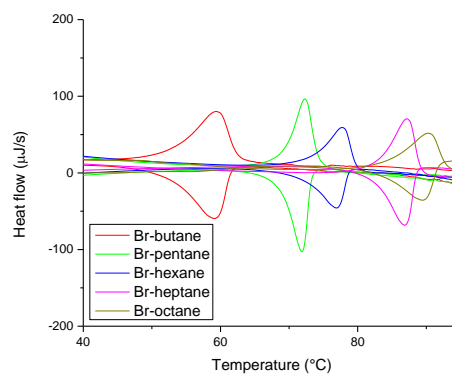


Figure 151 : nDSC traces of **H3C11Xyl** at 10 mM in Br-alkanes

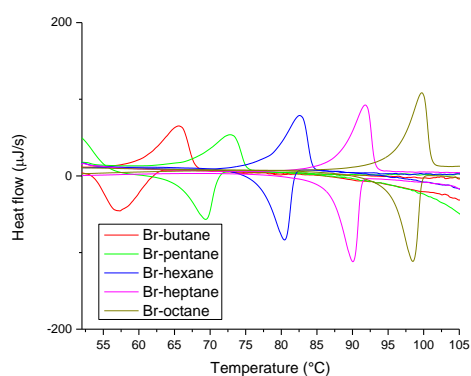


Figure 149 : nDSC traces of **Br3C11Xyl** at 10 mM in Br-alkanes

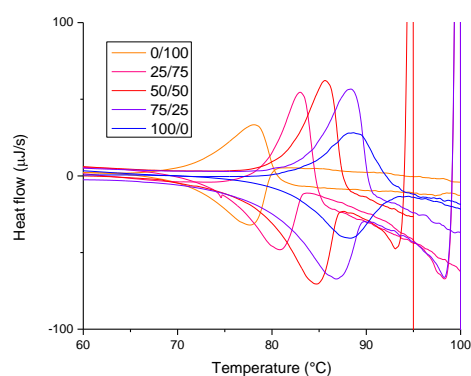


Figure 152 : nDSC traces of mixes of **Br3C11Xyl/H3C11Xyl** at 10 mM in Cl-hexane

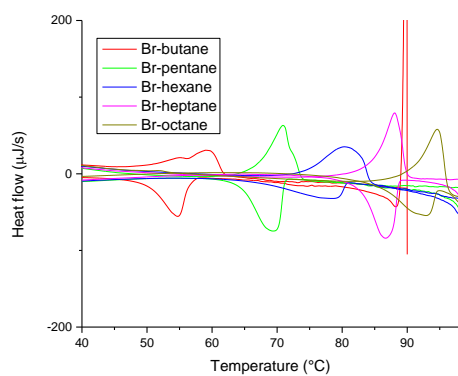


Figure 150 : nDSC traces of **Cl3C11Xyl** at 10 mM in Br-alkanes

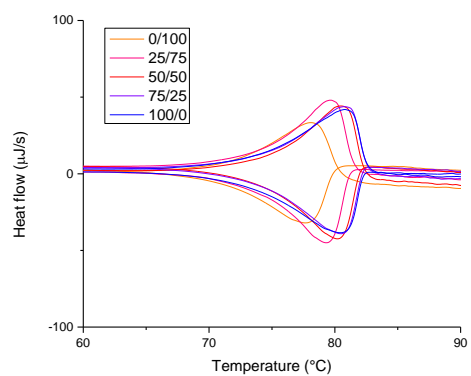


Figure 153 : nDSC traces of mixes of **Cl3C11Xyl/H3C11Xyl** at 10 mM in Cl-hexane

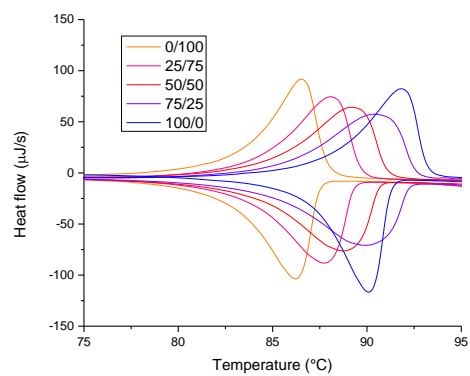


Figure 154 : nDSC traces of mixes of Br₃C11Xyl/H3C11Xyl at 10 mM in Br-heptane

- [1] K. Nakamoto, M. Margoshes, R. E. Rundle, *J. Am. Chem. Soc.* **1955**, *77*, 6480–6486.
- [2] P. Politzer, J. S. Murray, T. Clark, *Phys. Chem. Chem. Phys.* **2010**, *12*, 7748–7757.
- [3] G. R. Desiraju, P. S. Ho, L. Kloo, A. C. Legon, R. Marquardt, P. Metrangolo, P. Politzer, G. Resnati, K. Rissanen, *Pure Appl. Chem.* **2013**, *85*, 1711–1713.
- [4] M. M. Colin, *Ann. Chim.* **1814**, *91*, 252–272.
- [5] F. Guthrie, *J. Chem. Soc.* **1863**, *16*, 239–244.
- [6] R. S. Mulliken, *J. Am. Chem. Soc.* **1950**, *72*, 600–608.
- [7] T. Dahl, O. Hassel, I. J. Seppälä, K. Hedberg, K. Schaumburg, L. Ehrenberg, *Acta Chem. Scand.* **1971**, *25*, 2168–2174.
- [8] P. Pelletier, J. Caventou, *Ann. Chim. Phys.* **1819**, *10*, 142–177.
- [9] O. Rhoussopoulos, *Ber. Dtsch. Chem. Ges.* **1883**, *16*, 202–203.
- [10] I. Remsen, J. F. Norris, *J. Am. Chem. J.* **1896**, *18*, 90–95.
- [11] A. C. Legon, *Angew. Chem. Int. Ed.* **1999**, *38*, 2686–2714.
- [12] O. Hassel, K. O. Strømme, H. Haraldsen, A. Grönvall, B. Zaar, E. Diczfalussy, *Acta Chem. Scand.* **1958**, *12*, 1146–1146.
- [13] O. Hassel, K. O. Strømme, E. Hammarsten, C.-G. Hedén, B. Malmgren, H. Palmstierna, *Acta Chem. Scand.* **1959**, *13*, 1781–1786.
- [14] S. V. Rosokha, J. K. Kochi, in *Halogen Bonding*, Springer Berlin Heidelberg, **2007**, pp. 137–160.
- [15] H. A. Bent, *Chem. Rev.* **1968**, *68*, 587–648.
- [16] N. Ramasubbu, R. Parthasarathy, P. Murray-Rust, *J. Am. Chem. Soc.* **1986**, *108*, 4308–4314.
- [17] J.-M. Dumas, M. Gomel, M. Guerin, in *Halides, Pseudo-Halides Azides Part 2*, John Wiley & Sons, Ltd., Chichester, UK, **1983**, pp. 985–1020.
- [18] T. Brinck, J. S. Murray, P. Politzer, *Int. J. Quantum Chem.* **1992**, *44*, 57–64.
- [19] P. Metrangolo, G. Resnati, *Chem. Eur. J.* **2001**, *7*, 2511–2519.
- [20] P. Metrangolo, H. Neukirch, T. Pilati, G. Resnati, *Acc. Chem. Res.* **2005**, *38*, 386–395.
- [21] R. A. Zingaro, R. M. Hedges, *J. Phys. Chem.* **1961**, *65*, 1132–1138.
- [22] R. Glaser, R. F. Murphy, *CrystEngComm* **2006**, *8*, 948–951.
- [23] M. D. Esrafili, R. Nurazar, F. Mohammadian-Sabet, *Molecular Physics* **2015**, *113*, 3703–3711.
- [24] M. Saccone, G. Cavallo, P. Metrangolo, A. Pace, I. Pibiri, T. Pilati, G. Resnati, G. Terraneo, *CrystEngComm* **2013**, *15*, 3102–3105.
- [25] T. Clark, M. Hennemann, J. S. Murray, P. Politzer, *J. Mol. Model.* **2007**, *13*, 291–296.
- [26] R. Bianchi, A. Forni, T. Pilati, *Acta Cryst.* **2004**, *B60*, 559–568.
- [27] J. P. M. Lommerse, A. J. Stone, R. Taylor, F. H. Allen, *J. Am. Chem. Soc.* **1996**, *118*, 3108–3116.
- [28] G. Cavallo, P. Metrangolo, R. Milani, T. Pilati, A. Priimagi, G. Resnati, G. Terraneo, *Chem. Rev.* **2016**, *116*, 2478–2601.
- [29] P. Metrangolo, J. S. Murray, T. Pilati, P. Politzer, G. Resnati, G. Terraneo, *Cryst. Growth Des.* **2011**, *11*, 4238–4246.
- [30] P. Metrangolo, J. S. Murray, T. Pilati, P. Politzer, G. Resnati, G. Terraneo, *CrystEngComm* **2011**, *13*, 6593–6596.
- [31] C. Präsang, A. C. Whitwood, D. W. Bruce, *Cryst. Growth Des.* **2009**, *9*, 5319–5326.
- [32] K. Raatikainen, M. Cametti, K. Rissanen, *Beilstein J. Org. Chem.* **2010**, *6*, 4–12.
- [33] R. Liantonio, P. Metrangolo, T. Pilati, G. Resnati, A. Stevenazzi, *Cryst. Growth Des.* **2003**, *3*, 799–803.
- [34] K. Xu, D. M. Ho, R. A. Pascal, *J. Am. Chem. Soc.* **1994**, *116*, 105–110.
- [35] M. Müller, M. Albrecht, V. Gossen, T. Peters, A. Hoffmann, G. Raabe, A. Valkonen, K. Rissanen, *Chem. Eur. J.* **2010**, *16*, 12446–12453.
- [36] M. C. Etter, *Acc. Chem. Res.* **1990**, *23*, 120–126.
- [37] L. Russo, S. Biella, M. Lahtinen, R. Liantonio, P. Metrangolo, G. Resnati, K. Rissanen, *CrystEngComm* **2007**, *9*, 341–344.
- [38] A. Bondi, *J. Phys. Chem.* **1964**, *68*, 441–451.
- [39] S. M. Huber, E. Jimenez-Izal, J. M. Ugalde, I. Infante, *Chem. Comm.* **2012**, *48*, 7708–7710.
- [40] S. V. Rosokha, M. K. Vinakos, *Cryst. Growth Des.* **2012**, *12*, 4149–4156.

- [41] P. Politzer, J. S. Murray, T. Clark, in *Halogen Bond. I*, Springer International Publishing, **2014**, pp. 19–42.
- [42] R. Wang, T. S. Dols, C. W. Lehmann, U. Englert, *Zeitschrift für Anorg. und Allg. Chemie* **2013**, 639, 1933–1939.
- [43] R. Wang, T. S. Dols, C. W. Lehmann, U. Englert, *Chem. Comm.* **2012**, 48, 6830–6832.
- [44] M. G. Sarwar, B. Dragisic, L. J. Salsberg, C. Gouliaras, M. S. Taylor, *J. Am. Chem. Soc.* **2010**, 132, 1646–1653.
- [45] E. Cariati, G. Cavallo, A. Forni, G. Leem, P. Metrangolo, F. Meyer, T. Pilati, G. Resnati, S. Righetto, G. Terraneo, et al., *Cryst. Growth Des.* **2011**, 11, 5642–5648.
- [46] J. P.-W. Wong, A. C. Whitwood, D. W. Bruce, *Chem. Eur. J.* **2012**, 18, 16073–16089.
- [47] A. Vanderkooy, M. S. Taylor, *J. Am. Chem. Soc.* **2015**, 137, 5080–5086.
- [48] L. Meazza, J. A. Foster, K. Fücke, P. Metrangolo, G. Resnati, J. W. Steed, *Nature Chem.* **2013**, 5, 42–47.
- [49] M. Llinàs-Brunet, M. D. Bailey, N. Goudreau, P. K. Bhardwaj, J. Bordeleau, M. Bös, Y. Bousquet, M. G. Cordingley, J. Duan, P. Forgione, et al., *J. Med. Chem.* **2010**, 53, 6466–6476.
- [50] S. Schindler, S. M. Huber, in *Halogen Bond. II*, Springer International Publishing, **2014**, pp. 167–203.
- [51] T. Caronna, R. Liantonio, T. A. Logothetis, P. Metrangolo, T. Pilati, G. Resnati, *J. Am. Chem. Soc.* **2004**, 126, 4500–4501.
- [52] M. G. Sarwar, B. Dragisic, S. Sagoo, M. S. Taylor, *Angew. Chem. Int. Ed.* **2010**, 49, 1674–1677.
- [53] R. L. Collin, *Acta Cryst.* **1952**, 5, 431–432.
- [54] V. G. Tsirelson, P. F. Zhou, T.-H. Tang, R. F. W. Bader, *Acta Cryst.* **1995**, 51, 143–153.
- [55] T. Sakurai, M. Sundaralingam, G. A. Jeffrey, *Acta Cryst.* **1963**, 16, 354–363.
- [56] G. R. Desiraju, R. Parthasarathy, *J. Am. Chem. Soc.* **1989**, 111, 8725–8726.
- [57] A. Mukherjee, S. Tothadi, G. R. Desiraju, *Acc. Chem. Res.* **2014**, 47, 2514–2524.
- [58] F. F. Awwadi, R. D. Willett, K. a Peterson, B. Twamley, *Chem. Eur. J.* **2006**, 12, 8952–8960.
- [59] N. Izumiya, *Bull. Chem. Soc. Jpn.* **1953**, 26, 53–56.
- [60] S. Ghosh, M. K. Mishra, S. B. Kadambi, U. Ramamurty, G. R. Desiraju, *Angew. Chem. Int. Ed.* **2015**, 54, 2674–2678.
- [61] K. E. Riley, J. S. Murray, J. Fanfrlík, J. Řezáč, R. J. Solá, M. C. Concha, F. M. Ramos, P. Politzer, *J. Mol. Model.* **2011**, 17, 3309–3318.
- [62] A. Matsumoto, T. Tanaka, T. Tsubouchi, K. Tashiro, S. Saragai, S. Nakamoto, *J. Am. Chem. Soc.* **2002**, 124, 8891–8902.
- [63] W. Song, N. Martsinovich, W. M. Heckl, M. Lackinger, *Chem. Commun.* **2014**, 50, 13465–13468.
- [64] S. Kawai, A. Sadeghi, F. Xu, L. Peng, A. Orita, J. Otera, S. Goedecker, E. Meyer, *ACS Nano* **2015**, 9, 2574–2583.
- [65] D. Hauchecorne, W. A. Herrebout, *J. Phys. Chem. A* **2013**, 117, 11548–11557.
- [66] C. M. Reddy, M. T. Kirchner, R. C. Gundakaram, K. A. Padmanabhan, G. R. Desiraju, *Chem. Eur. J.* **2006**, 12, 2222–2234.
- [67] M. Dirany, V. Ayzac, B. Isare, M. Raynal, L. Bouteiller, *Langmuir* **2015**, 31, 11443–11451.
- [68] I. Giannicchi, B. Jouvet, B. Isare, M. Linares, A. Dalla Cort, L. Bouteiller, *Chem. Commun.* **2014**, 50, 611–613.
- [69] P. G. Jones, H. Hopf, A. Silaghi, C. Näther, *Acta Cryst.* **2011**, C67, 405–408.
- [70] M. Roman, C. Cannizzo, T. Pinault, B. Isare, B. Andrioletti, P. van der Schoot, L. Bouteiller, *J. Am. Chem. Soc.* **2010**, 132, 16818–16824.
- [71] I. A. Sedov, M. A. Stolov, B. N. Solomonov, *Thermochim. Acta* **2014**, 589, 247–251.

Chapter 5: Characterization and rheological properties of a new type of assembly

Abstract: In this chapter, we present an additional structure exhibited by particular ester bis-ureas. We used FTIR, CD and SANS analyses to determine the nature of this new hydrogen-bonded assembly and probed the influence of the chemical structure of the bis-ureas and of the experimental conditions (concentration, temperature, solvent) on its stability. Interestingly, the transition between this new structure and the double filament one is associated with an increase of viscosity. Those bis-ureas are thus good candidates as thermothickening additives.

During the study of the assembly properties of various ester bis-urea monomers, we observed in some cases the appearance of a third peak in the N-H region of the FTIR spectrum. As this region is particularly sensitive to changes in the HB network, we can assume that it corresponds to a new type of assembly. This chapter focuses on the characterization of this unexpected structure. Also, controlling the formation of this structure allows to tune the rheological properties of bis-urea solutions (see part F).

A. Characterization of the new assembly

We first observed this new assembly in the context of the supramolecular balance with ester bis-ureas bearing a linear alkyl chain or a CBr₃-alkyl chain. Indeed, FTIR analyses of these bis-ureas exhibited an unusual peak around 3354 cm⁻¹ at low temperature in halogenoalkanes.

To characterize this new interaction, we performed variable-temperature FTIR analyses of **H3C11Xyl** (Figure 155) between -70 and 115°C in Me-cyclohexane (Figure 156). H3C11Xyl was selected because: i) the interaction can be observed over a wide range of temperatures for this bis-urea monomer and ii) both the transitions between the new assembly and the double filament structure and the previously-characterized transition between the double filament and filament structure can be followed (*vide infra*).

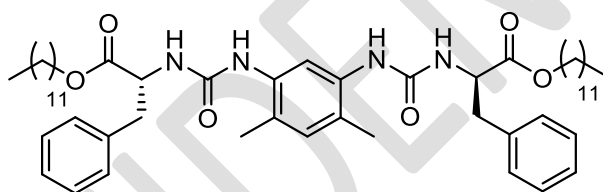


Figure 155 : Chemical structure of **H3C11Xyl**

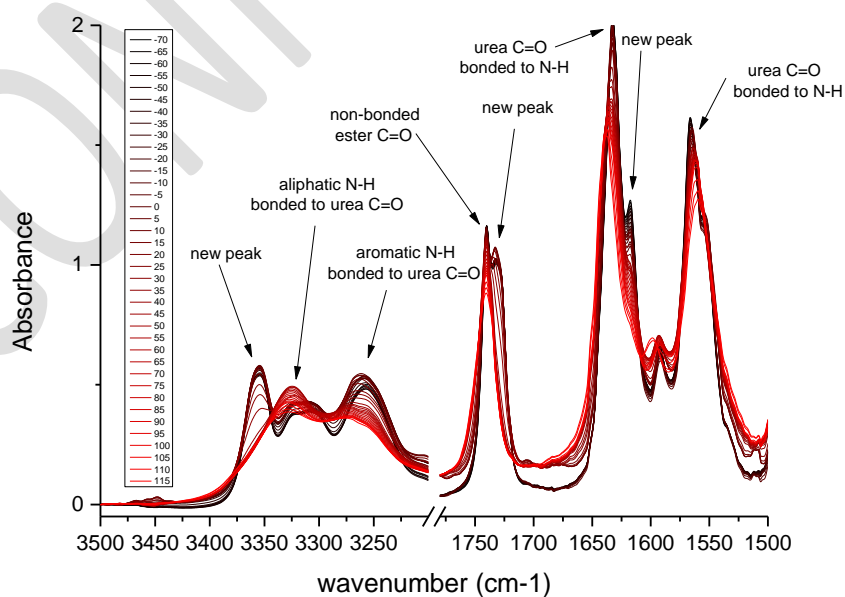


Figure 156 : FTIR spectra of **H3C11Xyl** between -70 and 115°C at 10 mM in Me-cyclohexane. Zoom on the NH and CO regions.

At temperatures below 35°C, we observe the presence of three unusual peaks in the NH and CO regions. The first one is at 3354 cm⁻¹ in the N-H region and most probably corresponds to a weakly bonded N-H as its value is intermediate between a non-bonded N-H (*ca.* 3425 cm⁻¹) and a N-H bonded to a urea C=O (3330-3250 cm⁻¹).^[1] The second one is at 1732 cm⁻¹ and is attributed to a weakly bonded ester C=O as it is next to the peak of the free ester C=O (1740 cm⁻¹). The third peak at 1617 cm⁻¹ is attributed to a new kind of bonded urea C=O as it is close to a usually bonded urea (1633 cm⁻¹) but far from free urea peak (*ca.* 1700 cm⁻¹). As the temperature is increased above 35°C, we observe the simultaneous decrease and disappearance of the three peaks, thus indicating that the HB acceptor is the oxygen of the C=O of the ester (or at least that it is close enough to it for the formation of this HB to have an impact on the C=O bond strength).

To gain more insight on the nature of this interaction, we compared the FTIR spectra of **H3C11Xyl** in Me-cyclohexane and in THF. In the latter solvent, characteristic FTIR peaks corresponding to free C=O and N-H solvated by THF are exhibited due to the highly dissociative nature of the solvent (Figure 157).

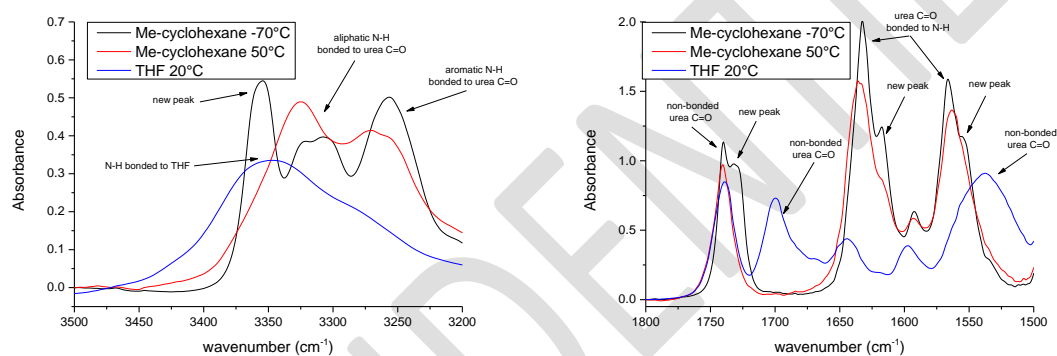


Figure 157 : FTIR spectra of **H3C11Xyl** at 10 mM in Me-cyclohexane and in THF . Left: zoom on the NH region. Right; zoom on the CO region. The spectrum at -70°C is characteristic of the new assembly whilst that at 50°C likely corresponds to the double filament structure (*vide infra*).

In the NH region (Figure 157 left), the peak at 3354 cm⁻¹ fits with the peak observed in THF confirming it corresponds to a weakly bonded N-H. Secondly, the presence of a new H-bond at -70°C is accompanied by a decrease of the intensity of the 3325 cm⁻¹ peak assigned to the aliphatic N-H bonded to the urea carbonyl.^[2] Therefore, at this temperature, part of the urea-urea hydrogen bonds between the aliphatic N-H and the urea C=O are replaced by this alternative hydrogen bond which involves the urea aliphatic N-H and the ester C=O.

Closer examination of the C=O peaks (Figure 157 right) is consistent with this interpretation. In THF, we observe the free ester C=O (1740 cm⁻¹) and free urea C=O (1700 cm⁻¹). In Me-cyclohexane at 50°C, we observe the free ester C=O (1740 cm⁻¹) and hydrogen bonded urea C=O (1633 cm⁻¹) corresponding to the usual assembly of bis-ureas in the double filament or filament structure. In contrast, at -70°C, two additional peaks are present: one at 1732 cm⁻¹ corresponding to the ester C=O either bonded or perturbed and another at 1618 cm⁻¹ corresponding to a bonded urea C=O. This second peak probably originates from the modification of the strength of the bond between the N-H which is not involved in the interaction with the ester C=O and the urea C=O. Thus it appears that the presence of the new interaction strengthens some of the interactions between the (probably aromatic) N-H and the urea C=O which could explain the good stability of this new assembly.

To monitor the disappearance of this interaction, we deconvoluted the ester C=O peaks and measured the ratio of the areas in order to approximate the proportion of ester moieties bonded to aliphatic N-H (Figure 158).

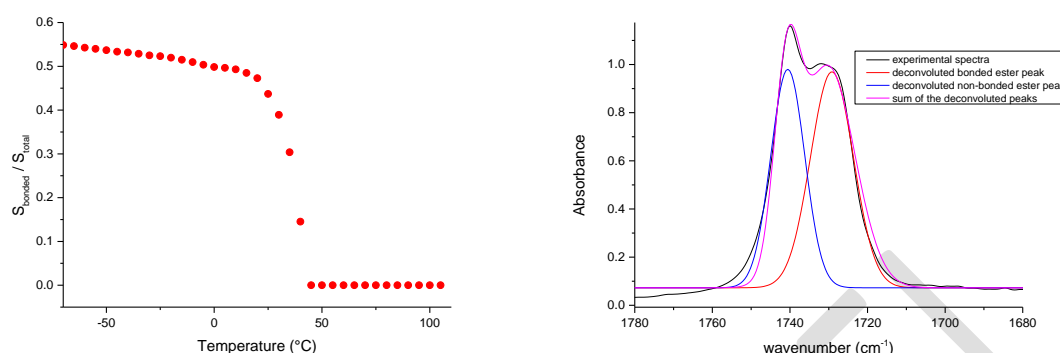


Figure 158 : Ratio of the areas for the bonded C=O ester peak (1732 cm^{-1}) to the whole C=O ester peak ($1732 + 1740\text{ cm}^{-1}$) as an estimation of the bonded ester proportion vs temperature (left) and example of deconvolution of the C=O ester peaks at -70°C (right) (**H3C11Xyl** at 10 mM in Me-cyclohexane).

We obtained a transition from a ratio (bonded/total) of around 50% to 0% at around 30°C indicating that on average, each monomer forms one hydrogen bond with an ester moiety below this temperature.

As this transition was quite sharp, it can also be characterized by nDSC (Figure 159).

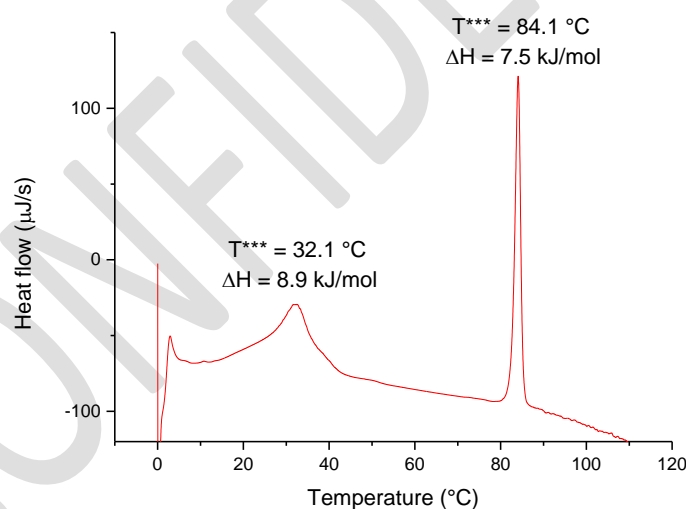


Figure 159 : nDSC trace of **H3C11Xyl** at 10 mM in Me-cyclohexane

We do observe a transition around 30°C . It is broad but still measurable. We also observe a second transition around 85°C which probably corresponds to a double filament to single filament transition as no free urea C=O peak is observed beyond this transition in FTIR (Figure 156). To have a closer look at the local arrangement of the bis-urea monomers in the new structure, we performed CD experiments at 0.1 mM in Me-cyclohexane (Figure 160).

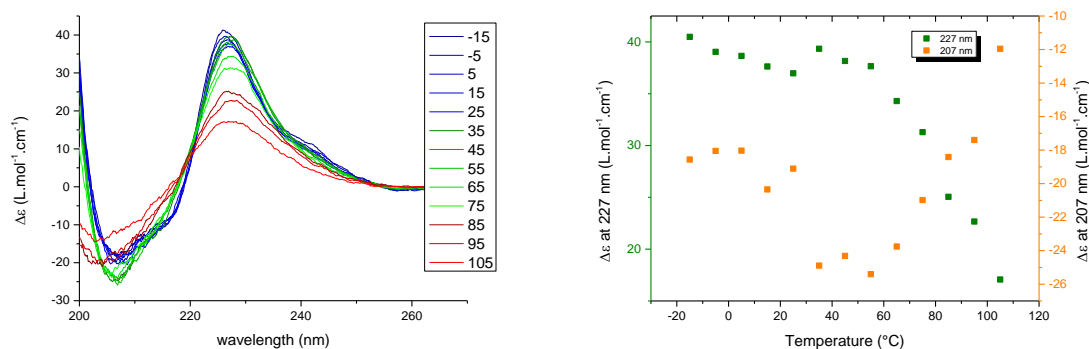


Figure 160 : CD spectra at different temperatures (left) and plot of the molar CD values ($\Delta\epsilon$) at 207 and 227 nm versus the temperature (right) of 0.1 mM Me-cyclohexane solutions of **H3C11Xyl**

Small but noticeable changes in the CD spectra are observed around 30 °C. Indeed, the peak at 207 nm increases slightly and the peak at 227 nm decreases upon heating above the transition between the new structure and the double filament structure (between 25 and 35 °C). These results confirm the changes of the local structure between the bonded and non-bonded ester assemblies, but the changes are rather small. At higher temperature (between 75 and 85 °C), a shift of the 207 nm peak occurs and is accompanied by a decrease of the peak at 227 nm. These effects should correspond to the double to single filament transition.

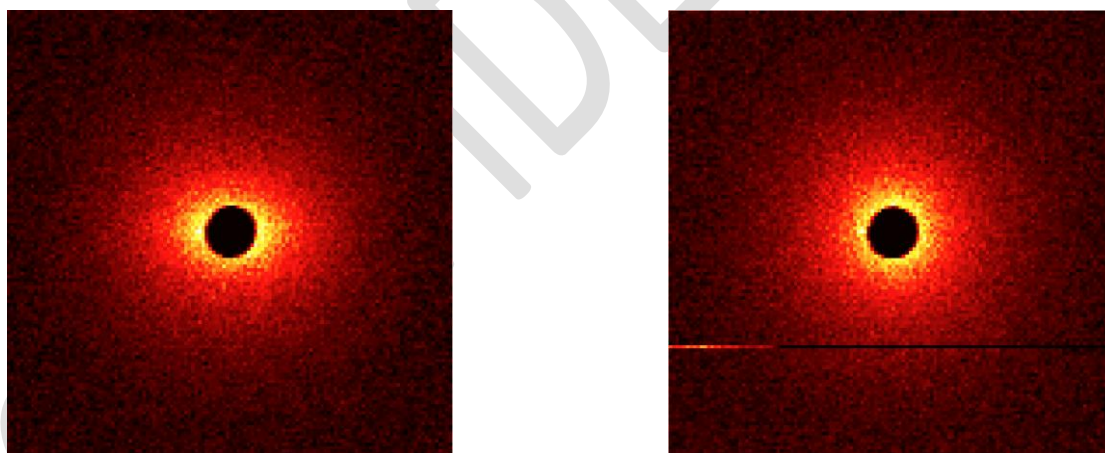


Figure 161 : Small angle neutron scattering patterns of **H3C11Xyl** at 10 °C (left) and 66 °C (right) in Me-cyclohexane-d₁₄ at ca. 0.6 wt%.

Interestingly, in SANS, an anisotropic pattern is observed below the bonded to non-bonded ester transition but not above (Figure 161). It means that the supramolecular assemblies present below the transition display some macroscopic orientation. The integration of the data according to an isotropic grouping is plotted in Figure 162. No difference can be seen between the two temperatures indicating the morphology of the assemblies is not affected by the presence of the hydrogen bonds to the ester. Moreover, the scattered intensity can be fitted with the form factor for rigid rods with a circular cross-section of radius 17 Å and a linear density that corresponds to 2.0 bis-ureas in the cross-section. Therefore, the change in the hydrogen bonding pattern does not significantly alter the

dimensions of the rods, but changes their long range orientation, maybe through a change in the rigidity of the objects.

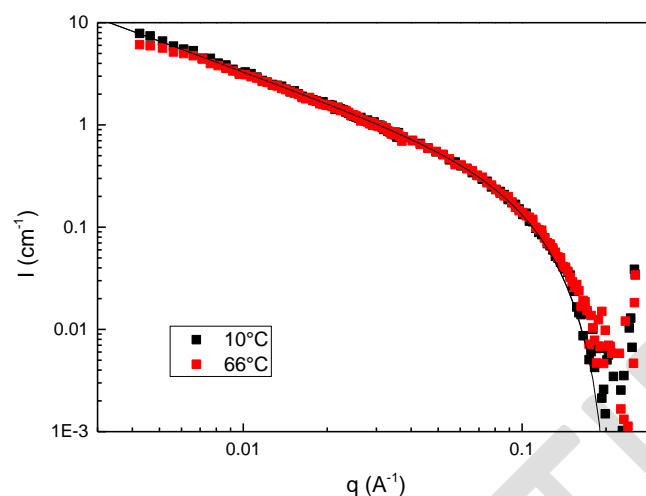


Figure 162: SANS experiments on **H3C11Xyl** in Me-cyclohexane- d_{14} at ca. 0.6 wt%. The line corresponds to a fit of the 10°C data according to the form factor for infinitely long rods of circular cross-section and homogeneous contrast.

To better visualize the results of this whole set of analyses, we propose on Figure 163 two tentative local structures involving either an intra- or an inter-molecular interaction between an aliphatic N-H and an ester C=O. Intramolecular five-membered ring hydrogen bonds of this geometry have been found to markedly stabilize synthetic β -sheets as well as the flat β -sheet of the amyloid state.^[3]

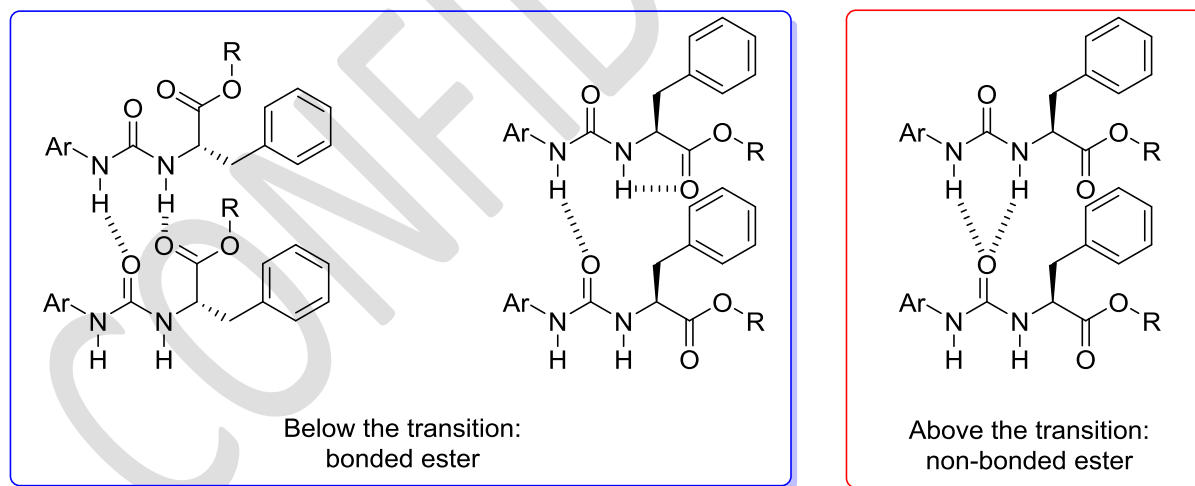


Figure 163 : possible structures of the bonded and non bonded ester hydrogen bond networks

Lazzaroni and coworkers (Mons University, Belgium) started a molecular modeling study on ester bis-ureas with Phe and a xyllyl spacer in order to better understand the structure of this new assembly. The preliminary results are available in the appendix (part G).

B. Influence of the chemical structure of the ester bis-ureas

As we found out the presence of this ester bonded interaction in different bis-ureas, we had a systematic look on the influence of the bis-urea structure on this assembly. In order to learn more about the nature of this interaction and to be able to tune it, we studied the influence of all three parts of an ester bis-urea: the spacer, the aminoacid and the side chain.

1. The spacer

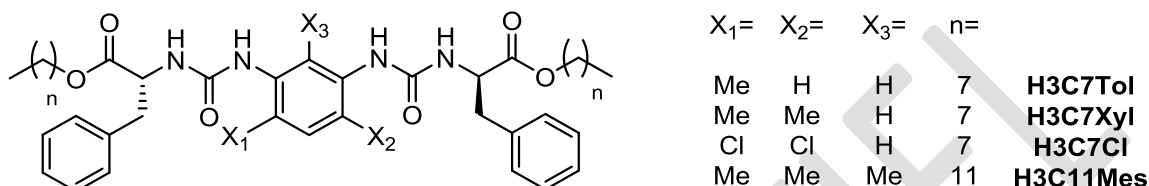


Figure 164 : chemical structures of **H3C7Tol**, **H3C7Xyl**, **H3C7Cl** and **H3C11Mes**

Four different spacers were compared: tolyl, 1,3-xylyl, 1,3-dichlorophenyl and mesityl (Figure 164). The FTIR spectra of the four molecules were measured in Me-cyclohexane every 5°C from -70 to 115°C (Figure 165).

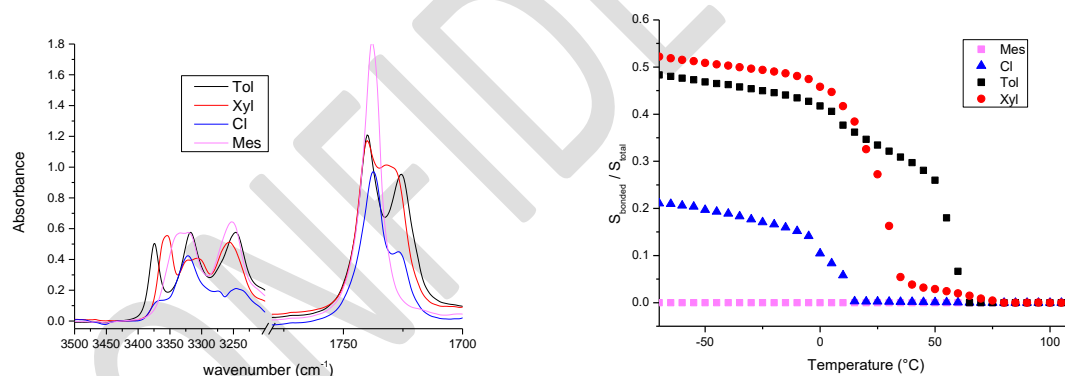


Figure 165 : FTIR spectra at -70°C (left) and estimated ratio of the area for the bonded C=O ester peak to the whole C=O ester peak (bonded + free) as an estimation of the bonded ester proportion vs temperature (right) for 10 mM solutions of **H3C7Tol**, **H3C7Xyl**, **H3C7Cl** and **H3C11Mes** in Me-cyclohexane

spacer	ν N-H bonded to ester (cm ⁻¹)	ν N-H bonded to aliphatic urea (cm ⁻¹)	$\Delta\nu$ N-H (cm ⁻¹)	ν non-bonded C=O (cm ⁻¹)	ν bonded C=O (cm ⁻¹)	$\Delta\nu$ C=O (cm ⁻¹)
Tol	3374	3318	56	1740	1726	14
Xyl	3354	3321 and 3308	33 and 46	1741	1729	12
Cl	3365	3322	43	1737	1727	10

Table 16 : some FTIR characteristic peaks observed for 10 mM solutions of **H3C7Tol**, **H3C7Xyl** and **H3C7Cl** at -70°C in Me-cyclohexane

Noticeably, the bis-urea with a mesityl spacer does not present any bonded ester C=O and that is not due to its different size of side chain (see page 146).

Bis-ureas with a tolyl, xylyl and dichlorophenyl spacer exhibit a similar behavior as they present both an additional N-H and an additional ester C=O peak albeit at slightly different wavenumbers. As the bonded N-H and free ester C=O peaks are not perfectly identical (mostly due to electronic density differences), we report on the shift between bonded ester C=O and non-bonded ester C=O peaks (Table 16). These shifts are similar for the three bis-ureas corroborating that the same interaction is present for these three bis-ureas.

The main difference observed between the bis-ureas with the xylyl and the dichlorophenyl spacer is that the ratio of bonded ester C=O is more than twice lower and the transition temperature 20°C lower for the dichlorophenyl spacer. In the case of **H3C7Cl**, the transition between the assembly with bonded ester and that with non-bonded ester functions is observed by FTIR (Figure 11), but not by nDSC (Figure 166). It is probably due to the fact that the transition occurs at too low temperature or is too broad (lack of cooperativity) to be observed with our nDSC instrument. The transition observed at 58.2°C by nDSC likely corresponds to the double filament / filament transition.

H3C7Tol possess approximately the same ratio of bonded ester CO in its low temperature assembly than **H3C7Xyl** (≈ 0.5). However, **H3C7Tol** assembly presents a different behavior as it undergoes two transitions towards the assembly without bonded ester C=O functions (around 10 and 60°C) compared to a single transition observed for **H3C7Xyl** (at 21.5°C) as determined by FTIR and nDSC analyses. . The second transition also corresponds to the double filament to filament transition (Figure 166 and as shown later in Figure 173). Moreover, the second transition of **H3C7Tol** exhibits a shape corresponding to a double to single filament transition and is thus most probably a ester bonded double filament to filament transition. We can assume that those differences are either due to the electronic density of the spacers or to their size and symmetry.

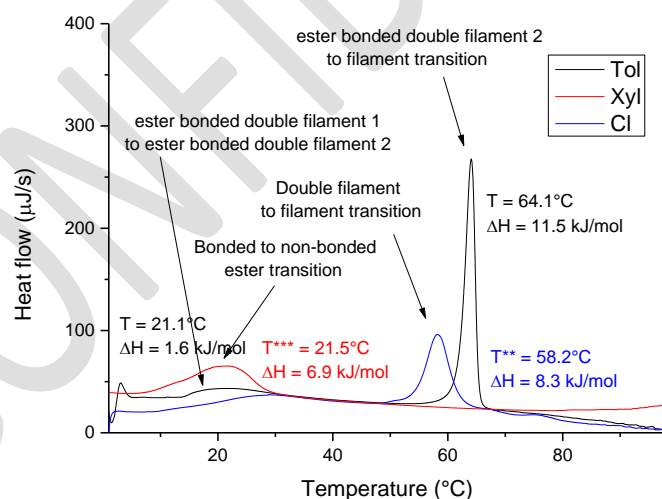
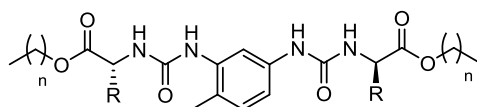


Figure 166 : nDSC traces of **H3C7Tol**, **H3C7Xyl** and **H3C7Cl** at 10 mM in Me-cyclohexane (heating rate = 1°C/min)

These results show that the nature of the spacer has a dramatic impact on the nature and stability of the ester-bonded double filament structure. It would be interesting to probe the influence of a bulkier spacer (such as diethyl benzene) or one bearing different substituents (such as dimethoxyphenyl).

2. The aminoacid

We then investigated the influence of the aminoacid using the more readily accessible tolyl spacer (TDI being the only commercial isocyanate of the series). Various sizes of alkyl chains were used because not all of these bis-ureas were prepared in the context of this study. Nevertheless, for each series, a bis-urea derived from L-phenylalanine with the same alkyl chain will serve as reference (Table 17).



	Phe	Ala	Cha	PhGly	F ₅ -Phe	d ₅ -Phe
R= n=						
7	H3C7Tol				H3C7F₅-PheTol	H3C7d₅-PheTol
11	H3C11Tol		H3C11ChaTol	H3C11PhGlyTol		
17	H3C17Tol	H3C17AlaTol				

Table 17 : Chemical structures of the different bis-ureas

a. The size of the aminoacid

To probe the influence of the size of the aminoacid, we synthesized a bis-urea bearing Ala and compared it to Phe (both of them with an octadecyl chain, **H3C17AlaTol** and **H3C17Tol**). FTIR analyses in Me-cyclohexane (Figure 167 and Figure 168) show that the two bis-ureas are associated (no free N-H band) but only the assemblies of **H3C17Tol** exhibit an interaction with the ester moiety.

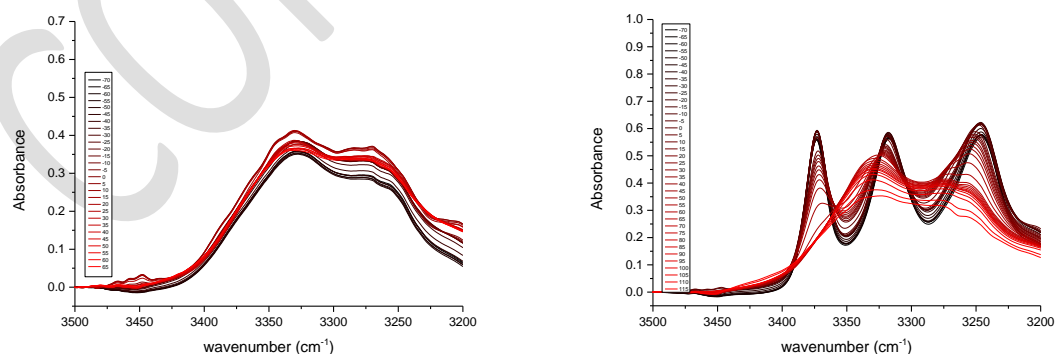


Figure 167 : FTIR spectra of **H3C17AlaTol** (left) and **H3C17Tol** (right) between -70 and 115°C at 10 mM in Me-cyclohexane. Zoom on the NH region.

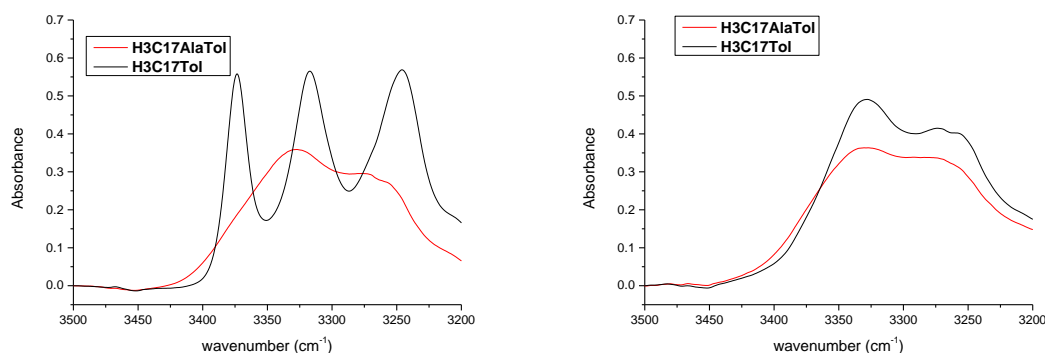


Figure 168 : FTIR spectra of **H3C17AlaTol** and **H3C17Tol** at -70 (left) and 60°C (right) at 10 mM in Me-cyclohexane. Zoom on the NH region.

The ester moiety is not involved in the assemblies formed by **H3C17AlaTol** at least in the range of temperatures and concentration investigated. Thus, this aminoacid may be too small or it just lacks an aromatic ring required to get an observable ester-bonded double filament structure.

b. The presence of a phenyl ring

As changing the nature of the aminoacid seemed to destroy the interaction with the ester moiety, we wondered if the phenyl ring had a role in the interaction. Thus, we synthesized a bis-urea bearing a Cha (cyclohexylalanine) aminoacid (*i.e.* no aromatic group but a similar size and shape than Phe) and PhGly (phenylglycine). **H3C11ChaTol** did not exhibit any interaction with the ester moiety (Figure 169). Interestingly, compared to **H3C11Tol**, **H3C11ChaTol** showed a shift of 21 cm^{-1} of its aliphatic N-H peak in the double filament (not in the single filament) indicating a difference in their double filament structure possibly due to the higher steric hindrance exerted by the Cha moiety (Figure 170).

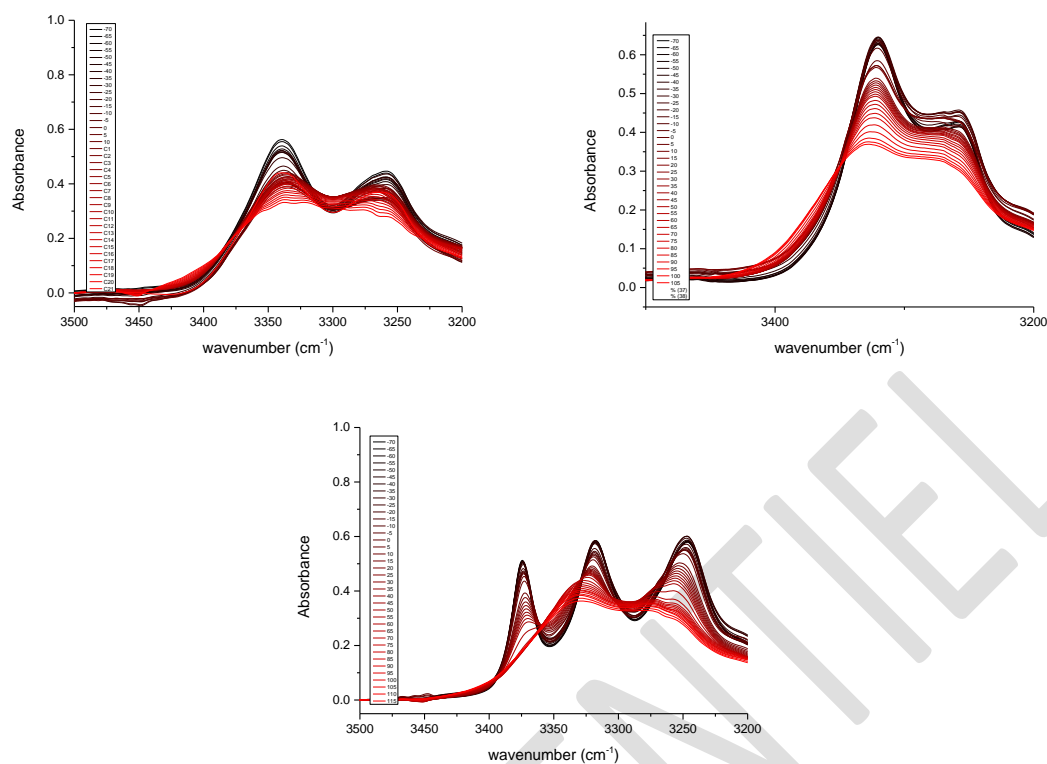


Figure 169 : FTIR spectra of **H3C11ChaTol** (left), **H3C11PhGlyTol** (right) and **H3C11Tol** (down) between -70 and 115°C at 10 mM in Me-cyclohexane. Zoom on the NH region.

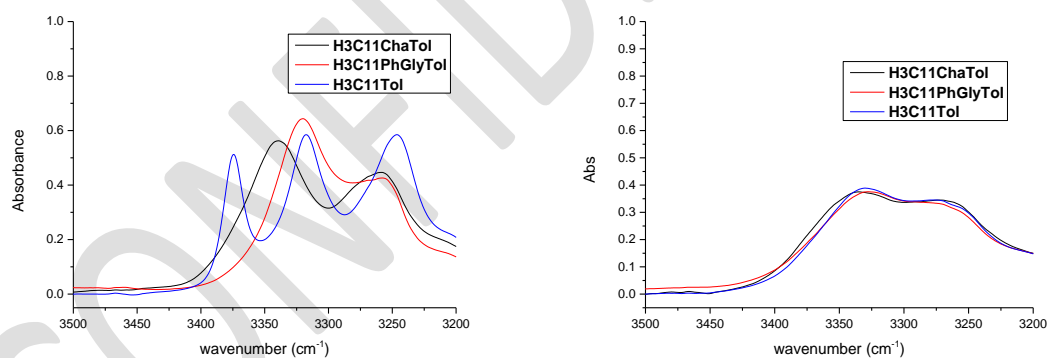


Figure 170 : FTIR spectra of **H3C11ChaTol**, **H3C11PhGlyTol** and **H3C11Tol** at -70 (left) and 100°C (right) at 10 mM in Me-cyclohexane. Zoom on the NH region.

H3C11PhGlyTol did not exhibit any interaction with the ester moiety either and shared similar IR spectra (at the exception of the signals related to bonded ester C=O) with **H3C11Tol** in both assemblies indicating similar assemblies.

In view of these results, we concluded that the Phe aminoacid presented the perfect geometry/size, and that large modification of the nature of the aminoacid was not possible. We thus thought about introducing substituents on the phenyl ring of the Phe.

c. Fluorination of the phenyl ring

A commercially available and affordable derivative of Phe is F₅-Phe. They present similar sizes (fluorine is known to be isosteric to hydrogen) but strongly different electronic properties.

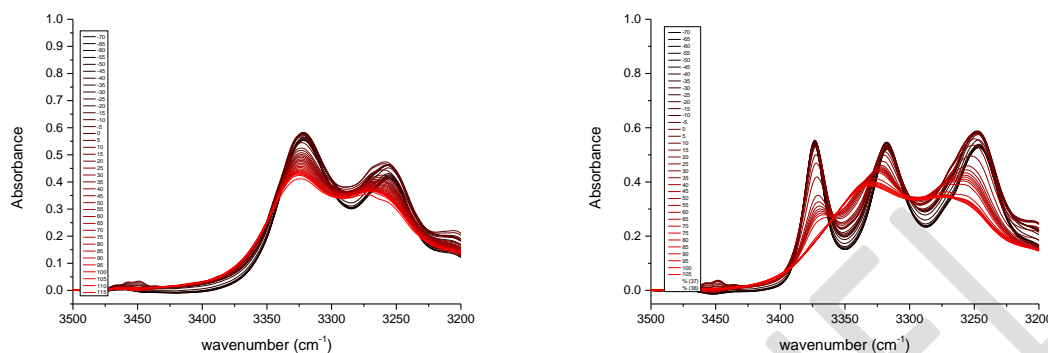


Figure 171 : FTIR spectra of **H3C7F₅-PheTol** (left) and **H3C7Tol** (right) between -70 and 115°C at 10 mM in Me-cyclohexane. Zoom on the NH region.

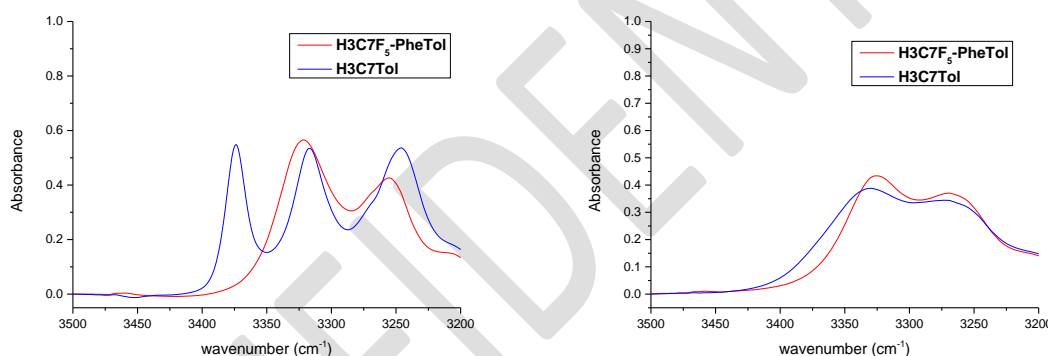


Figure 172 : FTIR spectra of **H3C7F₅-PheTol** and **H3C7Tol** at -70°C (left) and 100°C (right) at 10 mM in Me-cyclohexane. Zoom on the NH region.

Assemblies formed by **H3C7F₅-PheTol** did not show any NH bonded to ester moiety (Figure 171). At this exception, assemblies formed by **H3C7F₅-PheTol** and **H3C7Tol** are quite similar (Figure 172).

From this result, it appears that the bulkiness and geometry are probably not the issues with the Cha aminoacid but rather that the interaction with the ester moiety is linked to the electronic nature of the Phe aminoacid.

As only a minor change in the chemical structure of the ester bis-urea monomer seems to have a dramatic impact on the nature and stability of their assemblies, we sought to investigate the influence of tiny change: the deuteration of the phenyl ring.

d. Deuteration of the phenyl ring

d_5 -Phe is commercially available and is isoelectronic to Phe as confirmed by Shimizu and coworkers^[4].

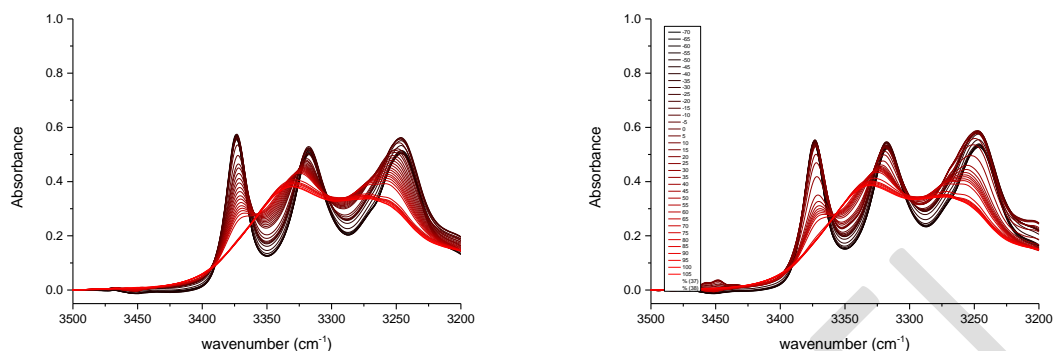


Figure 173 : FTIR spectra of **H3C7d₅-PhaTol** (left) and **H3C7Tol** (right) between -70 and 115°C at 10 mM in Me-cyclohexane. Zoom on the NH region.

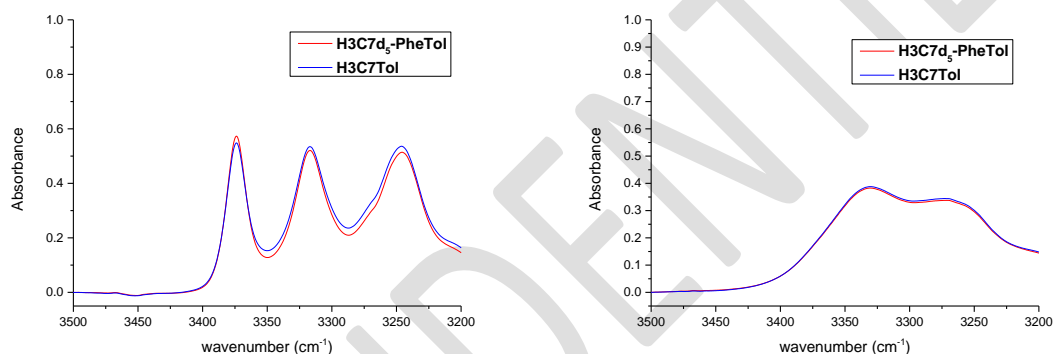


Figure 174 : FTIR spectra of **H3C7d₅-PheTol** and **H3C7Tol** at -70 (left) and 100°C (right) at 10 mM in Me-cyclohexane. Zoom on the NH region.

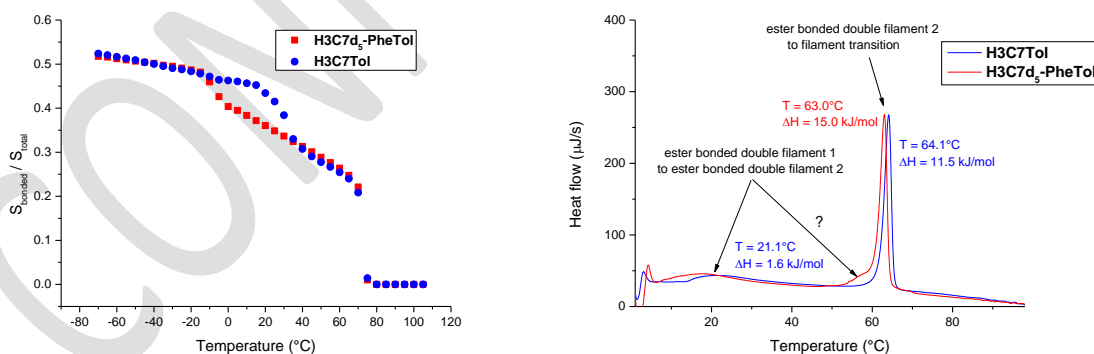


Figure 175 : Ratio of the area for the bonded C=O ester peak (1725 cm^{-1}) to the whole C=O ester peak ($1740 + 1725\text{ cm}^{-1}$) as an estimation of the bonded ester proportion vs temperature (left) and nDSC traces (heating rate = $1^\circ\text{C}/\text{min}$) (right) of **H3C7d₅-PheTol** and **H3C7Tol** at 10 mM in Me-cyclohexane)

We observed virtually identical FTIR spectra thus indicating a similar assembly in both the double filament and the single filament (Figure 173 and Figure 174).

Moreover, the plot of the bonded ester proportion (approximated via the ratio of the area of the ester C=O peaks, Figure 175) versus the temperature indicate two successive transitions for both **H3C7d₅-PheTol** and **H3C7Tol**. The second transition corresponds to the double filament to filament transition observed in nDSC and occurs at quasi-identical temperatures for both molecules. However,

the first temperature of the first transition is clearly affected. Although we have no idea of the phenomenon responsible for the first transition, it is interesting to note that **H3C7d₅-PheTol** exhibits this transition *ca.* forty degrees below than **H3C7Tol** thus indicating that this transition is sensitive to very small steric differences.

We can conclude that the nature of the aminoacid has a crucial role in promoting the interaction between the aliphatic N-H and the ester moiety and that the electronic property of the phenyl plays an important part in it. It would be interesting to study the impact of other substituents on the phenyl ring but it represents a significant synthetic effort.

We finally wanted to study the impact of the last component of those ester bis-ureas: the side chain.

3. The side chain

As the ester moiety was not involved in the assemblies formed by bis-ureas with a 2-ethylhexyl chain and a tolyl spacer (Figure 177), we wanted to confirm this observation for bis-ureas having other type of spacers.

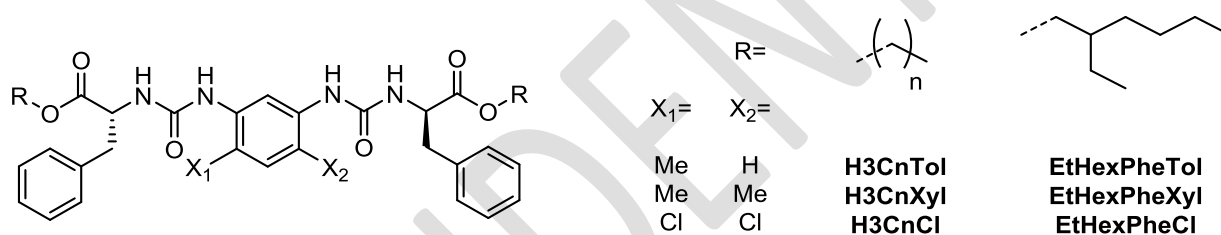


Figure 176 : Structure of bis-ureas bearing different alkyl chains and spacers

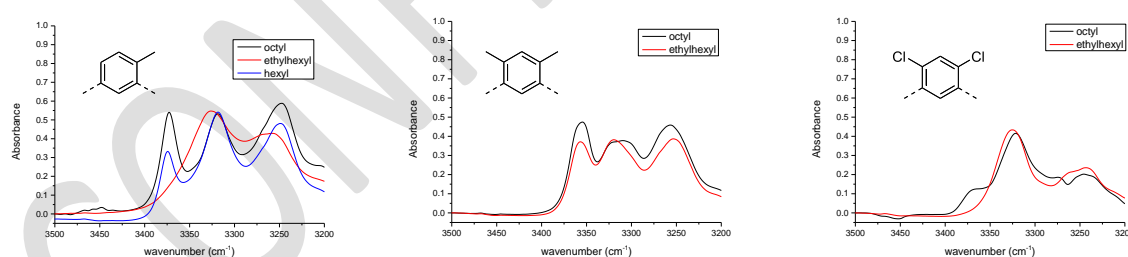


Figure 177 : IR spectrum of linear and branched bis-ureas bearing a tolyl (left), 1,3-xylyl (center) or 1,3-dichlorophenyl (right) spacer at -70°C and 10 mM in Me-cyclohexane. Zoom on the NH region.

Like the bis-urea with the tolyl spacer, the bis-urea with the 1,3-dichlorophenyl spacer and a 2-ethylhexyl side chain does not form assemblies in which the ester moiety is involved (Figure 177). With the xylyl spacer, only a slight decrease of the amount of bonded ester C=O is observed. It confirms that the xylyl spacer is the most efficient of the three spacers for promoting the formation of the ester-bonded double filament structure.

We also investigated the influence of the length of the linear alkyl chain on the nature and stability of the ester-bonded double filament structure formed by bis-ureas bearing a tolyl spacer ((Figure 178).

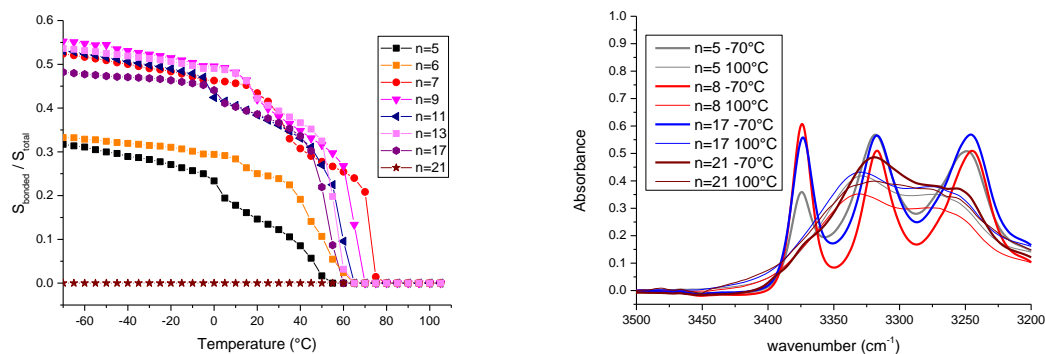


Figure 178 : Ratio of the area for the bonded C=O ester peak to the whole C=O ester peak (free + bonded) as an estimation of the bonded ester proportion vs temperature (left) for the whole **H3CnTol** series and FTIR spectra of **H3C5Tol**, **H3C8Tol**, **H3C17Tol** and **H3C21Tol** at -70 and 100°C (right) (10 mM Me-cyclohexane solutions in all cases). Zoom on the NH region.

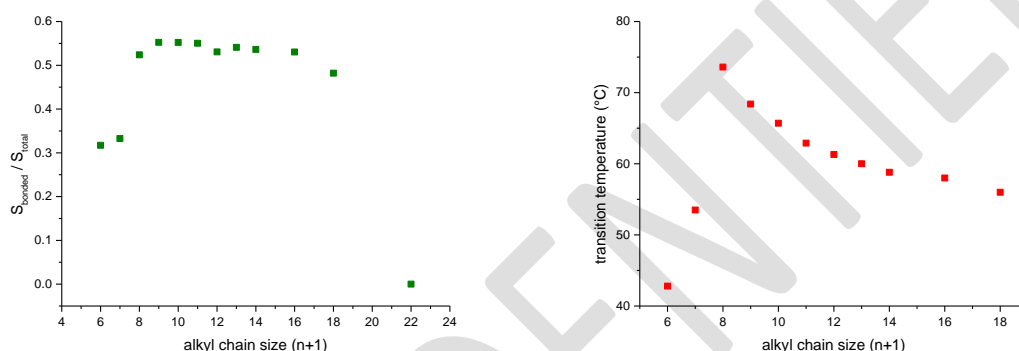


Figure 179 : estimated bonded ester proportion at -70°C for the whole **H3CnTol** series (left) and transition temperature between the ester-bonded double filament structure and the filament structure for the whole **H3CnTol** series except **H3C21Tol** (right) 10 mM in Me-cyclohexane solutions in all cases.

The plot of the ratio of bonded ester in the ester-bonded double filament structure versus the length of the alkyl chain for the **H3CnTol** series shows three regimes (Figure 179 left). A first regime shows an increase of the ratio when going from 6 to 9 carbon atoms then a plateau for the bis-ureas with 9 to 16 carbon atoms in the side chain and finally a rapid decrease to zero at 22 carbon atoms. It seems that at least 9 carbon atoms in the side chain are necessary to stabilize the interaction involving the ester moiety and that too long chains are not good for the interaction, probably due to steric hindrance. The length of the alkyl chain also strongly affects the overall stability of the ester-bonded double filament structure as reflected by the plot of the transition temperature versus the length of the alkyl chain for the **H3CnTol** series (Figure 25 right). Two competing effects seem to be involved and result in an optimal stability for the ester-bonded double structure formed by **H3C7Tol** (*i.e.* the bis-urea with 8 carbon atoms in the side chain, $T^{**}=73.6^{\circ}\text{C}$).

Such a study of the influence of the length of the alkyl side chain on the stability of the ester-bonded double filament structure would be interesting in the case of the bis-ureas bearing a xylyl spacer. Unfortunately, only three sizes of side chain were synthesized (8, 12 and 16 carbon atoms long) and the three bis-ureas form ester-bonded double filament structure with almost the same ratio of bonded ester functions and of similar stability (Figure 180).

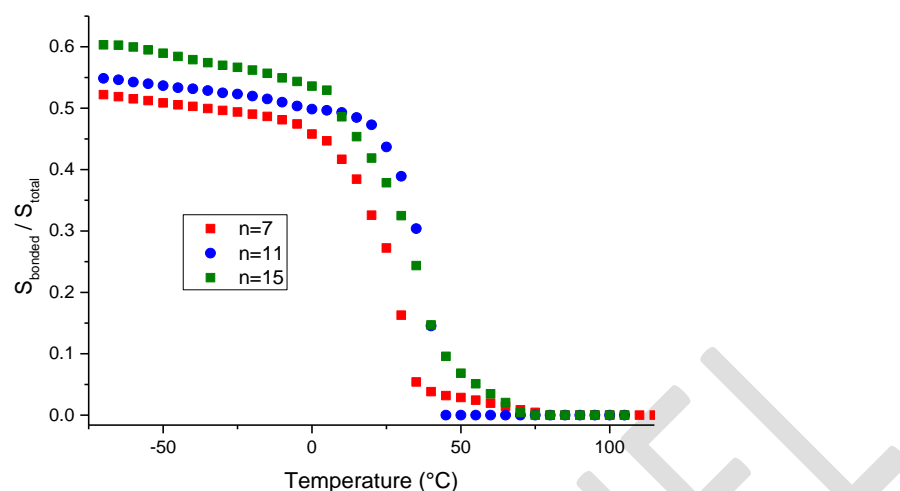


Figure 180 : Ratio of the area for the bonded C=O ester peak to the whole C=O ester peak (free + bonded) as an estimation of the bonded ester proportion vs temperature for 10 mM solutions of **H3C7Xyl**, **H3C11Xyl** and **H3C15Xyl** in Me-cyclohexane

It would be interesting to synthesize bis-ureas with a xylyl spacer and shorter or longer chains to probe whether the same trend as the one found for the bis-urea with a tolyl spacer is observed.

C. Influence of chirality

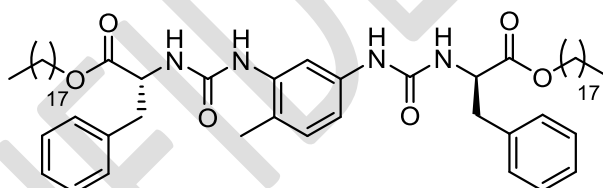


Figure 181 : Structure of **H3C17Tol**

As the filament and double filament assemblies of ester bis-ureas are chiral at the supramolecular level and highly sensitive to the enantiomeric excess (see chapter 3) we probed the influence of the enantiopurity of **H3C17Tol** on the stability of its ester-bonded double filament structure (Figure 182). In that aim we prepared mixtures of (*S,S*)-**H3C17Tol** and (*R,R*)-**H3C17Tol** with different enantiomeric excesses and measured the ratio of bonded ester functions and the stability of their ester-bonded double filament structure (when it formed).

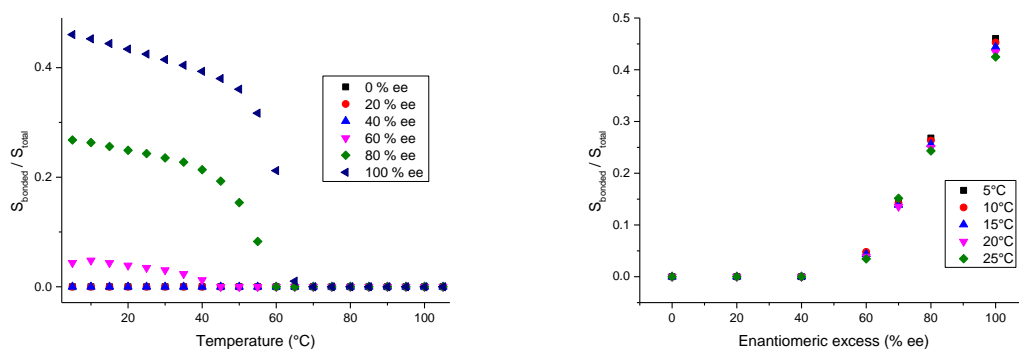


Figure 182 : Ratio of the area for the bonded C=O ester peak (1726 cm^{-1}) to the whole C=O ester peak ($1726 + 1740\text{ cm}^{-1}$) as an estimation of the bonded ester proportion vs temperature for **H3C17Tol** at different ee (left) and the same ratio vs ee at different temperatures (right). 10 mM solutions in Me-cyclohexane in all cases

We observe a strong dependence of ratio of bonded ester functions on the enantiomeric excess. Interestingly, the interaction with the ester moiety seems to be present only for mixtures with e.e. > 50%, which corresponds to a 3 to 1 ratio of the major to the minor enantiomer. On going from mixtures with 50 to 100% e.e. a linear increase of the ratio of bonded ester functions is observed. This indicates that, starting from the pure *S,S* enantiomer where each bis-urea forms 1 hydrogen bond to an ester moiety, each *R,R* enantiomer introduced prevents the formation of a hydrogen bond to an ester for 3 of its neighbors in the assembly. This property can be used to tune the quantity of bonded ester functions and shows once again that geometry is an important factor for the stability of this interaction.

D. Influence of the solvent

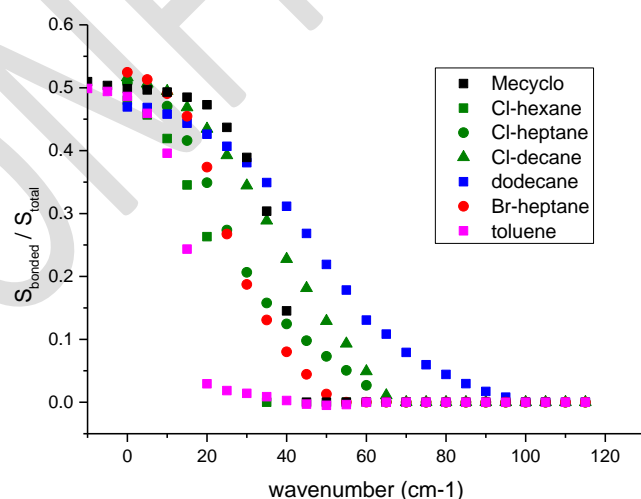


Figure 183 : Ratio of the area for the bonded C=O ester peak (1732 cm^{-1}) to the whole C=O ester peak ($1732 + 1740\text{ cm}^{-1}$) as an estimation of the bonded ester proportion vs temperature for 10 mM solutions of **H3C11Xyl** in various solvents. In case of toluene, the estimated bonded ester ratio is obtained the ratio of the amplitude of the N-H peaks (at 10 mM).

The formation of hydrogen bonds to the ester moiety has been observed in all solvents in which **H3C11Xyl** is assembled, with the same ratio of bonded ester functions at low temperature. However, we observe different transition temperatures between the ester-bonded double filament and the

double filament structure upon changing the solvent as well as a different degree of cooperativity for this transition (Figure 183). In the case of halogenoalkanes, the transition gets wider and the transition temperature gets higher when increasing the number of carbon atoms of the solvent. Cl-heptane and Br-heptane exhibit quasi-identical transitions for both the bonded to non-bonded ester double filament transition and the double to single filament transition (Figure 184).

In the case of toluene, the estimated ester bonded ratio could not be estimated by deconvolution of the ester C=O peaks as toluene absorbs in the ester C=O region and was thus estimated by the ratio of the amplitude of the N-H peaks. The transition was observed at a lower temperature of *ca.* 20°C and the double to single filament transition is 32°C lower in toluene than in Me-cyclohexane.

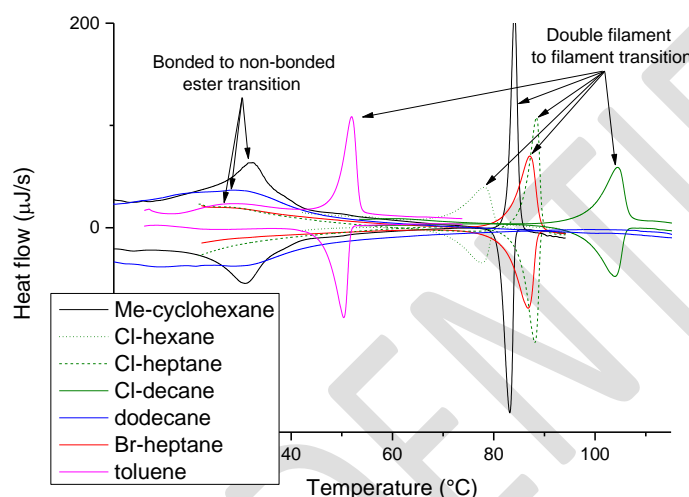


Figure 184 : nDSC traces of **H3C11Xyl** at 10 mM in different solvents

E. Influence of the concentration

As bis-urea assemblies are known to exhibit transition temperatures which depend on their concentration,^[2] we probed the influence of the concentration on the stability of the ester-bonded double filament structure. We observed a very low dependence of the temperature of the bonded to non-bonded ester transition on the concentration (Figure 186).

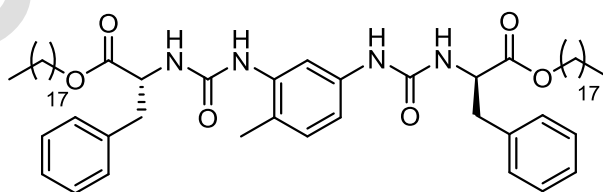


Figure 185 : Structure of **H3C17Tol**

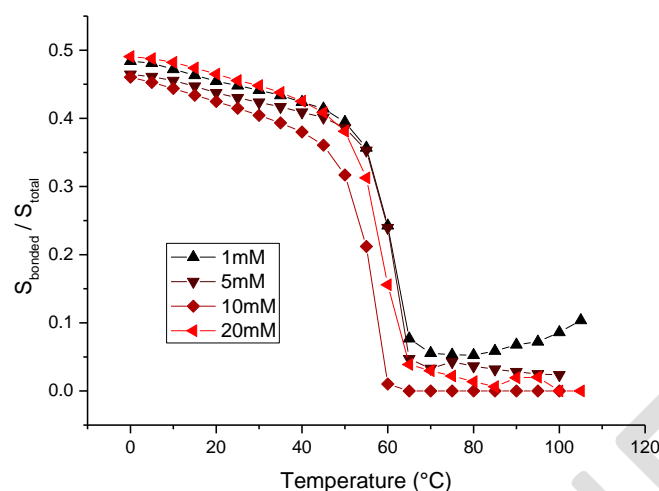


Figure 186 : Ratio of the area for the bonded C=O ester peak (1726 cm^{-1}) to the whole C=O ester peak ($1726 + 1740\text{ cm}^{-1}$) as an estimation of the bonded ester proportion vs temperature for Me-cyclohexane solutions of **H3C17Tol** at different concentrations).

As this bonded ester transition can be coupled to the double filament to filament transition in the case of **H3C17Tol**, we also probed the transition between the ester-bonded double filament and the double filament exhibited by **H3C11Xyl** at different concentrations. This was done in dodecane using nDSC (Figure 187).

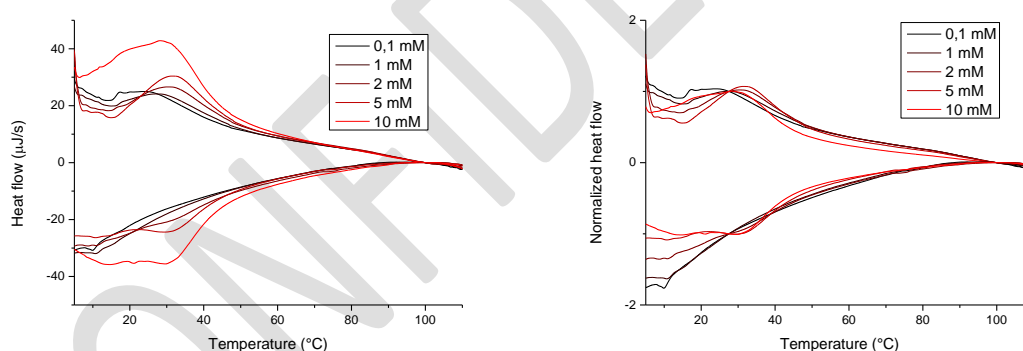


Figure 187 : raw (left) and normalized with concentration (right) nDSC traces of **H3C11Xyl** in dodecane at different concentrations. In that case the observed transition corresponds to the transition between the ester-bonded double filament structure and the double filament structure. The double filament to filament transition occurs at too high temperature to be observed in this solvent.

The nDSC results confirm that there is a negligible influence of the concentration on the stability of the ester-bonded double filament structure of **H3C11Xyl**. It could be explained by an intramolecular H-bonding between the aliphatic urea N-H and the ester C=O (Figure 163).

F. Towards a thermothickening additive

As solutions of bis-ureas are known to exhibit large changes in their rheological properties^[5] during the transition between two assemblies, we wondered if it was also the case for the transition between the ester-bonded double filament and the double filament structure. We thus measured

the evolution of the relative viscosity with temperature of a 0.1 mM solution of **H3C11Xyl** in Me-cyclohexane and dodecane (Figure 189).

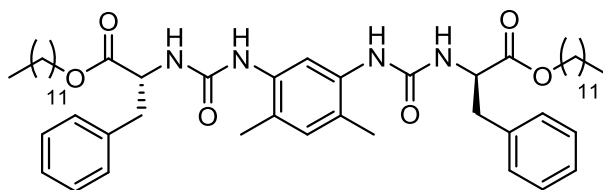


Figure 188 : structure of **H3C11Xyl**

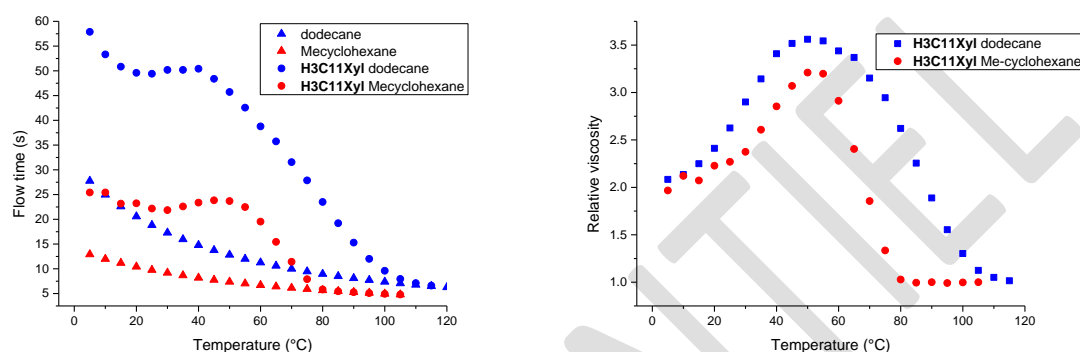


Figure 189 : flow time (t) and relative viscosity (t/t_0) of 0.1 mM solution of **H3C11Xyl** in Me-cyclohexane or dodecane

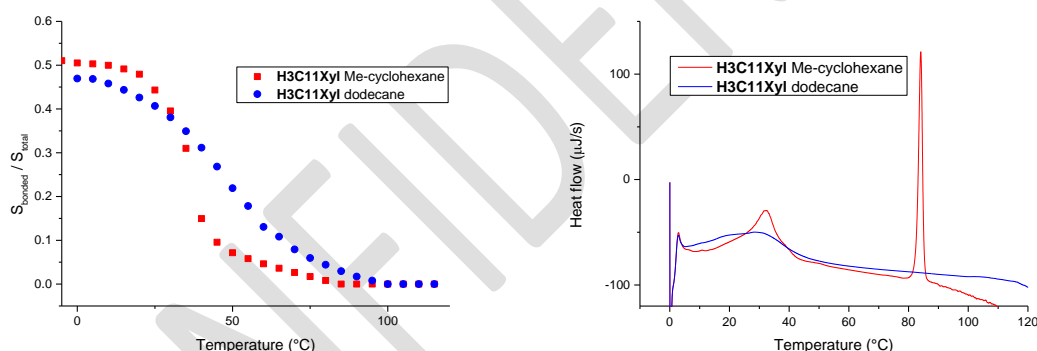


Figure 190 : Ratio of the area for the bonded C=O ester peak (1732 cm^{-1}) to the whole C=O ester peak ($1732 + 1740\text{ cm}^{-1}$) as an estimation of the bonded ester proportion vs temperature (left) and nDSC traces (right) for 10 mM solutions of **H3C11Xyl** in Me-cyclohexane or dodecane

As expected both the bonded to non-bonded ester double filament transition and the double to single filament transition exhibit a change in viscosity but to our great surprise, the first transition is actually associated with an *increase* of the viscosity.

We observe the same bonded to non-bonded ester transition at a similar temperature in both solvents but it is far less cooperative in dodecane (Figure 190). We also observe in nDSC that the double to single filament transition is now above 120°C in dodecane (maximum operable temperature of the nDSC).

We wanted to investigate the influence of the length of the alkyl chain as well and thus compared a bis-urea with an octyl chain and a dodecyl chain (in Me-cyclohexane) and a dodecyl chain and a pentadecyl chain (in dodecane)

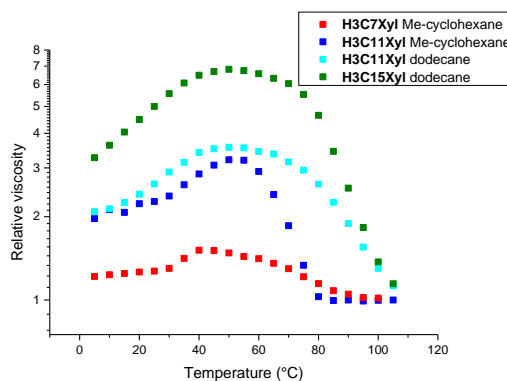


Figure 191 : relative viscosity of 0.1 mM solution of **H3CnXyl** in Me-cyclohexane or dodecane

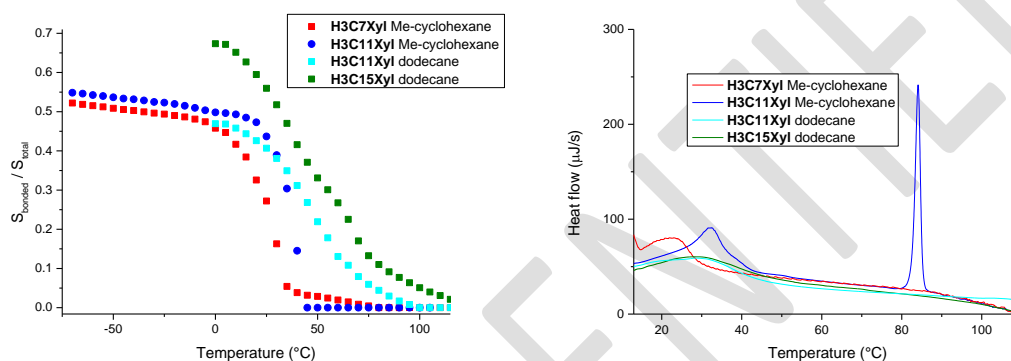


Figure 192 : Ratio of the area for the bonded C=O ester peak to the whole C=O ester peak (free + bonded) as an estimation of the bonded ester proportion vs temperature (left) and nDSC traces (right) for 10 mM solutions of **H3CnXyl** at 10 mM in Me-cyclohexane or dodecane

In both solvents, we observe a large increase of the relative viscosity at room temperature when increasing the length of the side chain (Figure 37). Moreover, the four bis-urea solutions display an increase in their relative viscosity when going from 5 to 50°C. This temperature range corresponds to the disappearance of the hydrogen bonds to the ester groups (Figure 192).

These results were obtained on very dilute solutions (0.1 mM) to allow measuring the viscosity by capillary flow. Higher concentrations yield gels that have to be characterized by rheology. Therefore, a solution of **H3C11Xyl** at 5 mM in dodecane was characterized by rheology by Guylaine Ducouret (SIMM, ESPCI).

A frequency sweep was performed in the linear regime to measure the elastic (G') and viscous moduli (G'') at 20 and 50°C twice in a row (Figure 193).

The complex viscosity can be deduced by the equation: $|\eta^*| = \left[\left(\frac{G''}{\omega} \right)^2 + \left(\frac{G'}{\omega} \right)^2 \right]^{1/2}$

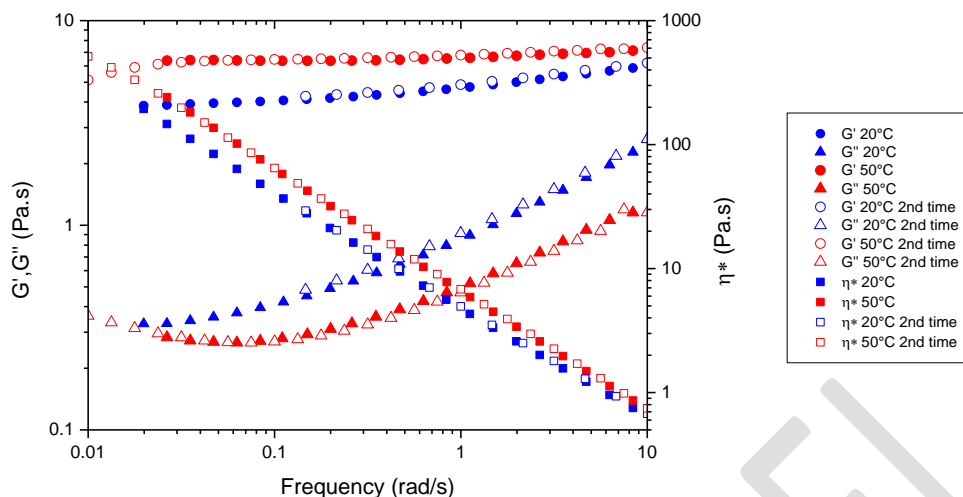


Figure 193 : G' , G'' and η^* of 5 mM solution of **H3C11Xy a** in dodecane

This experiment performed at 5 mM confirms that the viscosity increases from 20 to 50°C, in agreement with the previous capillary viscosity measurement performed at 0.1 mM. Moreover, the frequency dependent experiment further shows that the increase in viscosity is actually due to an increase in elastic modulus. This can in turn be related to an increase in the density of entanglements of the long rod-like assemblies.

An increase in viscosity with temperature has been seen with other systems such as many polymers showing a LCST in water like poly(N-isopropylacrylamide) [PNIPAM]^[6,7], block or random copolymers of ethylene oxide and propylene oxide [PEPO]^[8] and polysaccharides derivatives^[9]. There are also other examples of thermothickening polymers in water based on the hydrophobic effect.^[10,11] There are examples of coordination polymers in water based on the equilibrium between linear and cyclic species.^[12,13] The only example we found of a supramolecular polymer exhibiting an increase of viscosity in an organic solvent is due to an equilibrium between a cyclic and a linear hydrogen-bonded polymer.^[14] The increase in temperature shifts the equilibrium towards the linear chains because of their larger conformational entropy. Unlike the system reported in this chapter, this effect is highly dependent on the concentration.

In conclusion, we showed that the structure of the ester bis-urea has a great impact on the existence of this new thick assembly. Indeed, this assembly apparently needs Phe as the amino-acid to be stable, and is the most stable with a side chain of intermediary length and a xylyl spacer. Our bis-urea system is quite promising for the design of a thermothickening additive but a few limitations exist as (i) the temperature of the bonded to non-bonded ester transition is quasi-independent of the concentration but dependent on the solvent and (ii) the second transition temperature (double to single filament) is highly dependent of the concentration and the solvent and can thus be too close of the first transition.

The next steps are (i) to continue to study the influence of the side chain size in bis-ureas bearing a xylyl spacer and (ii) to find a better spacer, for example dimethoxybenzene, in order to vary the transition temperature of the bonded to non-bonded ester transition.

G. Appendix: molecular modeling

To investigate the structure of the single and double filaments of bisurea systems, we performed a conformational search varying the periodical motif along the assembly direction.

For single filaments, a previous study^[15] found that the urea groups are tilted with respect to the core by *ca.* $|140|^\circ$, but that the sign of the torsion can vary from one monomer to the next along the assembly axis, thus giving rise to *nxm* periodical motifs (*n* is the number of successive monomers with torsions of one sign, followed by *m* successive monomers with torsions of the opposite sign). When *n* is infinite and *m* is 0 (or the opposite), an helix is obtained. See Figure 194, left. Here, we compared the stability of the M-helix, and of the 1x1, 2x2, and 3x3 structures.

For double filaments, we evaluated two categories of assemblies. The first category is composed of structures where each monomer interacts by hydrogen bonds with four neighboring molecules, instead of two as in a single filament. Three of those alternated structures were investigated, see Figure 194, right. The second category is based on two single filaments joined and maintained together by their long-range interactions. Double filaments based on the M-helix, and the 1x1, 2x2, and 3x3 structures were investigated.

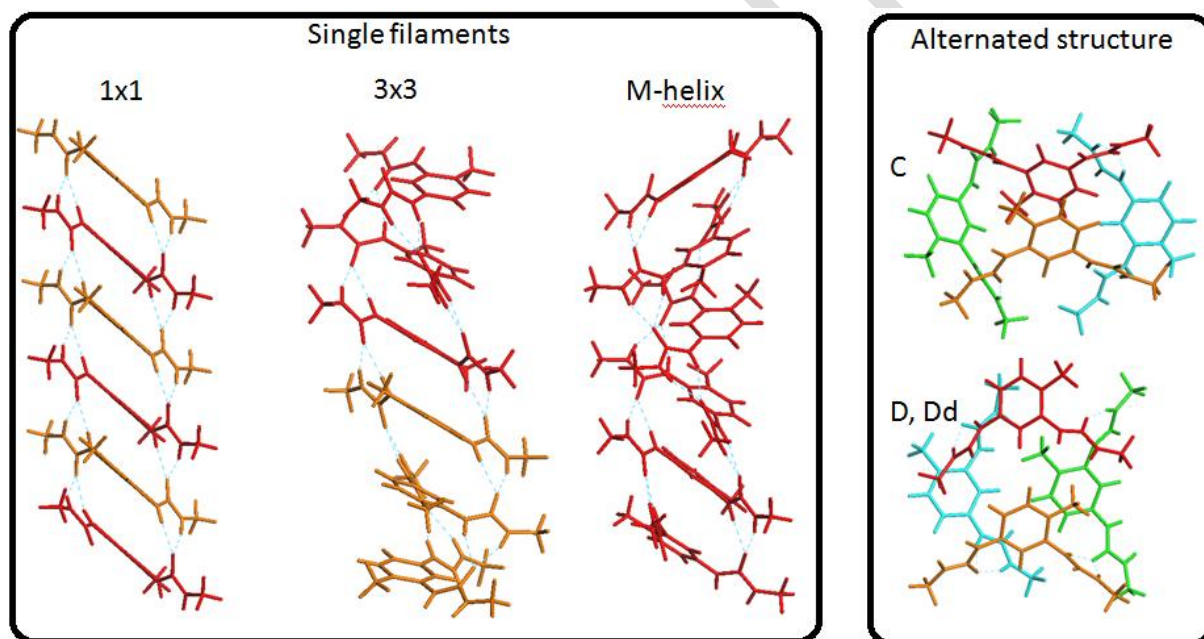


Figure 194 : (Left) Assembly of six bis-urea monomers in a 1x1, a 3x3, and an helical single filament; the monomers in red have a positive sign for the dihedral angle responsible of the orientation of the urea with respect to the core; the sign is negative for the monomers in orange. (Right) Motifs for double filaments where each monomer makes hydrogen bonds with four neighboring molecules. In Dd, the motif displayed is adjoined by another one on top of it (not represented), and rotated by 90° .

Following the methodology described above to generate the conformations, we then performed 1500 ps MD, and compared the various filaments for **H3C0Xyl**, which is a good approximation of the **H3C11Xyl** molecule (the C12 alkyl chain was replaced by a methyl group for alleviating the computational cost).

The energy analyses (Figure 195) show that the helix is the most stable structure in both the single and double filament categories. In addition, simulated CD spectra (Figure 196) show that the helical structures have intense bisignated signals with a positive band at ca. 210 nm followed by a negative one at ca. 205 nm. Such a pattern is observed experimentally for the related molecule, **H3C11Xyl**, though with different intensities, which could result from the high temperature in which the experiment was performed (50-90°C) when compared to the simulation temperature (27°C). The other simulated structures have a featureless CD signal, especially the other double filament structures proposed, or a signal that has no resemblance to the experimental results. The helical filaments, both single and double, thus appear as good candidates to explain the experimental results.

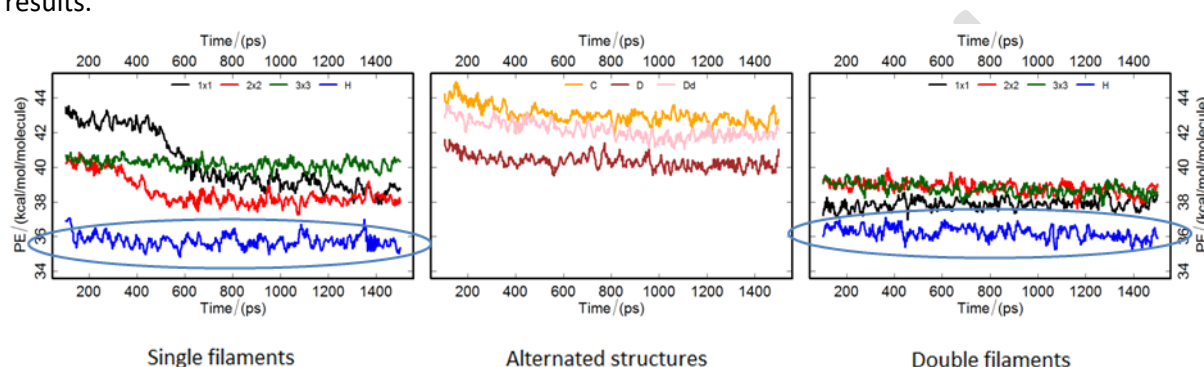


Figure 195 : Evolution of the potential energy of the different structures for **H3C0Xyl** as single or double filaments during 1500 ps MD. The reference energy level is arbitrary.

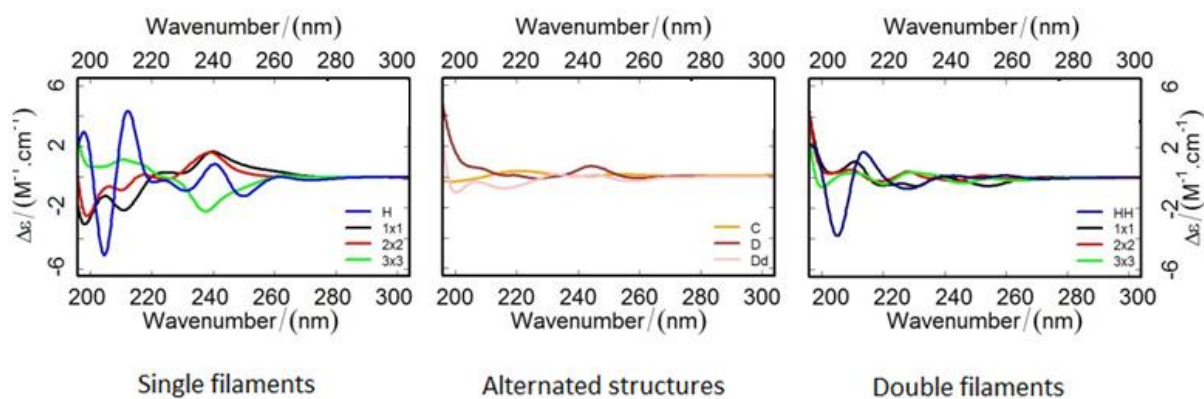


Figure 196 : Simulated CD spectra of the single and double filaments for **H3C0Xyl**.

For the rest of the analysis, we thus focused on the helical single and double filaments, whose structures are displayed in Figure 197. They have a linear density of ca. 0.25 \AA^{-1} and 0.54 \AA^{-1} . Assuming a repeat distance of 4.6 \AA between the monomers, *i.e.* the same value used for interpreting the SANS measurements, the number of molecules in the cross section, is of ca. 1.2 and 2.5, for the single and double filaments, respectively. These values can be compared to the experimental related molecule **H3C11Xyl**, which has 0.9 molecules per section at 65°C (single filament) and 2.3 at 20°C (double filament).

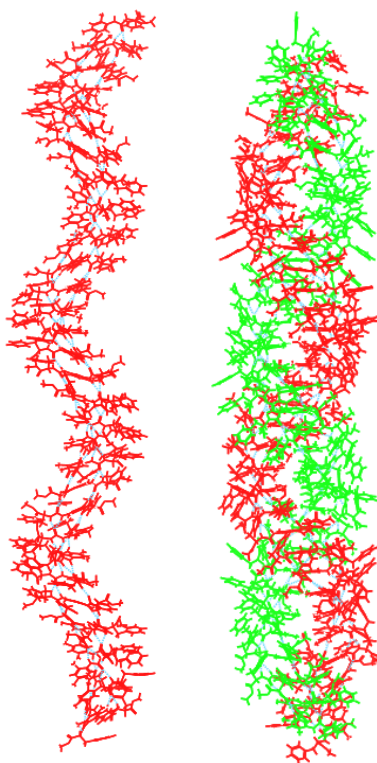


Figure 197 : Representative structure of a single (left) and double (right) filament for **H3COXyl** generated during MD.

To characterize their hydrogen bond network, we calculated the radial distribution function between the hydrogen atoms of the urea moieties and the oxygen atoms of either the urea, either the ester moieties. Hydrogen bonds give rise to a peak at 2 Å, which is very intense for urea, almost absent for ester in the single filament and in the double filament (Figure 198). To quantify the proportion of hydrogen bonds with both acceptors, we calculated the cumulative number of oxygen atoms, n_O , found in function of the distance from the hydrogen atoms of the urea moieties. At 2.5 Å, a threshold below which most hydrogen bonds take place, the proportion of hydrogen bonds with ester groups is found to be 0,6% and 3,1% for the single and double filaments, respectively. Most hydrogen bonds thus occur with the urea moieties, shown by $n_{O_{urea}}$ jumping from 0 to close to 1 at 2 Å. These results also show that all urea hydrogen atoms are likely involved in hydrogen bonds (with the exception of the hydrogen atoms belonging to the monomer(s) located at one extremity of the helix).

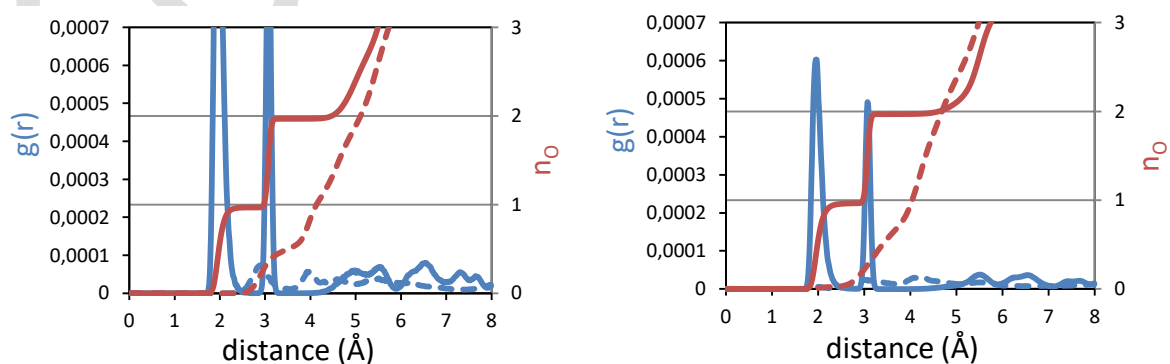


Figure 198 : Radial distribution function, $g(r)$, between H_{urea} and O, and cumulative number of O around H_{urea} in function of the H_{urea} -O distance, for the single (left) and double (right) filaments for **H3COXyl**. The oxygen atoms are either O_{urea} (plain line) or O_{ester} (dotted line).

- [1] M. Dirany, V. Ayzac, B. Isare, M. Raynal, L. Bouteiller, *Langmuir* **2015**, *31*, 11443–11451.
- [2] V. Simic, L. Bouteiller, M. Jalabert, *J. Am. Chem. Soc.* **2003**, *125*, 13148–13154.
- [3] R. W. Newberry, R. T. Raines, *Nat. Chem. Biol.* **2016**, 1–6.
- [4] C. Zhao, R. M. Parrish, M. D. Smith, P. J. Pellechia, C. D. Sherrill, K. D. Shimizu, *J. Am. Chem. Soc.* **2012**, *134*, 14306–14309.
- [5] F. Lortie, S. Boileau, L. Bouteiller, C. Chassenieux, B. Demé, G. Ducouret, M. Jalabert, F. Lauprêtre, P. Terech, *Langmuir* **2002**, *18*, 7218–7222.
- [6] G. Bokias, Y. Mylonas, *Macromolecules* **2001**, *34*, 885–889.
- [7] T. Aubry, F. Bossard, G. Staikos, G. Bokias, *J. Rheol.* **2003**, *47*, 577–587.
- [8] H. Kitazono, E. Kaneko, *Temperature-Responsive Hydrogel EP1659143 A1*, **2006**.
- [9] C. Karakasyan, S. Lack, F. Brunel, P. Maingault, D. Hourdet, *Biomacromolecules* **2008**, *9*, 2419–2429.
- [10] X. Zhang, X. Jiang, X. Zhang, H. Dai, *J. Polym. Sci. B Polym. Phys.* **2010**, *48*, 1799–1808.
- [11] R. Kumar, S. R. Raghavan, *Langmuir* **2010**, *26*, 56–62.
- [12] T. Vermonden, J. Van Der Gucht, P. De Waard, A. T. M. Marcelis, N. A. M. Besseling, E. J. R. Sudhölter, G. J. Fleer, M. A. Cohen Stuart, *Macromolecules* **2003**, *36*, 7035–7044.
- [13] T. Vermonden, M. J. van Steenberg, N. a M. Besseling, A. T. M. Marcelis, W. E. Hennink, E. J. R. Sudhölter, M. a Cohen Stuart, *J. Am. Chem. Soc.* **2004**, *126*, 15802–15808.
- [14] B. J. B. Folmer, R. P. Sijbesma, E. W. Meijer, *J. Am. Chem. Soc.* **2001**, *123*, 2093–2094.
- [15] P. Brocorens, M. Linares, C. Guyard-Duhayon, R. Guillot, B. Andrioletti, D. Suhr, B. Isare, R. Lazzaroni, L. Bouteiller, *J. Phys. Chem. B* **2013**, *117*, 5379–5386.

General conclusion

In order to expand the synthetic accessibility of bis-urea systems, we developed a new family of bis-ureas by adding an ester moiety in the side chains. Unexpectedly, this modification changed dramatically the assembly and the properties of solutions of such bis-ureas. Initially the purpose of developing such compounds was to use them in a supramolecular balance to measure weak interactions but different side projects appeared along the way.

We started by characterizing the assemblies formed by these ester bis-ureas and showed that they form different assemblies than the highly studied alkyl bis-ureas even though a cooperative transition between two assemblies at a fixed temperature could still be observed. Contrary to the alkyl bis-ureas which exhibit at low temperature a thick assembly, called the tube, bearing three monomers per section and a cavity inside the assembly, the ester bis-ureas exhibits a thick assembly, called the double filament, without cavity and bearing only two molecules per section. In both cases the assemblies are helical when using a chiral bis-urea. At higher temperature, after the transition, alkyl bis-ureas assemblies are not CD-active contrary to the ester bis-ureas assemblies which are chiral filaments.

The properties of amplification of chirality and more precisely the majority rules effect exhibited by the ester bis-ureas were studied and a structure to properties relationship was determined. Indeed, the comparison of the different types of assemblies revealed that the thickness of the structure had an impact on both the helix reversal penalty (HRP) and the mismatch penalty (MMP). A more rigid structure such as the nanotube of EHUT presents a higher HRP as a helix reversal implies the destabilization of more bonds than in the case of a double or single filament. In contrast, the decrease of the MMP in the case of thicker assemblies could be tentatively explained by an increase of the pitch of the helix.

Concerning the main objective, we used the supramolecular balance principle to measure halogen...halogen interactions as those had never been measured nor observed in solution. After many twists and turns in the design of our final system, we finally succeeded in obtaining a molecule bearing a simple interacting moiety (CBr_3) and its reference. Both compounds possess (i) a suitable solubility, and (ii) the expected assembly structures with a cooperative transition between both assemblies in a measurable temperature range. It took some time to understand the influence of the solvent on the interactions and to identify a solvent that would both allow the interactions to occur and in which the compound would still be soluble. In order to obtain quantitative measurements, we had to devise a simple model taking into account both the interactions within the assembly and with the solvent. By mixing both the CBr_3 bis-urea and its reference bis-urea in different proportions in chlorohexane, we were able to link the dependence of the transition temperature with the bis-urea composition to the value of the halogen...halogen interaction energy.

Of course, this value is only a crude approximation because the exact supramolecular structures are not known and because the model may be too simplistic. Still, we offer a proof of the existence of halogen...halogen interactions in solution.

Once fully developed, this approach can be easily transposed to other interactions but structural studies will be needed each time to quantify the number of interactions involved during the transition.

A highly interesting aspect of the research we performed on ester bis-ureas is the property of some of them to form a third type of assembly at lower temperatures while the two classical structures still exist at higher temperatures. We showed that this new assembly is highly similar to the previously observed double filament but with an additional interaction. We characterized this interaction as an HB between the ester moiety and an aliphatic urea N-H. We varied the structure of every part of the ester bis-urea in order to understand the impact of the structure of the bis-urea on the assembly. We observed that the phenylalanine moiety seems to be essential for the interaction to take place. We also showed that out of the four different spacers used, the xylene spacer is the most interesting as it showed the largest effect and presented good association and solubility properties. The influence of the side chain was studied as well and it was shown that branched alkyl chains destabilize this new assembly. The impact of the length of the alkyl chain was investigated and the optimum chain length seems to $10 < n < 20$. We also showed that the enantiomeric excess has a dramatic impact on the quantity of bonded ester as no interactions with the ester moiety were observed below 50% ee. This new transition exhibits interesting rheological properties as an increase in viscosity is observed when heating through the transition. We can thus characterize these compounds as potential thermothickener additives. Of course many characteristics remain to be optimized in order to envision a practical application. In particular, a promising way to increase the thermal stability of the assemblies is to tune the structure of the aromatic spacer. It should also be possible to mix different bis-ureas to vary the transition and thus tune the viscosity increase.

The study of ester bis-ureas is far from finished and it would be interesting to perform more advanced structural studies. For instance, NMR studies would help greatly to characterize the structure of the assemblies. Up to now, such studies have not been possible because of the severe line broadening of these gels (even with an HR-MAS probe). In order to obtain a good signal in NMR, it would be interesting to synthesize chain stoppers in order to form shorter assemblies as it should highly decrease the viscosity of the solution and allow measurements in NMR.

A better understanding of the structure, particularly in the case of Phe based bis-ureas would allow a precise assignment of the interactions measured with the supramolecular balance and it may also allow to better understand the interaction between the N-H and the ester moieties, which would then allow to optimize the properties of the thermothickening additives more rationally.

Chapter 6 : Synthesis and characterization techniques

A. Characterization techniques

1. SANS

Small-angle neutron scattering measurements were made at the LLB (Saclay, France) on the Pace instrument for the toluene-d₈ solutions or at the ILL (Grenoble, France) on the D11 instrument for the Me-cyclohexane-d₁₄ solutions. Measurements were taken at two distance-wavelength combinations to cover the 4×10^{-3} to 0.24 \AA^{-1} q-range, where the scattering vector q is defined as usual, assuming elastic scattering ($q = (4\pi/\lambda)\sin(\theta/2)$, where θ is the angle between incident and scattered beam). Data were corrected for the empty cell signal and the solute and solvent incoherent background. A light water standard was used to normalize the scattered intensities to cm^{-1} units.

The following form factor for infinitely long rigid fibrillar objects of homogeneous contrast (specific contrast, $\overline{\Delta b^2}$) and circular cross-section (radius, r) was used to fit the data for all bisureas except for *rac-i-BuAla*, *rac-EtHexVal*, *rac-EtHexPhe* and *rac-EtHexAla* at 70°C in toluene:

$$I = \frac{\pi c}{q} \overline{\Delta b^2} \frac{n_L M_0}{N_a} \left[2 \frac{J_1(qr)}{qr} \right]^2$$

N_a is Avogadro number, c the concentration (g cm^{-3}), M_0 the bis-urea molar mass and J_1 the Bessel function of the first kind. The values of the specific contrast ($\overline{\Delta b^2}$) were calculated based on the measured density of **EtHex** (1.06 g cm^{-3}) and are given in Table 18 and Table 19.

The experimental curves were adjusted by linear regression in a $\ln(qI)$ versus q^2 plot. The number n of molecule in the cross-section can be derived from n_L (the number of molecule per unit length) by assuming an average intermolecular distance of 4.6 \AA , which is the usual spacing for hydrogen bonded urea groups:

$$n = 4.6 \times n_L$$

The following form factor for long rigid fibrillar objects of length $2H$, homogeneous contrast and circular cross-section was used to fit the data for *rac-i-BuAla*, *rac-EtHexVal*, *rac-EtHexPhe* and *rac-EtHexAla* at 70°C in toluene.

$$I = c \overline{\Delta b^2} 2H \frac{n_L M_0}{N_a} \int_0^{\pi/2} \left[\frac{\sin(qH \cos \alpha)}{qH \cos \alpha} 2 \frac{J_1(qr \sin \alpha)}{qr \sin \alpha} \right]^2 \sin \alpha d\alpha$$

diMeHex	EtHex	HexEtHex	i-BuAla	EtHexVal	EtHexPhe	EtHexAla
2.15	2.15	2.08	1.74	2.09	1.80	2.00

Table 18 : Values of the specific contrast $\overline{\Delta b^2}$ ($10^{21} \text{ cm}^2 \text{ g}^{-2}$) used for racemic bis-urea in toluene-d₈.

S-EtHexAla	S-EtHexLeu	S-EtHexVal
2,15	2,15	2,15

Table 19 : Values of the specific contrast $\overline{\Delta b^2}$ ($10^{21} \text{ cm}^2 \text{ g}^{-2}$) used for enantiopure bis-ureas in Me-cyclohexane-d₁₄.

2. FTIR

FT-IR measurements were performed on a Nicolet iS10 spectrometer in a CaF₂ cell of 1.0 mm pathlength and are corrected for air, solvent and cell absorption.

3. CD

CD measurements were performed on a Jasco J-1500 spectrometer equipped with a Peltier thermostated cell holder and Xe laser (lamp XBO 150W/4). Data was recorded with the following parameters: 20 nm.min⁻¹ sweep rate, 0.05 nm data pitch and 1.0 nm bandwidth and between 300 and 200 nm. Temperature dependent measurements were recorded at a 100 nm.min⁻¹ sweep rate, heating at 1°C.min⁻¹. Spectra were corrected for solvent and cell contribution. For CD measurements, a 1 mm quartz cell was used. Molar CD values are reported in L.mol⁻¹.cm⁻¹ and are expressed as follows: $\Delta\epsilon = \theta / (32980 \times l \times c)$ where θ is the measured ellipticity (mdeg), l is the optical path length in cm and c is the total concentration in mol.L⁻¹. For all samples, LD contribution was negligible ($\Delta LD < 0.005$ dOD).

4. Rheology

Rheology measurements were performed on a Haake RS600 rheometer equipped with a sandblasted stainless steel cone/plate geometry with a 35 mm diameter, a 53 μ m gap and a 2° angle. The temperature is controlled with a Peltier thermostat.

5. ITC

Isothermal titrating calorimetry (ITC) data were recorded on a Microcal VP-ITC apparatus, injecting a toluene solution of the sample into neat toluene. Injections of 5 μ L over 10 seconds were performed every 300 seconds at a stirring rate of 260 rpm.

6. nDSC

Solution-phase differential scanning calorimetry (nDSC) measurements were performed on a TA Instruments nDSC III system in aromatic solvents using 3 full heating/cooling cycles, at 1°C.min⁻¹.

7. Molecular modeling

a. Obtaining the assemblies

All our structures have been modelled with the Materials Studio 6.0 modelling package (Biovia, formerly Accelrys), by molecular mechanics (MM) and molecular dynamics (MD) methods. The Dreiding^[1] force field was used. The charges on the atoms were assigned from the PCFF force field^[2,3], the dielectric constant was distance-dependent, and a long-range interaction cutoff distance was set to 14 Å with a spline width of 3 Å. Guess stacks of 64 bisurea molecules were built, and were first optimized by MM. Then, constrained MD simulations were run (at 300K for 100ps) by keeping fix the position of the urea groups in order to further release the stress in the side groups without breaking

the hydrogen bonds network. At this stage, it appeared that starting MD simulations directly at 300K can break the hydrogen bonds network for some of the structures, due to residual strains. Thus, to gradually thermalize the structures, short (100ps) MD simulations were first run at 150K. Finally, the structures were equilibrated at 300K for 1.5 ns (or 20 ns for S-EtHex^{Ala}). The MM energy minimizations were performed with a conjugate gradient algorithm until a convergence criterion of 0.001 kcal/mol.Å was reached.

The MD simulations were performed in the canonical (N,V,T) ensemble. The Nosé thermal bath coupling^[4] was used to maintain the temperature at 300 K, with a coupling constant of 0.1. The Verlet velocity algorithm was used to integrate the equations of motion with a 1 fs time step.

b. Analyses of the assemblies

To account for thermal fluctuations, the all the analyses were performed over the second half of the last MD performed at 300K. For the absorption and CD spectra, the excitonic model has been applied to each frame of the trajectories: a supra-molecular Hamiltonian was built on the basis of localised excited states. Those states were obtained from CIS calculations performed on individual molecules using the ZINDO parameterization implemented in the Gaussian package.^[5] To ensure the convergence of the spectra at high energy, 150 excited states have been considered. After diagonalization of this Hamiltonian, supra-molecular transition dipole and magnetic moments were calculated and used to compute the oscillator and rotatory strengths. Finally, a Gaussian broadening of 0.1 eV was applied before averaging over the MD.

B. Synthesis

1. Common synthetic methods

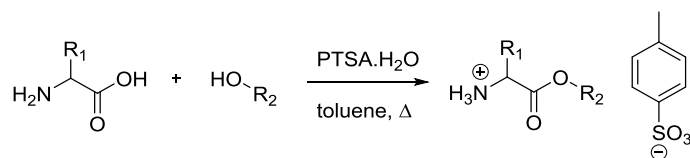
All amino acids were purchased from Sigma-Aldrich or Alfa Aesar (99% purity) and used as received. TDI was purchased from Sigma Aldrich (purity \geq 98%) and was used directly.

Chromatography-grade solvents were used as received. Dried CH₂Cl₂ and THF were obtained from an SPS solvent purification system (IT-Inc) and stored on 4Å molecular sieves. NEt₃ and DIEA were dried by distillation over CaH₂ and stored over 4Å molecular sieves.

NMR spectra were recorded on a Bruker Avance 400, 300 or 200 spectrometers and calibrated to the residual solvent peak. Peaks are reported in ppm with their corresponding multiplicity (s: singlet; d: doublet, t: triplet; q: quartet; quint: quintet; hept: heptuplet; dt: doublet of triplets; td: triplet of doublets), integration, and respective J coupling constants are given in hertz. Exact mass measurements (HRMS) were obtained on TQ R30-10 HRMS spectrometer by ESI+ ionization and are reported in m/z for the major signal.

The flash chromatography purification was made with a Grace Reveleris and columns of the same brand. The water was purified using a milli-Q system.

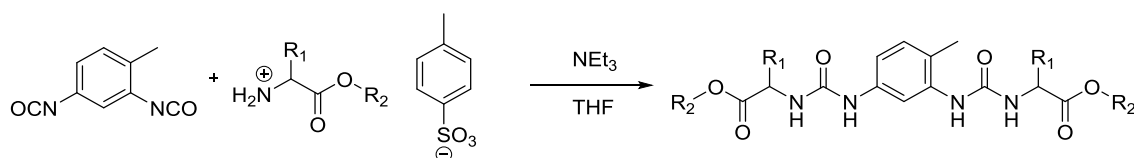
a. Synthesis of ester ammonium tosylate salts (Method A)



This synthesis was adapted from: S. Cantekin, H. M. M. ten Eikelder, A. J. Markvoort, M. A. J. Veld, P. A. Korevaar, M. M. Green; A. R. A. Palmans, E. W. Meijer, *Angew. Chem. Int. Ed.* **2012**, 51, 6426-6431.

1eq. of amino acid, 1.1 eq. of alcohol and 1.1 eq. of PTSA.H₂O were added to toluene (0.15M) and the mixture was stirred under reflux equipped with a Dean-Starck apparatus for 12h. The mixture was then concentrated under reduced pressure and diluted in Et₂O. The solution was put into ice to precipitate for a couple of hours. The precipitate was then filtered, washed with cold Et₂O and dried under vacuum.

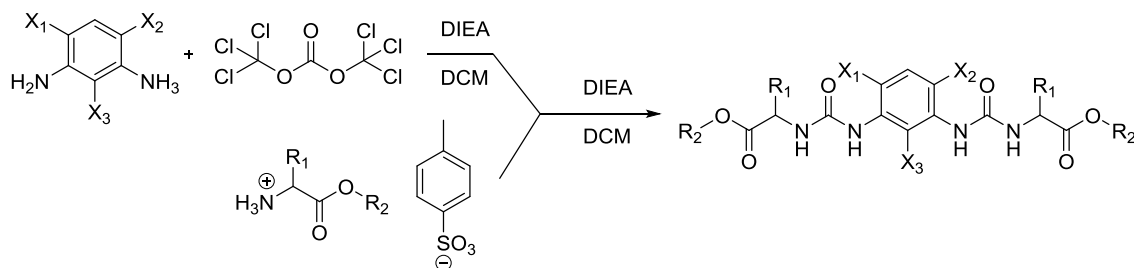
b. Synthesis of ester bis-ureas with a toluene spacer (Method B)



This synthesis was adapted from: F. Lortie, S. Boileau, L. Bouteiller, C. Chassenieux, B. Demé, G. Ducouret, M. Jalabert, F. Lauprêtre, P. Terech, *Langmuir* **2002**, 18, 7218–7222.

2.2 eq. of the ammonium ester tosylate was dissolved in anhydrous THF (0.05 M) under Ar. 2.2 eq. of NEt₃ and 1 eq. of TDI were added to the mixture. The mixture was stirred at room temperature for 48h. The mixture was then concentrated under reduced pressure and either purified by column chromatography or recrystallized from acetonitrile.

c. Synthesis of ester bis-ureas with other spacers (Method C)

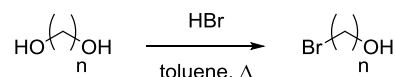


This synthesis was adapted from: I. Giannicchi, B. Jouvelet, B. Isare, M. Linares, A. Dalla Cort, L. Bouteiller, *Chem. Commun.* **2014**, 50, 611–613.

Under Ar atmosphere, a 70 mM solution of the diaminobenzene derivative and 2 eq. of DIEA in DCM was added at 2.5 mL/h to a 60 mM solution of 0.66 eq. of triphosgene in DCM. The mixture was

stirred for 1h after addition and a 0.3 M solution of 2.1 eq. of the ammonium ester tosylate and 6.3 eq. of DIEA in DCM was added to the mixture. The solution was concentrated under reduced pressure and the product was either purified by column chromatography or recrystallized from acetonitrile.

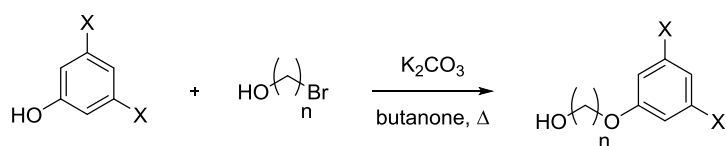
d. Synthesis of bromoalcohols (Method D)



This synthesis was adapted from: F. L. M. Pattison, J. B. Stothers, R. G. Woolford *J. Am. Chem. Soc.*, **1956**, 78 (10), pp 2255–2259.

The diol was dissolved in toluene (0.3 M) and 1.2eq of 48 wt% aqueous HBr was added to the mixture. The mixture was stirred and heated at reflux for 36h. A further 0.5eq of 48 wt% aqueous HBr was added and the mixture was heated to reflux for 36h. If some starting product was remaining, the mixture was refluxed for an additional 36h. The mixture was then diluted with Et₂O and washed with a solution of NaOH 1M and then brine. The organic phase was dried with MgSO₄ and concentrated under reduced pressure. The product was purified by flash chromatography.

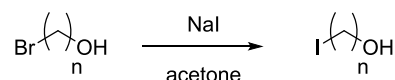
e. Synthesis of phenoxy alcohols (Method E)



This synthesis was adapted from: W. Huang, M. Wang, C. Du, Y. Chen, R. Qin, L. Su, C. Zhang, Z. Liu, C. Li, Z. Bo, *Chem. Eur. J.* **2011**, 17, 440–4.

The phenol derivative and 1.1 eq. of a bromoalcohol were dissolved in butanone (0.3 M), 1.1 eq. of K₂CO₃ was added and the mixture was stirred under Ar at reflux temperature for 24h. The mixture was then washed with water and extracted with DCM. The organic phase was dried with MgSO₄ and concentrated under reduced pressure. The product was purified by flash chromatography.

f. Synthesis of iodoalcohols (Method F)

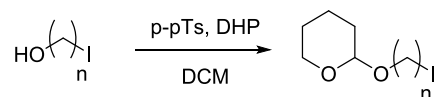


This synthesis was adapted from: H. Finkelstein, *Ber. Dtsch. Chem. Ges.* **1910**, 43, 1528–1532.

A bromoalcohol was added to 1.1 eq. of a 0.5M NaI solution in acetone. The mixture was stirred at room temperature for 3h. A NaBr precipitate was observed. The mixture was extracted with DCM

and washed with water. The organic phase was dried with MgSO_4 and concentrated under reduced pressure. The product was purified by flash chromatography.

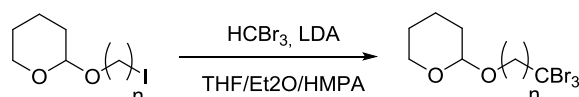
g. Synthesis of THP-protected iodoalcohols (Method G)



This synthesis was adapted from: B. C. Gorske, C. T. Mbofana, S. J. Miller, *Org. Lett.* **2009**, *11*, 4318–21.

A iodoalcohol and 0.15 eq. of pyridinium p-toluene sulfonate were dissolved in DCM (0.5 M) and 1.5 eq. of dihydropyran was added to the mixture. The mixture was stirred at room temperature overnight in the dark. The mixture was then concentrated under reduced pressure and the product was purified by flash chromatography.

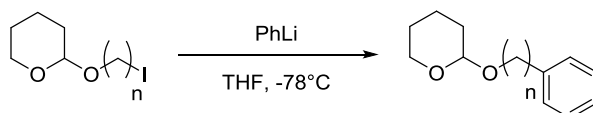
h. Synthesis of THP-protected tribromomethylalcohols (Method H)



This synthesis was adapted from: E. Lee, C. M. Park, J. S. Yun, *J. Am. Chem. Soc.* **1995**, *117*, 8017–8018.

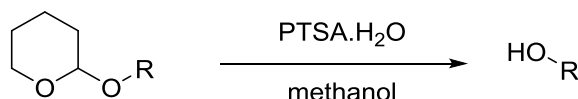
Under Ar atmosphere, a 0.33M solution of 3.3 eq. of DIPA in a 50/50 mix of THF and Et_2O was cooled to -110°C (ethanol bath) and 3 eq. of BuLi (1.6M in hexane) was added dropwise. A 1.5M solution of 3 eq. of HBr_3 in a 2/1/1 mix of THF, Et_2O and HMPA was added to the LDA solution. The reaction mixture was then warmed to -80°C by adding acetone to the bath and a 0.8M solution of 1 eq. of the THP-protected iodoalcohol in THF was added to the mixture. After 30 min the mixture was warmed to room temperature. The mixture was then quenched with a saturated NH_4Cl aqueous solution and extracted with Et_2O . The organic phase was dried with MgSO_4 and concentrated under reduced pressure. The product was purified by flash chromatography.

i. Synthesis of THP-protected phenylalcohols (Method I)



2.5 eq. of phenyl lithium (1.8M in hexane) was added to a solution of THP-protected iodoalcohol in THF (0.3 M) at -78°C under Ar. After 30 minutes the mixture was warmed to room temperature. The mixture was then quenched with a saturated NH_4Cl aqueous solution and extracted with DCM. The organic phase was dried with MgSO_4 and concentrated under reduced pressure. The product was purified by flash chromatography.

j. Deprotection of protected THP alcohols (Method J)



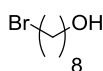
This synthesis was adapted from: E. Lee, C. M. Park, J. S. Yun, *J. Am. Chem. Soc.* **1995**, *117*, 8017–8018.

The THP-protected alcohol and 0.1 eq. of PTSA.H₂O were added to methanol (0.3 M) and the mixture was stirred overnight. The mixture was diluted in DCM and washed with brine. The organic phase was dried with MgSO₄ and concentrated under reduced pressure. The product was purified by flash chromatography.

2. Precursors

a. Bromoalcohols

8-bromooctanol



Preparation was achieved following the method D using commercially available octan-1,8-diol.

The product was purified by flash chromatography (0 to 20% acetone/PE).

13.150 g (92%) of pure product were obtained as a yellow oil.

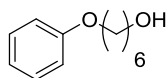
¹H NMR (300 MHz, CDCl₃) δ 3.61 (t, 2H, HO-CH₂, ²J = 6.5 Hz), 3.39 (t, 2H, Br-CH₂, ²J = 6.8 Hz), 1.84 (p, 2H, Br-CH₂-CH₂, ²J = 7.1 Hz), 1.54 (p, 2H, HO-CH₂-CH₂, ²J = 6.7 Hz), 1.48-1.24 (m, 8H, CH₂)

¹³C NMR (101 MHz, CDCl₃) δ 62.93, 34.05, 32.84, 32.46, 29.26, 28.76, 28.14, 25.68.

HRMS (ESI, m/z) not observed due to high reactivity of the compound but structure confirmed in HRMS later in the reaction chain

b. Phenoxyalcohols

6-phenoxyhexanol



Preparation was achieved following the method E using commercially available 6-bromohexanol and phenol.

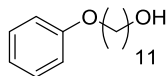
The product was purified by flash chromatography (20% AcOEt/PE).

2.859 g (93%) of pure product were obtained as a low viscous translucent oil.

¹H NMR (300 MHz, CDCl₃) δ 7.35-7.25 (m, 2H, ArH), 6.99-6.88 (m, 3H, ArH), 3.97 (t, 2H, Ar-O-CH₂, ²J = 6.4 Hz), 3.65 (t, 2H, HO-CH₂, ²J = 6.2 Hz), 1.84-1.72 (m, 2H, Ar-O-CH₂CH₂), 1.67-1.55 (m, 2H, HO-CH₂CH₂), 1.55-1.35 (m, 4H, CH₂).

¹³C NMR (101 MHz, CDCl₃) δ 159.15, 129.51, 120.62, 114.60, 67.83, 62.95, 32.73, 29.37, 26.01, 25.65.

11-phenoxyundecanol



Preparation was achieved following the method E using commercially available 11-bromoundecanol and phenol.

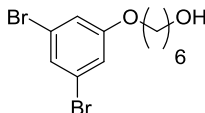
The product was purified by flash chromatography (DCM).

1.825 g (87%) of pure product were obtained as a low viscous translucent oil.

¹H NMR (300 MHz, CDCl₃) δ 7.35-7.25 (m, 2H, ArH), 6.99-6.88 (m, 3H, ArH), 3.97 (t, 2H, Ar-O-CH₂, ²J = 6.4 Hz), 3.65 (t, 2H, HO-CH₂, ²J = 6.2 Hz), 1.84-1.72 (m, 2H, Ar-O-CH₂CH₂), 1.67-1.55 (m, 2H, HO-CH₂CH₂), 1.55-1.25 (m, 14H, CH₂).

¹³C NMR (101 MHz, CDCl₃) δ 129.50, 120.56, 114.63, 68.01, 63.16, 32.93, 29.70 (2C), 29.67, 29.63, 29.54, 29.51, 29.43, 26.18, 25.87.

6-(3,5-dibromophenoxy)hexanol



Preparation was achieved following the method E using commercially available 6-bromohexanol and 3,5-dibromophenol.

The product was purified by flash chromatography (0 to 100% DCM/PE).

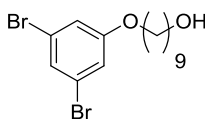
2.743 g (98%) of pure product were obtained as a translucent oil.

¹H NMR (300 MHz, CDCl₃) δ 7.23 (t, 1H, ArH, ²J = 1.6 Hz), 6.98 (d, 2H, ArH, ²J = 1.6 Hz), 3.92 (t, 2H, Ar-O-CH₂, ²J = 6.5 Hz), 3.66 (t, 2H, HO-CH₂, ²J = 6.5 Hz), 1.84-1.72 (m, 2H, Ar-O-CH₂CH₂), 1.67-1.55 (m, 2H, HO-CH₂CH₂), 1.55-1.35 (m, 4H, CH₂).

¹³C NMR (75 MHz, CDCl₃) δ 160.39, 126.31, 123.17, 117.04, 68.58, 62.90, 32.72, 29.08, 25.88, 25.59.

HRMS (ESI, m/z) 374.9391 [M + Na]⁺, 374.9389 calculated for C₁₂H₁₆Br₂O₂Na

9-(3,5-dibromophenoxy)nonanol



Preparation was achieved following the method E using commercially available 9-bromononanol and 3,5-dibromophenol.

The product was purified by flash chromatography (0 to 100% DCM/PE).

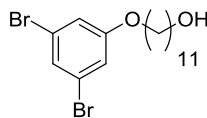
3.079 g (98%) of pure product were obtained as translucent crystals.

¹H NMR (300 MHz, CDCl₃) δ 7.23 (t, 1H, ArH, ²J = 1.6 Hz), 6.98 (d, 2H, ArH, ²J = 1.6 Hz), 3.92 (t, 2H, Ar-O-CH₂, ²J = 6.5 Hz), 3.66 (t, 2H, HO-CH₂, ²J = 6.5 Hz), 1.84-1.72 (m, 2H, Ar-O-CH₂CH₂), 1.67-1.55 (m, 2H, HO-CH₂CH₂), 1.55-1.35 (m, 10H, CH₂).

¹³C NMR (101 MHz, CDCl₃) δ 160.44, 126.26, 123.16, 117.04, 68.72, 63.11, 32.87, 29.58, 29.44, 29.32, 29.08, 26.00, 25.84.

HRMS (ESI, m/z) 416.9859 [M + Na]⁺, 416.9858 calculated for C₁₅H₂₂Br₂O₂Na

11-(3,5-dibromophenoxy)undecanol



Preparation was achieved following the method E using commercially available 11-bromoundecanol and 3,5-dibromophenol.

The product was purified by flash chromatography (0 to 100% DCM/PE).

1.428 g (85%) of pure product were obtained as translucent crystals.

¹H NMR (300 MHz, CDCl₃) δ 7.23 (t, 1H, ArH, ²J = 1.6 Hz), 6.98 (d, 2H, ArH, ²J = 1.6 Hz), 3.92 (t, 2H, Ar-O-CH₂, ²J = 6.5 Hz), 3.66 (t, 2H, HO-CH₂, ²J = 6.5 Hz), 1.84-1.72 (m, 2H, Ar-O-CH₂CH₂), 1.67-1.55 (m, 2H, HO-CH₂CH₂), 1.55-1.35 (m, 14H, CH₂).

¹³C NMR (101 MHz, CDCl₃) δ 160.49, 126.28, 123.18, 117.07, 68.76, 63.20, 32.94, 29.70, 29.63, 29.61, 29.55, 29.40, 29.11, 26.03, 25.88.

HRMS (ESI, m/z) 445.0172 [M + Na]⁺, 445.0171 calculated for C₁₇H₂₆Br₂O₂Na

c. Iodoalcohols

8-iodooctanol



Preparation was achieved following the method F using 8-bromooctanol.

The product was purified by flash chromatography (10% AcOEt/PE).

3.26 g (91%) of a pure product were obtained as a slightly yellow crystalline powder.

¹H NMR (200 MHz, CDCl₃) δ 3.64 (t, 2H, HO-CH₂, ²J = 6.5 Hz), 3.19 (t, 2H, I-CH₂, ²J = 7.0 Hz), 1.82 (p, 2H, I-CH₂-CH₂, ²J = 7.1 Hz), 1.57 (p, 2H, HO-CH₂-CH₂, ²J = 6.5 Hz), 1.45-1.20 (m, 12H, CH₂)

¹³C NMR (101 MHz, CDCl₃) δ 63.07, 33.49, 32.55, 30.41, 29.18, 28.48, 25.63, 7.28.

HRMS (ESI, m/z) not observed due to high reactivity of the compound but structure confirmed in HRMS later in the reaction chain

11-iodoundecanol



Preparation was achieved following the method F using commercially available 11-bromoundecanol.

The product was purified by flash chromatography (10% AcOEt/PE).

8.328 g (95%) of a pure product were obtained as a slightly yellow crystalline powder.

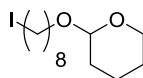
¹H NMR (300 MHz, CDCl₃) δ 3.63 (t, 2H, HO-CH₂, ²J = 6.5 Hz), 3.19 (t, 2H, I-CH₂, ²J = 6.8 Hz), 1.83 (p, 2H, I-CH₂-CH₂, ²J = 7.1 Hz), 1.57 (p, 2H, HO-CH₂-CH₂, ²J = 6.7 Hz), 1.45-1.25 (m, 14H, CH₂)

¹³C NMR (101 MHz, CDCl₃) δ 63.17, 33.69, 32.92, 30.62, 29.66, 29.57, 29.52, 29.51, 28.65, 25.86, 7.44.

HRMS (ESI, m/z) not observed due to high reactivity of the compound but structure confirmed in HRMS later in the reaction chain

d. THP-protected alcohols

2-(8-iodooctyloxy)tetrahydropyran



Preparation was achieved following the method G using 8-iodooctanol.

The product was purified by flash chromatography (50% DCM/PE).

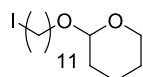
9.898 g (91%) of pure product were obtained as a translucent oil.

¹H NMR (300 MHz, CDCl₃) δ 4.58 (t, 1H, O-CH-O, ²J = 3.0 Hz), 3.70 (AB spin system, 2H, O-CH₂, ²J = 70.3Hz), 3.56 (AB spin system, 2H, O-CH₂, ²J = 59.8Hz), 3.19 (t, 2H, I-CH₂, ²J = 7.1 Hz), 1.90-1.68 (m, 2H, CH₂), 1.68-1.48 (m, 2H, CH₂), 1.48-1.25 (m, 20H, CH₂)

¹³C NMR (101 MHz, CDCl₃) δ 98.91, 67.65, 62.40, 33.60, 30.87, 30.51, 29.77, 29.31, 28.55, 26.23, 25.60, 19.79, 7.27.

HRMS (ESI, m/z) 363.0790 [M + Na]⁺, 363.0791 calculated for C₁₃H₂₅IO₂Na

2-(11-iodoundecyloxy)tetrahydropyran



Preparation was achieved following the method G using 11-iodoundecanol.

The product was purified by flash chromatography (50% DCM/PE).

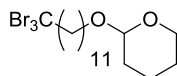
9.898 g (91%) of pure product were obtained as a translucent oil.

¹H NMR (300 MHz, CDCl₃) δ 4.58 (t, 1H, O-CH-O, ²J = 3.0 Hz), 3.70 (AB spin system, 2H, O-CH₂, ²J = 70.3Hz), 3.56 (AB spin system, 2H, O-CH₂, ²J = 59.8Hz), 3.19 (t, 2H, I-CH₂, ²J = 7.1 Hz), 1.90-1.68 (m, 2H, CH₂), 1.68-1.48 (m, 2H, CH₂), 1.48-1.25 (m, 20H, CH₂)

¹³C NMR (75 MHz, CDCl₃) δ 98.76, 67.60, 62.25, 33.55, 30.77, 30.48, 29.73, 29.50, 29.44, 29.37, 28.51, 26.22, 25.52, 19.68, 7.17.

HRMS (ESI, m/z) 405.1264 [M + Na]⁺, 405.1261 calculated for C₁₆H₃₁IO₂Na

2-(12-tribromododecyloxy)tetrahydropyran



Preparation was achieved following the method H using 2-(11-iodoundecyloxy)tetrahydropyran.

The product was purified by flash chromatography (40% DCM/PE).

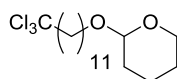
7.364 g (92%) of pure product were obtained as a brown oil.

¹H NMR (300 MHz, CDCl₃) δ 4.58 (t, 1H, O-CH-O, ²J = 3.0 Hz), 3.70 (AB spin system, 2H, O-CH₂, ²J = 70.3Hz), 3.56 (AB spin system, 2H, O-CH₂, ²J = 59.8Hz), 2.98 (t, 2H, CBr₃-CH₂, ²J = 7.8 Hz), 1.90-1.68 (m, 2H, CH₂), 1.68-1.48 (m, 2H, CH₂), 1.48-1.25 (m, 20H, CH₂)

¹³C NMR (101 MHz, CDCl₃) δ 98.95, 67.79, 62.45, 60.08, 42.80, 30.92, 29.88, 29.66, 29.65, 29.62, 29.59, 29.55, 29.43, 28.01, 26.36, 25.65, 19.83.

HRMS (ESI, m/z) 528.9750 [M + Na]⁺, 528.9746 calculated for C₁₇H₃₁Br₃O₂Na

2-(12-trichlorododecyloxy)tetrahydropyran



Preparation was achieved following the method H using 2-(11-iodoundecyloxy)tetrahydropyran.

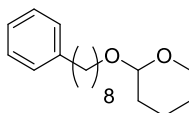
The product was purified by flash chromatography (40% DCM/PE).

1.520 g (78%) of pure product were obtained as a translucent oil.

¹H NMR (300 MHz, CDCl₃) δ 4.58 (t, 1H, O-CH-O, ²J = 3.0 Hz), 3.70 (AB spin system, 2H, O-CH₂, ²J = 70.3Hz), 3.56 (AB spin system, 2H, O-CH₂, ²J = 59.8Hz), 2.67 (t, 2H, CCl₃-CH₂, ²J = 8.0 Hz), 1.90-1.68 (m, 2H, CH₂), 1.68-1.48 (m, 2H, CH₂), 1.48-1.25 (m, 20H, CH₂)

¹³C NMR (75 MHz, CDCl₃) δ 100.24, 98.82, 67.65, 62.31, 55.20, 30.79, 29.75, 29.52, 29.48, 29.45, 29.39, 29.26, 28.32, 26.38, 26.22, 25.51, 19.70.

2-(8-phenyloctyloxy)tetrahydropyran



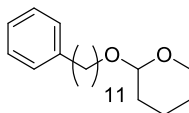
Preparation was achieved following the method I using 2-(8-iodooctyloxy)tetrahydropyran.

The product was purified by flash chromatography (25% DCM/PE).

681 mg (72%) of pure product were obtained as a translucent oil.

¹H NMR (300 MHz, CDCl₃) δ 7.33-7.13 (m, 5H, Ar), 4.59 (t, 1H, O-CH-O, ²J = 3.7 Hz), 3.70 (AB spin system, 2H, O-CH₂, ²J = 70.3Hz), 3.56 (AB spin system, 2H, O-CH₂, ²J = 59.8Hz), 3.42 (t, 2H, Ph-CH₂, ²J = 6.9 Hz), 1.90-1.68 (m, 2H, CH₂), 1.68-1.48 (m, 2H, CH₂), 1.48-1.25 (m, 20H, CH₂)

2-(11-phenylundecyloxy)tetrahydropyran



Preparation was achieved following the method I using 2-(11-iodoundecyloxy)tetrahydropyran.

The product was purified by flash chromatography (25% DCM/PE).

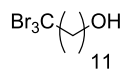
9.520 g (80%) of pure product were obtained as a translucent oil.

¹H NMR (400 MHz, CDCl₃) δ 7.37 – 7.26 (m, 2H, Ar), 7.21 (d, 3H, Ar, J = 7.3 Hz), 4.62 (dd, 1H, O-CH-O, J = 4.4, 2.8 Hz), 3.92 (ddd, 1H, O-CH₂, J = 11.1, 7.4, 3.4 Hz), 3.77 (dt, 1H, O-CH₂, J = 9.6, 6.9 Hz), 3.59 – 3.49 (m, 1H, O-CH₂), 3.42 (dt, 1H, O-CH₂, J = 9.6, 6.7 Hz), 2.68 – 2.60 (m, 2H, Ph-CH₂), 1.93-1.82 (m, 1H, CH₂), 1.84 – 1.69 (m, 1H, CH₂), 1.68 – 1.50 (m, 4H, CH₂), 1.44 – 1.29 (m, 16H, CH₂).

¹³C NMR (101 MHz, CDCl₃) δ 142.93, 128.39, 128.20, 125.53, 98.84, 67.70, 62.31, 36.01, 31.53, 30.82, 29.79, 29.60, 29.58, 29.52, 29.50, 29.35, 26.27, 25.55, 19.72.

e. Trihalogenomethylalcohols

12-tribromododecanol



Preparation was achieved following the method J using 2-(12-tribromododecyloxy)tetrahydropyran.

The product was purified by flash chromatography (40% DCM/PE).

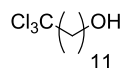
838 mg (98%) of pure product were obtained as a highly viscous brown oil.

¹H NMR (300 MHz, CDCl₃) δ 3.64 (t, 2H, CH₂-OH, ²J = 6.5 Hz), 2.97 (t, 2H, CBr₃-CH₂, ²J = 7.8 Hz), 1.90-1.68 (m, 2H, CH₂), 1.68-1.48 (m, 2H, CH₂), 1.48-1.25 (m, 20H, CH₂)

¹³C NMR (101 MHz, CDCl₃) δ 63.21, 60.10, 42.81, 32.94, 29.69, 29.66, 29.62, 29.56, 29.55, 29.44, 28.02, 25.88.

HRMS (ESI, m/z) not observed due to high reactivity of the compound but structure confirmed in HRMS later in the reaction chain

12-trichlorododecanol



Preparation was achieved following the method J using 2-(12-trichlorododecyloxy)tetrahydropyran.

The product was purified by flash chromatography (40% DCM/PE).

420 mg (37%) of pure product were obtained as a highly viscous translucent oil.

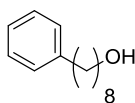
¹H NMR (400 MHz, CDCl₃) δ 3.63 (t, 2H, Cl₃C-CH₂, ²J = 6.6 Hz), 2.69 – 2.62 (m, 2H, OH-CH₂), 1.76 (ddd, 2H, CH₂, J = 11.6, 9.4, 6.1 Hz), 1.62 – 1.51 (m, 2H, CH₂), 1.47 – 1.23 (m, 16H, CH₂).

¹³C NMR (101 MHz, CDCl₃) δ 63.04, 55.20, 32.79, 29.54, 29.47, 29.40, 29.39, 29.26, 28.32, 26.38, 25.73.

HRMS (ESI, m/z) not observed due to high reactivity of the compound but structure confirmed in HRMS later in the reaction chain

f. Phenylalcohols

8-phenyloctanol



Preparation was achieved following the method J using 2-(8-phenyloctyloxy)tetrahydropyran.

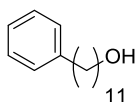
The product was purified by flash chromatography (25% AcOEt/PE).

440 mg (90%) of pure product were obtained as a highly viscous translucent oil.

¹H NMR (400 MHz, CDCl₃) δ 7.31 – 7.24 (m, 2H, Ar-H), 7.21 – 7.15 (m, 3H, Ar-H), 3.63 (t, 2H, Ph-CH₂, J = 6.7 Hz), 2.65 – 2.57 (m, 2H, OH-CH₂), 1.70 – 1.49 (m, 4H, CH₂), 1.43 – 1.25 (m, 8H, CH₂).

¹³C NMR (101 MHz, CDCl₃) δ 142.98, 128.50, 128.33, 125.67, 63.13, 36.08, 32.89, 31.59, 29.57, 29.47, 29.35, 25.85.

11-phenylundecanol



Preparation was achieved following the method J using 2-(11-phenylundecyloxy)tetrahydropyran.

The product was purified by flash chromatography (25% AcOEt/PE).

555 mg (95%) of pure product were obtained as a highly viscous translucent oil.

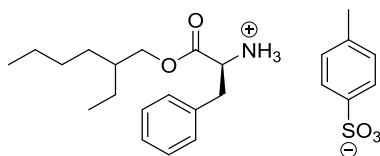
¹H NMR (300 MHz, CDCl₃) δ 7.32 – 7.23 (m, 2H, Ar-*H*), 7.22 – 7.13 (m, 3H, Ar-*H*), 3.64 (t, 2H, Ph-CH₂, *J* = 6.6 Hz), 2.60 (t, 2H, OH-CH₂, *J* = 7.1 Hz), 1.73 – 1.49 (m, 4H, CH₂), 1.49 – 1.21 (m, 14H, CH₂).

¹³C NMR (101 MHz, CDCl₃) δ 129.50, 120.56, 114.63, 68.01, 63.16, 32.93, 29.70, 29.67, 29.63, 29.54, 29.51, 29.43, 26.18, 25.87.

3. Ester ammonium tosylate salts

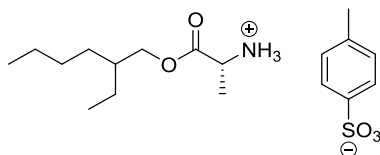
a. Ramified

2-ethylhexyl (S)-phenylalaninate ammonium tosylate salt



The synthesis of this compound was described in: Dirany, M.; Ayzac, V.; Isare, B.; Raynal, M.; Bouteiller, L. *Langmuir* **2015**, *31*, 11443

2-ethylhexyl (R)-alaninate ammonium tosylate salt



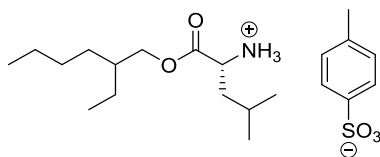
Preparation was achieved following the method A using commercially available 2-ethylhexanol and (R)-Ala.

1.703 g (65%) of product were obtained as a white powder.

¹H NMR (400 MHz, CDCl₃) δ 8.14 (s, 3H, NH₃), 7.73 (d, 2H, Ar-*H*, ²*J* = 8.2 Hz), 7.10 (d, 2H, Ar-*H*, ²*J* = 8.0 Hz), 4.05-3.95 (m, 2H, COO-CH₂), 3.91-3.91 (m, 1H, NH₃-CH), 2.32 (s, 3H, Ar-CH₃), 1.48 (p., 1H, COO-CH₂CH, ²*J* = 5.6 Hz), 1.41 (d, 2H, NH₃-CHCH₃, ²*J* = 7.2 Hz), 1.30-1.14 (m, 8H, CH₂), 0.84 (t, 2H, CH₃, ²*J* = 6.7 Hz), 0.79 (t, 2H, CH₃, ²*J* = 7.3 Hz)

¹³C NMR (101 MHz, CDCl₃) δ 170.05, 141.46, 140.27, 128.80, 126.09, 68.58, 49.10, 38.46, 30.11, 30.03, 28.76, 22.89, 21.30, 15.90, 14.00, 10.81.

2-ethylhexyl (R)-Leucinate ammonium tosylate salt



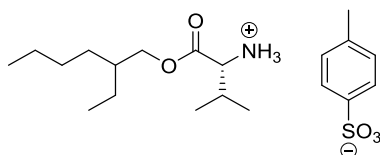
Preparation was achieved following the method A using commercially available 2-ethylhexanol and (R)-Leu.

1.125 g (35%) of product were obtained as a white powder.

^1H NMR (400 MHz, CDCl_3) δ 8.16 (s, 3H, NH_3), 7.75 (d, 2H, Ar-H, $^2J = 7.6$ Hz), 7.11 (d, 2H, Ar-H, $^2J = 7.8$ Hz), 4.05-3.95 (m, 1H, $\text{NH}_3\text{-CH}$), 3.95-3.85 (m, 2H, COO-CH_2), 2.32 (s, 3H, Ar-CH₃), 1.76-1.54 (m, 3H, $\text{NH}_3\text{-CH}$ and $\text{COO-CH}_2\text{CH}$), 1.54-1.43 (m, 1H, $\text{NH}_3\text{-CHCH}_2\text{CH}$), 1.32-1.14 (m, 8H, CH₂), 0.90-0.72 (m, 12H, CH₃)

^{13}C NMR (101 MHz, CDCl_3) δ 170.23, 141.84, 140.19, 128.85, 126.36, 68.75, 68.66, 51.81, 39.61, 38.57, 38.54, 30.28, 30.22, 28.96, 28.85, 24.46, 23.64, 23.59, 23.07, 22.33, 21.97, 21.44, 14.14, 10.97, 10.87. (7 additional peaks due to diastereoisomers)

2-ethylhexyl (R)-valinate ammonium tosylate salt

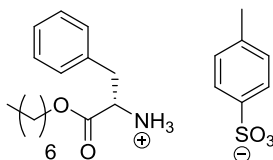


The synthesis of this compound is described in: Dirany, M.; Ayzac, V.; Isare, B.; Raynal, M.; Bouteiller, L. *Langmuir* **2015**, 31, 11443

b. Linear

i. Synthesized from phenylalanine

heptyl (S)-phenylalaninate ammonium tosylate salt



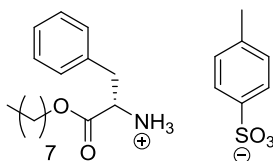
Preparation was achieved following the method A using commercially available heptanol and (S)-Phe.

3.405 g (99%) of product were obtained as a white powder.

^1H NMR (400 MHz, CDCl_3) δ 8.24 (s, 3H, NH_3), 7.74 (d, 2H, Ar-H, $J = 7.8$ Hz), 7.20 – 7.03 (m, 7H, Ar-H), 4.31 – 4.18 (m, 1H, $\text{NH}_3\text{-CH}$), 3.94 – 3.77 (m, 2H, COO-CH_2), 3.24 (dd, 1H, $\text{NH}_3\text{-CH-CH}_2$, $J = 14.0, 5.3$ Hz), 3.04 (dd, $\text{NH}_3\text{-CH-CH}_2$, 1H, $J = 14.0, 8.2$ Hz), 2.32 (s, 3H, Ar-CH₃), 1.37-1.07 (m, 12H, CH₂), 1.07 – 0.97 (m, 2H, CH₂), 0.88 (t, 3H, CH₃, $J = 6.5$ Hz).

^{13}C NMR (101 MHz, CDCl_3) δ 169.02, 141.70, 140.33, 134.48, 129.57, 128.92, 128.69, 127.34, 126.34, 54.34, 36.53, 32.07, 29.86, 29.80, 29.65, 29.50, 29.37, 28.23, 25.75, 22.83, 21.45, 14.25.

octyl (S)-phenylalaninate ammonium tosylate salt

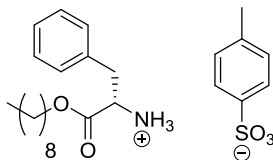


Preparation was achieved following the method A using commercially available octanol and (S)-Phe. 5.943 g (95%) of product were obtained as a white powder.

¹H NMR (300 MHz, CDCl₃) δ 8.44 (s, 3H, NH₃), 7.50 (d, 2H, Ar-H, ²J = 7.6 Hz), 7.38-7.02 (m, 7H, Ar-H), 4.25 (t, 1H, NH₃-CH, ²J = 6.6 Hz), 3.99 (t, 2H, COO-CH₂, ²J = 6.3 Hz), 3.08 (AB spin sytem, 2H, NH₃-CH-CH₂, ²J = 8.1 Hz), 1.80 (quin, 2H, COO-CH₂-CH₂, ²J = 1.8 Hz), 2.27 (s, 3H, Ar-CH₃), 1.39 (quin, 2H, COO-CH₂-CH₂-CH₂, ²J = 6.5 Hz), 1.30-1.00 (m, 10H, CH₂), 0.85 (t, 3H, CH₃, ²J = 7.0 Hz)

¹³C NMR (101 MHz, CDCl₃) δ 169.01, 141.69, 140.33, 134.49, 129.56, 128.91, 128.67, 127.33, 126.33, 66.37, 54.33, 31.93, 29.28, 29.25, 28.21, 25.72, 22.77, 21.44, 14.22.

nonyl (S)-phenylalaninate ammonium tosylate salt

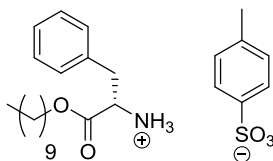


Preparation was achieved following the method A using commercially available nonanol and (S)-Phe. 5.322 g (91%) of product were obtained as a white powder.

¹H NMR (300 MHz, CDCl₃) δ 8.24 (s, 3H, NH₃), 7.75 (d, 2H, Ar-H, ²J = 8.1 Hz), 7.19-7.03 (m, 7H, Ar-H), 4.30-4.20 (m, 1H, NH₃-CH), 3.95-3.80 (m, 2H, COO-CH₂), 3.15 (AB spin sytem, 2H, NH₃-CH-CH₂), 2.33 (s, 3H, Ar-CH₃), 1.39-1.00 (m, 14H, CH₂), 0.90 (t, 3H, CH₃, ²J = 7.0 Hz)

¹³C NMR (101 MHz, CDCl₃) δ 168.86, 141.53, 140.23, 134.32, 129.44, 128.79, 128.56, 127.22, 126.21, 66.26, 54.20, 36.39, 31.87, 29.44, 29.28, 29.21, 28.10, 25.60, 22.67, 21.31, 14.11.

decyl (S)-phenylalaninate ammonium tosylate salt

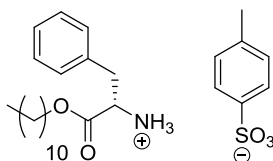


Preparation was achieved following the method A using commercially available decanol and (S)-Phe. 3.218 g (59%) of product were obtained as a white powder.

¹H NMR (300 MHz, CDCl₃) δ 8.24 (s, 3H, NH₃), 7.75 (d, 2H, Ar-H, ²J = 8.1 Hz), 7.19-7.03 (m, 7H, Ar-H), 4.30-4.20 (m, 1H, NH₃-CH), 3.95-3.80 (m, 2H, COO-CH₂), 3.15 (AB spin sytem, 2H, NH₃-CH-CH₂), 2.33 (s, 3H, Ar-CH₃), 1.39-1.00 (m, 16H, CH₂), 0.90 (t, 3H, CH₃, ²J = 7.0 Hz)

¹³C NMR (101 MHz, CDCl₃) δ 169.01, 141.67, 140.36, 134.47, 129.57, 128.92, 128.69, 127.35, 126.34, 66.39, 54.34, 36.53, 32.04, 29.71, 29.62, 29.46, 29.35, 28.23, 25.74, 22.82, 21.45, 14.25.

undecyl (S)-phenylalaninate ammonium tosylate salt



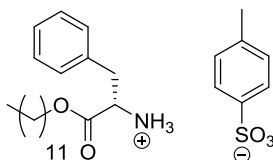
Preparation was achieved following the method A using commercially available undecanol and (S)-Phe.

2.133 g (82%) of product were obtained as a white powder.

¹H NMR (300 MHz, CDCl₃) δ 8.24 (s, 3H, NH₃), 7.75 (d, 2H, Ar-H, ²J = 8.1 Hz), 7.19-7.03 (m, 7H, Ar-H), 4.30-4.20 (m, 1H, NH₃-CH), 3.95-3.80 (m, 2H, COO-CH₂), 3.15 (AB spin sytem, 2H, NH₃-CH-CH₂), 2.33 (s, 3H, Ar-CH₃), 1.39-1.00 (m, 18H, CH₂), 0.90 (t, 3H, CH₃, ²J = 7.0 Hz)

¹³C NMR (101 MHz, CDCl₃) δ 169.01, 141.70, 140.33, 134.49, 129.57, 128.92, 128.67, 127.33, 126.34, 66.38, 54.34, 36.53, 32.06, 29.82, 29.79, 29.77, 29.63, 29.50, 29.36, 25.74, 22.83, 21.44, 14.25.

dodecyl (S)-phenylalaninate ammonium tosylate salt



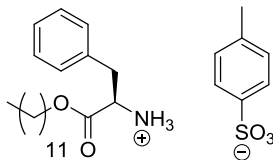
Preparation was achieved following the method A using commercially available dodecanol and (S)-Phe.

10.622 g (86%) of product were obtained as a white powder.

¹H NMR (400 MHz, CDCl₃) δ 8.24 (s, 3H, NH₃), 7.74 (d, 2H, Ar-H, J = 8.2 Hz), 7.20 – 7.04 (m, 6H, Ar-H), 4.29 – 4.19 (m, 1H, NH₃-CH), 3.93 – 3.77 (m, 2H, COO-CH₂), 3.24 (dd, 1H, NH₃-CH-CH₂, J = 14.0, 5.3 Hz), 3.04 (dd, 1H, NH₃-CH-CH₂, J = 14.0, 8.4 Hz), 2.32 (s, 3H, Ar-CH₃), 1.38 – 1.08 (m, 14H, CH₂), 1.08 – 0.96 (m, 2H, CH₂), 0.89 (t, 3H CH₃, J = 6.8 Hz).

¹³C NMR (101 MHz, CDCl₃) δ 169.02, 141.70, 140.31, 134.52, 129.56, 128.90, 128.65, 127.30, 126.33, 66.35, 54.34, 36.53, 32.05, 29.81, 29.78, 29.76, 29.62, 29.49, 29.35, 28.21, 25.73, 22.81, 21.43, 14.24.

dodecyl (R)-phenylalaninate ammonium tosylate salt



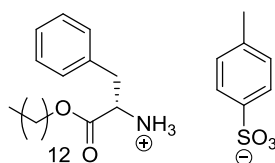
Preparation was achieved following the method A using commercially available dodecanol and (R)-Phe.

2.125 g (86%) of product were obtained as a white powder.

¹H NMR (300 MHz, CDCl₃) δ 8.21 (s, 3H, NH₃), 7.72 (d, 2H, Ar-H, ²J = 8.1 Hz), 7.18-7.03 (m, 7H, Ar-H), 4.30-4.16 (m, 1H, NH₃-CH), 3.94-3.76 (m, 2H, COO-CH₂), 3.14 (AB spin sytem, 2H, NH₃-CH-CH₂), 2.31 (s, 3H, Ar-CH₃), 1.40-0.97 (m, 28H, CH₂), 0.87 (t, 2H, CH₃, ²J = 7.0 Hz)

¹³C NMR (101 MHz, CDCl₃) δ 169.02, 141.70, 140.32, 134.52, 129.56, 128.91, 128.66, 127.31, 126.34, 66.36, 54.34, 36.53, 32.05, 29.76, 29.63, 29.49, 29.35, 28.22, 25.73, 22.82, 21.43, 14.24.

tridecyl (S)-phenylalaninate ammonium tosylate salt

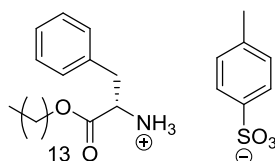


Preparation was achieved following the method A using commercially available decanol and (S)-Phe. 4.138 g (88%) of product were obtained as a white powder.

¹H NMR (400 MHz, CDCl₃) δ 8.18 (s, 3H, NH₃), 7.76 (d, 2H, Ar-H, *J* = 7.9 Hz), 7.23 – 7.05 (m, Ar-H, 7H), 4.27 (dd, NH₃-CH, 1H, *J* = 8.1, 5.3 Hz), 3.88 (m, 2H, COO-CH₂), 3.27 (dd, 1H, NH₃-CH-CH₂, *J* = 14.1, 5.3 Hz), 3.07 (dd, 1H, NH₃-CH-CH₂, *J* = 14.1, 8.2 Hz), 2.35 (s, 3H, Ar-CH₃), 1.43 – 1.11 (m, 20H, CH₂), 1.06 (q, 2H, CH₂, *J* = 7.7 Hz), 0.91 (t, 3H, CH₃, *J* = 6.6 Hz).

¹³C NMR (101 MHz, CDCl₃) δ 141.69, 140.35, 134.45, 129.57, 128.93, 128.70, 127.36, 126.32, 66.40, 54.34, 29.84, 29.82, 29.80, 29.77, 29.63, 29.50, 29.36, 28.23, 25.75, 22.83, 21.45, 14.25.

tetradecyl (S)-phenylalaninate ammonium tosylate salt

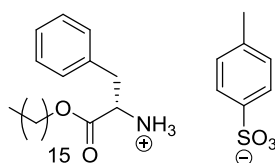


Preparation was achieved following the method A using commercially available decanol and (S)-Phe. 1.471 g (33%) of product were obtained as a white powder.

¹H NMR (400 MHz, CDCl₃) δ 8.24 (s, 3H, NH₃), 7.74 (d, 2H, Ar-H, *J* = 8.0 Hz), 7.21 – 7.02 (m, 7H, Ar-H), 4.24 (dd, 1H, NH₃-CH, *J* = 8.2, 5.3 Hz), 3.95 – 3.76 (m, 2H, COO-CH₂), 3.24 (dd, 1H, NH₃-CH-CH₂, *J* = 14.1, 5.3 Hz), 3.05 (dd, 1H, NH₃-CH-CH₂, *J* = 14.0, 8.2 Hz), 2.33 (s, 3H, Ar-CH₃), 1.45 – 1.09 (m, 21H, CH₂), 1.04 (q, 2H, CH₂, *J* = 7.7 Hz), 0.89 (t, 3H, CH₃, *J* = 6.7 Hz).

¹³C NMR (101 MHz, CDCl₃) δ 141.70, 140.35, 134.45, 129.58, 128.93, 128.70, 127.36, 126.33, 66.40, 54.33, 29.85, 29.83, 29.81, 29.78, 29.64, 29.51, 29.37, 28.24, 25.75, 22.83, 21.45, 14.25.

hexadecyl (S)-phenylalaninate ammonium tosylate salt

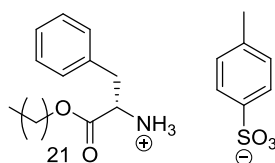


Preparation was achieved following the method A using commercially available decanol and (S)-Phe. 5.844 g (92%) of product were obtained as a white powder.

¹H NMR (300 MHz, CDCl₃) δ 8.21 (s, 3H, NH₃), 7.72 (d, 2H, Ar-H, ²*J* = 8.2 Hz), 7.16-7.034 (m, 7H, Ar-H), 4.27-4.17 (m, 1H, NH₃-CH), 3.91-3.77 (m, 2H, COO-CH₂), 3.12 (AB spin sytem, 2H, NH₃-CH-CH₂), 2.31 (s, 3H, Ar-CH₃), 1.35-1.06 (m, 28H, CH₂), 0.86 (t, 3H, CH₃, ²*J* = 7.0 Hz)

¹³C NMR (101 MHz, CDCl₃) δ 168.88, 141.56, 140.21, 134.34, 129.44, 128.79, 128.56, 127.22, 126.21, 66.26, 54.21, 36.40, 31.94, 29.73, 29.71, 29.68, 29.66, 29.52, 29.37, 29.24, 28.11, 25.62, 22.70, 21.32, 14.12.

docosyl (S)-phenylalaninate ammonium tosylate salt



Preparation was achieved following the method A using commercially available docosanol and (S)-Phe.

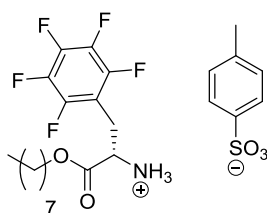
1.680 g (94%) of product were obtained as a white powder.

¹H NMR (400 MHz, CDCl₃) δ 8.23 (s, 3H, NH₃), 7.74 (d, 2H, Ar-*H*, *J* = 8.0 Hz), 7.20 – 7.03 (m, 7H, Ar-*H*), 4.30 – 4.19 (m, 1H, NH₃-CH), 3.94 – 3.78 (m, 2H, COO-CH₂), 3.24 (dd, 1H, NH₃-CH-CH₂, *J* = 14.0, 5.3 Hz), 3.04 (dd, 1H, NH₃-CH-CH₂, *J* = 14.1, 8.2 Hz), 2.32 (s, 3H, Ar-CH₃), 1.38 – 1.08 (m, 38H, CH₂), 1.08 – 0.97 (m, 2H, CH₂), 0.88 (t, 3H, CH₃, *J* = 6.7 Hz).

¹³C NMR (101 MHz, CDCl₃) δ 169.02, 141.68, 140.35, 134.48, 129.58, 128.93, 128.69, 127.35, 126.35, 66.39, 54.34, 36.54, 32.07, 29.89, 29.86, 29.81, 29.66, 29.51, 29.38, 28.24, 25.76, 22.84, 21.45, 14.26.

ii. Synthesized from other aminoacids

octyl (S)-pentafluorophenylalaninate ammonium tosylate salt



Preparation was achieved following the method A using commercially available octanol and (S)-F₅-Phe.

416 mg (79%) of product were obtained as a white powder.

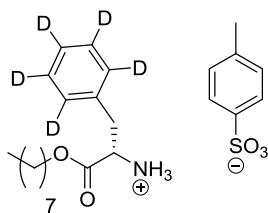
¹H NMR (300 MHz, CDCl₃) δ 8.50 (s, 3H, NH₃), 7.68 (d, 2H, Ar-*H*, ²*J* = 8.2 Hz), 7.10 (d, 2H, Ar-*H*, ²*J* = 8.0 Hz), 4.20-4.04 (m, 1H, NH₃-CH), 4.01-3.84 (m, 2H, COO-CH₂), 3.33-3.17 (m, 2H, NH₃-CH-CH₂), 2.31 (s, 3H, Ar-CH₃), 1.42-0.99 (m, 12H, CH₂), 0.86 (t, 2H, CH₃, ²*J* = 7.0 Hz)

¹³C NMR (101 MHz, CDCl₃) δ 167.79, 141.02, 140.50, 128.74, 125.90, 77.32, 77.01, 76.69, 66.93, 51.82, 31.77, 29.16, 29.12, 28.00, 25.60, 23.42, 22.60, 21.21, 14.01.

¹⁹F NMR (376 MHz, CDCl₃) δ -141.19, -154.77, -162.26.

HRMS (ESI, *m/z*) 368.1644 [*M*]⁺, 368.1643 calculated for C₁₇H₂₃F₅NO₂

octyl (S)-d₅-phenylalaninate ammonium tosylate salt



Preparation was achieved following the method A using commercially available octanol and (S)-d₅-Phe.

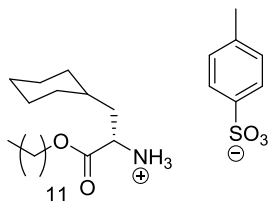
2.322 g (85%) of product were obtained as a white powder.

¹H NMR (300 MHz, DMSO-*d*₆) δ 8.45 (s, 3H, NH₃), 7.23 (d, 2H, Ar-*H*, ²*J* = 8.1 Hz), 6.84 (d, 2H, Ar-*H*, ²*J* = 8.0 Hz), 4.28 (t, 1H, NH₃-CH, ²*J* = 6.9 Hz), 4.02 (t, 2H, COO-CH₂, ²*J* = 6.4 Hz), 3.10 (AB system, 2H, NH₃-CHCH₂), 2.29 (s, 3H, Ar-CH₃), 1.48-1.34 (m, 2H, COO-CH₂CH₂), 1.34-1.06 (m, 10H, CH₂), 0.87 (t, 12H, CH₃, ²*J* = 6.8 Hz)

¹³C NMR (75 MHz, DMSO-*d*₆) δ 127.81, 125.22, 65.27, 52.98, 35.78, 30.91, 28.23, 27.49, 24.82, 21.79, 20.48, 13.64.

HRMS (ESI, *m/z*) 283.2428 [*M*]⁺, 283.2428 calculated for C₁₇H₂₃D₅NO₂

dodecyl (S)-cyclohexylalaninate ammonium tosylate salt



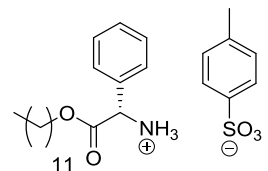
Preparation was achieved following the method A using commercially available dodecanol and (S)-Cha.

1.450 g (58%) of product were obtained as a white powder.

¹H NMR (400 MHz, CDCl₃) δ 8.14 (s, 3H, NH₃), 7.77 (d, 2H, Ar-*H*, *J* = 7.8 Hz), 7.13 (d, 2H, Ar-*H*, *J* = 7.8 Hz), 4.12 – 3.86 (m, 3H, NH₃-CH and NH₃-CHCH₂), 2.34 (s, 3H, Ar-CH₃), 1.71 – 1.46 (m, 8H), 1.45 – 1.34 (m, 1H, CH), 1.34 – 1.17 (m, 18H, CH₂), 1.17 – 0.97 (m, 4H, CH₂), 0.88 (t, 3H, CH₃, *J* = 6.5 Hz), 0.82 – 0.63 (m, 2H, CH₂).

¹³C NMR (101 MHz, CDCl₃) δ 170.10, 141.85, 140.21, 128.85, 126.38, 66.40, 51.14, 38.21, 33.45, 32.89, 32.47, 32.05, 29.77, 29.71, 29.49, 29.40, 28.43, 26.37, 25.95, 25.92, 22.82, 21.45, 14.24.

dodecyl (S)-phenylglycinate ammonium tosylate salt



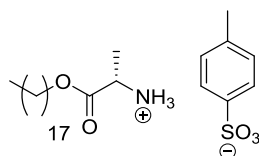
Preparation was achieved following the method A using commercially available dodecanol and (S)-PhGly.

4.263 g (89%) of product were obtained as a white powder.

¹H NMR (400 MHz, CDCl₃) δ 8.63 (s, 3H, NH₃), 7.53 (d, 2H, Ar-H, ²J = 7.5 Hz), 7.40-7.14 (m, 5H, Ar-H), 7.02 (d, 2H, Ar-H, ²J = 7.5 Hz), 5.08 (s, 1H, NH₃-CH), 4.04-3.82 (m, 2H, COO-CH₂), 2.34 (s, 3H, Ar-CH₃), 1.46-0.98 (m, 12H, CH₂), 0.89 (t, 2H, CH₃, ²J = 7.0 Hz)

¹³C NMR (101 MHz, CDCl₃) δ 168.22, 167.13, 141.45, 139.79, 131.87, 129.13, 128.86, 128.57, 128.14, 126.16, 66.50, 56.71, 31.92, 29.65, 29.55, 29.47, 29.36, 29.09, 28.09, 25.46, 22.69, 21.33, 14.11.

octadecyl (S)-alaninate ammonium tosylate salt



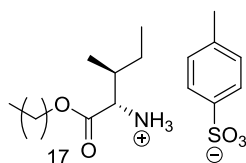
Preparation was achieved following the method A using commercially available octadecanol and (S)-Ala.

1.180 g (69%) of product were obtained as a white powder.

¹H NMR (400 MHz, CDCl₃) δ 8.15 (s, 3H, NH₃), 7.75 (d, 2H, Ar-H, J = 8.0 Hz), 7.13 (d, 2H, Ar-H, J = 7.9 Hz), 4.11 – 3.91 (m, 3H, NH₃-CH and COO-CH₂), 2.34 (s, 3H, Ar-CH₃), 1.52 (t, 2H, J = 6.7 Hz, CH₂), 1.43 (d, 3H, NH₃-CH-CH₃, J = 7.2 Hz), 1.37 – 1.14 (m, 28H, CH₂), 0.88 (t, 3H, CH₃, J = 6.7 Hz).

¹³C NMR (101 MHz, CDCl₃) δ 170.02, 141.62, 140.45, 128.96, 126.21, 66.52, 49.25, 32.07, 29.86, 29.86, 29.84, 29.81, 29.80, 29.69, 29.51, 29.40, 28.41, 25.84, 22.83, 21.46, 16.02, 14.25.

octadecyl (S)-i-Leucinate ammonium tosylate salt



Preparation was achieved following the method A using commercially available octadecanol and (S)-i-Leu.

963 mg (52%) of product were obtained as a white powder.

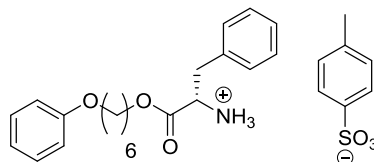
¹H NMR (400 MHz, CDCl₃) δ 8.05 (s, 2H, NH₃), 7.75 (d, 2H, Ar-H, J = 7.8 Hz), 7.13 (d, 2H, Ar-H, J = 7.8 Hz), 4.11 – 3.92 (m, 3H, NH₃-CH and COO-CH₂), 3.62 (t, 2H, CH₂, J = 6.7 Hz), 2.34 (s, 3H, Ar-CH₃), 2.00 – 1.87 (m, 1H, NH₃-CH-CH), 1.60 – 1.46 (m, 2H, CH₂), 1.37 – 1.16 (m, 30H, CH₂), 0.95 – 0.83 (m, 6H, CH₃), 0.79 (t, 3H, CH₃, J = 7.4 Hz).

¹³C NMR (101 MHz, CDCl₃) δ 168.69, 141.44, 140.23, 128.78, 126.12, 66.19, 66.19, 63.01, 63.01, 57.29, 36.24, 32.77, 31.93, 29.71, 29.68, 29.62, 29.54, 29.46, 29.36, 29.19, 28.30, 25.78, 25.76, 25.69, 22.69, 21.31, 14.20, 11.54.

c. Functionalized

i. With a phenoxy moiety

6-phenoxyhexyl (S)-phenylalaninate ammonium tosylate salt



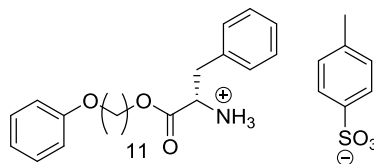
Preparation was achieved following the method A using 6-phenoxyhexanol and (S)-phenylalanine.

1.534 g (81%) of product were obtained as a white powder.

¹H NMR (300 MHz, CDCl₃) δ 8.28 (s, 3H, NH₃), 7.74 (d, 2H, ArH, ²J = 8.3 Hz), 7.28 (t, 2H, ArH, ²J = 8.1 Hz), 7.20-7.04 (m, 7H, ArH), 6.95 (d, 1H, ArH, ²J = 7.3 Hz), 6.90 (d, 2H, ArH, ²J = 7.7 Hz), 4.32-4.17 (m, 1H, NH₃-CH), 3.96 (t, 2H, Ar-O-CH₂, ²J = 6.5 Hz), 3.87 (t, 2H, COO-CH₂, ²J = 7.0 Hz), 3.16 (AB spin sytem, 2H, NH₃-CH-CH₂, ²J = 13.9 Hz), 2.34 (s, 3H, Ar-CH₃), 1.78-1.60 (m, 2H, Ar-O-CH₂-CH₂), 1.50-1.20 (m, 4H, CH₂), 1.20-1.00 (m, 2H, CH₂)

¹³C NMR (101 MHz, CDCl₃) δ 169.00, 159.15, 140.46, 134.47, 129.54, 128.96, 128.71, 127.38, 126.34, 120.64, 114.57, 67.71, 66.20, 54.37, 36.57, 29.22, 28.15, 25.78, 25.51, 21.44.

11-phenoxyundecyl (S)-phenylalaninate ammonium tosylate salt



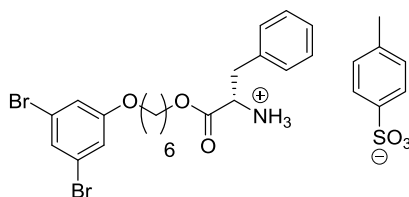
Preparation was achieved following the method A using 11-phenoxyundecanol and (S)-phenylalanine.

2.962 g (95%) of product were obtained as a white powder.

¹H NMR (300 MHz, CDCl₃) δ 8.23 (s, 3H, NH₃), 7.74 (d, 2H, ArH, ²J = 8.3 Hz), 7.28 (t, 2H, ArH, ²J = 8.1 Hz), 7.20-7.04 (m, 7H, ArH), 6.95 (d, 1H, ArH, ²J = 7.3 Hz), 6.90 (d, 2H, ArH, ²J = 7.7 Hz), 4.32-4.17 (m, 1H, NH₃-CH), 3.96 (t, 2H, Ar-O-CH₂, ²J = 6.5 Hz), 3.87 (t, 2H, COO-CH₂, ²J = 7.0 Hz), 3.16 (AB spin sytem, 2H, NH₃-CH-CH₂, ²J = 13.9 Hz), 2.34 (s, 3H, Ar-CH₃), 1.79 (quin, 2H, Ar-O-CH₂-CH₂, ²J = 7.0 Hz), 1.50-1.00 (m, 16H, CH₂)

¹³C NMR (101 MHz, CDCl₃) δ 169.00, 159.22, 141.67, 140.31, 134.50, 129.54, 129.49, 128.90, 128.65, 127.30, 126.32, 120.55, 114.59, 67.95, 66.33, 54.32, 36.51, 29.69, 29.66, 29.58, 29.54, 29.43, 29.32, 28.19, 26.20, 25.71, 21.43.

6-(3,5-dibromophenoxy)hexyl (S)-phenylalaninate ammonium tosylate salt



Preparation was achieved following the method A using 6-(3,5-dibromophenoxy)hexanol and (S)-phenylalanine.

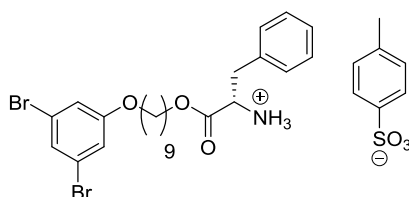
2.337 g (74%) of product were obtained as a white powder.

¹H NMR (300 MHz, CDCl₃) δ 8.27 (s, 3H, NH₃), 7.74 (d, 2H, ArH, ²J = 8.2 Hz), 7.24 (t, 1H, ArH, ²J = 1.6 Hz), 7.21-7.05 (m, 7H, ArH), 6.96 (d, 2H, ArH, ²J = 1.5 Hz), 4.33-4.18 (m, 1H, NH₃-CH), 3.90 (t, 2H, Ar-O-CH₂, ²J = 6.7 Hz), 3.82 (t, 2H, COO-CH₂), 3.15 (AB spin system, 2H, NH₃-CH-CH₂, ²J = 13.9 Hz), 2.32 (s, 3H, Ar-CH₃), 1.64 (quin, 2H, Ar-O-CH₂-CH₂, ²J = 7.0 Hz), 1.45-1.00 (m, 6H, CH₂)

¹³C NMR (101 MHz, CDCl₃) δ 168.97, 160.35, 140.48, 134.51, 129.53, 128.95, 128.67, 127.35, 126.33, 123.20, 116.99, 115.09, 68.47, 66.08, 54.39, 36.56, 28.89, 28.10, 25.60, 25.40, 21.45.

HRMS (ESI, m/z) 500.0255 [M]⁺, 500.0253 calculated for C₂₁H₂₆Br₂NO₃

9-(3,5-dibromophenoxy)nonyl (S)-phenylalaninate ammonium tosylate salt



Preparation was achieved following the method A using 9-(3,5-dibromophenoxy)nonanol and (S)-phenylalanine.

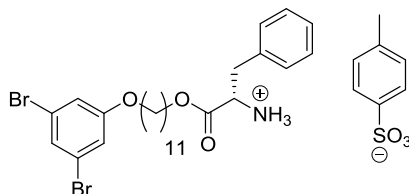
2.713 g (75%) of product were obtained as a white powder.

¹H NMR (300 MHz, CDCl₃) δ 8.22 (s, 3H, NH₃), 7.74 (d, 2H, ArH, ²J = 8.2 Hz), 7.23 (t, 1H, ArH, ²J = 1.6 Hz), 7.21-7.05 (m, 7H, ArH), 6.98 (d, 2H, ArH, ²J = 1.5 Hz), 4.33-4.18 (m, 1H, NH₃-CH), 3.91 (t, 2H, Ar-O-CH₂, ²J = 6.7 Hz), 3.94-3.84 (m, 2H, COO-CH₂), 3.91 (AB spin system, 2H, NH₃-CH-CH₂, ²J = 13.9 Hz), 2.34 (s, 3H, Ar-CH₃), 1.75 (quin, 2H, Ar-O-CH₂-CH₂, ²J = 7.0 Hz), 1.50-1.00 (m, 12H, CH₂)

¹³C NMR (101 MHz, CDCl₃) δ 168.99, 160.45, 141.62, 140.39, 134.46, 129.55, 128.93, 128.69, 127.36, 126.31, 123.19, 117.04, 68.70, 66.32, 54.35, 36.52, 29.47, 29.37, 29.23, 29.11, 28.19, 26.04, 25.70, 21.47.

HRMS (ESI, m/z) 542.0726 [M]⁺, 542.0723 calculated for C₂₄H₃₂Br₂NO₃

11-(3,5-dibromophenoxy)undecyl (S)-phenylalaninate ammonium tosylate salt



Preparation was achieved following the method A using 11-(3,5-dibromophenoxy)undecanol and (S)-phenylalanine.

1.382 g (87%) of product were obtained as a white powder.

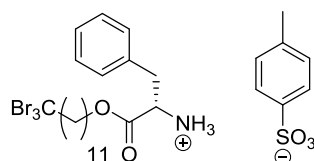
¹H NMR (300 MHz, CDCl₃) δ 8.22 (s, 3H, NH₃), 7.74 (d, 2H, ArH, ²J = 8.2 Hz), 7.23 (t, 1H, ArH, ²J = 1.6 Hz), 7.21-7.05 (m, 7H, ArH), 6.98 (d, 2H, ArH, ²J = 1.5 Hz), 4.33-4.18 (m, 1H, NH₃-CH), 3.91 (t, 2H, Ar-O-CH₂, ²J = 6.7 Hz), 3.94-3.84 (m, 2H, COO-CH₂), 3.91 (AB spin sytem, 2H, NH₃-CH-CH₂, ²J = 13.9 Hz), 2.34 (s, 3H, Ar-CH₃), 1.75 (quin, 2H, Ar-O-CH₂-CH₂, ²J = 7.0 Hz), 1.50-1.00 (m, 16H, CH₂)

¹³C NMR (101 MHz, CDCl₃) δ 168.99, 160.46, 141.61, 140.39, 134.46, 129.56, 128.93, 128.69, 127.35, 126.31, 126.28, 123.18, 117.05, 68.73, 66.36, 54.35, 36.52, 29.66, 29.59, 29.44, 29.32, 29.12, 28.22, 26.06, 25.73, 21.47.

HRMS (ESI, m/z) 570.1039 [M + H]⁺, 570.1036 calculated for C₂₆H₃₆Br₂N₁O₃

ii. With an halogen moiety

12-tribromododecyl (S)-phenylalaninate ammonium tosylate salt



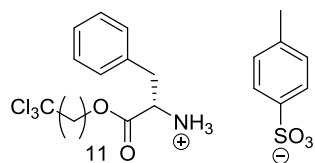
Preparation was achieved following the method A using 12-tribromododecanol and (S)-phenylalanine. 6,575 g (85%) of product were obtained as a white powder.

¹H NMR (300 MHz, CDCl₃) δ 8.41 (s, 3H, NH₃), 7.50 (d, 2H, Ar-H, ²J = 8.0 Hz), 7.32 (q, 3H, Ar-H, ²J = 7.3 Hz), 7.22 (d, 2H, Ar-H, ²J = 7.1 Hz), 7.12 (d, 2H, Ar-H, ²J = 7.9 Hz), 4.29 (t, 1H, NH₃-CH, ²J = 6.9 Hz), 4.02 (t, 2H, COO-CH₂, ²J = 6.4 Hz), 3.09 (AB spin sytem, 2H, NH₃-CH-CH₂, ²J = 21.7 Hz), 2.96 (t, 2H, CBr₃-CH₂, ²J = 7.8 Hz), 2.29 (s, 3H, Ar-CH₃), 1.68 (quin, 2H, COO-CH₂-CH₂, ²J = 7.4 Hz), 1.50-1.08 (m, 16H, CH₂)

¹³C NMR (101 MHz, CDCl₃) δ 169.02, 141.64, 140.35, 134.43, 129.56, 128.92, 128.70, 127.37, 126.30, 66.37, 60.06, 54.33, 42.77, 36.51, 29.65, 29.57, 29.45, 29.31, 28.21, 28.01, 25.72, 21.48.

HRMS (ESI, m/z) 570.0044 [M]⁺, 570.0035 calculated for C₂₁H₃₃Br₃NO₂

12-trichlorododecyl (S)-phenylalaninate ammonium tosylate salt



Preparation was achieved following the method A using 12-trichlorododecanol and (S)-phenylalanine. 617 mg (76%) of product were obtained as a white powder.

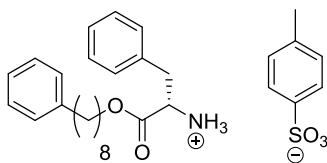
¹H NMR (300 MHz, CDCl₃) δ 8.22 (s, 3H, NH₃), 7.74 (d, 2H, Ar-H, ²J = 8.2 Hz), 7.21-7.07 (m, 7H, Ar-H), 4.35-4.20 (m, 1H, NH₃-CH), 3.98-3.82 (m, 2H, COO-CH₂), 3.17 (AB spin sytem, 2H, NH₃-CH-CH₂, ²J = 5.9 Hz), 2.67 (t, 2H, CCl₃-CH₂, ²J = 8.0 Hz), 2.34 (s, 3H, Ar-CH₃), 1.78 (quin, 2H, COO-CH₂-CH₂, ²J = 7.4 Hz), 1.48-1.00 (m, 16H, CH₂)

¹³C NMR (101 MHz, CDCl₃) δ 169.00, 141.62, 140.40, 134.46, 129.57, 128.94, 128.70, 127.37, 126.32, 66.37, 55.34, 54.35, 36.53, 29.65, 29.56, 29.44, 29.32, 28.48, 28.22, 26.53, 25.73, 21.47.

HRMS (ESI, m/z) 436.1575 [M]⁺, 436.1571 calculated for C₂₁H₃₃Cl₃NO₂

iii. With a phenyl moiety

8-phenyloctyl (S)-phenylalaninate ammonium tosylate salt



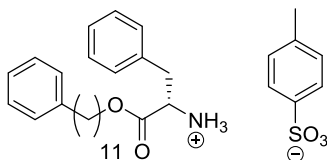
Preparation was achieved following the method A using 8-phenyloctanol and (S)-phenylalanine.

1.241 g (83%) of product were obtained as a white powder.

¹H NMR (400 MHz, CDCl₃) δ 8.23 (s, 3H, NH₃), 7.78 – 7.70 (m, 2H, Ar-*H*), 7.31 – 7.25 (m, 2H, Ar-*H*), 7.23 – 7.04 (m, 10H, Ar-*H*), 4.30 – 4.20 (m, 1H, NH₃-CH), 3.94 – 3.78 (m, 2H, COO-CH₂), 3.25 (dd, 1H, NH₃-CH-CH₂, *J* = 14.0, 5.3 Hz), 3.05 (dd, 1H, NH₃-CH-CH₂, *J* = 14.0, 8.2 Hz), 2.60 (t, 2H, Ar-CH₂, *J* = 7.6, 6.1 Hz), 2.32 (s, 3H, Ar-CH₃), 1.65 – 1.54 (m, 2H, CH₂), 1.39 – 1.08 (m, 8H, CH₂), 1.04 (q, 2H, CH₂, *J* = 8.1 Hz).

¹³C NMR (101 MHz, CDCl₃) δ 169.00, 142.90, 141.61, 140.40, 134.43, 129.56, 128.94, 128.71, 128.50, 128.36, 127.38, 126.31, 125.73, 66.37, 54.34, 36.53, 36.09, 31.61, 29.46, 29.38, 29.26, 28.20, 25.71, 21.46.

11-phenylundecyl (S)-phenylalaninate ammonium tosylate salt



Preparation was achieved following the method A using 11-phenylundecanol and (S)-phenylalanine.

3.144 g (83%) of product were obtained as a white powder.

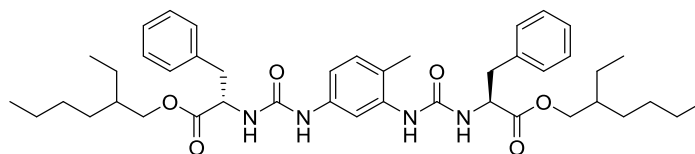
¹H NMR (400 MHz, CDCl₃) δ 8.20 (s, 3H, NH₃), 7.71 (d, 2H, Ar-*H*, *J* = 8.1 Hz), 7.23 (d, 2H, Ar-*H*, *J* = 6.9 Hz), 7.18 – 7.02 (m, 10H, Ar-*H*), 4.27 – 4.16 (m, 1H, NH₃-CH), 3.90 – 3.75 (m, 2H, COO-CH₂), 3.21 (dd, 1H, NH₃-CH-CH₂, *J* = 14.1, 5.3 Hz), 3.02 (dd, 1H, NH₃-CH-CH₂, *J* = 14.0, 8.2 Hz), 2.57 (t, 2H, Ar-CH₂, *J* = 7.6 Hz), 2.29 (s, 3H, Ar-CH₃), 1.58 (p, 2H, CH₂, *J* = 7.3 Hz), 1.36 – 1.05 (m, 8H, CH₂), 1.05 – 0.94 (m, 2H, CH₂).

¹³C NMR (101 MHz, CDCl₃) δ 169.00, 143.02, 141.65, 140.37, 134.45, 129.57, 128.93, 128.70, 128.51, 128.34, 127.36, 126.33, 125.68, 66.39, 54.34, 36.53, 36.13, 31.66, 29.75, 29.73, 29.68, 29.61, 29.49, 29.34, 28.23, 25.74, 21.46.

4. Ramified ester bis-ureas

The synthesis of all the alkyl bis-ureas and racemic ester bis-ureas presented in the second chapter are described in: Dirany, M.; Ayzac, V.; Isare, B.; Raynal, M.; Bouteiller, L. *Langmuir* **2015**, *31*, 11443

EtHexPheTol



Preparation was achieved following the method B using 2-ethylhexyl (S)-phenylalaninate ammonium tosylate salt.

The product is recrystallized in acetonitrile.

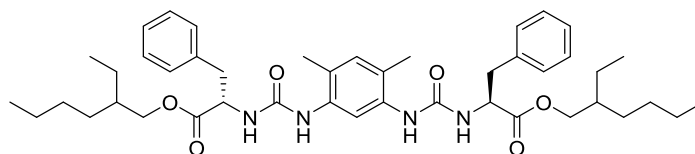
822 mg (89%) of a pure product were obtained as a white paste.

¹H NMR (400 MHz, DMSO-*d*₆) δ 8.59 (s, 1H, NH), 7.80 (s, 1H, NH), 7.69 (d, 1H, ArH, *J* = 2.2 Hz), 7.35 – 7.16 (m, 11H, ArH), 7.11 (dd, 1H, ArH, *J* = 8.2, 2.3 Hz), 6.93 (dd, 2H, NH, *J* = 8.1, 6.3 Hz), 6.26 (d, 1H, ArH, *J* = 8.0 Hz), 4.51 (p, 2H, NH-CH, *J* = 8.2, 7.7 Hz), 3.94 (d, 4H, COO-CH₂, *J* = 5.7 Hz), 3.07 – 2.93 (m, 4H, NH3-CH-CH₂), 2.08 (s, 3H, Ar-CH₃), 1.47 – 1.35 (m, 2H, CH), 1.31 – 1.18 (m, 16H, CH₂), 0.87 – 0.74 (m, 12H, CH₃).

¹³C NMR (101 MHz, DMSO-*d*₆) δ 172.26, 154.66, 154.52, 138.06, 137.76, 136.87, 136.79, 129.95, 129.08, 128.29, 126.58, 119.55, 111.71, 110.09, 66.13, 54.02, 53.79, 39.61, 37.66, 37.52, 22.60, 17.17, 10.82, 10.77.

HRMS (ESI, *m/z*) 751.4406 [*M* + Na]⁺, 751.4405 calculated for C₄₃H₆₀N₄O₆Na

EtHexPheXyl



Preparation was achieved following the method C using 2-ethylhexyl (S)-phenylalaninate ammonium tosylate salt and 4,6-dimethyl-1,3-diaminobenzène.

The product is recrystallized in acetonitrile.

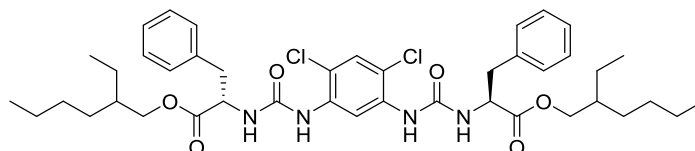
512 mg (65%) of a pure product were obtained as a white paste.

¹H NMR (400 MHz, DMSO-*d*₆) δ 7.92 (s, 1H, ArH), 7.75 (s, 2H, NH), 7.34 – 7.16 (m, 10H, ArH), 6.86 (s, 1H, ArH), 6.69 (d, 2H, NH, *J* = 8.0 Hz), 4.51 (q, 2H, NH-CH, *J* = 7.2 Hz), 4.01 – 3.85 (m, 4H, COO-CH₂), 3.08 – 2.92 (m, 4H, NH-CH-CH₂), 2.05 (s, 6H, Ar-CH₃), 1.53 – 1.42 (m, 2H, CH), 1.30 – 1.15 (m, 16H, CH₂), 0.90 – 0.76 (m, 12H, CH₃).

¹³C NMR (101 MHz, DMSO-*d*₆) δ 172.35, 154.74, 136.89, 135.23, 131.19, 129.05, 128.25, 126.54, 122.54, 115.85, 66.46, 66.44, 53.94, 38.04, 37.73, 29.63, 28.31, 28.27, 23.05, 22.34, 17.15, 13.86, 10.77, 10.72.

HRMS (ESI, *m/z*) 765.4564 [*M* + Na]⁺, 765.4562 calculated for C₄₄H₆₂N₄O₆Na

EtHexPheCl



Preparation was achieved following the method C using 2-ethylhexyl (S)-phenylalaninate ammonium tosylate salt and 4,6-dichloro-1,3-diaminobenzène.

The product is recrystallized in acetonitrile.

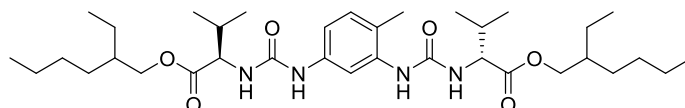
362 mg (44%) of a pure product were obtained as a white paste.

¹H NMR (400 MHz, DMSO-*d*₆) δ 8.88 (s, 1H, ArH), 8.20 (s, 2H, NH), 7.47 (s, 1H, ArH), 7.39 (d, 2H, *J* = 7.8 Hz), 7.33 – 7.28 (m, 4H, ArH), 7.26 – 7.18 (m, 6H, ArH and NH), 4.57 – 4.41 (m, 2H, NH-CH), 3.93 (d, 4H, COO-CH₂, *J* = 5.6 Hz), 3.10 – 2.89 (m, 4H, NH-CH-CH₂), 1.52 – 1.41 (m, 2H, CH), 1.29 – 1.14 (m, 16H, CH₂), 0.87 – 0.76 (m, 12H, CH₃).

¹³C NMR (101 MHz, DMSO-*d*₆) δ 172.07, 153.91, 136.76, 135.40, 129.01, 128.29, 128.13, 126.61, 114.46, 113.03, 66.57, 54.03, 38.04, 37.47, 29.64, 28.30, 28.26, 23.06, 23.04, 22.34, 13.83, 10.78, 10.74.

HRMS (ESI, *m/z*) 805.3482 [*M* + Na]⁺, 805.3469 calculated for C₄₂H₅₆N₄O₆Na

(R)-EtHexValTol



Preparation was achieved following the method B using 2-ethylhexyl (R)-valinate ammonium tosylate salt.

The product is recrystallized in acetonitrile.

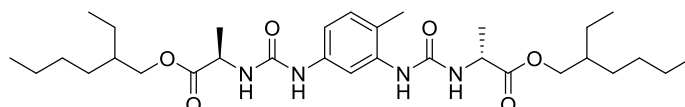
80 mg (11%) of a pure product were obtained as a white paste. The S enantiomer was synthesized as well (76% yield).

¹H NMR (400 MHz, DMSO-*d*₆) δ 8.52 (s, 1H, NH), 7.79 (s, 2H, ArH and NH, ²*J* = 2.1 Hz), 7.12 (dd, 1H, ArH, ²*J* = 8.2 Hz, ²*J* = 2.0 Hz), 7.00-6.90 (m, 2H, ArH and NH), 6.31 (d, 1H, NH, ²*J* = 8.7 Hz), 4.21-4.10 (m, 2H, NH-CH), 4.07-3.87 (m, 4H, COO-CH₂), 2.20-1.96 (m, 5H, Ar-CH₃ and NH-CH-CH), 1.62-1.44 (m, 2H, COO-CH₂-CH), 1.40-1.09 (m, 16H, CH₂), 0.96-0.70 (m, 24H, CH₃)

¹³C NMR (101 MHz, DMSO-*d*₆) δ 172.4, 155.0, 154.9, 138.1, 138.0, 130.0, 118.8, 118.7, 109.2, 111.1, 66.2, 66.1, 57.6, 57.4, 38.1, 30.3, 30.2, 29.7, 29.6, 28.3, 28.2, 23.2, 23.1, 22.3, 19.0, 17.7, 17.5, 17.2, 13.8, 10.8, 10.7

HRMS (ESI, *m/z*) 655.4402 [*M* + Na]⁺, 655.4405 calculated for C₃₅H₆₀N₄O₆Na

(R)-EtHexAlaTol



Preparation was achieved following the method B using 2-ethylhexyl (R)-alaninate ammonium tosylate salt.

The product is recrystallized in acetonitrile.

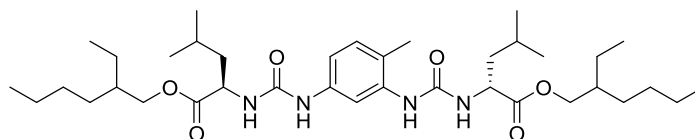
301 mg (47%) of a pure product were obtained as a white paste. The S enantiomer was synthesized as well (46% yield).

¹H NMR (400 MHz, DMSO-*d*₆) δ 8.47 (s, 1H, NH), 7.74 (d, 1H, ArH ²*J* = 2.1 Hz), 7.70 (s, 1H, NH), 7.11 (dd, 1H, ArH, ²*J* = 8.2 Hz, ²*J* = 2.2 Hz), 6.95 (d, 1H, ArH, ²*J* = 7.2 Hz), 6.94 (d, 1H, NH, ²*J* = 8.1 Hz), 6.34 (d, 1H, NH, ²*J* = 7.9 Hz), 4.28-4.16 (m, 2H, NH-CH), 4.07-3.89 (m, 4H, COO-CH₂), 2.10 (s, 3H, Ar-CH₃), 1.58-1.48 (m, 2H, COO-CH₂-CH), 1.35-1.19 (m, 22H, CH₂ and CH₃), 0.87-0.81 (m, 12H, CH₃)

¹³C NMR (101 MHz, DMSO-*d*₆) δ 173.46, 173.43, 154.64, 154.53, 138.12, 137.83, 129.88, 119.29, 111.65, 109.92, 66.32, 48.12, 38.19, 29.74, 28.25, 23.11, 22.35, 17.91, 17.12, 13.83, 10.79.

HRMS (ESI, *m/z*) 599.3782 [*M* + Na]⁺, 599.3779 calculated for C₃₁H₅₂N₄O₆Na

(R)-EtHexLeuTol



Preparation was achieved following the method B using 2-ethylhexyl (R)-Leucinate ammonium tosylate salt.

The product is recrystallized in acetonitrile.

281 mg (38%) of a pure product were obtained as a white paste. The S enantiomer was synthesized as well (58% yield).

¹H NMR (400 MHz, DMSO-*d*₆) δ 8.44 (s, 1H, NH), 7.77 (d, 1H, ArH ²*J* = 2.0 Hz), 7.68 (s, 1H, NH), 7.09 (dd, 1H, ArH, ²*J* = 8.1 Hz, ²*J* = 2.1 Hz), 6.94 (d, 1H, NH, ²*J* = 8.1 Hz), 6.92 (d, 1H, ArH, ²*J* = 7.1 Hz), 6.29 (d, 1H, NH, ²*J* = 8.1 Hz), 4.29-4.17 (m, 2H, NH-CH), 4.04-3.90 (m, 4H, COO-CH₂), 2.10 (s, 3H, Ar-CH₃), 1.75-1.60 (m, 2H, COO-CH₂-CH), 1.60-1.46 (m, 6H, NH-CH-CH₂ and NH-CH-CH₂-CH), 1.37-1.18 (m, 16H, CH₂ and CH₃), 0.96-0.79 (m, 24H, CH₃)

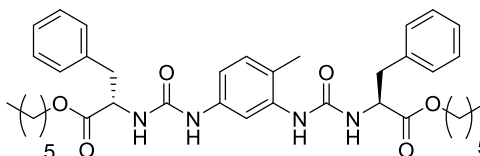
¹³C NMR (101 MHz, DMSO-*d*₆) δ 173.36, 154.81, 154.69, 138.12, 137.89, 129.91, 66.34, 66.26, 51.01, 40.92, 40.85, 38.14, 29.80, 29.73, 28.32, 28.24, 24.34, 23.25, 23.16, 22.58, 22.37, 22.37, 21.67, 21.63, 17.13, 13.82, 10.82, 10.75.

HRMS (ESI, *m/z*) 683.4722 [*M* + Na]⁺, 683.4718 calculated for C₃₇H₆₄N₄O₆Na

5. Non-ramified ester bis-ureas

a. Bis-ureas synthetized from Phe

H3C5Tol



Preparation was achieved following the method B using hexyl (S)-phenylalaninate ammonium tosylate salt.

The product is recrystallized in acetonitrile.

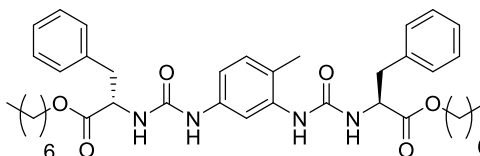
726 mg (85%) of a pure product were obtained as a white paste.

¹H NMR (400 MHz, DMSO-*d*₆) δ 8.60 (s, 1H, NH), 7.81 (s, 1H, NH), 7.73 (d, 1H, ArH, *J* = 2.2 Hz), 7.35 – 7.17 (m, 11H, ArH), 7.11 (dd, 1H, ArH, *J* = 8.2, 2.2 Hz), 6.94 (d, 2H, NH, *J* = 8.0 Hz), 6.28 (d, 1H, ArH, *J* = 7.9 Hz), 4.58 – 4.45 (m, 2H, NH-CH), 4.02 (t, 4H, COO-CH₂, *J* = 6.5 Hz), 3.09 – 2.93 (m, 4H, NH₃-CH-CH₂), 2.08 (s, 3H, Ar-CH₃), 1.58 – 1.45 (m, 4H, CH₂), 1.31 – 1.17 (m, 13H, CH₂), 0.84 (t, 6H, CH₃, *J* = 6.8 Hz).

¹³C NMR (101 MHz, DMSO-*d*₆) δ 172.20, 154.63, 154.48, 138.10, 137.80, 136.85, 136.78, 129.94, 129.13, 128.26, 126.58, 119.48, 111.64, 110.01, 64.46, 53.97, 53.73, 37.72, 37.56, 30.83, 27.99, 24.95, 21.94, 17.18, 13.82.

HRMS (ESI, *m/z*) 695.3783 [*M* + Na]⁺, 695.3779 calculated for C₃₉H₅₂N₄O₆Na

H3C6Tol



Preparation was achieved following the method B using heptyl (S)-phenylalaninate ammonium tosylate salt.

The product is recrystallized in acetonitrile.

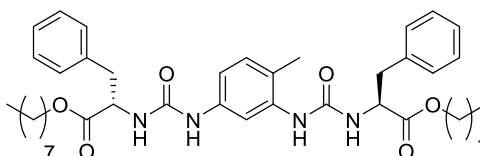
823 mg (88%) of a pure product were obtained as a white paste.

¹H NMR (400 MHz, DMSO-*d*₆/THF-*d*₈ 2/1) δ 8.60 (s, 1H, NH), 7.81 (s, 1H, NH), 7.77 (s, 1H, ArH), 7.34 – 7.15 (m, 13H, ArH), 6.96 (d, 1H, NH, *J* = 7.8 Hz), 6.90 (d, 1H, NH, *J* = 8.3 Hz), 6.28 (d, 1H, ArH, *J* = 8.0 Hz), 4.57 (h, 2H, NH-CH, *J* = 7.0 Hz), 4.04 (t, 4H, COO-CH₂, *J* = 6.7 Hz), 3.12 – 2.92 (m, 4H, NH₃-CH-CH₂), 2.11 (s, 3H, Ar-CH₃), 1.62 – 1.48 (m, 4H, CH₂), 1.26 (s, 16H, CH₂), 0.87 (t, 6H, CH₃, *J* = 6.5 Hz).

¹³C NMR (101 MHz, DMSO-*d*₆/THF-*d*₈ 2/1) δ 172.10, 154.58, 154.44, 138.39, 137.97, 136.96, 129.65, 129.10, 128.06, 126.37, 118.98, 114.60, 111.35, 109.69, 64.36, 53.95, 53.72, 38.04, 37.87, 31.43, 25.45, 22.18, 17.03, 13.58.

HRMS (ESI, *m/z*) 723.4100 [*M* + Na]⁺, 723.4092 calculated for C₄₆H₅₆N₄O₆Na

H3C7Tol



Preparation was achieved following the method B using heptyl (S)-phenylalaninate ammonium tosylate salt.

The product is recrystallized in acetonitrile.

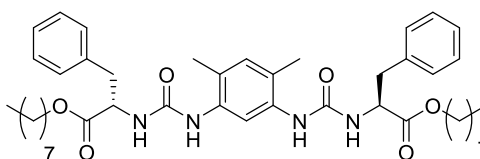
920 mg (91%) of a pure product were obtained as a white paste.

¹H NMR (400 MHz, DMSO-*d*₆) δ 8.59 (s, 1H, ArH), 7.80 (s, 1H, ArH), 7.72 (d, 1H, ArH, *J* = 2.2 Hz), 7.33 – 7.27 (m, 4H, NH and ArH), 7.26 – 7.17 (m, 7H, ArH), 7.11 (dd, 1H, ArH, *J* = 8.2, 2.2 Hz), 6.93 (d, 2H, NH, *J* = 8.0 Hz), 6.26 (d, 1H, ArH, *J* = 7.9 Hz), 4.56 – 4.44 (m, 2H, NH-CH), 4.01 (t, 4H, COO-CH₂, *J* = 6.5 Hz), 3.07 – 2.93 (m, 4H, NH₃-CH-CH₂), 2.07 (s, 3H, Ar-CH₃), 1.56 – 1.45 (m, 4H, CH₂), 1.32 – 1.16 (m, 20H, CH₂), 0.85 (t, 6H, CH₃, *J* = 7.1 Hz).

¹³C NMR (101 MHz, DMSO-*d*₆) δ 172.18, 154.47, 138.09, 137.79, 136.85, 136.78, 129.93, 129.12, 128.25, 126.57, 119.41, 111.59, 109.95, 64.45, 53.96, 53.73, 37.70, 37.53, 31.20, 28.60, 28.55, 28.02, 25.28, 22.06, 17.18, 13.89.

HRMS (ESI, *m/z*) 751.4405 [*M* + Na]⁺, 751.4405 calculated for C₄₃H₆₀N₄O₆Na

H3C7Xyl



Preparation was achieved following the method C using octyl (S)-phenylalaninate ammonium tosylate salt and 4,6-dimethyl-1,3-diaminobenzène.

The product is recrystallized in acetonitrile.

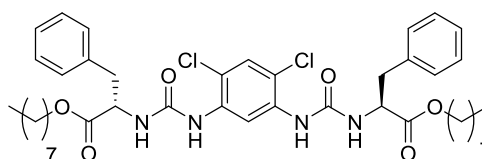
963 mg (61%) of a pure product were obtained as a white paste.

¹H NMR (300 MHz, DMSO-*d*₆) δ 7.94 (s, 1H, ArH), 7.75 (s, 2H, NH), 7.36-7.15 (m, 10H, ArH and NH), 6.85 (s, 1H, ArH), 6.69 (d, 2H, ArH, ²*J* = 7.9 Hz), 4.49 (q, 2H, NH-CH, ²*J* = 7.2 Hz), 4.00 (t, 4H, COO-CH₂, ²*J* = 6.5 Hz), 3.08-2.91 (m, NH₃-CH-CH₂, 4H), 2.05 (s, 6H, Ar-CH₃), 1.50 (q, 4H, COOCH₂CH₂, ²*J* = 6.0 Hz), 1.30-1.15 (m, 20H, CH₂), 0.85 (t, 6H, CH₃, ²*J* = 6.7 Hz)

¹³C NMR (101 MHz, DMSO-*d*₆) δ 172.27, 154.73, 136.87, 135.27, 131.20, 129.12, 128.22, 126.53, 122.40, 115.64, 64.42, 53.91, 37.74, 31.20, 28.59, 28.54, 28.01, 25.27, 22.06, 17.17, 13.90.

HRMS (ESI, *m/z*) 765.4570 [*M* + Na]⁺, 765.4562 calculated for C₄₄H₆₂N₄O₆Na

H3C7Cl



Preparation was achieved following the method C using octyl (S)-phenylalaninate ammonium tosylate salt and 4,6-dichloro-1,3-diaminobenzène.

The product is recrystallized in acetonitrile.

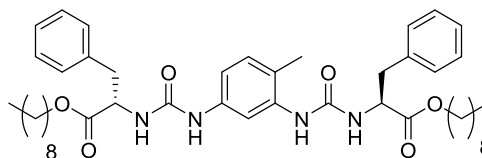
457 mg (55%) of pure product were obtained as a white powder.

¹H NMR (400 MHz, DMSO-*d*₆) δ 8.91 (s, 1H, ArH), 8.21 (s, 2H, NH), 7.46 (s, 1H, ArH), 7.41 (d, 2H, *J* = 7.7 Hz, ArH), 7.34 – 7.17 (m, 12H, ArH and NH), 4.49 (q, 2H, NH-CH, *J* = 7.7 Hz), 4.01 (t, 4H, COO-CH₂, *J* = 6.2 Hz), 3.08 – 2.91 (m, 4H NH₃-CH-CH₂), 1.55 – 1.42 (m, 4H, CH₂), 1.30 – 1.13 (m, 20H, CH₂), 0.83 (t, 6H, CH₃, *J* = 6.8 Hz).

¹³C NMR (101 MHz, DMSO-*d*₆) δ 172.00, 153.90, 136.74, 135.43, 129.07, 128.28, 126.61, 114.37, 112.83, 64.52, 54.01, 37.48, 31.19, 28.59, 28.55, 28.00, 25.28, 22.06, 13.89.

HRMS (ESI, *m/z*) 805.3468 [*M* + Na]⁺, 805.3469 calculated for C₄₂H₅₆Br₄Cl₂N₄O₆Na

H3C8Tol



Preparation was achieved following the method B using nonyl (S)-phenylalaninate ammonium tosylate salt.

The product is recrystallized in acetonitrile.

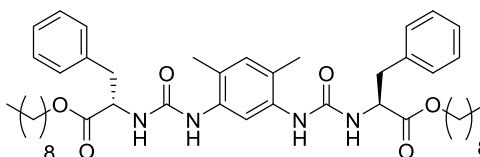
1.420 g (83%) of a pure product were obtained as a white paste.

¹H NMR (300 MHz, DMSO-*d*₆) δ 8.58 (s, 1H, ArH), 7.75 (d, 2H, NH, ²*J* = 30.5 Hz), 7.35-7.15 (m, 10H, ArH), 7.10 (d, 1H, NH, ²*J* = 8.3 Hz), 6.92 (d, 2H, ArH, ²*J* = 7.9 Hz), 6.26 (d, 1H, NH, ²*J* = 7.9 Hz), 4.49 (p, 2H, NH-CH, ²*J* = 7.3 Hz), 4.01 (t, 4H, COO-CH₂, ²*J* = 6.4 Hz), 3.06-2.92 (m, 4H, NH₃-CH-CH₂), 2.07 (s, 3H, Ar-CH₃), 1.55-1.44 (m, 4H, COO-CH₂-CH₂), 1.30-1.15 (m, 24H, CH₂), 0.85 (t, 3H, CH₃, ²*J* = 6.9 Hz)

¹³C NMR (101 MHz, DMSO-*d*₆) δ 172.18, 154.61, 154.46, 138.07, 137.78, 136.84, 136.78, 129.93, 129.11, 128.25, 126.57, 119.41, 111.58, 109.94, 64.44, 53.96, 53.73, 37.68, 37.52, 31.24, 28.84, 28.62, 28.01, 25.27, 22.06, 17.18, 13.91.

HRMS (ESI, *m/z*) 779.4716 [*M* + Na]⁺, 779.4718 calculated for C₄₅H₆₄N₄O₆Na

H3C8Xyl



Preparation was achieved following the method C using nonyl (S)-phenylalaninate ammonium tosylate salt and 4,6-dimethyl-1,3-diaminobenzène.

The product is recrystallized in acetonitrile.

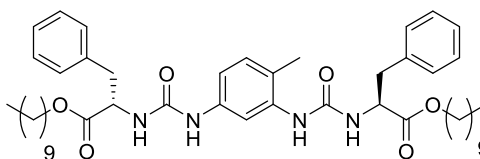
465 mg (59%) of a pure product were obtained as a white paste.

¹H NMR (300 MHz, DMSO-*d*₆) δ 7.94 (s, 1H, ArH), 7.75 (s, 2H, NH), 7.36-7.15 (m, 10H, ArH and NH), 6.85 (s, 1H, ArH), 6.69 (d, 2H, ArH, ²*J* = 7.9 Hz), 4.49 (q, 2H, NH-CH, ²*J* = 7.2 Hz), 4.00 (t, 4H, COO-CH₂, ²*J* = 6.5 Hz), 3.08-2.91 (m, NH₃-CH-CH₂, 4H), 2.05 (s, 6H, Ar-CH₃), 1.50 (q, 4H, COOCH₂CH₂, ²*J* = 6.0 Hz), 1.30-1.15 (m, 24H, CH₂), 0.85 (t, 6H, COO-CH₂, ²*J* = 6.7 Hz)

¹³C NMR (101 MHz, DMSO-*d*₆) δ 172.27, 154.73, 136.87, 135.26, 131.19, 129.11, 128.22, 126.52, 122.38, 64.41, 53.90, 37.73, 31.25, 28.62, 28.00, 25.26, 22.07, 17.17, 13.91.

HRMS (ESI, *m/z*) 793.4886 [M + Na]⁺, 793.4875 calculated for C₄₆H₆₆N₄O₆Na

H3C9Tol



Preparation was achieved following the method B using decyl (S)-phenylalaninate ammonium tosylate salt.

The product is recrystallized in acetonitrile.

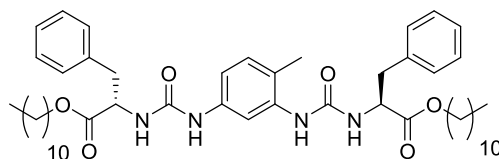
1.420 g (83%) of a pure product were obtained as a white paste.

¹H NMR (400 MHz, DMSO-*d*₆) δ 8.60 (s, 1H, ArH), 7.78 (d, 2H, NH, ²*J* = 28.8 Hz), 7.42-7.12 (m, 10H, ArH), 7.12 (d, 1H, NH, ²*J* = 6.9 Hz), 6.94 (d, 2H, ArH, ²*J* = 5.1 Hz), 6.28 (d, 1H, NH, ²*J* = 6.7 Hz), 4.59-4.44 (m, 2H, NH-CH), 4.02 (t, 4H, COO-CH₂, ²*J* = 6.4 Hz), 3.06-2.92 (m, 4H, NH₃-CH-CH₂), 2.09 (s, 3H, Ar-CH₃), 1.58-1.45 (m, 4H, COO-CH₂-CH₂), 1.30-1.15 (m, 28H, CH₂), 0.86 (t, 3H, CH₃, ²*J* = 6.9 Hz)

¹³C NMR (101 MHz, DMSO-*d*₆) δ 172.17, 154.61, 154.46, 138.09, 137.79, 136.84, 136.78, 129.91, 129.11, 128.23, 126.55, 119.38, 111.58, 109.94, 64.44, 53.96, 53.73, 37.71, 37.55, 31.28, 28.93, 28.92, 28.90, 28.69, 28.64, 28.02, 25.28, 22.09, 17.18, 13.90.

HRMS (ESI, *m/z*) 807.5029 [M + Na]⁺, 807.5031 calculated for C₄₇H₆₈N₄O₆Na

H3C10Tol



Preparation was achieved following the method B using undecyl (S)-phenylalaninate ammonium tosylate salt.

The product is recrystallized in acetonitrile.

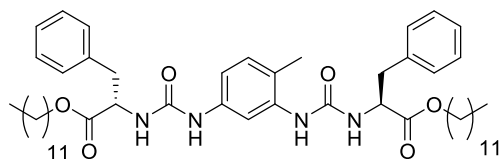
1.820 g (99%) of a pure product were obtained as a white paste.

¹H NMR (400 MHz, DMSO-*d*₆) δ 8.60 (s, 1H, ArH), 7.78 (d, 2H, ArH, ²*J* = 27.5 Hz), 7.37-7.14 (m, 10H, ArH), 7.12 (d, 1H, NH, ²*J* = 6.7 Hz), 6.94 (d, 2H, ArH, ²*J* = 5.1 Hz), 6.28 (d, 1H, NH, ²*J* = 6.0 Hz), 4.59-4.44 (m, 2H, NH-CH), 4.02 (t, 4H, COO-CH₂, ²*J* = 6.4 Hz), 3.06-2.92 (m, 4H, NH₃-CH-CH₂), 2.09 (s, 3H, Ar-CH₃), 1.58-1.45 (m, 4H, COO-CH₂-CH₂), 1.30-1.15 (m, 32H, CH₂), 0.86 (t, 3H, CH₃, ²*J* = 6.9 Hz)

¹³C NMR (101 MHz, DMSO-*d*₆) δ 172.16, 154.45, 138.10, 137.79, 136.84, 136.77, 129.90, 129.10, 128.22, 126.54, 119.36, 111.58, 109.94, 64.43, 53.95, 53.72, 37.71, 37.56, 31.29, 28.99, 28.90, 28.71, 28.65, 28.02, 25.29, 22.09, 17.18, 13.89.

HRMS (ESI, *m/z*) 835.5352 [*M* + Na]⁺, 835.5344 calculated for C₄₉H₇₂N₄O₆Na

H3C11Tol



Preparation was achieved following the method B using undecyl (S)-phenylalaninate ammonium tosylate salt.

The product is recrystallized in acetonitrile.

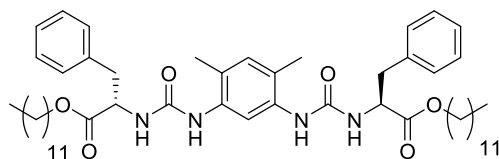
1.720 g (93%) of a pure product were obtained as a white paste.

¹H NMR (400 MHz, DMSO-*d*₆) δ 8.58 (s, 1H, ArH), 7.79 (s, 1H, ArH), 7.73 (d, 1H, ArH, *J* = 2.2 Hz), 7.34 – 7.26 (m, 5H, ArH and NH), 7.26 – 7.15 (m, 7H, ArH), 7.10 (dd, 1H, ArH, *J* = 8.2, 2.2 Hz), 6.96 – 6.89 (m, 2H, ArH), 6.26 (d, 1H, ArH, *J* = 8.0 Hz), 4.55 – 4.44 (m, 2H, NH-CH), 4.01 (t, 4H, COO-CH₂, *J* = 6.4 Hz), 3.07 – 2.93 (m, 4H, NH₃-CH-CH₂), 2.07 (s, 3H, Ar-CH₃), 1.56 – 1.43 (m, 4H, COO-CH₂-CH₂), 1.33 – 1.13 (m, 32H, CH₂), 0.85 (t, 6H, CH₃, *J* = 6.8 Hz).

¹³C NMR (101 MHz, DMSO-*d*₆) δ 172.16, 154.45, 138.09, 137.78, 136.84, 136.77, 129.90, 129.10, 128.22, 126.54, 111.58, 109.94, 64.43, 53.96, 53.73, 37.70, 37.54, 31.29, 29.04, 29.01, 28.97, 28.90, 28.72, 28.64, 28.02, 25.29, 22.08, 17.18, 13.90.

HRMS (ESI, *m/z*) 864.5697 [*M* + Na]⁺, 864.5691 calculated for C₅₁H₇₆N₄O₆Na

H3C11Xyl



Preparation was achieved following the method C using dodecyl (S)-phenylalaninate ammonium tosylate salt and 4,6-dimethyl-1,3-diaminobenzène.

The product is recrystallized twice in acetonitrile.

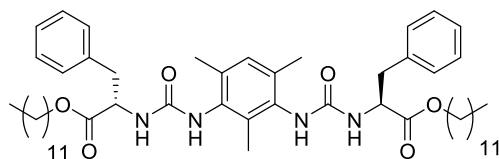
1.488 g (62%) of a pure product were obtained as a white paste.

¹H NMR (300 MHz, DMSO-*d*₆/THF-*d*₈ 2/1) δ 7.95 (s, 1H, ArH), 7.75 (s, 2H, NH), 7.36-7.15 (m, 10H, ArH and NH), 6.85 (s, 1H, ArH), 6.70 (d, 2H, ArH, ²*J* = 7.6 Hz), 4.49 (q, 2H, NH-CH, ²*J* = 6.7 Hz), 4.00 (t, 4H, COO-CH₂, ²*J* = 6.2 Hz), 3.08-2.91 (m, NH₃-CH-CH₂, 4H), 2.05 (s, 6H, Ar-CH₃), 1.50 (q, 4H, COOCH₂CH₂, ²*J* = 6.0 Hz), 1.30-1.15 (m, 36H, CH₂), 0.85 (t, 6H, COO-CH₂, ²*J* = 6.7 Hz)

¹³C NMR (101 MHz, DMSO-*d*₆/THF-*d*₈ 2/1) δ 173.59, 156.09, 138.36, 136.86, 132.38, 130.49, 129.43, 127.72, 123.84, 117.23, 65.74, 55.28, 39.42, 32.81, 30.56, 30.53, 30.51, 30.43, 30.24, 30.19, 29.52, 26.81, 25.65, 25.45, 25.25, 25.05, 23.56, 18.43, 14.99.

HRMS (ESI, *m/z*) 877.5807 [M + Na]⁺, 877.5814 calculated for C₅₂H₇₈N₄O₆Na

H3C11Mes



Preparation was achieved following the method C using dodecyl (S)-phenylalaninate ammonium tosylate salt and 2,4,6-trimethyl-1,3-diaminobenzène.

The product is recrystallized twice in acetonitrile.

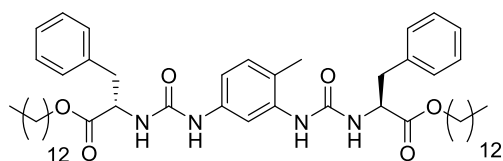
1.132 g (69%) of a pure product were obtained as a white paste.

¹H NMR (400 MHz, DMSO-*d*₆/THF-*d*₈ 2/1) δ 7.61 (s, 2H, NH), 7.33 – 7.15 (m, 10H, ArH), 6.83 (s, 1H, ArH), 6.44 (s, 2H, NH), 4.54 (q, 2H, NH-CH, *J* = 7.1 Hz), 4.03 (t, 4H, COO-CH₂, *J* = 6.6 Hz), 3.12 – 2.94 (m, 4H, NH₃-CH-CH₂), 2.08 (s, 6H, Ar-CH₃), 1.60 – 1.49 (m, 4H, CH₂), 1.36 – 1.19 (m, 36H, CH₂), 0.87 (t, 6H, CH₂, *J* = 6.9 Hz).

¹³C NMR (101 MHz, DMSO-*d*₆/THF-*d*₈ 2/1) δ 172.12, 155.25, 137.02, 133.54, 129.05, 127.90, 126.18, 114.48, 64.23, 53.84, 53.84, 37.75, 31.32, 29.07, 29.04, 29.02, 28.95, 28.74, 28.70, 28.06, 25.32, 22.07, 17.65, 13.51, 13.29.

HRMS (ESI, *m/z*) 891.5983 [M + Na]⁺, 891.5970 calculated for C₅₃H₈₀N₄O₆Na

H3C12Tol



Preparation was achieved following the method B using tridecyl (S)-phenylalaninate ammonium tosylate salt.

The product is recrystallized in acetonitrile.

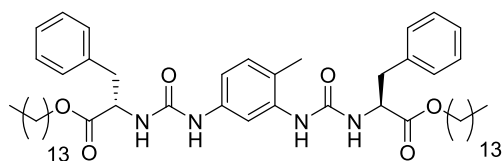
757 mg (99%) of a pure product were obtained as a white paste.

¹H NMR (400 MHz, DMSO-*d*₆) δ 8.58 (s, 1H, ArH), 7.79 (s, 1H, NH), 7.73 (s, 1H, NH), 7.35 – 7.14 (m, 11H, ArH), 7.09 (d, 2H, ArH, *J* = 7.6 Hz), 6.92 (d, 2H, NH, *J* = 8.2 Hz), 6.26 (d, 1H, ArH, *J* = 7.9 Hz), 4.56 – 4.43 (m, 2H, NH-CH), 4.00 (t, 4H, COO-CH₂, *J* = 6.5 Hz), 2.99 (q, 4H, NH₃-CH-CH₂, *J* = 7.3, 6.4 Hz), 2.07 (s, 3H, Ar-CH₃), 1.58 – 1.41 (m, 4H, CH₂), 1.36 – 1.07 (m, 36H, CH₂), 0.85 (t, 6H, CH₃, *J* = 6.6 Hz).

¹³C NMR (101 MHz, DMSO-*d*₆) δ 172.16, 154.60, 138.09, 137.78, 136.84, 136.77, 129.90, 129.10, 128.22, 126.54, 119.37, 111.58, 109.95, 64.42, 53.96, 53.73, 37.69, 37.54, 31.29, 29.05, 29.02, 28.97, 28.89, 28.71, 28.64, 28.02, 25.28, 22.08, 17.18, 13.89.

HRMS (ESI, *m/z*) 891.5964 [*M* + Na]⁺, 891.5970 calculated for C₅₃H₈₀N₄O₆Na

H3C13Tol



Preparation was achieved following the method B using tetradecyl (S)-phenylalaninate ammonium tosylate salt.

The product is recrystallized in acetonitrile.

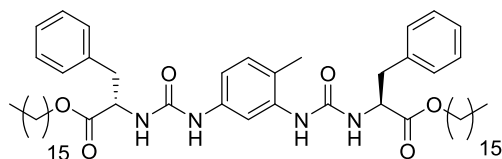
746 mg (96%) of a pure product were obtained as a white paste.

¹H NMR (400 MHz, DMSO-*d*₆/THF-*d*₈ 2/1) δ 8.60 (s, 1H, ArH), 7.79 (d, 2H, NH, *J* = 16.7 Hz), 7.38 – 7.15 (m, 10H, ArH), 6.96 (d, 1H, ArH, *J* = 7.8 Hz), 6.90 (d, 1H, ArH, *J* = 8.3 Hz), 6.28 (d, 1H, NH, *J* = 8.0 Hz), 4.57 (dd, 2H, NH-CH, *J* = 14.9, 7.4 Hz), 4.03 (t, 4H, COO-CH₂, *J* = 6.7 Hz), 3.12 – 2.94 (m, 4H, NH₃-CH-CH₂), 2.11 (s, 3H, Ar-CH₃), 1.64 – 1.46 (m, 4H, CH₂), 1.43 – 1.06 (m, 40H, CH₂), 0.87 (t, 6H, CH₃, *J* = 6.5 Hz).

¹³C NMR (101 MHz, DMSO-*d*₆/THF-*d*₈ 2/1) δ 172.11, 154.58, 154.45, 138.39, 137.97, 136.96, 136.90, 129.66, 129.10, 128.07, 126.37, 118.99, 114.60, 111.37, 109.69, 64.38, 53.94, 53.72, 38.04, 37.86, 31.43, 31.43, 29.19, 29.06, 28.85, 28.16, 25.44, 22.18, 22.18, 17.04, 13.59.

HRMS (ESI, *m/z*) 919.6298 [*M* + Na]⁺, 919.6283 calculated for C₅₅H₈₄N₄O₆Na

H3C15Tol



Preparation was achieved following the method B using hexadecyl (S)-phenylalaninate ammonium tosylate salt.

The product is recrystallized in acetonitrile.

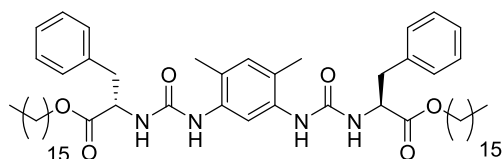
2.009 g (93%) of a pure product were obtained as a white paste.

¹H NMR (400 MHz, DMSO-*d*₆) δ 8.59 (s, 1H, NH), 7.81 (s, 1H, NH), 7.77 (d, 1H, ArH, *J* = 2.2 Hz), 7.33 – 7.26 (m, 4H, ArH), 7.26 – 7.17 (m, 7H, ArH), 6.96 (d, 1H, ArH, *J* = 7.8 Hz), 6.90 (d, 1H, NH, *J* = 8.3 Hz), 6.27 (d, 1H, NH, *J* = 7.9 Hz), 4.63 – 4.47 (m, 2H, NH-CH), 4.03 (t, 4H, COO-CH₂, *J* = 6.7 Hz), 3.11 – 2.94 (m, 4H, NH₃-CH-CH₂), 2.10 (s, 3H, Ar-CH₃), 1.60 – 1.48 (m, 4H, CH₂), 1.37 – 1.18 (m, 52H, CH₂), 0.87 (t, 6H, CH₃, *J* = 6.7 Hz).

¹³C NMR (101 MHz, DMSO-*d*₆) δ 172.00, 154.48, 154.34, 138.25, 137.85, 136.84, 136.78, 129.57, 128.99, 127.98, 126.28, 118.93, 111.29, 109.62, 66.30, 66.08, 65.87, 65.65, 64.28, 53.84, 53.62, 37.90, 37.72, 31.31, 29.07, 29.03, 28.94, 28.73, 28.04, 25.32, 24.17, 23.97, 23.77, 22.07, 16.94, 13.51.

HRMS (ESI, *m/z*) 835.5340 [*M* + Na]⁺, 853.5344 calculated for C₄₉H₇₂N₄O₆Na

H3C15Xyl



Preparation was achieved following the method C using hexadecyl (S)-phenylalaninate ammonium tosylate salt and 4,6-dimethyl-1,3-diaminobenzène.

The product is recrystallized twice in acetonitrile.

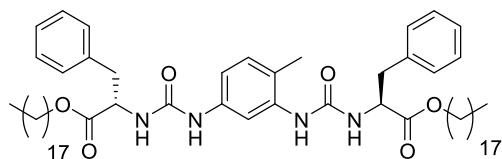
1.0555 g (64%) of a pure product were obtained as a white paste.

¹H NMR (400 MHz, DMSO-*d*₆/THF-*d*₈ 2/1) δ 8.02 (s, 1H, ArH), 7.77 (s, 2H, NH), 7.33 – 7.15 (m, 12H, ArH), 6.83 (s, 1H, ArH), 6.71 (d, 2H, NH, *J* = 8.0 Hz), 4.57 (q, 2H, NH-CH, *J* = 7.0 Hz), 4.02 (t, 4H, COO-CH₂, *J* = 6.5 Hz), 3.02 (dd, NH₃-CH-CH₂, 4H, *J* = 6.6, 3.3 Hz), 2.08 (s, 6H, Ar-CH₃), 1.60 – 1.45 (m, 4H, CH₂), 1.39 – 1.13 (m, 62H, CH₂), 0.87 (t, H, CH₃, *J* = 6.7 Hz).

¹³C NMR (101 MHz, DMSO-*d*₆/THF-*d*₈ 2/1) δ 172.11, 154.61, 136.88, 135.36, 130.90, 129.01, 127.95, 126.24, 122.33, 115.73, 64.25, 53.80, 31.31, 29.07, 29.03, 28.94, 28.73, 28.70, 28.03, 25.32, 22.07, 16.95, 13.51.

HRMS (ESI, *m/z*) 989.7085 [*M* + Na]⁺, 989.7066 calculated for C₆₀H₉₄N₄O₆Na

H3C17Tol



Preparation was achieved following the method B using octadecyl (S)-phenylalaninate ammonium tosylate salt.

The product is recrystallized in acetonitrile.

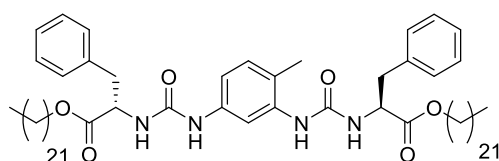
923 mg (92%) of a pure product were obtained as a white paste. The S enantiomer was synthesized as well (88% yield).

¹H NMR (400 MHz, DMSO-*d*₆/THF-*d*₈ 2/1) δ 8.60 (s, 1H, NH), 7.82 (s, 1H, NH), 7.77 (d, 1H, ArH, *J* = 2.2 Hz), 7.34 – 7.17 (m, 12H, ArH), 6.97 (d, 1H, NH, *J* = 7.9 Hz), 6.90 (d, 1H, NH, *J* = 8.3 Hz), 6.29 (d, 1H, ArH, *J* = 8.0 Hz), 4.64 – 4.48 (m, 2H, NH-CH), 4.09 – 3.98 (m, 4H, COO-CH₂), 3.12 – 2.95 (m, 4H, NH₃-CH-CH₂), 2.20 – 2.05 (m, 3H, Ar-CH₃), 1.54 (p, 4H, CH₂, *J* = 6.5 Hz), 1.36 – 1.17 (m, 60H, CH₂), 0.87 (t, 6H, CH₃, *J* = 6.7 Hz).

¹³C NMR (101 MHz, DMSO-*d*₆/THF-*d*₈ 2/1) δ 172.10, 154.59, 154.44, 138.40, 137.98, 136.97, 136.91, 129.64, 129.10, 128.05, 126.36, 118.98, 111.37, 109.70, 64.36, 53.95, 53.73, 38.05, 37.87, 31.44, 29.20, 29.16, 29.08, 28.86, 28.17, 25.46, 25.44, 22.19.

HRMS (ESI, *m/z*) 1031.7550 [*M* + Na]⁺, 1031.7535 calculated for C₆₃H₁₀₀N₄O₆Na

H3C21Tol



Preparation was achieved following the method B using docosyl (S)-phenylalaninate ammonium tosylate salt.

The product is recrystallized in acetonitrile.

750 mg (96%) of a pure product were obtained as a white paste.

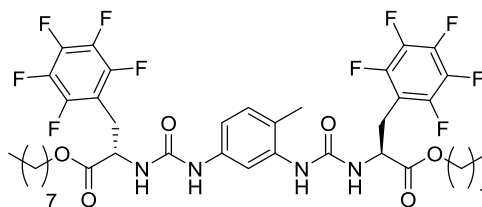
¹H NMR (400 MHz, THF-*d*₈) δ 7.91 (s, 1H, NH), 7.69 (d, 1H, NH, *J* = 2.2 Hz), 7.45 (dd, 1H, ArH, *J* = 8.2, 2.2 Hz), 7.27 (s, 1H, ArH), 7.25 – 7.08 (m, 11H, ArH), 6.86 (d, 1H, NH, *J* = 8.3 Hz), 6.21 (d, 1H, NH, *J* = 7.8 Hz), 5.63 (d, 1H, ArH, *J* = 7.9 Hz), 4.76 – 4.67 (m, 2H, NH-CH), 4.12 – 3.95 (m, 4H, COO-CH₂), 3.18 – 2.99 (m, 4H, NH₃-CH-CH₂), 2.05 (s, 3H, Ar-CH₃), 1.65 – 1.50 (m, 4H, CH₂), 1.39 – 1.17 (m, 72H, CH₂), 0.86 (t, 6H, CH₃, *J* = 6.6 Hz).

¹³C NMR (101 MHz, THF-*d*₈) δ 173.10, 173.06, 155.47, 155.26, 140.04, 139.19, 138.26, 130.88, 130.53, 129.12, 129.09, 127.46, 127.41, 120.18, 117.99, 113.32, 111.16, 65.70, 54.97, 54.79, 39.48, 33.03, 30.81, 30.76, 30.68, 30.47, 30.43, 29.72, 27.05, 27.03, 23.72, 17.40, 14.61.

HRMS (ESI, *m/z*) 1143.8808 [*M* + Na]⁺, 1143.8787 calculated for C₇₁H₁₁₆N₄O₆Na

b. Bis-ureas synthesized from other aminoacids

H3C7F₅-PheTol



Preparation was achieved following the method B using octyl (S)-pentafluorophenylalaninate ammonium tosylate salt.

The product is recrystallized in acetonitrile.

183 mg (32%) of a pure product were obtained as a white paste.

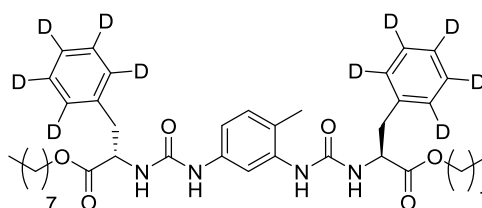
¹H NMR (400 MHz, DMSO-*d*₆) δ 8.61 (s, 1H, *NH*), 7.82 (s, 1H, *NH*), 7.62 (s, 1H, *ArH*), 7.04 (d, 2H, *ArH*, ²*J* = 7.3 Hz), 6.94 (d, 1H, *NH*, ²*J* = 8.4 Hz), 6.43 (d, 1H, *NH*, ²*J* = 8.4 Hz), 4.62-4.44 (m, 2H, *NH-CH*), 4.14-3.98 (m, 4H, *COO-CH₂*), 3.25-3.07 (m, 4H, *NH₃-CH-CH₂*), 2.05 (s, 3H, *Ar-CH₃*), 1.58-1.45 (m, 4H, *COO-CH₂-CH₂*), 1.30-1.15 (m, 20H, *CH₂*), 0.84 (t, 3H, *CH₃*, ²*J* = 6.3 Hz)

¹³C NMR (101 MHz, DMSO-*d*₆) δ 172.20, 154.62, 154.48, 138.10, 137.79, 136.66, 136.59, 129.93, 119.43, 111.61, 109.97, 64.45, 53.96, 53.74, 37.60, 37.44, 31.20, 28.60, 28.55, 28.02, 25.28, 22.06, 17.18, 13.89.

¹⁹F NMR (376 MHz, DMSO-*d*₆) δ -142.35 (ddd, *J* = 24.9, 17.2, 7.7 Hz), -156.91 (t, *J* = 22.0 Hz), -163.36 (dq, *J* = 23.1, 7.8 Hz).

HRMS (ESI, *m/z*) 931.3480 [*M* + Na]⁺, 931.3463 calculated for C₄₃H₅₀F₁₀N₄O₆Na

H3C7d₅-PheTol



Preparation was achieved following the method B using octyl (S)-d₅-phenylalaninate ammonium tosylate salt.

The product is recrystallized in acetonitrile.

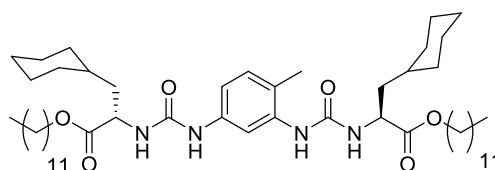
649 mg (73%) of a pure product were obtained as a white paste.

¹H NMR (300 MHz, DMSO-*d*₆) δ 8.59 (s, 1H, *NH*), 7.80 (s, 1H, *ArH*), 7.72 (s, 1H, *NH*), 7.10 (d, 1H, *NH*, ²*J* = 8.3 Hz), 6.93 (d, 2H, *ArH*, ²*J* = 7.4 Hz), 6.27 (d, 1H, *NH*, ²*J* = 8.1 Hz), 4.49 (qi, 2H, *NH-CH*, ²*J* = 7.2 Hz), 4.01 (t, 4H, *COO-CH₂*, ²*J* = 6.5 Hz), 3.05-2.95 (m, 4H, *COO-CH₂-CH₂*), 2.07 (s, 3H, *Ar-CH₃*), 1.56-1.44 (m, 4H, *COO-CH₂-CH₂-CH₂*), 1.33-1.15 (m, 44H, *CH₂*), 0.84 (t, 3H, *CH₃*, ²*J* = 6.5 Hz)

¹³C NMR (101 MHz, DMSO-*d*₆) δ 172.20, 154.62, 154.48, 138.10, 137.79, 136.66, 136.59, 129.93, 119.43, 111.61, 109.97, 64.45, 53.96, 53.74, 37.60, 37.44, 31.20, 28.60, 28.55, 28.02, 25.28, 22.06, 17.18, 13.89.

HRMS (ESI, *m/z*) 761.5039 [*M* + Na]⁺, 761.5033 calculated for C₃₅H₅₀D₁₀N₄O₆Na

H3C11ChaTol



Preparation was achieved following the method B using dodecyl (S)-cyclohexylalaninate ammonium tosylate salt.

The product is recrystallized in acetonitrile.

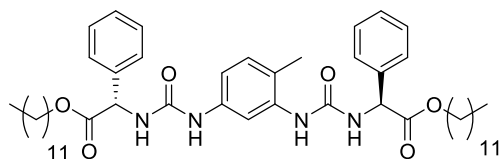
697 mg (61%) of a pure product were obtained as a white paste.

¹H NMR (300 MHz, DMSO-*d*₆) δ 8.43 (s, 1H, *NH*), 7.80 (s, 1H, *ArH*), 7.68 (s, 1H, *NH*), 7.07 (d, 1H, *NH*, ²*J* = 7.6 Hz), 6.91 (t, 2H, *ArH*, ²*J* = 7.6 Hz), 6.27 (d, 1H, *NH*, ²*J* = 7.7 Hz), 4.34-4.15 (m, 2H, *NH-CH*), 4.15-3.93 (m, 4H, *COO-CH₂*), 2.10 (s, 3H, *Ar-CH₃*), 1.80-1.04 (m, 44H, *CH₂*), 0.85 (t, 3H, *CH₃*, ²*J* = 6.5 Hz)

¹³C NMR (75 MHz, DMSO-*d*₆) δ 173.92, 155.28, 155.15, 138.65, 138.40, 130.39, 119.55, 111.96, 110.16, 64.74, 50.82, 34.07, 33.44, 32.48, 31.79, 29.48, 29.42, 29.20, 29.10, 28.59, 26.44, 26.20, 26.06, 25.84, 22.58, 17.65, 14.36.

HRMS (ESI, *m/z*) 875.6594 [*M* + Na]⁺, 875.6596 calculated for C₅₁H₈₆N₄O₆Na

H3C11PhGlyTol



Preparation was achieved following the method B using dodecyl (S)-phenylglycinate ammonium tosylate salt.

The product is recrystallized in acetonitrile.

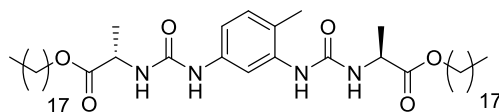
714 mg (78%) of a pure product were obtained as a white paste.

¹H NMR (300 MHz, DMSO-*d*₆) δ 8.58 (s, 1H, NH), 7.83 (s, 2H, ArH), 7.50 (d, 1H, NH, ²*J* = 6.8 Hz), 7.47-7.28 (m, 10H, ArH and NH), 7.10 (d, 1H, NH, ²*J* = 8.0 Hz), 6.94 (d, 1H, NH, ²*J* = 8.0 Hz), 6.98 (d, 1H, ArH, ²*J* = 7.1 Hz), 5.35-5.25 (m, 2H, NH-CH), 4.16-3.96 (m, 4H, COO-CH₂), 2.10 (s, 3H, Ar-CH₃), 1.54-1.40 (m, 4H, CH₂), 1.36-1.04 (m, 40H, CH₂), 0.85 (t, 3H, CH₃, ²*J* = 6.5 Hz)

¹³C NMR (101 MHz, THF-*d*₈) δ 172.43, 155.30, 155.06, 139.90, 139.87, 139.71, 139.14, 130.90, 129.46, 129.39, 128.75, 128.64, 128.26, 128.20, 119.99, 113.29, 110.83, 65.96, 58.10, 57.88, 33.04, 30.77, 30.75, 30.68, 30.62, 30.47, 30.29, 29.61, 26.83, 26.81, 23.73, 17.33, 14.61.

HRMS (ESI, *m/z*) 835.5357 [*M* + Na]⁺, 833.5344 calculated for C₄₉H₇₂N₄O₆Na

H3C17AlaTol



Preparation was achieved following the method B using octadecyl (S)-Alaninate ammonium tosylate salt.

The product is recrystallized in acetonitrile.

102 mg (15%) of a pure product were obtained as a white paste.

¹H NMR (400 MHz, DMSO-*d*₆/THF-*d*₈ 2/1) δ 8.49 (s, 1H, ArH), 7.80 (s, 1H, NH), 7.71 (s, 1H, NH), 7.23 (d, 1H, ArH, *J* = 8.2 Hz), 6.98 (d, 1H, ArH, *J* = 7.4 Hz), 6.90 (d, 1H, NH, *J* = 8.3 Hz), 6.32 (d, 1H, NH, *J* = 7.6 Hz), 4.38 – 4.20 (m, 2H, NH-CH), 4.16 – 4.00 (m, 4H, COO-CH₂), 2.13 (s, 3H, Ar-CH₃), 1.67 – 1.54 (m, 4H, CH₂), 1.42 – 1.14 (m, 66H, CH₂ and CH₃), 0.87 (t, 6H, CH₃, *J* = 6.6 Hz).

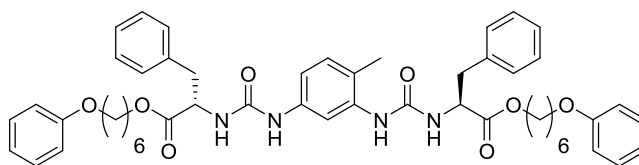
¹³C NMR (101 MHz, DMSO-*d*₆/THF-*d*₈ 2/1) δ 188.82, 170.04, 169.91, 154.00, 153.52, 144.98, 134.06, 126.69, 124.88, 79.70, 63.66, 63.47, 46.92, 44.68, 44.64, 44.59, 44.34, 44.32, 43.74, 43.72, 40.94, 40.91, 37.65, 33.41, 32.37, 28.89.

HRMS (ESI, *m/z*) 879.6902 [*M* + Na]⁺, 879.6909 calculated for C₅₁H₉₂N₄O₆Na

6. Functionalized ester bis-ureas

a. Bis-ureas bearing a phenoxy moiety

PhO6Tol



Preparation was achieved following the method B using 6-phenoxyhexyl (S)-phenylalaninate ammonium tosylate salt.

The product was purified by flash chromatography (5 to 20% AcOEt/DCM).

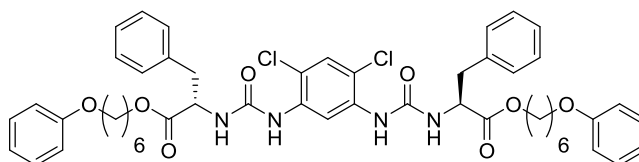
749 mg (88%) of a pure product were obtained as a white paste.

¹H NMR (300 MHz, DMSO-*d*₆) δ 8.68 (s, 1H, NH), 7.82 (s, 1H, NH), 7.74 (d, 1H, ArH, ²*J* = 2.2 Hz), 7.40-6.80 (m, 21H, ArH and NH), 6.28 (d, 1H, ArH, ²*J* = 7.9 Hz), 4.50 (p, 2H, NH-CH, ²*J* = 7.2 Hz), 4.07-3.97 (m, 4H, COO-CH₂), 3.90 (t, 4H, ArO-CH₂, ²*J* = 6.3 Hz), 3.00 (AB spin system, NH₃-CH-CH₂, 4H), 2.07 (s, 3H, Ar-CH₃), 1.66 (p, 4H, COO-CH₂-CH₂, ²*J* = 7.0 Hz), 1.53 (p, 4H, ArO-CH₂-CH₂, ²*J* = 7.0 Hz), 1.45-1.15 (m, 8H, CH₂)

¹³C NMR (101 MHz, DMSO-*d*₆) δ 172.20, 158.60, 154.48, 138.06, 137.77, 136.84, 136.78, 129.38, 129.12, 128.26, 126.57, 120.27, 114.49, 114.33, 69.83, 67.09, 64.40, 37.50, 28.52, 27.96, 25.14, 25.04, 17.18.

HRMS (ESI, m/z) 879.4317 [M + Na]⁺, 879.4303 calculated for C₅₁H₆₀N₄O₈Na

PhO6Cl



Preparation was achieved following the method C using 6-phenoxyhexyl (S)-phenylalaninate ammonium tosylate salt and 4,6-dichloro-1,3-diaminobenzène.

The product is recrystallized in acetonitrile.

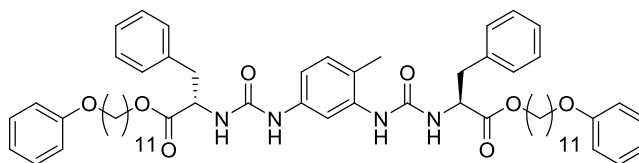
323 mg (53%) of pure product were obtained as a white powder.

¹H NMR (300 MHz, DMSO-*d*₆) δ 8.92 (s, 1H, ArH), 8.24 (s, 2H, NH), 7.60-7.05 (m, 19H, ArH and NH), 6.89 (d, 4H, ArH, ²*J* = 7.1 Hz), 4.50 (q, 2H, NH-CH, ²*J* = 6.6 Hz), 4.03 (t, 4H, COO-CH₂, ²*J* = 4.7 Hz), 3.90 (t, 4H, ArO-CH₂, ²*J* = 4.7 Hz), 3.00 (AB spin system, NH₃-CH-CH₂, 4H), 1.78-1.58 (m, 4H, COO-CH₂-CH₂), 1.58-1.45 (m, 4H, ArO-CH₂-CH₂), 1.45-1.18 (m, 8H, CH₂)

¹³C NMR (101 MHz, DMSO-*d*₆) δ 172.02, 158.61, 153.92, 136.72, 135.43, 129.37, 129.08, 128.28, 128.21, 126.61, 120.26, 114.45, 114.32, 112.89, 67.09, 64.48, 54.01, 37.52, 28.53, 27.95, 25.15, 25.05.

HRMS (ESI, m/z) 933.3386 [M + Na]⁺, 933.3367 calculated for C₅₀H₅₆Cl₂N₄O₈Na

PhO11Tol



Preparation was achieved following the method B using 11-phenoxyundecyl (S)-phenylalaninate ammonium tosylate salt.

The product was purified by flash chromatography (5 to 20% AcOEt/DCM).

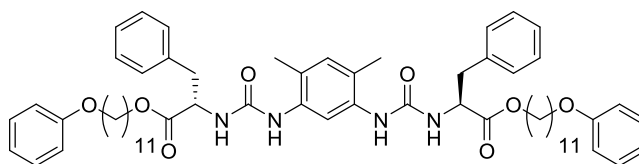
378 mg (22%) of a pure product were obtained as a white paste.

¹H NMR (400 MHz, DMSO-*d*₆) δ 8.59 (s, 1H, ArH), 7.80 (s, 1H, ArH), 7.73 (d, 1H, ArH, *J* = 2.2 Hz), 7.38 – 7.16 (m, 15H, ArH and NH), 7.11 (dd, 1H, ArH, *J* = 8.2, 2.3 Hz), 6.96 – 6.85 (m, 7H, ArH and NH), 6.26 (d, 1H, ArH, *J* = 7.9 Hz), 4.54 – 4.44 (m, 2H, NH-CH), 4.00 (d, 4H, COO-CH₂, *J* = 6.5 Hz), 3.92 (t, 4H, ArO-CH₂, *J* = 6.5 Hz), 3.07 – 2.92 (m, 4H, CH₂), 2.07 (s, 3H, Ar-CH₃), 1.73 – 1.62 (m, 4H, CH₂), 1.56 – 1.43 (m, 4H, CH₂), 1.43 – 1.33 (m, 4H, CH₂), 1.33 – 1.12 (m, 28H, CH₂).

¹³C NMR (101 MHz, DMSO-*d*₆) δ 172.17, 158.63, 154.61, 138.09, 137.79, 136.84, 136.77, 129.93, 129.36, 129.11, 128.24, 126.56, 120.25, 119.38, 114.31, 109.92, 53.97, 53.73, 37.69, 37.54, 28.97, 28.90, 28.86, 28.76, 28.69, 28.62, 28.01, 25.51, 25.26, 17.19.

HRMS (ESI, *m/z*) 1019.5862 [*M* + Na]⁺, 1019.5868 calculated for C₆₁H₈₀N₄O₈Na

PhO11Xyl



Preparation was achieved following the method C using 11-phenoxyundecyl (S)-phenylalaninate ammonium tosylate salt and 4,6-dimethyl-1,3-diaminobenzène.

The product is recrystallized in acetonitrile.

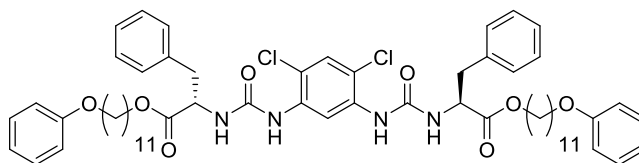
605 mg (73%) of a pure product were obtained as a white paste.

¹H NMR (300 MHz, DMSO-*d*₆) δ 7.96 (s, 1H, ArH), 7.76 (s, 2H, NH), 7.40-7.10 (m, 15H, ArH and NH), 6.98-6.80 (m, 8H, ArH and NH), 6.72 (d, 2H, ArH, ²*J* = 7.8 Hz), 4.49 (q, 2H, NH-CH, ²*J* = 7.0 Hz), 3.99 (t, 4H, COO-CH₂, ²*J* = 6.7 Hz), 3.92 (t, 4H, ArO-CH₂, ²*J* = 6.7 Hz), 2.98 (AB spin system, NH₃-CH-CH₂, 4H), 2.05 (s, 6H, Ar-CH₃), 1.80-1.58 (m, 4H, COO-CH₂-CH₂), 1.58-1.10 (m, 32H, CH₂)

¹³C NMR (101 MHz, DMSO-*d*₆) δ 172.26, 158.62, 154.72, 136.86, 135.27, 131.19, 129.36, 129.11, 128.21, 126.52, 122.36, 120.24, 115.60, 114.31, 67.19, 64.41, 53.90, 37.74, 28.97, 28.90, 28.86, 28.76, 28.69, 28.62, 28.00, 25.52, 25.26, 17.17.

HRMS (ESI, *m/z*) 1033.6019 [*M* + Na]⁺, 1033.6025 calculated for C₆₂H₈₂N₄O₈Na

PhO11Cl



Preparation was achieved following the method C using 11-phenoxundecyl (S)-phenylalaninate ammonium tosylate salt and 4,6-dichloro-1,3-diaminobenzène.

The product is recrystallized in acetonitrile.

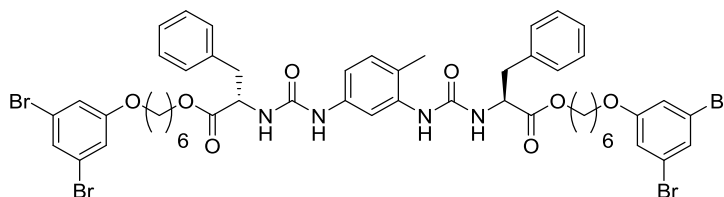
917 mg (77%) of pure product were obtained as a white powder.

¹H NMR (300 MHz, DMSO-*d*₆) δ 8.92 (s, 1H, ArH), 8.20 (s, 2H, NH), 7.50-7.10 (m, 23H, ArH and NH), 6.89 (d, 4H, ArH, ²*J* = 7.1 Hz), 4.50 (q, 2H, NH-CH, ²*J* = 7.0 Hz), 4.00 (t, 4H, COO-CH₂, ²*J* = 4.7 Hz), 3.00 (AB spin system, NH₃-CH-CH₂, 4H), 1.78-1.58 (m, 4H, COO-CH₂-CH₂), 1.65-1.40 (m, 8H, CH₂), 1.45-1.18 (m, 32H, CH₂)

¹³C NMR (101 MHz, DMSO-*d*₆) δ 171.98, 153.87, 142.24, 136.72, 135.44, 129.05, 128.25, 128.16, 128.12, 126.58, 125.49, 114.31, 64.50, 53.99, 37.48, 35.15, 30.98, 28.96, 28.92, 28.86, 28.84, 28.64, 28.61, 27.98, 25.27.

HRMS (ESI, *m/z*) 1073.4949 [*M* + Na]⁺, 1073.4932 calculated for C₆₀H₇₆Cl₂N₄O₈Na

BrPhO6Tol



Preparation was achieved following the method B using 6-(3,5-dibromophenoxy)hexyl (S)-phenylalaninate ammonium tosylate salt.

The product is recrystallized in acetonitrile.

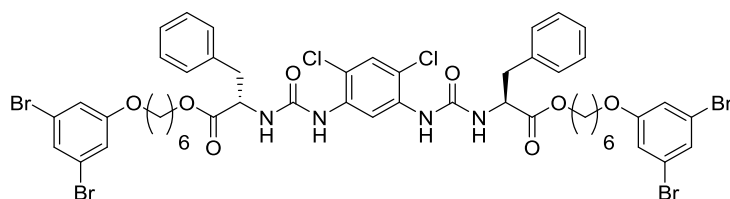
685 mg (53%) of a pure product were obtained as a white powder.

¹H NMR (300 MHz, DMSO-*d*₆) δ 8.68 (s, 1H, NH), 7.82 (s, 1H, NH), 7.74 (d, 1H, ArH, ²*J* = 2.2 Hz), 7.40-6.80 (m, 17H, ArH and NH), 6.28 (d, 1H, ArH, ²*J* = 7.9 Hz), 4.50 (p, 2H, NH-CH, ²*J* = 7.2 Hz), 4.07-3.97 (m, 4H, COO-CH₂), 3.95 (t, 4H, ArO-CH₂, ²*J* = 6.3 Hz), 3.00 (AB spin system, NH₃-CH-CH₂, 4H), 2.07 (s, 3H, Ar-CH₃), 1.63 (p, 4H, COO-CH₂-CH₂, ²*J* = 7.0 Hz), 1.53 (p, 4H, ArO-CH₂-CH₂, ²*J* = 7.0 Hz), 1.45-1.15 (m, 8H, CH₂)

¹³C NMR (101 MHz, DMSO-*d*₆) δ 172.20, 160.23, 154.63, 154.49, 138.06, 137.77, 136.83, 136.77, 129.95, 129.11, 128.25, 126.57, 125.38, 122.75, 122.75, 119.47, 116.92, 109.99, 68.29, 64.38, 53.98, 53.75, 37.66, 37.49, 28.22, 27.94, 24.95, 17.19.

HRMS (ESI, *m/z*) 1195.0711 [*M* + Na]⁺, 1195.0683 calculated for C₅₁H₅₆Br₄N₄O₈Na

BrPhO6Cl



Preparation was achieved following the method C using 6-(3,5-dibromophenoxy)hexyl (S)-phenylalaninate ammonium tosylate salt and 4,6-dichloro-1,3-diaminobenzène.

The product is recrystallized in acetonitrile.

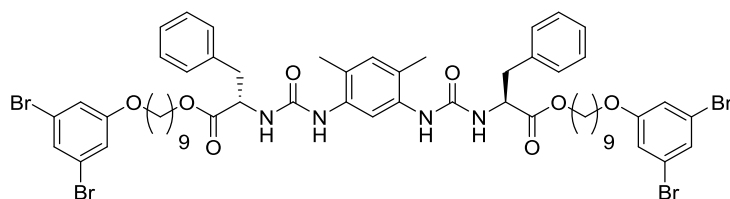
1.524 g (57%) of pure product were obtained as a white powder.

¹H NMR (300 MHz, DMSO-*d*₆) δ 7.96 (s, 1H, ArH), 7.76 (s, 2H, NH), 7.35-7.15 (m, 17H, ArH and NH), 6.84 (s, 1H, ArH), 6.71 (d, 2H, ArH, ²*J* = 8.0 Hz), 4.49 (q, 2H, NH-CH, ²*J* = 7.1 Hz), 3.99 (t, 4H, COO-CH₂, ²*J* = 6.7 Hz), 3.97 (t, 4H, ArO-CH₂, ²*J* = 6.7 Hz), 2.98 (AB spin system, NH₃-CH-CH₂, 4H), 1.65 (p, 4H, COO-CH₂-CH₂, ²*J* = 6.8 Hz), 1.56-1.42 (m, 4H, ArO-CH₂-CH₂), 1.42-1.15 (m, 8H, CH₂)

¹³C NMR (101 MHz, DMSO-*d*₆) δ 172.01, 160.22, 153.90, 136.71, 135.40, 129.07, 128.27, 126.59, 125.37, 122.73, 116.90, 114.42, 112.86, 68.28, 64.45, 54.00, 37.48, 28.21, 27.91, 24.94.

HRMS (ESI, *m/z*) 1248.9755 [*M* + Na]⁺, 1248.9747 calculated for C₅₀H₅₂Br₄Cl₂N₄O₈Na

BrPhO9Xyl



Preparation was achieved following the method C using 9-(3,5-dibromophenoxy)nonyl (S)-phenylalaninate ammonium tosylate salt and 4,6-dimethyl-1,3-diaminobenzène.

The product is recrystallized in acetonitrile.

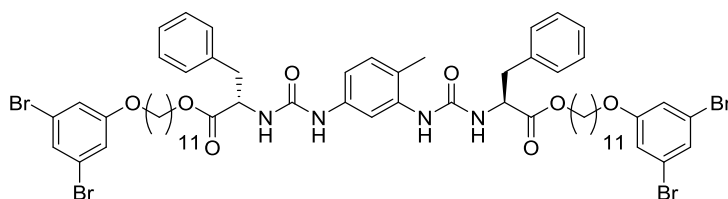
277 mg (66%) of a pure product were obtained as a white paste.

¹H NMR (300 MHz, DMSO-*d*₆) δ 7.96 (s, 1H, ArH), 7.76 (s, 2H, NH), 7.35-7.15 (m, 17H, ArH and NH), 6.84 (s, 1H, ArH), 6.71 (d, 2H, ArH, ²*J* = 8.0 Hz), 4.49 (q, 2H, NH-CH, ²*J* = 7.1 Hz), 3.99 (t, 4H, COO-CH₂, ²*J* = 6.7 Hz), 3.97 (t, 4H, ArO-CH₂, ²*J* = 6.7 Hz), 2.98 (AB spin system, NH-CH-CH₂, 4H), 2.05 (s, 6H, Ar-CH₃), 1.65 (p, 4H, COO-CH₂-CH₂, ²*J* = 6.8 Hz), 1.56-1.42 (m, 4H, ArO-CH₂-CH₂), 1.42-1.15 (m, 20H, CH₂)

¹³C NMR (101 MHz, DMSO-*d*₆) δ 172.27, 160.24, 154.71, 136.86, 135.26, 131.19, 129.11, 128.21, 126.52, 125.36, 122.75, 122.34, 116.91, 115.59, 68.38, 64.40, 53.90, 37.72, 28.79, 28.55, 28.35, 27.99, 25.28, 25.24, 17.18.

HRMS (ESI, *m/z*) 1293.1786 [*M* + Na]⁺, 1293.1778 calculated for C₅₈H₇₀Br₄N₄O₈Na

BrPhO11Tol



Preparation was achieved following the method B using 11-(3,5-dibromophenoxy)undecyl (S)-phenylalaninate ammonium tosylate salt.

The product was purified by flash chromatography (5 to 20% AcOEt/DCM).

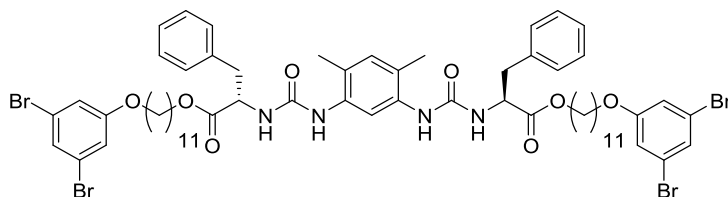
257 mg (12%) of a pure product were obtained as a slightly yellow paste.

¹H NMR (400 MHz, DMSO-*d*₆) δ 8.58 (s, 1H, NH), 7.79 (s, 1H, NH), 7.72 (d, 1H, ArH, *J* = 2.2 Hz), 7.36 – 7.06 (m, 18H, ArH), 6.92 (d, 2H, NH, *J* = 8.2 Hz), 6.25 (d, 1H, ArH, *J* = 8.0 Hz), 4.55 – 4.43 (m, 2H, NH-CH), 4.06 – 3.91 (m, 8H, COO-CH₂ and ArO-CH₂), 3.07 – 2.92 (m, 4H, NH-CH-CH₂), 2.06 (s, 3H, Ar-CH₃), 1.70 – 1.60 (m, 4H, CH₂), 1.54 – 1.44 (m, 4H, CH₂), 1.40 – 1.30 (m, 4H, CH₂), 1.30 – 1.15 (m, 24H, CH₂).

¹³C NMR (101 MHz, DMSO-*d*₆) δ 172.16, 160.24, 154.60, 154.44, 138.08, 137.78, 136.84, 136.76, 129.92, 129.10, 128.23, 126.55, 125.36, 122.74, 119.35, 116.90, 109.91, 68.38, 64.43, 53.96, 53.72, 37.67, 28.93, 28.87, 28.63, 28.35, 28.01, 25.30, 17.19.

HRMS (ESI, *m/z*) 1335.2278 [*M* + Na]⁺, 1335.2248 calculated for C₆₁H₇₆Br₄N₄O₈Na

BrPhO11Xyl



Preparation was achieved following the method C using 11-(3,5-dibromophenoxy)undecyl (S)-phenylalaninate ammonium tosylate salt and 4,6-dimethyl-1,3-diaminobenzène.

The product is recrystallized in acetonitrile.

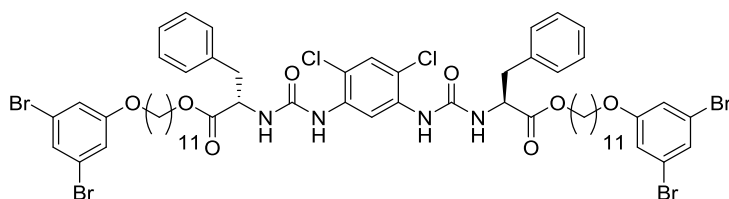
720 mg (79%) of a pure product were obtained as a white paste.

¹H NMR (400 MHz, DMSO-*d*₆) δ 7.96 (s, 1H, ArH), 7.76 (s, 2H, NH), 7.36 – 7.11 (m, 19H, ArH), 6.84 (s, 1H, ArH), 6.71 (d, 2H, NH, *J* = 7.8 Hz), 4.50 (q, 2H, NH-CH, *J* = 7.1 Hz), 4.03 – 3.91 (m, 8H, COO-CH₂ and ArO-CH₂), 3.07 – 2.92 (m, 4H, NH-CH-CH₂), 2.05 (s, 6H, Ar-CH₃), 1.65 (p, 4H, CH₂, *J* = 6.7 Hz), 1.56 – 1.42 (m, 4H, CH₂), 1.42 – 1.12 (m, 28H, CH₂).

¹³C NMR (101 MHz, DMSO-*d*₆) δ 172.26, 160.24, 154.72, 136.86, 135.27, 131.17, 129.10, 128.20, 126.51, 125.36, 122.74, 122.34, 116.90, 68.38, 64.41, 53.89, 37.73, 28.94, 28.88, 28.86, 28.64, 28.36, 28.00, 25.31, 25.27, 17.18.

HRMS (ESI, *m/z*) 1349.2435 [*M* + Na]⁺, 1349.2404 calculated for C₆₂H₇₈Br₄N₄O₈Na

BrPhO11Cl



Preparation was achieved following the method C using 11-(3,5-dibromophenoxy)undecyl (S)-phenylalaninate ammonium tosylate salt and 4,6-dichloro-1,3-diaminobenzène.

The product is recrystallized in acetonitrile.

890 mg (96%) of pure product were obtained as a white powder.

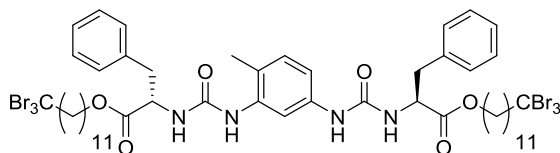
¹H NMR (400 MHz, DMSO-*d*₆) δ 8.93 (s, 1H, ArH), 8.20 (s, 2H, NH), 7.43 (s, 1H, ArH), 7.41 (d, 2H, ArH, $J = 7.8$ Hz), 7.31 (t, 2H, ArH, $J = 1.6$ Hz), 7.31 – 7.17 (m, 10H, ArH), 7.14 (d, 4H, ArH and NH, $J = 1.7$ Hz), 4.49 (q, 2H, NH-CH, $J = 7.4$ Hz), 4.00 (t, 4H, COO-CH₂, $J = 6.4$ Hz), 3.96 (t, 4H, Ar-O-CH₂, $J = 6.4$ Hz), 2.99 (m, 4H, NH₃-CH-CH₂), 1.65 (p, 4H, COO-CH₂-CH₂, $J = 6.7$ Hz), 1.54 – 1.41 (m, 4H, CH₂), 1.41 – 1.29 (m, 4H, CH₂), 1.29 – 1.10 (m, 28H, CH₂).

¹³C NMR (101 MHz, DMSO-*d*₆) δ 171.97, 160.23, 153.86, 136.71, 135.43, 129.04, 128.24, 128.13, 126.57, 125.35, 122.73, 116.89, 114.28, 68.37, 64.50, 53.97, 37.48, 28.94, 28.87, 28.64, 28.62, 28.36, 27.99, 25.28.

HRMS (ESI, *m/z*) 1389.1322 [*M* + Na]⁺, 1389.1312 calculated for C₆₀H₇₂Br₄Cl₂N₄O₈Na

b. Bis-ureas bearing an halogen moiety

Br3C11Tol



Preparation was achieved following the method B using 12-tribromododecyl (S)-phenylalaninate ammonium tosylate salt.

The product is recrystallized in acetonitrile.

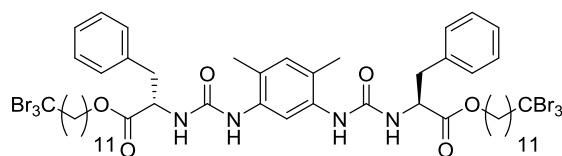
2.036 g (84%) of a pure product were obtained as a white paste.

¹H NMR (300 MHz, DMSO-*d*₆) δ 8.59 (s, 1H, NH), 7.80 (s, 1H, NH), 7.72 (d, 1H, ArH, $^2J = 1.7$ Hz), 7.36-7.02 (m, 11H, ArH and NH), 6.93 (d, 2H, ArH, $^2J = 8.2$ Hz), 6.27 (d, 2H, ArH, $^2J = 7.7$ Hz), 4.48 (p, 2H, NH-CH, $^2J = 7.0$ Hz), 4.01 (t, 4H, COO-CH₂, $^2J = 6.3$ Hz), 3.06-2.90 (m, 8H, NH₃-CH-CH₂ and CBr₃-CH₂), 2.07 (s, 3H, Ar-CH₃), 1.67 (p, 4H, COO-CH₂-CH₂, $^2J = 7.5$ Hz), 1.59-1.45 (m, 4H, ArO-CH₂-CH₂), 1.45-1.15 (m, 28H, CH₂)

¹³C NMR (101 MHz, DMSO-*d*₆) δ 172.17, 154.60, 138.08, 137.78, 136.84, 136.77, 129.93, 129.12, 128.25, 126.57, 119.38, 111.58, 109.92, 64.45, 58.68, 53.72, 43.37, 37.69, 37.54, 29.16, 28.86, 28.74, 28.62, 28.02, 27.08, 25.27, 17.22.

HRMS (ESI, *m/z*) 1335.0275 [*M* + Na]⁺, 1335.0247 calculated for C₅₁H₇₀Br₆N₄O₆Na

Br3C11Xyl



Preparation was achieved following the method C using 12-tribromododecyl (S)-phenylalaninate ammonium tosylate salt and 4,6-dimethyl-1,3-diaminobenzène.

The product is recrystallized in acetonitrile.

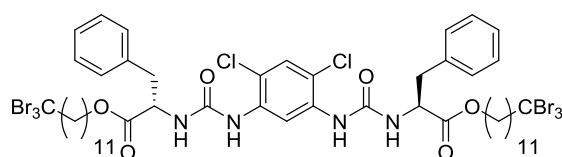
707 mg (28%) of a pure product were obtained as a white paste.

¹H NMR (300 MHz, DMSO-*d*₆) δ 7.95 (s, 1H, ArH), 7.75 (s, 2H, NH), 7.35-7.15 (m, 13H, ArH and NH), 6.98-6.80 (m, 8H, ArH and NH), 6.85 (s, 1H, ArH), 6.70 (d, 2H, ArH, ²J = 7.8 Hz), 4.49 (q, 2H, NH-CH, ²J = 7.2 Hz), 4.00 (t, 4H, COO-CH₂, ²J = 6.4 Hz), 3.05-2.90 (m, CBr₃-CH₂ and NH₃-CH-CH₂, 8H), 2.05 (s, 6H, Ar-CH₃), 1.67 (p, 4H, COO-CH₂-CH₂, ²J = 7.3 Hz), 1.58-1.15 (m, 32H, CH₂)

¹³C NMR (101 MHz, DMSO-*d*₆) δ 172.26, 154.71, 144.47, 137.61, 136.86, 135.25, 131.18, 129.11, 128.22, 126.53, 122.38, 64.42, 58.65, 53.90, 43.37, 37.72, 29.15, 28.83, 28.71, 28.60, 28.00, 27.06, 25.25, 17.18.

HRMS (ESI, m/z) 1349.0413 [M + Na]⁺, 1349.0403 calculated for C₅₂H₇₂Br₆N₄O₆Na

Br3C11Cl



Preparation was achieved following the method C using 12-tribromododecyl (S)-phenylalaninate ammonium tosylate salt and 4,6-dichloro-1,3-diaminobenzène.

The product is recrystallized in acetonitrile.

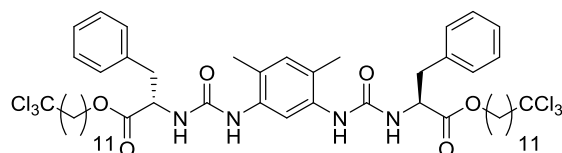
1.092 g (68%) of pure product were obtained as a white powder.

¹H NMR (300 MHz, DMSO-*d*₆) δ 8.91 (s, 1H, ArH), 8.19 (s, 2H, NH), 7.50-7.12 (m, 13H, ArH and NH), 4.57-4.42 (m, 2H, NH-CH), 4.00 (t, 4H, COO-CH₂, ²J = 4.7 Hz), 2.97 (m, NH₃-CH-CH₂ and CBr₃-CH₂, 8H), 1.78-1.58 (m, 4H, COO-CH₂-CH₂), 1.65-1.10 (m, 32H, CH₂)

¹³C NMR (101 MHz, DMSO-*d*₆) δ 171.97, 153.86, 136.72, 135.42, 129.05, 128.26, 128.13, 126.59, 114.30, 112.77, 64.50, 58.67, 53.98, 43.36, 37.48, 29.15, 28.85, 28.73, 28.61, 27.99, 27.08, 25.27.

HRMS (ESI, m/z) 1388.9324 [M + Na]⁺, 1388.9311 calculated for C₅₀H₆₆Br₆Cl₂N₄O₆Na

Cl3C11Xyl



Preparation was achieved following the method C using 12-trichlorododecyl (S)-phenylalaninate ammonium tosylate salt and 4,6-dimethyl-1,3-diaminobenzène.

The product is recrystallized in acetonitrile.

291 mg (64%) of a pure product were obtained as a white paste.

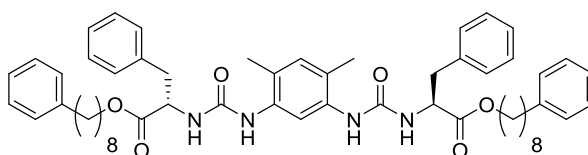
¹H NMR (300 MHz, DMSO-*d*₆) δ 7.95 (s, 1H, ArH), 7.75 (s, 2H, NH), 7.35-7.15 (m, 15H, ArH and NH), 6.98-6.80 (m, 8H, ArH and NH), 6.85 (s, 1H, ArH), 6.70 (d, 2H, ArH, ²*J* = 7.8 Hz), 4.49 (q, 2H, NH-CH, ²*J* = 7.2 Hz), 4.00 (t, 4H, COO-CH₂, ²*J* = 6.4 Hz), 3.04-2.94 (m, NH₃-CH-CH₂, 4H), 2.72 (t, CCl₃-CH₂, ²*J* = 7.9 Hz), 2.05 (s, 6H, Ar-CH₃), 1.67 (p, 4H, COO-CH₂-CH₂, ²*J* = 7.3 Hz), 1.58-1.15 (m, 32H, CH₂)

¹³C NMR (75 MHz, DMSO-*d*₆) δ 172.76, 155.22, 137.37, 135.77, 131.69, 129.61, 128.72, 127.02, 122.89, 116.16, 101.03, 64.92, 54.62, 54.41, 38.25, 29.34, 29.31, 29.17, 29.11, 28.51, 27.98, 26.59, 25.77, 17.68.

HRMS (ESI, m/z) 1083.3474 [M + Na]⁺, 1083.3446 calculated for C₅₂H₇₂Cl₆N₄O₆Na

c. Bis ureas bearing a phenyl moiety

PhC8Xyl



Preparation was achieved following the method C using 8-phenyloctyl (S)-phenylalaninate ammonium tosylate salt and 4,6-dimethyl-1,3-diaminobenzène.

The product is recrystallized in acetonitrile.

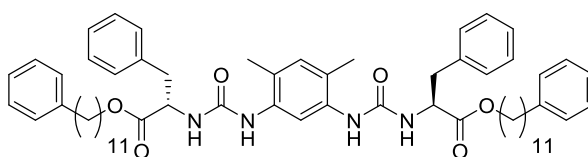
472 mg (58%) of a pure product were obtained as a white paste.

¹H NMR (400 MHz, DMSO-*d*₆) δ 7.97 (s, 1H, ArH), 7.77 (s, 2H, NH), 7.39 – 7.05 (m, 20H, ArH), 6.85 (s, 1H, ArH), 6.71 (d, 2H, NH, *J* = 8.0 Hz), 4.51 (q, 2H, NH-CH, *J* = 7.1 Hz), 3.99 (t, 4H, COO-CH₂, *J* = 6.5 Hz), 3.11 – 2.87 (m, 4H, NH₃-CH-CH₂), 2.54 (t, 4H, Ph-CH₂, *J* = 7.7 Hz), 2.06 (s, 6H, Ar-CH₃), 1.65 – 1.38 (m, 8H, CH₂), 1.38 – 1.09 (m, 16H, CH₂).

¹³C NMR (101 MHz, DMSO-*d*₆) δ 172.26, 154.73, 142.25, 136.86, 135.27, 131.20, 129.11, 128.22, 128.17, 128.13, 126.52, 125.50, 122.38, 115.62, 114.49, 64.40, 53.90, 37.74, 35.14, 30.96, 28.69, 28.57, 27.98, 25.24, 17.18.

HRMS (ESI, m/z) 917.5201 [M + Na]⁺, 917.5188 calculated for C₅₆H₇₀N₄O₆Na

PhC11Xyl



Preparation was achieved following the method C using 11-phenylundecyl (S)-phenylalaninate ammonium tosylate salt and 4,6-dimethyl-1,3-diaminobenzène.

The product is recrystallized in acetonitrile.

833 mg (73%) of a pure product were obtained as a white paste.

¹H NMR (300 MHz, DMSO-*d*₆) δ 7.95 (s, 1H, ArH), 7.75 (s, 2H, NH), 7.38-7.10 (m, 20H, ArH and NH), 6.84 (s, 1H, ArH), 6.69 (d, 2H, ArH, ²*J* = 8.1 Hz), 4.49 (q, 2H, NH-CH, ²*J* = 7.0 Hz), 3.99 (t, 4H, COO-CH₂, ²*J* = 6.6 Hz), 3.10-2.90 (m, NH₃-CH-CH₂, 4H), 2.54 (t, 4H, Ph-CH₂, ²*J* = 6.7 Hz), 2.05 (s, 6H, Ar-CH₃), 1.51 (p, 4H, COO-CH₂-CH₂, ²*J* = 7.9 Hz), 1.58-1.15 (m, 28H, CH₂)

¹³C NMR (101 MHz, DMSO-*d*₆) δ 172.26, 154.72, 142.24, 136.86, 135.27, 131.19, 129.10, 128.21, 128.16, 128.12, 126.51, 125.50, 122.36, 115.62, 64.41, 53.90, 53.90, 37.73, 35.15, 30.98, 28.96, 28.93, 28.84, 28.64, 28.61, 28.00, 25.26, 17.17, 17.17.

HRMS (ESI, m/z) 1001.6121 [M + Na]⁺, 1001.6127 calculated for C₆₂H₈₂N₄O₆Na

- [1] S. L. Mayo, B. D. Olafson, W. A. Goddard, *J. Phys. Chem.* **1990**, *94*, 8897–8909.
- [2] H. Sun, *Macromolecules* **1995**, *28*, 701–712.
- [3] H. Sun, *J. Comput. Chem.* **1994**, *15*, 752–768.
- [4] S. Nosé, Shūichi, *Molecular Physics* **1984**, *52*, 255–268.
- [5] M. J. Frisch, G. W. Trucks, H. B. Schlegel, G. E. Scuseria, M. A. Robb, J. R. Cheeseman, G. V. Scalmani, B. Barone, G. A. Mennucci, H. Petersson, et al., *Gaussian 09, Revision E.01*, Gaussian, Inc., Wallingford CT, **2009**.

Title: Engineering new urea-based supramolecular polymers for the characterization of weak interactions in solution : the supramolecular balance

Abstract: New self-assembling bis-urea molecules bearing an ester moiety have been synthesized and their properties studied. These ester bis-ureas display two new assemblies: a helical filament and a double helical filament. A cooperative transition is observed between the two structures at a temperature T^{**} . The structure of these assemblies was studied using a combination of FTIR, SANS, CD and molecular modeling. This new design allows an easy access to chiral bis-ureas that were used in the context of three different projects. (1) In the context of chirality amplification, the majority rules effect in ester bis-ureas was studied in order to determine a structure-property relationship. (2) Some ester bis-ureas presented all the necessary properties for their use as a supramolecular balance designed to measure weak interactions in solution. We used this system to measure halogen...halogen interactions in low polarity solvents as those were, to our knowledge, never observed in solution. (3) With specific ester bis-ureas, a third type of assembly was observed at lower temperature that is characterized by the formation of hydrogen bonds between urea and ester moieties. Surprisingly, the reorganization of these hydrogen bonds during heating is responsible for an increase in viscosity. This property allows these compounds to be potential thermothickening additives.

Keywords: bis-urea; supramolecular polymer; majority rules; supramolecular balance; weak interactions; halogen...halogen interactions; thermothickening additive

Titre : Ingénierie de nouveaux polymères supramoléculaires à base d'urées pour la caractérisation d'interactions faibles en solution : la balance supramoléculaire

Résumé : De nouvelles molécules de bis-urée contenant une fonction ester et ayant la capacité de s'auto-assembler en solution ont été synthétisées. Ces bis-urées ester forment deux types d'assemblages : un filament hélicoïdal et un double filament hélicoïdal. Une transition coopérative entre les deux structures est observée à une température T^{**} . La structure de ces assemblages a été étudiée à l'aide d'une combinaison de FTIR, SANS, CD et modélisation moléculaire. Ce nouveau design permet un accès simplifié à des structures chirales qui ont été utilisées dans le contexte de trois projets différents. (1) Dans le contexte de l'amplification de chiralité, l'effet « majority rules » que présente les bis-urées ester a été étudié de façon à déterminer une relation structure-propriété. (2) Certaines bis-urées ester présentent toutes les propriétés nécessaires à leur utilisation en tant que balance supramoléculaire pour la mesure d'interactions faibles en solution. Nous avons utilisé ce système pour mesurer des interactions halogène...halogène dans des solvants de faible polarité. A notre connaissance, ces dernières n'avaient jamais été observées en solution. (3) Dans le cas de quelques bis-urées ester, un troisième type d'assemblage est observé à plus basse température qui est caractérisé par la formation de liaisons hydrogène entre les groupements urée et ester. De manière surprenante, la réorganisation de ces liaisons hydrogène pendant le chauffage est responsable d'une augmentation de la viscosité. Cette propriété fait de ces composés de potentiels additifs thermoépaississants.

Mots-clefs : bis-urée ; polymère supramoléculaire ; majority rules ; balance supramoléculaire ; interactions faibles ; interactions halogène...halogène ; additif thermoépaississant